

ゼオライト担持金属二元機能触媒による脂肪酸エステルの水
素化脱酸素および異性化反応に関する研究

2016.3

東京農工大学大学院

生物システム応用科学府

生物システム応用科学専攻

陳 寧

**Study on Hydrodeoxygenation and Isomerization of
Fatty Acid Esters over Bifunctional Zeolite-
Supported Metal Catalysts**

**Graduate School of Bio-Applications and Systems Engineering,
Tokyo University of Agriculture and Technology**

Ning Chen

2016.2

Contents

Chapter 1

General Introduction	1
1.1 Transformation of Natural Triglycerides into Biofuels.....	1
1.2 Deoxygenation of Triglyceride-Related Compounds over Transition Metal Sulfide (TMS) Catalysts.....	5
1.2.1 Deoxygenation Kinetics and Reaction Pathways	5
1.2.2 Deoxygenation Mechanisms	9
1.2.3 Catalyst Deactivation	13
1.3 Deoxygenation of Triglyceride-Related Compounds over Supported Noble Metal Catalysts.....	14
1.3.1 Deoxygenation Kinetics and Reaction Pathways	14
1.3.2 Deoxygenation Mechanisms	17
1.3.2 Catalyst Deactivation	18
1.4 Deoxygenation of Triglyceride-Related Compounds over Supported Nickel Catalysts.....	20
1.4.1 Deoxygenation Kinetics and Reaction Pathways	20
1.4.2 Deoxygenation Mechanisms	27
1.4.3 Catalyst Deactivation	28
1.5 Bifunctional Catalysts for Simultaneous Deoxygenation-Isomerization of Triglyceride-Related Compounds.....	30
1.6 Purpose of This Study	38
References.....	44

Chapter 2

Simultaneous Hydrodeoxygenation-Isomerization of Jatropha Oil and Methyl Laurate over Reduced NiMo Catalysts	52
2.1 Introduction	53
2.2 Experimental Section.....	55
2.2.1 Catalyst Preparation	55
2.2.2 Catalyst Characterization	55
2.2.3 Activity Test	57
2.3 Results and Discussion	59
2.3.1 Catalyst Characterization	59

2.3.2 Hydrotreating of Jatropha Oil over Reduced NiMo Catalysts	68
2.3.3 Effect of Reduction Temperature on NiMo/SAPO-11 in Hydrotreating of Methyl Laurate	72
2.3.4 Catalyst Structure-Performance Relationship	79
2.4 Conclusions	86
References.....	87

Chapter 3

Enhanced Activity of PtSn/SAPO-11 for Simultaneous Hydrodeoxygenation-Isomerization of Methyl Palmitate **90**

3.1 Introduction	91
3.2 Experimental Section.....	94
3.2.1 Catalyst Preparation	94
3.2.2 Catalyst Characterization	94
3.2.3 Activity Test	96
3.3 Results and Discussion	98
3.3.1 Screening of PtX/SAPO-11 Catalysts for Hydrotreating of Methyl Stearate	98
3.3.2 Effect of Sn/Pt Ratio on the Activity of PtSn/SAPO-11	99
3.3.3 Catalyst Characterization	103
3.3.4 Catalyst Structure-Performance Relationship	114
3.4 Conclusions	120
References.....	121

Chapter 4

Selective Formation of Mono-Branched Isomers in Hydrotreating of Methyl Palmitate Using Bifunctional Catalysts Supported on Core-shell Structural Zeolite **125**

4.1 Introduction	126
4.2 Experimental Section.....	129
4.2.1 Materials	129
4.2.2 Synthesis of ZSM-22 and ZSM-22@SiO ₂	129
4.2.3 Catalyst Preparation	130
4.2.4 Catalyst Characterization	130
4.2.5 Activity Test	132
4.3 Results and Discussion	134
4.3.1 Characterization of the support	134

4.3.2 Effect of Silica Coating Amount and SiO ₂ /Al ₂ O ₃ Ratio on the Catalytic Performance	142
4.3.3 Enhanced Activity of Silica-Coated Catalysts by Using Bimetals	148
4.3.4 Structure-Performance Relationship	150
4.4 Conclusions	157
References.....	158

Chapter 5

General Conclusions	162
----------------------------	------------

List of Publications	165
-----------------------------	------------

List of Related Publications	166
-------------------------------------	------------

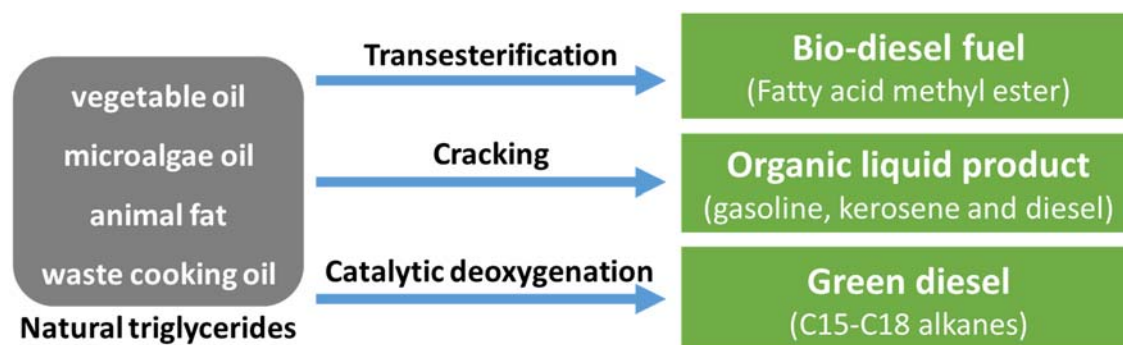
Acknowledgements	167
-------------------------	------------

Chapter 1

General Introduction

1.1 Transformation of Natural Triglycerides into Biofuels

To reduce dependence on petroleum and increase related concerns about global environmental conservation, transition of feedstock from petroleum to biomass has become highly desirable.¹ Biomass such as rice straw and vegetable oils can be transformed into biofuels or petrochemicals through chemical conversions. Compared to fossil fuels, biofuels are a kind of more sustainable and cleaner energy carrier; they are naturally carbon neutral and thus substantially cut the CO₂ emissions. Only trace amounts of S and N exist in biofuels, which could radically resolve those environmental problems originated from S- and N- containing pollutants in petroleum-derived transportation fuels. Among many renewable resources, triglyceride- or fatty acid-containing bioresources, *e.g.*, vegetable oils, microalgae oils, animal fats and waste cooking oils, have advantages of high energy density and structural similarity to petroleum-based fuels. However, directly using these compounds for diesel engines would cause many problems including carbon deposits, coking on the injectors and oil ring sticking due to their high viscosity, low volatility, and the presence of a large number of unsaturated bonds. As a result, three upgrading routes, *i.e.*, catalytic cracking, transesterification and catalytic deoxygenation, have been proposed to produce bio-fuels from triglycerides (**Scheme 1.1**).

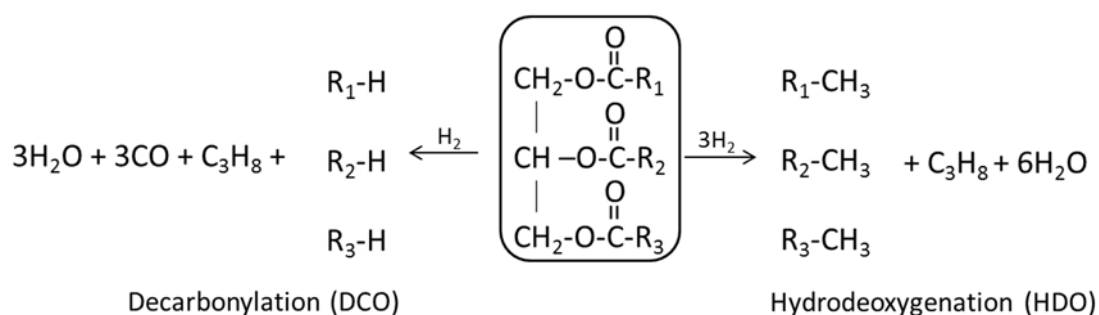


Scheme 1.1 Main routes for upgrading natural triglycerides.

Transesterification is the major commercial process for triglycerides upgrading. Products from this process are fatty acid methyl esters (FAMES), the so-called first generation biodiesel fuel (BDF). BDF is mostly popular in Europe because of its strict environmental regulations and the highest share of diesel-engine-driven cars in the world. Transesterification can be catalyzed by acid catalysts, base catalysts or enzymes. Because of the high activity of alkaline catalysts such as sodium and potassium hydroxide, they were employed as the first generation catalysts for commercial transesterification processes. Unfortunately, a side reaction, *i.e.*, saponification of fatty acids, simultaneously occurs in the presence of an alkaline catalyst, resulting in additional requirements of neutralization and separation. In this sense, solid acid catalysts are developed to tackle this problem. However, acid catalysts showed much lower activity, requiring a higher reaction temperature and longer reaction time, which would significantly raise the process cost. Consequently, development of an efficient acid catalyst is of importance prior to extensive scale-up.

Catalytic cracking is usually operated at a relatively high temperature, *i.e.*, 350–550 °C, and under atmospheric pressure. Catalysts used for this process possess a strong acid function. To our knowledge, catalytic cracking processes of triglycerides date back to the 1920s. Early researches used Al₂O₃ or MgO as a catalyst to decompose the large molecule at high temperatures (400–500 °C). New generation catalysts based on amorphous aluminosilicates and zeolites (*e.g.*, HZSM-5, HBEA, USY and SAPO-5) have been developed. Owing to their strong acidity and special pore structures, the reaction temperature could be lowered, down to 350–450 °C. Main products of acid-catalyzed cracking reaction are hydrocarbon gases (C₃–C₅), organic liquid products (OLP, *i.e.*, a mixture of aliphatic and aromatic hydrocarbons) and coke. Obviously, OLP are the most desired products for potential fuels and petrochemicals. Hierarchically structural materials such as HZSM-5/MCM-41 and HZSM-5/SBA-15, which have a composite microporous/mesoporous structure, have been employed to decrease the formation of gaseous products and coke, thereby enhancing the OLP yield. Although many studies have been done for this process, low selectivity of the desired product limits its application to a large-scale process.

Hydrotreating of natural triglycerides is receiving increased attention in the context of upgrading bio-based feedstocks. Triglycerides can be converted into diesel-like hydrocarbons, which are entirely fungible with fossil fuels. In addition, the hydrotreating process would require minimal changes in the present infrastructure; the equipment used for petroleum refining can be conveniently employed for hydrotreating of triglycerides. In hydrotreating of triglycerides, two major reaction pathways have been proposed: hydrodeoxygenation (HDO) and decarbonylation (DCO).^{2, 3, 4, 5, 6, 7, 8} Example reactions are displayed in **Scheme 1.2**. For the HDO route, oxygen is removed as water, and the resulting hydrocarbons have the same carbon numbers with the corresponding fatty acid bound in the original triglyceride. In contrast, DCO refers to a route where the oxygen in the carboxylic acid group is removed as CO and H₂O, generating hydrocarbons with one carbon atom lesser than the corresponding fatty acid chain. A deoxygenation reaction proceeds *via* a DCO route would reduce the liquid product yield by approximately 5%. In contrast, DCO would be superior to HDO when considering the hydrogen consumption.



Scheme 1.2 General reaction pathways in hydrotreating of triglycerides.

Several reviews dealing with the deoxygenation of triglyceride-related compounds have been published. Most of them focused on the process such as reaction conditions and feedstocks rather than catalysis. However, catalysis is a major science behind sustainable energy, and whatever the energy source is, a clean and sustainable energy future will involve catalysis.⁹ In this chapter, recent studies

(mainly within 5 years) concerning the fundamental of catalysis for hydrotreating of triglycerides and related model compounds (hereafter denotes as TG-related compounds) were reviewed. These studies are particularly useful in comparing the performance of catalysts, especially in understanding the reaction kinetics and mechanism. The chapter will be divided into two main sections based on the reaction in hydrotreating of TG-related compounds. In the first part, deoxygenation reactions with special attention on research that aimed at understanding deoxygenation mechanisms over different types of metal catalysts are reviewed. The nature of supported metals and the way of promoting deoxygenation rate are discussed. Mechanisms, reaction pathways and structure-function relationships are emphasized. The second section will focus on those catalysts that used in the simultaneous deoxygenation-isomerization of TG-related compounds to produce green diesel fuels with good cold flow properties. The catalytic performance in this tandem reaction is strongly dependent on the property of support. Therefore, the nature of supports (*i.e.*, acidity and porosity) becomes the main consideration.

1.2 Deoxygenation of Triglyceride-Related Compounds over Transition Metal Sulfide (TMS) Catalysts

TMS catalysts belong to the most important industrial catalysts since they have been used in hydrotreating processes (*i.e.*, hydrodesulfurization and hydrodenitrogenation) for decades. These catalysts typically comprise sulfided molybdenum (15-20 wt%) on an gamma-alumina ($\gamma\text{-Al}_2\text{O}_3$) support with nickel or cobalt (3-6 wt%) as a promoter. Other base metals such as tungsten and ruthenium have been investigated as well but have not found widespread use commercially. The TMS catalysts possess high heteroatom removal capability in hydrotreating processes. It is therefore no surprise that they have been employed for the hydrodeoxygenation of renewable feedstocks. To date, the only industrial application of triglyceride hydrotreatment relies on the use of supported metal sulfide catalysts. Hydrotreating of TG-related compounds over TMS catalysts is usually conducted above 300 °C with a high hydrogen pressure (5-10 MPa) in order to achieve a complete deoxygenation. Reactions conducted below this temperature or under a lower hydrogen pressure would enhance the formation of oxygenates such as fatty alcohols and esters. Recently, studies using model compounds provided both insight into the mechanism on the molecular level and evidence on how to control the deoxygenation pathway. In this section, the deoxygenation mechanism, kinetics and relative activity of catalysts are discussed to show the potential benefits and detriments of using a sulfided catalyst for the deoxygenation of TG-related compounds.

1.2.1 Deoxygenation Kinetics and Reaction Pathways

The reactivity of TG-related compounds follows the trend: aliphatic alcohols > aliphatic aldehydes > alkyl ethers > carboxylic acids > triglycerides.¹⁰ In addition, evidence from comparing the reactivity of dibenzothiophene and dibenzofuran demonstrated that HDO is a slower reaction than HDS.¹¹ Therefore, more efficient

catalysts should be designed for HDO processes. The activity of TMS catalysts in deoxygenation reactions is generally following the trend: NiMo > CoMo > Mo > Ni. Bimetallic catalysts, *i.e.*, NiMo and CoMo, are reported to exhibit higher activity than single metal catalysts due to their “synergy effects”; i) “ensemble effect” caused by the influence of geometry and ii) “ligand effect” due to the influence of electronic interaction.¹² Promoters could increase the catalytic activity of the main active metal by donating electrons to the metal, and thus weakening the metal-S bond. However, the amount of promoter is a crucial parameter in bimetallic TMS catalysts. Ferdous *et al.* found that excess promoters can accumulate on the desired MoS₂ phase and make the catalyst inactive.¹³

Brimont *et al.* investigated the deoxygenation of ethyl heptanoate catalyzed by three unsupported TMS catalysts, *i.e.*, MoS₂, Ni₃S₂ and Ni-promoted MoS₂.¹⁰ Deoxygenation activities of the studied catalysts followed the trend: NiMoS (0.43) > MoS₂ > NiMoS (0.2) ≈ NiMoS (0.1) >> Ni₃S₂ (the numbers in the brackets denotes the atom ratio of Ni to Mo). Results highlight the promoting effect of Ni on the MoS₂ phase for deoxygenation reaction. “Synergy effect” induced by the formation of NiMoS phase can be used to interpret this behavior. This promoting effect could be also explained by a density functional theory (DFT) calculation.¹⁴ Calculation results suggest that the energy barriers for hydrogenation of C=O and C-OH bonds are smaller on NiMoS with respect to MoS₂. Unlike those Al₂O₃-supported catalysts, however, the addition of a small amount of Ni to the MoS₂ phases would reduce the deoxygenation activity of unsupported catalysts. This behavior might be related to the difference in stacking layer or crystal size between supported and unsupported catalysts. In the deoxygenation of fatty acids or esters, total conversion is always higher on Ni-promoted catalysts than on Co-promoted catalysts, suggesting that the NiMo catalyst is more active for deoxygenation of aliphatic oxygen-containing compounds.^{5, 7, 15, 16, 17, 18, 19} Senol *et al.* compared the performance of sulfided CoMo/Al₂O₃ and NiMo/Al₂O₃ catalysts in hydrotreating of methyl heptanoate.²⁰ Heptane was the major hydrocarbon product on the NiMo/Al₂O₃ catalyst, while heptene became major on CoMo/Al₂O₃. The NiMo catalyst was thus considered to

possess higher hydrogenation activity. A reaction pathway of C–O bond cleavage and further hydrogenation of the resulting alkene (direct deoxygenation, DDO) was proposed taken into account of this result (**Figure 1.1**). In contrast, another reaction pathway of alcohol hydrodeoxygenation (HDO) was favorable on CoMo/Al₂O₃. These behaviors of CoMo and NiMo catalysts in deoxygenation of TG-related compounds are similar to those in the deoxygenation of phenol, in which HDO and DDO are involved.^{21, 22, 23} It should be noted that a large amount of hydrogen is required to reach the point of full deoxygenation by either pathway. In this sense, NiMo catalysts are more efficient in hydrotreating of TG-related compounds because of their high hydrogenation activity.

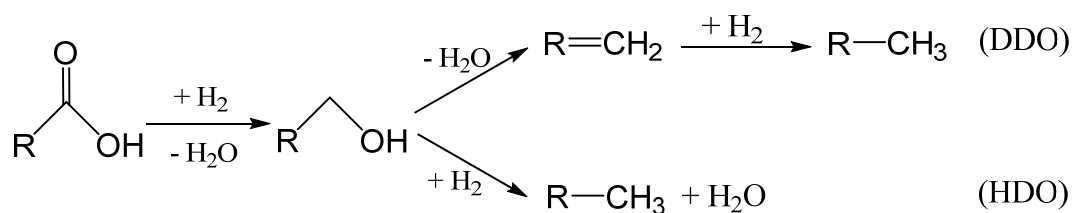
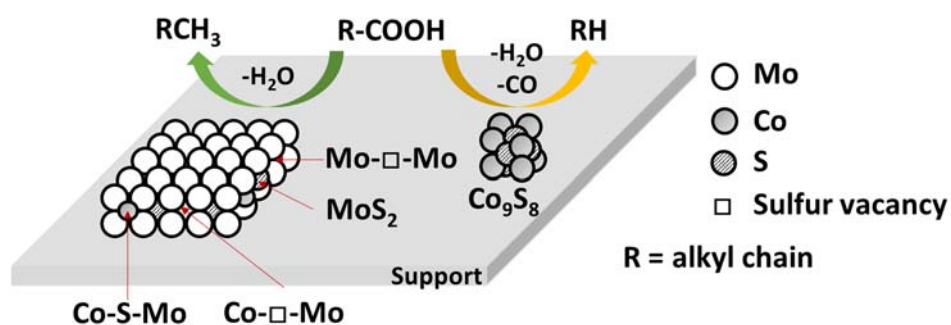


Figure 1.1 Example HDO and DDO reaction pathways of alcohol over TMS catalysts (R refers to an aliphatic chain).

On the other hand, using those promoters, *i.e.*, boron or phosphorous, would create new Lewis and Brønsted acid sites, increasing the overall acidity of the catalyst. In addition, boron can change the structure of molybdenum oxides by enhancing the density of octahedral species rather than tetrahedral species. Moreover, these promoters can also change the catalyst geometry by increasing the number of stacks. Kubicka *et al.* investigated the effect of acidity on the deoxygenation activity of sulfided CoMo catalysts supported on Al-MCM-41 (an ordered mesoporous silica) with different Si/Al ratios, and found that the lower Si/Al ratio of the support was, the higher deoxygenation acidity would be.¹⁸

Recent studies on hydrotreating of TG-related compounds over TMS catalysts show more interest in discussion of the reaction pathways. Although fatty acids bound

in a natural triglyceride usually have an even number of carbons in their carbon chains, the resulting hydrocarbons from a hydrotreating process have either even or odd number of carbons because the deoxygenation reaction could proceed *via* HDO or DCO routes. If it doesn't take hydrogen consumption into account, HDO is more desired because the carbons bound in the fatty acid is preserved and the by-product is water only. HDO or DCO selectivity is largely influenced by the active phase, support and reaction conditions. Kubicka *et al.* studied the deoxygenation behaviors over sulfided Ni/Al₂O₃, Mo/Al₂O₃ and NiMo/Al₂O₃ catalysts.⁵ The HDO selectivity decreased in the order Mo/Al₂O₃ > NiMo/Al₂O₃ > Ni/Al₂O₃. Especially on the Ni/Al₂O₃ catalyst, only DCO products can be generated. Unsupported catalysts showed a similar result. According to DFT calculations, decarbonylation of aldehyde, a main intermediate compound in deoxygenation of fatty acids or fatty acid methyl esters, occurs *via* its dehydrogenation into the alkanoyl and/or ketene intermediates on the Ni₃S₂ (111) surface. This pathway is more favorable on Ni₃S₂ than on MoS₂-based catalysts. Moreover, DCO activity could monotonously increase with increasing surface nickel density on NiMoS catalysts. Therefore, it is suggested that Ni₃S₂ species are the active sites in the sulfided NiMo catalyst. Similar to sulfided NiMo catalysts, the addition of Co into a MoS₂ catalyst would result in a decrease in HDO selectivity as well. The reason for this behavior could be attributed to the presence of sulfided Co species (*i.e.*, Co₉S₈). Consequently, different active sites on the sulfided catalyst show different deoxygenation behaviors; HDO is favored on the MoS₂ or Co/(Ni)MoS site, whereas DCO proceeds on the Co₉S₈ or Ni₃S₂ site (**Scheme 1.3**).



Scheme 1.3 HDO and DCO active sites in the TMS catalyst.

Hydrotreating performance of a catalyst might involve a contribution of the support. For example, γ - Al_2O_3 alone also has considerable activity in deoxygenation reactions due to its Lewis acid sites.²⁴ Supports with different pore sizes and surface areas exhibit different activity and selectivity. Kubicka *et al.* compared four CoMo catalysts with different supports; one was supported on a commercial γ - Al_2O_3 , two of those were supported on ordered mesoporous Al_2O_3 synthesized by different methods, and another one is supported on MCM-41.⁷ Ordered mesoporous Al_2O_3 -supported CoMo catalysts exhibited an HDO/DCO ratio (93:7) than the commercial catalyst (80:20). However, the HDO/DCO ratio over the MCM-41-supported catalyst was only 66:34. Two factors were considered to influence the reaction pathway: i) the type of metal oxide in those supports affects the nature of active phases through the metal–support interaction; ii) the pore structure of support affects the dispersion of active phases, including the length or the number of stacking layers in MoS_2 crystals. In addition, the dispersion might also influence the number of Ni_3S_2 or Co_9S_8 phase.

Reaction conditions such as temperature, hydrogen pressure and space velocity could also affect the reaction pathway. It was reported that an increase in the reaction temperature promoted DCO over HDO at a constant hydrogen pressure.^{5, 8, 25, 26, 27} Under an identical reaction temperature, an increase in hydrogen pressure suppressed DCO at the expense of HDO.^{18, 25, 26, 28} An increase in space velocity was unfavorable to HDO.^{5, 26} These findings were also supported by thermodynamic calculations.⁴¹ On the other hand, different catalysts were found to have different sensitivity to reaction conditions. For example, a promotion of DCO pathway by raising the reaction temperature was more sensitive over a NiMo catalyst than a CoMo catalyst.²⁹ A NiW catalyst showed higher sensitivity to the variation of hydrogen pressure than a NiMo or a CoMo catalyst.²

1.2.2 Deoxygenation Mechanisms

Reaction mechanisms on TMS catalysts are mainly hydrodeoxygenation (HDO) and decarbonylation (DCO). In brief, an HDO route involves initial hydrogenation of

the hydroxyl group ($-OH$) and carbonyl $C=O$ bond of a fatty acid, followed by dehydration or hydrogenation of the resulting alcohol to yield a hydrocarbon and water. In contrast, a DCO route involves hydrogenation of hydroxyl group and hydrogenolysis of $C-C$ bond that adjacent to the carbonyl group ($C-C(=O)$) to yield a hydrocarbon and CO . On the other hand, although CO_2 could also be found in gaseous products when the reaction is conducted at a higher temperature (above $350^\circ C$), the formation of CO_2 is extremely small compared to that of CO .^{30,31} It is possible that the generated CO_2 from a decarboxylation (DCO_2) reaction is converted into CH_4 through the methanation reaction, which is thermodynamically favored under those reaction conditions. Brillouet *et al.* designed an experiment to verify the reactivity of CO_2 , in which CO_2 was introduced into the reactor together with a fatty acid. In the outlet gas stream of the reactor, the same partial pressure of CO_2 was detected, indicating that CO_2 did not react with H_2 . Therefore, hydrocarbons with one carbon number lesser than the corresponding fatty acid could be only obtained by DCO.

As discussed above, the support has been considered to significantly affect a deoxygenation reaction. Kubickova *et al.* investigated the effect of support-active phase interactions on the catalytic activity and the reaction pathway in the deoxygenation of triglycerides. The study demonstrated that the nature of a support, *i.e.*, specific surface area, pore size distribution and acidity would largely affect the cluster size and the reducibility of the active phase.³² In this sense, the use of an unsupported catalyst is a good alternative to investigate the activity of the active phase. It is now well accepted that the active site of a TMS catalyst is those coordinatively unsaturated sites (CUS) at the edges of molybdenum crystals. These sites exhibit Lewis acidity, which can adsorb atoms with unpaired electrons. For a TMS catalyst, heteroatoms (*e.g.*, oxygen, sulfur or nitrogen) in the reactant could be adsorbed on these vacancies, while molecular hydrogen is activated on saturated edge and plane sites to form S-H groups. The synergistic effect makes the deoxygenation proceed smoothly.

Brillouet *et al.* proposed a mechanism for the deoxygenation of decanoic acid over an unsupported MoS_2 catalyst (**Figure 1.4**).¹⁰ The first step of the proposed

mechanism requires a dissociated adsorption of molecular hydrogen to generate a metal hydride (Mo–H) and a sulfhydryl (–SH) group (**Figure 1.4b**). The formation of –SH and Mo–H at the sulfur vacancy is exothermal and requires the minimal dissociation energy.³³ Decanoic acid could be adsorbed through its carbonyl group (C=O) on a sulfur vacancy (**Figure 1.4c**). The next step could be a protonation of decanoic acid due to the acidity of the –SH group (**Figure 1.4d**). After water elimination, the adsorbed carbocation is assumed to be a key intermediate (**Figure 1.4e**). This intermediate could undergo either an HDO route or a DCO route to generate the corresponding hydrocarbon (**Figure 1.5**). In the case of a MoS₂ catalyst, the addition of dissociated hydrogen (Mo–H) to the cationic intermediate leads to a scission of Mo–C bond, and other dissociated hydrogen preferentially interacts with C and O to form C–H and O–H bonds, respectively. Finally, the alcohol would undergo another C–O bond scission to form decane, and the catalyst surface restores to its original state. In contrast, C–C bond breaking could occur through a basic attack on the hydrogen atom in β -position because the carbon atom carries a positive charge of the cationic intermediate over a Ni(Co)-promoted catalyst, and the final production should be nonane and CO. The basic site could be a sulfur anion (S²⁻) species adjacent to the sulfur vacancy.³⁴ In addition, Co or Ni could increase the electron density of sulfur atoms, which can be a reasonable explanation for the promotion effect of Co or Ni on a DCO route. This type of mechanism was also proposed to explain the C-S bond scission occurring in the DDS way of dibenzothiophene.³⁵ Zhang *et al.* proposed a similar mechanism to explain the HDO route, while they made a different hypothesis for the DCO route.³⁶ In their hypothesis, a fatty acid adsorbed on highly nucleophilic HS groups through its C–C bond that adjacent to the C=O group (**Figure 1.6**). Subsequently, a scission of the weakened C–C bond occurs, resulting in the formation of a hydrocarbon with one carbon number lesser than the original fatty acid.

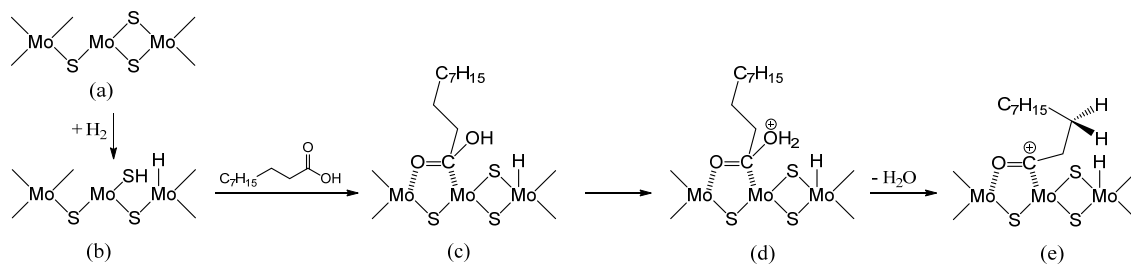


Figure 1.4 Proposed mechanism for the deoxygenation of decanoic acid on an unsupported active phase. Adapted from Brillouet *et al.*¹⁰

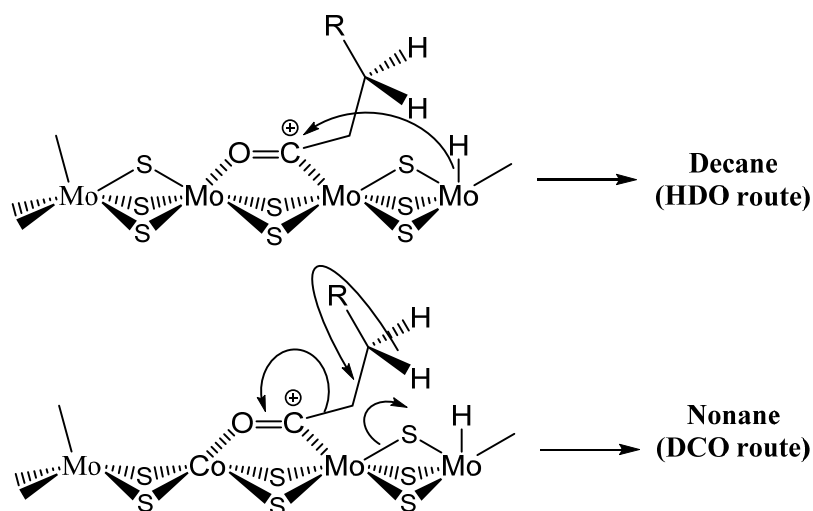


Figure 1.5 Description of elementary steps being likely to occur from the cationic intermediate adsorbed: hydrogenation of the cationic intermediate adsorbed onto an unprompted site (up); elimination step over a promoted site (down). Adapted from Brillouet *et al.*¹⁰

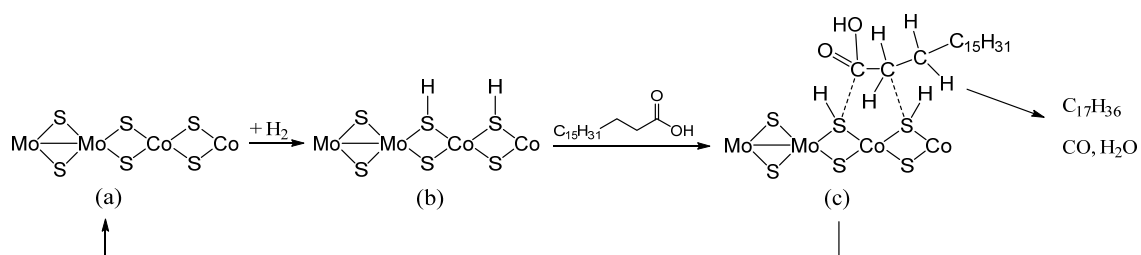


Figure 1.6 Main deoxygenation mechanism on CoMoS. Adapted from Zhang *et al.*³⁶

1.2.3 Catalyst Deactivation

The deactivation of a TMS catalyst is related to operating conditions, the composition of feedstock and impurities. Triglycerides, fatty acids and alkyl esters were reported to produce minimal coke as long as care is taken to remove inorganic impurities from the feed stream.^{37, 38} The triglyceride in vegetable oils always contains a large number of unsaturated bonds, which could significantly enhance the coke formation. In the hydrotreating process, however, a high hydrogen pressure is required, which may help to slow down the rate of coke formation.³⁹ Sulfur species are continuously removed from the catalyst by reacting with hydrogen to form H₂S or by binding to the reactant. This problem can be solved by adding some sulfur-containing compounds such as dimethyl disulfide (DMDS) into the feedstock or by adding a small amount of H₂S into the stream to maintain sulfur species.^{17, 40, 41, 42, 43} Reactant stream could oxidize the catalyst if it is not continuously sulfided. The promoter made this oxidation energetically less favorable but could not completely prevent it.⁴³ Unlike the deactivation mentioned above, the influence of which can be reversed through re-sulfidation, contaminants in crude vegetable oils would result in a permanent deactivation.⁴⁰ Kubicka *et al.* used several rapeseed oils with different upgrading degrees as feedstocks to investigate the deactivation factor for a sulfided CoMo/ γ -Al₂O₃ catalyst.⁴² These rapeseed oils differed in the concentration of alkalis, water, free fatty acids and phospholipids. They found that alkalis or phospholipids deposited on the active site could be the main reason of catalyst deactivation. In this sense, a crude feedstock without any purify process is not suitable for the hydrotreating process.

1.3 Deoxygenation of Triglyceride-Related Compounds over Supported Noble Metal Catalysts

Catalysts based on noble metals, *e.g.*, Pt, Pd, Ru, Ir and Rh, have been applied in various reactions. The most important application could be hydrogenation, including selective hydrogenation of oxygen-containing compounds, isomerization, cyclization, hydrocracking and dehydrogenation of hydrocarbons. For the deoxygenation of TG-related compounds, research attention has been turned to noble metal catalysts in response to the deactivation of TMS catalysts during hydrotreating processes.

1.3.1 Deoxygenation Kinetics and Reaction Pathways

Supported noble metal catalysts are attractive because of their high H₂ activation capacity and less susceptible to deactivation by water. These catalysts exhibit higher activity than Co or Ni and possess longer catalyst lifetimes. Early research work that used a noble metal for the deoxygenation of fatty acids was conducted in the absence of hydrogen (H₂-free) or just under a low hydrogen pressure.^{44, 45, 46, 47, 48, 49, 50} Snare *et al.* screened a number of metals (Pd, Pt, Ru, Ir, Rh, Os, Ni and NiMo) supported on carbon or other oxides (SiO₂, Al₂O₃, MgO and Cr₂O₃).⁵⁰ The deoxygenation pathway over these catalysts are decarboxylation or decarbonylation, yielding hydrocarbons with one carbon number less than the original fatty acid. The order of deoxygenation activity was Pd > Pt > Ni > Rh > Ir > Ru > Os. Palladium and platinum catalysts with active carbon as support exhibited high activity and selectivity toward heptadecane in the deoxygenation of stearic acid. Interestingly, the reaction pathways over the two catalysts are different; decarboxylation and decarbonylation are dominant on Pd/C and Pt/C, respectively. Studies concerning the deoxygenation of TG-related compounds over noble metal catalysts in the presence of H₂ were fewer than that over TMS catalysts. This might be due to the high cost of noble metal, and thus it seems difficult for them to be employed in a large-scale application. Nevertheless, if a noble catalyst with ultra-low metal containing but high activity and

reusability, it can be considered as an efficient catalyst for industrial use. In this context, several fundamental research work recently has been conducted for supported Pt catalysts.

Deoxygenation of heptanoic acid was studied over platinum catalysts supported on active carbons, which were named Norit carbon and Vulcan carbon, and silicon carbide.⁵¹ Decarbonylation was the main reaction route under different reaction conditions. Under liquid-phase operating conditions, *i.e.*, 300 °C and 3.7 MPa, hexenes and CO were the primary products at very low conversions; as conversion increased from 1% to 5%, substantial amounts of hexane and CO₂ were observed. However, the CO₂ formation was presumably from a side reaction, water-gas shift (WGS) reaction, instead of direct decarboxylation. In addition, the turnover frequency (TOF) was independent of Pt loading under this condition. For gas-phase operating condition, *i.e.*, 0.1 MPa, a terminal olefin was observed with high selectivity (57%). Under higher reaction pressure, the terminal olefin would undergo isomerization over Pt particles due to the high reactivity of their double bonds. As raised the reduction temperature from 350 to 500 °C, the dispersion of Pt particles dropped from 49% to 13%, accompanying with decreasing conversions, indicating that the sintering of Pt particles occurred in the pretreatment stage, and thus a high reduction temperature (> 400 °C) was not appropriate for Pt catalysts. The Pt particle size increased from 1.9 nm to 2.3 nm after the reaction, indicating that the sintering during the reaction could be also observed but was not severer. Although catalyst regeneration studies were performed over spent catalysts, it was fail to restore the catalytic activity.

The influence of support, platinum source, and reaction temperature on decarboxylation of oleic acid was investigated over Pt catalysts supported on zeolites and hydrotalcite.⁵² Decarbonylation selectivity could be enhanced by increasing the reaction temperature. Pt/SAPO-34 displayed a high selectivity to heptadecane and dodecylbenzene. An initially formed paraffin intermediate could be further transformed to branched, cyclic or alkyl aromatic hydrocarbon due to restricted transition state of shape-selectivity limitation in the SAPO-34 pore system. The Pt

catalyst prepared by using tetraammine platinum nitrate as the precursor had well-dispersed Pt metal nanoparticles, and thus showed higher deoxygenation activity. Metal precursor was proved to have an important role in the structure of final metal particle structure and dispersion.^{53, 54, 55}

A promotion effect based on Nb₂O₅ has been recently demonstrated.⁵⁶ Two studies reported the high activity and HDO selectivity of Pt and Pd supported on Nb₂O₅ and Nb₂O₅-SiO₂, respectively. Under 0.8 MPa H₂ pressure and at 180–250 °C, the Pt/Nb₂O₅ was efficient for hydrodeoxygenation of fatty acids and triglycerides. The catalyst gave high yields (88–100%) of linear alkanes with the same carbon number as the starting compound. A possible role of Nb₂O₅ as adsorption sites for carbonyl groups was evidenced by infrared (IR) study of acetic acid adsorption. A Lewis acid–base interaction between NbO_x cation and carbonyl oxygen was observed. Similar result can be found in the hydrodeoxygenation of model compounds over Pd/Nb₂O₅-SiO₂.⁵⁷ Stability tests showed that these Nb₂O₅ supported or added catalysts were hard to be deactivated. For Pt/Nb₂O₅, a much higher turnover number (TON) was obtained, which is 60 times higher than previously reported catalysts; for Pd/Nb₂O₅-SiO₂, the catalyst was stable during a 150 h time-on-stream test.⁵⁸

Deoxygenation of a fatty acid ester was performed over Ru/TiO₂ under a mild reaction condition of 200–240 °C and 3.0 MPa.⁵⁹ Although the reaction temperature was much lower than those reported in other literatures (300–360 °C), nearly 100% selectivity to hydrocarbons heptadecane and octadecane was obtained at complete conversion of the fatty acid ester. High activity of Ru/TiO₂ compared to other SiO₂- or Al₂O₃-supported catalysts could be attributed to a synergistic effect. The carboxylic group of a fatty acid ester could adsorb on the surface of TiO₂, followed by reacting with the dissociated hydrogen that spills from Ru nanoparticles.^{60, 61, 62} However, the catalytic activity showed a slight decrease during stability tests due to the leaching of Ru species.

Fewer studies concerning the hydrotreating of natural triglycerides used noble metal catalysts. Hydrodeoxygenation of a microalgae oil over 1% Pt/Al₂O₃, 0.5% Rh/Al₂O₃ and sulfided NiMo/Al₂O₃ were investigated.⁵⁸ The highest yield of

hydrocarbon was obtained over Pt/Al₂O₃ at 310 °C. At a lower reaction temperature, Pt/Al₂O₃ showed similar activity to NiMo/Al₂O₃, indicating that the use of Pt/Al₂O₃ can reduce the energy consumption to some degree. Reaction pathway over the sulfided NiMo/Al₂O₃ catalyst was affected by reaction conditions. As the H₂/oil ratio decreased, the reaction pathway was changed from HDO to DCO over NiMo/Al₂O₃. In contrast, reaction conditions can fairly affect the reaction pathway when Pt/Al₂O₃ or Rh/Al₂O₃ was used as a catalyst. Pt/Al₂O₃ and Rh/Al₂O₃, especially Rh/Al₂O₃, were found to be active for CH₄ formation, while no detectable amount of CH₄ was formed over NiMo/Al₂O₃. Methanation is an undesirable side reaction in hydrotreating of TG-related compounds because it would largely increase the hydrogen consumption.

Bimetallic PtRe/HZSM-5 catalysts with different Re loading were developed and used in the hydrotreating of Jatropha oil.⁶³ The addition of Re substantially enhanced deoxygenation activity of the catalyst. Under a high weight hourly space velocity (WHSV = 10 h⁻¹), the rhenium-modified Pt/HZSM-5 catalyst (Re/Al = 0.8) gave a high yield (67%) of C₁₅-C₁₈ alkanes, while only 2.3% was obtained over the monometallic Pt/HZSM-5 catalyst. In addition, the reaction over PtRe catalysts mainly proceeded *via* HDO. The promotion effect of Re could be also applicable for other metals such as Ni, Co, Pd and Ru.

1.3.2 Deoxygenation Mechanisms

Supported noble metal catalysts are well-known hydrotreating catalysts due to its high hydrogenation activity. This high activity can be related to its hydrogen dissociation ability and hydrogen spillover effect. Detailed structure–function analyses correlated to catalyst performance have led to the popular view that the metal activates hydrogen while the support and the metal–support interface are involved to transfer surface-H species (H*) to the substrate.⁶⁴ This synergistic effect between metal and support is represented in deoxygenation of a fatty acid in **Figure 1.7**. In the deoxygenation of fatty acid, hydrogen is dissociatively adsorbed on the surface of metal particles to form active H*, while the oxygen-containing substrate can be

adsorbed and activated on either metal sites or the oxygen vacancies. Subsequently, the dissociated hydrogen is transferred from metal particles to the adsorbed intermediate, leading to the cleavage of C-O bond accompanying with water formation. Polar molecular such as those have a carbonyl group are especially interactive with the support through the oxygen functionality.^{65, 66}

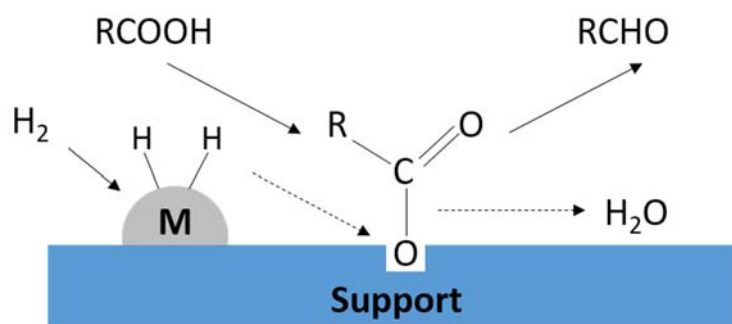


Figure 1.7 Deoxygenation mechanism over noble metal catalysts. Adapted from Mendes *et al.*⁶⁷ and Pestman *et al.*⁶⁶

1.3.2 Catalyst Deactivation

Possible reason for deactivation of noble metal catalysts could be poisoning, coking and sintering.⁶⁸ In deoxygenation of bio-oils, coking can be the main deactivation pathway because the process is usually conducted at a relatively high reaction temperature (> 400 °C). In contrast, coke formation could not be large in deoxygenation of TG-related compounds. It was reported that coke formation gradually increased with time on stream over a NiMo/Al₂O₃ catalyst in hydrotreating of a microalgae oil, while only a small amount of coke was found in the initial reaction time over a Pt/Al₂O₃ or a Rh/Al₂O₃ catalyst.⁶⁹ Noble metal catalysts could inhibit the carbon formation through their high hydrogen dissociation capacity, by which coke precursors could be readily hydrogenated.

Compared to coking, sintering of metal particles is a common deactivation pathway for noble metal catalysts. Studies evidenced that sintering of noble metal could be occurred during reduction at a temperature higher than 400 °C.⁵¹ On the other hand, water could significantly enhance the sintering rate. It should be noted

that even a small amount of water generated during the reduction process should be rapidly removed by controlling the hydrogen flow. However, a large amount of water could be formed in hydrodeoxygenation reaction, which would strongly affect the metal dispersion. Many studies have reported this kind of deactivation for noble catalysts.^{51, 59, 70} Adding another metal species to form alloy or adding metal oxides is available to stabilize the noble metal and prevent sintering.^{56, 57, 63}

In addition, noble metal catalysts are known to be poisoned by sulfur, nitrogen and phosphide species. Although monometallic catalysts are sensitive to S and N on a ppm level, bimetallic catalysts were reported to have greater tolerance of these poisons.^{64, 71} For example, supported PtPd catalysts were studied for HDS and HDN of gas-oils, and the catalyst with a Pd/Pt atomic ratio of 3.7 exhibited high S and N tolerance in a feedstock having 300 ppm S and 200 ppm N.⁷¹ Although poison is not a significant issue in the model compound studies, it represents a pathway for catalyst deactivation during hydrotreating of natural triglycerides, especially in the microalgae oil, which commonly have a considerable amount of nitrogen species. However, few studies investigated the poison of noble metal catalysts in hydrotreating of natural triglycerides. It might be that the hydrotreating process for natural triglycerides using a noble metal catalyst is still under less consideration to be a large scale.

1.4 Deoxygenation of Triglyceride-Related Compounds over Supported Nickel Catalysts

Research attention turned to supported nickel catalysts in response to the deactivation of TMS catalysts and the high cost of noble metal catalysts. To our knowledge, the first effort to investigate deoxygenation of TG-related compounds over a supported nickel catalyst was reported at 2006 by Snare *et al.*⁵⁰ In the study, however, very low catalytic activity was obtained, probably due to the absence of hydrogen. The second work concerning supported nickel catalysts was reported by Yakovlev *et al.* after three years (2009), and this could be the first contribution to the possibility of using a supported nickel catalyst in the deoxygenation of TG-related compounds.⁷² After 2012, an increasing number of contributions (approximately 15 reports per year) devoted to nickel-based catalysts were reported. In this section, the very recent studies relevant to the deoxygenation of TG-related compounds over supported nickel catalysts are summarized. **Table 1.1** gives the representative of recent literatures in this field including catalyst type, reactant, reaction conditions and dominant products.

1.4.1 Deoxygenation Kinetics and Reaction Pathways

Lercher's group did systematic studies of supported nickel catalysts. First, they investigated the effect of support acidity on the catalytic performance in deoxygenation of stearic acid and microalgae oil (Table 1.1, entry 1).⁷³ Two types of zeolites, *i.e.*, HZSM-5 and Hbeta, with different Si/Al ratios were used. The Ni/HZSM-5 catalyst with the lowest Si/Al ratio gave the highest conversion. However, severe cracking was found on this catalyst due to the strong acidity of HZSM-5 zeolite. Although the cracking could be reduced by raising the Si/Al ratio of the zeolite, the decrease in acidity also caused a considerable decrease in the activity; conversion dropped from 100% (Si/Al = 45) to 60% (Si/Al = 200). These results suggest that acid sites on the support have deoxygenation activity or create a "synergy effect" with Ni particles. In contrast, Hbeta-supported catalysts were not

sensitive to acidity. As the number of acid sites decreased from 0.171 to 0.053 mmol/g, the conversion only changed 2%. In addition, cracking selectivities over these catalysts were less than 1%. The author did not explain the reason for the higher activity of Hbeta zeolite, but this plausibly due to its larger surface area and pore size.

In the second work of Lercher's group (Table 1.1, entry 2), the effect of metal loading amount and the nature of support on the deoxygenation activity were investigated.⁷⁴ ZrO₂ was used as a support and the nickel loading was varied from 0 to 15%. The conversion and total hydrocarbon yield increased with increasing nickel loading until it reached to 10%. Further increasing the nickel loading can barely enhance the activity. Therefore, the nickel loading was fixed to 10%, and various metal oxides, *i.e.*, zirconia, titania, ceria, alumina and silica, were employed for comparison. TOF of the studied catalysts in stearic acid deoxygenation demonstrated that catalyst with a reducible support, *i.e.*, Ni/ZrO₂, Ni/TiO₂ and Ni/CeO₂, exhibited much higher activity than the catalyst with an unreducible support, *i.e.*, Ni/SiO₂ and Ni/Al₂O₃. The high activity of the catalyst with slightly reducible support could be due to the fact that some oxygen vacancies on the support surface participate in the deoxygenation reaction. The most active catalyst, *i.e.*, 10%Ni/ZrO₂, was finally used in the hydrotreating of a microalgae oil. It is remarkable that no considerable deactivation could be observed in the catalyst for a time on stream over 70 h, indicating its high stability.

Table 1.1 Summary of recent results from supported nickel catalyst studies of TG-related compounds deoxygenation.

Entry ^{ref}	Catalyst	Reactant	Reaction conditions	Conversion (%)	Selectivity (%)		
					HDO	DCO/DCO ₂	Cracking
1 ⁷³	10%Ni/HZSM-5(45)			100	47.4	9.6	42.7
	10%Ni/HZSM-5(120)			65	75.1	8.8	15.9
	10%Ni/HZSM-5(200)	1.0 g Stearic acid	Reactant weight = 1.0 g Catalyst weight = 0.2 g	60	86.4	6.1	7.2
	5%Ni/Hbeta(5)	in	T = 260 °C	96	81.5	17.6	0.7
	5%Ni/Hbeta(10)	100 mg dodecane	P = 40 bar Time = 8 h stirring = 600 rpm	96	88.8	10.4	0.4
	10%Ni/Hbeta(5)			100	82.7	16.4	0.6
	10%Ni/Hbeta(10)			98	89.8	9.5	0.4
2 ⁷⁴	ZrO ₂			13	–	3.2	–
	3%Ni/ZrO ₂			96	2.5	51	3.4
	5%Ni/ZrO ₂			100	2.0	90	1.0
	10%Ni/ZrO ₂	1.0 g Stearic acid	Reactant weight = 1.0 g Catalyst weight = 0.5 g	100	1.5	96	1.2
	15%Ni/ZrO ₂	in	T = 260 °C	100	1.5	96	1.3
	10%Ni/TiO ₂	100 mg dodecane	P = 4 MPa Time = 8 h stirring = 600 rpm	98	5	87	0.9
	10%Ni/CeO ₂			100	0.4	93	2.8
	10%Ni/Al ₂ O ₃			63	0.7	81	0.9
3 ⁷⁵	10%Ni/SiO ₂			45	1.5	57	1.3
	7%Ni/SiO ₂		Reactant weight = 30 g Catalyst weight = 1.0 g	49	6.0	61.0	24.5
	7%Ni/Al ₂ O ₃		T = 220 °C	91	16.7	71.7	5.1
	7%Ni/SAPO-11(0.1)	Methyl Palmitate	P = 2 MPa H ₂ flowing rate = 500 ml/min Time = 6 h	100	42.5	47.6	4.8
	7%Ni/HZSM-5(38)			100	22.5	30.5	42.0
4 ^{a76}	7%Ni/HY(2.9)			99	10.0	20.2	63.6
	5%Ni/Hbeta(75)-IM	1.0 g Stearic acid	Reactant weight = 1.0 g Catalyst weight = 0.2 g	33	19.4	9.2	4.1
	5%Ni/Hbeta(75)-EX	in	T = 260 °C	97	63.5	33.0	3.5
	5%Ni/Hbeta(75)-DP	100 mg dodecane	P = 4 MPa Time = 2 h stirring = 700 rpm	100	63.3	34.0	3.3
5 ^{b77}	5%Ni/Hbeta(75)-NP			100	63.4	32.0	3.8
	15%Ni/MAC	0.21 g Stearic acid	Reactant weight = 0.21 g Catalyst weight = 0.075 g	30.2	2.3	27.8	0.1
	25%Ni/MAC	in 5 mL dodecane	T = 260 °C P = 0.6 MPa Time = 8 h stirring = 800 rpm	77.4	2.7	74.7	–
6 ⁷⁸	35%Ni/MAC			76.5	3.9	67.1	5.5
	9%Ni11%Mo/Al ₂ O ₃			90	54.0	31.0	1.5
	13%Ni5%Cu/Al ₂ O ₃			60	2.8	77.3	1.0
	12.4%Ni4.8%Cu 2.2%Mo/Al ₂ O ₃	A mixture of methyl palmitate and ethyl caprate	T = 300 °C P = 0.25 MPa LHSV = 3 h ⁻¹	63	3.0	91.2	1.5
	11.7%Ni4.5Cu 3.9%Mo/Al ₂ O ₃			78	7.1	83.0	1.5
	11.3%Ni4.3%Cu 5.6%Mo/Al ₂ O ₃			81	9.2	81.0	1.2
	10.1%Ni3.8%Cu 6.9%Mo/Al ₂ O ₃			90	11.5	81.0	1.2

^a Catalysts were prepared by different method: (I) impregnation, (E) ion-exchange/precipitation, (D) deposition-precipitation, (N) grafting of as-synthesized Ni nanoparticles. ^b MAC refers to mesoporous active carbon.

By comparing the first work and second work of Lercher' group, one may observe that the zeolite is a promising support for the nickel-based catalyst. Zeolite-supported catalysts exhibited higher deoxygenation activity compared to other metal oxide-supported catalysts. Despite of insufficient evidence, researchers suggested that this behavior might be related to a synergistic effect of nickel and acid sites. M/SBA-15 and M/Al-SBA-15 (M=Ni, Co) were synthesized and their catalytic activity were studied in the hydrotreating of methyl esters to produce hydrocarbons in diesel range.⁷⁹ Bifunctional M/Al-SBA-15 were more active and promoted the formation of HDO products. Based on these results, it could be inferred that nickel would be more efficient in deoxygenation when loaded on the support with more acid sites. On the other hand, compared to unreducible supports, a reducible support is more efficient for deoxygenation. A recent report showed that even a metal oxide without other active metals loading, *i.e.*, CeO₂-ZrO₂, are active for the deoxygenation.⁸⁰ Other reducible metal oxides, *e.g.*, MoO₃ and Fe₂O₃,^{81, 82} also showed deoxygenation activity. The reaction is suggested to proceed on oxygen vacancies by an inverse Mars–van Krevelen mechanism.⁸³

After investigating the influences of support and metal loading on the catalyst performance of nickel catalyst, the Lercher's group continued their work of zeolite-supported nickel catalysts on optimizing the preparation method. They used four different methods, namely impregnation (IM), ion exchange/precipitation (EX), deposition precipitation (DP) and nanoparticles grafting (NP), to prepare a 5%Ni/Hbeta catalyst (Table 1.1, entry 4).⁷⁶ Catalysts prepared by EX, DP and NP methods showed much higher activity than the conventional IM method in the deoxygenation of stearic acid. The high activity of these catalysts can be explained by their higher nickel dispersion and thus smaller nickel particle size. However, the catalyst prepared by EX method showed an increase in particle size, *i.e.*, sintering, accompanying with a loss of activity during a recycling test. They used the Ostwald ripening mechanism^{84, 85} to explain the rapid sintering of the catalyst prepared by EX method, and highlighted the importance of narrowing the size distribution of the particles.

Many other research groups followed on using nickel-based catalysts for hydrotreating of TG-based catalysts. Changing the support would alter the performance of nickel catalysts. Zuo *et al.* studied the 7% Ni catalysts supported on various supports (SiO_2 , $\gamma\text{-Al}_2\text{O}_3$, SAPO-11, HZSM-5 and HY).⁷⁵ The silica-supported catalyst gave the lowest conversion compared to other catalyst with acid supports, indicating that there might be a synergistic effect of metal Ni and acid sites on the supports. In addition, Ni/SAPO-11 with moderate acidity showed high yield of C_{15+} alkanes due to its lower cracking activity. After finding the good performance of Ni/SAPO-11 catalyst, they synthesized nano-sized SAPO-11 supports with superior pore structure.⁸⁶ Compared to the commercial support, the synthesized support had larger surface area and mesopores, which offered sufficient space for better dispersing nickel particles. Hydrotreating of palm oil demonstrated that the nano-sized SAPO-11 supported Ni catalysts showed higher hydrocarbons yield, higher isomerization selectivity and excellent stability. These can be due to its appropriate acidity, higher Ni dispersity, balanced metal and acid functionalities and fast diffusion for bulky reactant and products.

The method of modifying a microporous zeolite to create new mesoporous structure as well as improving its surface area was proved to be efficient for nickel dispersing. Zhao's group further promoted the performance of Ni/Hbeta by using a nano-sized hierarchically structured zeolite or encapsulating nickel nanoparticles into/onto intra-mesoporous of single-crystalline Hbeta. They did alkaline treatment for Hbeta using basic solutions (TPAOH/NaOH or NaCO_3), vapor streaming or soft template promoted NaOH leaching (CTAB/NaOH).⁸⁷ The TPAOH/NaOH introduction lead to the formation of more homogeneously dispersed inter-mesopores of a much smaller crystal size, resulting in higher dispersion of supported nickel nanoparticles. The novel catalyst showed a faster rate (19 $\text{g/g}_{\text{cat}}/\text{h}$) for stearic acid hydrotreating, which is nearly four times higher than untreated Ni/Hbeta (5 $\text{g/g}_{\text{cat}}/\text{h}$), and an ultra-high stability in four consecutive recycling tests. For the encapsulating method, nickel nanoparticles ($d = 5.6 \text{ nm}$) was encapsulated into/onto the uniform and inter-connected intra-mesopores (7–8 nm) of single-crystalline Hbeta, achieving

highly dispersive nickel nanoparticles.⁸⁸ The hydrotreating of stearic acid demonstrated that the novel catalyst led to a significant high initial rate of 38 g/g_{cal.}/h at a lower reaction temperature (260 °C). Noted that special rates for sulfided NiMo/Al₂O₃ and Pd/C are reported to 3.9 g/g_{cal.}/h and 0.9 g/g_{cal.}/h.^{89, 90} In this sense, the Ni/Hbeta catalyst could be considered as an efficient catalysts for upgrading of TG-related compounds into green diesel.

Lercher' group studied the reaction pathway for transformation of microalgae oil and fatty acids over bifunctional Ni/Hbeta catalysts.^{73, 91} Hydrotreating of microalgae oil would yield stearic acid of approximately 70% in 1 h. Taking into account the composition of the microalgae oil, in which the percentage of unsaturated fatty acids reach to 88.4%, they concluded that hydrogenation of the unsaturated bonds in the alkyl chain occurs fast. As shown in **Figure 1.8**, after hydrogenation of the unsaturated triglyceride, hydrolysis of the saturated triglyceride product fatty acids (stearic acid) and propane as primary products. The formation of stearic acid gradually decreased with an increased alkane (octadecane and heptadecane) formation. Then, they selected fatty acids for studies to understand further hydrodeoxygenation steps. The subsequent hydrogenation of the carboxylic group of fatty acid leads to the corresponding aldehyde, which is considered to be the rate-determining step. Afterward, two reaction pathways are available to the formation of alkanes; decarbonylation of the aldehyde to generate alkane with one carbon number less than the fatty acid (DCO pathway) or hydrogenation of the aldehyde to produce alcohol. The produced alcohol undergoes sequential acid-catalyzed dehydration and metal-catalyzed hydrogenation leading to the final alkane with the same carbon number to the fatty acid (HDO pathway). Acid sites in zeolite support promote hydroisomerization and hydrocracking of the alkanes. The CO produced from the DCO route may further react with H₂ to produce methane due to the high methanation activity of nickel metal. This result is consistent with Kumar' work, which develop an empirical kinetic model for stearic acid deoxygenation over Ni/γ-Al₂O₃.⁹²

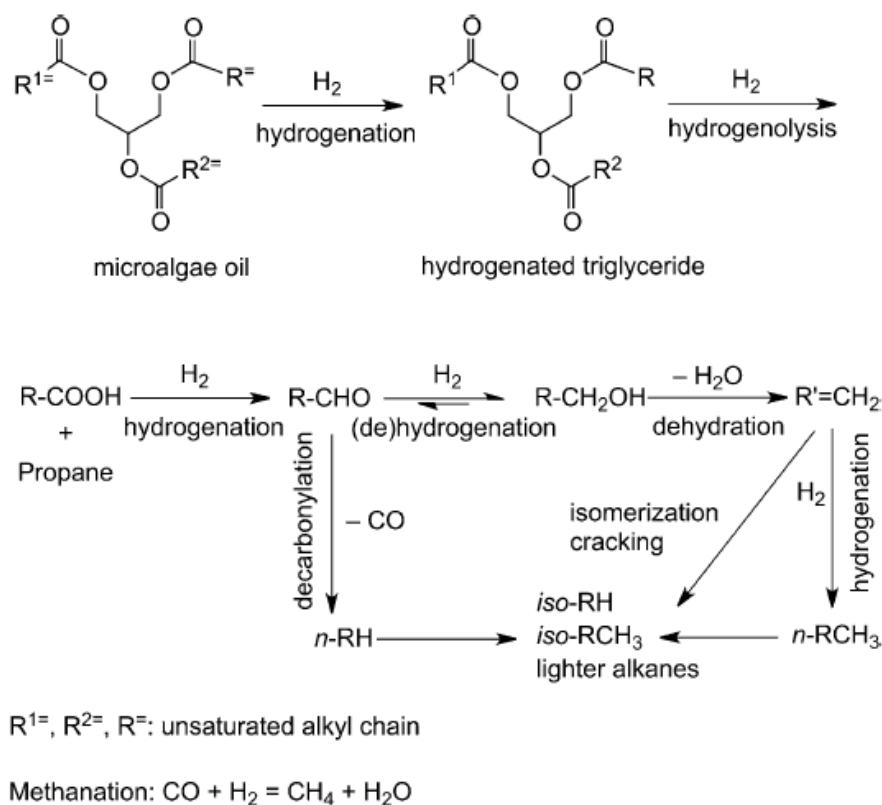


Figure 1.8 Proposed reaction pathway for transformation of microalgae oil to alkanes over bifunctional Ni/Hbeta catalysts. Reproduced from Peng *et al.*⁷³

Different from TMS catalysts, the support in nickel catalysts can substantially alter the reaction pathway. To date, supports used in nickel catalysts can be divided into two categories: metal oxides and acid materials (*e.g.*, zeolite, Al-SBA-15). For the metal oxide-supported nickel catalysts, deoxygenation mainly proceeds *via* a DCO route. The HDO selectivity over Ni/oxides catalysts are in the following order: Ni/CeO₂ > Ni/Al₂O₃ > Ni/ZrO₂ > Ni/SiO₂ > Ni/TiO₂.⁷⁴ However, even if Ni/TiO₂ gives the lowest DCO selectivity among these catalysts, the DCO/HDO ratio of ~18 is still high. As mentioned above, DCO will result in the decrease of liquid yield due to that one mol of CO is generated as by-product and thus reduce the length of carbon chain. Researchers used nickel catalysts for deoxygenation of TG-related compounds usually appeal the advantage of lower hydrogen consumption by proceeding a reaction through the DCO route. However, they did not concern the hydrogen consumption of a side reaction, CO methanation, which costs three mol of hydrogen to transform one mol of CO. Furthermore, monometallic nickel catalysts showed

extremely high activity in this side reaction, and thus all of the CO generated can be transformed into CH₄ under given reaction conditions.⁹³ Bimetallic catalysts such as nickel-copper were proved to prevent the methane formation over wide temperature range (280-340 °C).⁷²

In contrast, the use of zeolite as a support for nickel catalyst can alter the predominant reaction pathway from DCO to HDO. A nano-sized SAPO-11 supported nickel catalyst can achieve a HDO/DCO ratio around 2.⁸⁶ Ni/Hbeta gave an ultra-high HDO product yield (96%).⁸⁸ Similarly, a nickel catalyst supported on an aluminum modified SBA-15, Al-SBA-15, showed much higher HDO selectivity than that supported on the original SBA-15.⁷⁹ A possible reason is that hydroxyl groups on the zeolite could provide the adsorption site for oxygenates, and the adsorption mode of these oxygenates might be changed. Nickel supported on an mesoporous active carbon also showed high DCO selectivity due to the low acidity of the support (Table 1.1, entry 5).⁷⁷

1.4.2 Deoxygenation Mechanisms

Lercher's group proposed a deoxygenation mechanism for Ni/ZrO₂ (**Figure 1.9**). Based on kinetics studies, the reduction of stearic acid to the octadecanal is the rate determining step and proceeds *via* two routes. One is directly reduced on nickel particles and the other is activated by the ZrO₂ support. After the former route, the produced aldehyde, which is equilibrium with the corresponding alcohol *via* hydrogenation-dehydrogenation, rapidly undergo decarbonylation to produce *n*-heptadecane on nickel particles. The latter deoxygenation route demonstrated a synergistic effect of nickel particles and the ZrO₂ support. The stearic acid adsorbed on oxygen vacancies of ZrO₂, which can be formed by the reduction, resulting in carboxylate species. This kind of adsorption of carboxylic acids on a partially reducible metal oxides such as zirconia, titania and ceria was reported in other studies.^{94, 95, 96} The α -hydrogen atoms of the carboxylate can be subsequently abstracted to produce a ketene intermediate, followed by being hydrogenated to octadecanal on nickel particles. These dual routes create a redundancy in the surface

reaction, and therefore accelerate the deoxygenation rate. The presence of ketene intermediate was corroborated in their further work by *in situ* IR spectroscopy.

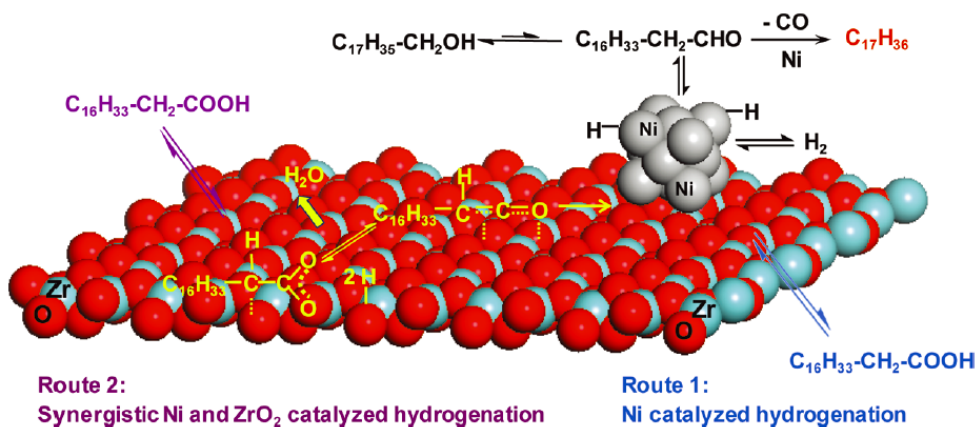


Figure 1.9 Proposed reaction mechanism for deoxygenation of stearic acid to C₁₇ *n*-heptadecane *via* synergistic catalysis over Ni/ZrO₂. Reproduced from Peng *et al.*⁷⁴

1.4.3 Catalyst Deactivation

Nickel particles are known to favor aggregation during the hydrotreating reaction. Additionally, the amount of metal loading for nickel catalysts are usually high due to their lower TOF. This leads to their fast sintering compared to noble metal catalysts. On the other hand, nickel is hard to reduce compared to noble metal catalysts, and therefore, a relatively higher reduction temperature (>450 °C) is required, which causes a severe sintering during reduction stage. Ni/Hbeta bifunctional catalysts prepared by conventional impregnation method were reported to suffer from sintering during the reduction stage. Much lower initial activity was obtained for the catalyst prepared by conventional impregnation compared to other preparation methods due to lower nickel dispersion.⁹⁷ The catalyst prepared by ion exchange method showed high initial activity, indicating that the sintering occurring during reduction state can be efficiently prevented by using this method; however, a dramatical particle size increase accompanied with a loss in activity was found during the recycling test. The group using a deposition-precipitation (DP) or a two-step synthesis involving preparing nickel nanoparticles and grafting them into the

support to decrease the sintering during reaction. Therefore, it could be concluded that the preparation method has a key role in the activity and stability of nickel catalysts, and the conventional impregnation method is not suitable for dispersing nickel on the support. Further work on improving the Ni/Hbeta catalyst by encapsulating nickel particles into mesopores single-crystalline Hbeta demonstrated higher stability as well as activity.⁸⁸ In contrast, Ni/ZrO₂ showed high stability (> 70 h) in hydrotreating of microalgae oil.⁷⁴

Carbon deposition is another factor that influence the stability of nickel catalysts. Deactivation and regeneration behaviors of Ni/ γ -Al₂O₃ and Co/ γ -Al₂O₃ catalysts in the hydrotreating of palm oil were investigated at 300 °C and 5 MPa in a trickle bed reactor. After 150 h on stream, the product yield dramatically decreased over the Co catalyst (88.6% to ca. 56.6%), whereas a decrease from 92.2 to 76.2% was observed on the Ni catalyst. TPO analysis showed that the amount of carbon deposition on the Co catalyst was larger than that on the Ni catalyst. Although some sintering was also observed, the carbon deposition was considered as the major deactivation reason. Regeneration of the catalysts can completely restore the catalytic activity.⁹⁸

1.5 Bifunctional Catalysts for Simultaneous Deoxygenation-Isomerization of Triglyceride-Related Compounds

In previous sections, hydrotreating of TG-related catalysts to produce green hydrocarbons using TMS, noble metal and nickel catalysts were reviewed. Complete deoxygenation is attainable under suitable reaction conditions, and the obtained liquid product has an extremely high cetane number close to 100. Nevertheless, the main composition of the liquid product is normal alkanes (*n*-alkanes) with carbon numbers of 15–18. The cold flow properties of these *n*-alkanes are quite unfavorable due to their high freezing points (**Figure 1.10**), which strictly limits their application for “ready-to-use” bio-fuels. Isomerization of *n*-alkanes to produce branched isomers is regarded as a feasible and promising method to improve cold flow property. A two-steps hydrotreating process, *i.e.*, deoxygenation of triglycerides and isomerization of the obtained *n*-alkanes being conducted separately, has been commercialized by Neste Oil. Taking account of the cost and process efficiency, however, producing high quality fuels through a single-step process is highly desirable. The one-step hydrotreating of TG-related compounds to produce isomerized alkanes (*iso*-alkanes) has been widely studied. These studies suggested that a metal-acid bifunctional catalyst could increase the concentration of *iso*-alkanes in the final product. In this section, recent studies on the one-step hydrotreating of TG-related compounds over bifunctional catalysts are reviewed.

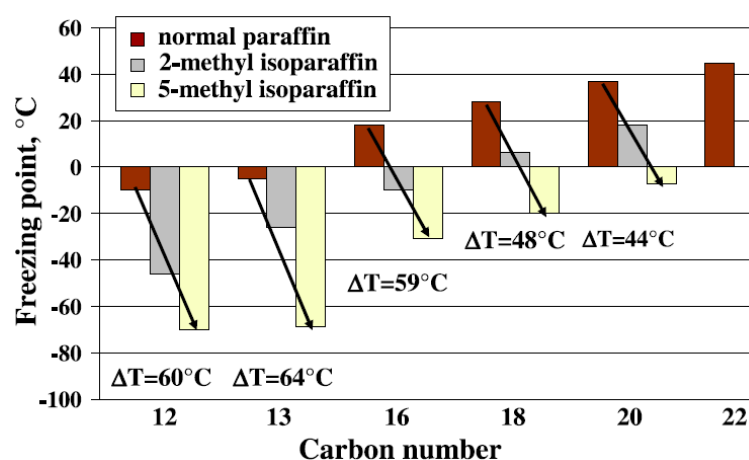


Figure 1.10 Freezing point of paraffins as a function of the number of carbon atoms. Reproduced from Hancsok *et al.*⁹⁹

Usually, the acid function in a bifunctional catalyst is realized by the zeolite. Zeolites can be defined as crystalline microporous aluminosilicates, in which the primary building blocks are TO_4 ($\text{T} = \text{Si}$ or Al) tetrahedra.¹⁰⁰ In the tetrahedra structure, a Si^{4+} or Al^{3+} cation locates at the center and oxygen atoms locate at the corners (**Figure 1.11**). Due to the different charge between Si^{4+} and Al^{3+} , the TO_4 tetrahedra unit can have a negative charge (AlO_4) or can be neutral (SiO_4). Zeolites usually show high Brønsted acidity because of the presence of protons that balance the negative charges generated from trivalent Al atoms with tetrahedral coordination environment.

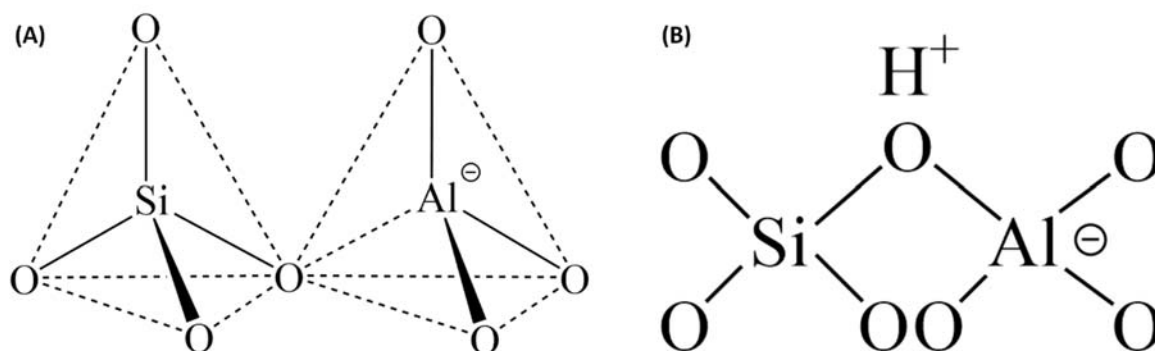


Figure 1.11 Primary building blocks and Brønsted acid sites in zeolites.

The protonic forms of zeolites as solid acids differ from conventional molecular acids since they have a distribution of sites with different acid strength. Theoretically, the acid strength of a particular $\equiv\text{Si}-(\text{OH})-\text{Al}\equiv$ site depends on the electronegativity of the cations, Si^{4+} or Al^{3+} , present in the second coordination sphere around the bridging OH group.¹⁰¹ The consequence of this relationship between Al^{3+} content and the strength of the zeolite is that, as it is experimentally observed, zeolites having high Al^{3+} content exhibit a high density of low strength acid sites, while on the other hand dealuminated zeolites have a low density of acid sites, but of higher acid strength. Besides the composition, the acidity of the zeolites also depends on their structure. It has been found that for similar chemical composition, the strength of acid

sites in medium pore size zeolites is higher than that found in large pore size zeolites.^{102, 103} In addition to the chemical composition, the pore dimensions and topology defining the crystalline structure is another important feature of zeolites. The international Zeolite Association (IZA) recognizes 231 different structures, which can be classified depending on the oxygen atoms in the pore mouth or the number of dimensions through which a molecule can diffuse in the crystals (**Figure 1.12**).

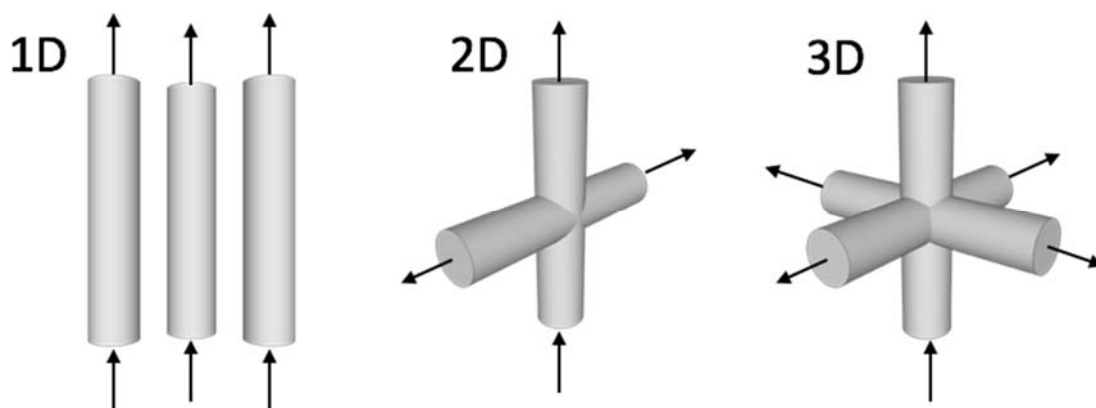


Figure. 1.12 Dimensions through which a molecule can diffuse in the crystal of zeolite.

Zeolites can be classified by the pore size as small, medium and large size zeolites when the openings of the micropores are constituted by rings of eight, ten or twelve oxygen atoms, respectively.¹⁰⁴ Shape-selectivity is attributed to the pore size and is responsible for the control of the product distribution. There are three kinds of shape-selectivity proved by previous experimental results (**Figure 1.13**): (a) reactant selectivity: the pore opening transmits reactants which have a sufficiently narrow kinetic diameter and sieves out the bulkier ones; (b) product selectivity: only products which are sufficiently slim can leave the zeolite cage reactor and others are further catalytically rearranged until they can exit; (c) transition state selectivity: the shape of the cage imposes constraints on the steric demand of possible products. This is the

case of xylene isomerization, toluene disproportionation or alkylation in ZSM-5 as solid acid, processes that are carried out on a very large scale in petrochemistry. In this case, the thermodynamic mixture at equilibrium should contain *o*- and *p*-xylenes, with lesser amounts of the meta isomer. However, when carrying out the reaction inside the medium pore zeolite ZSM-5, in which the pore dimension only allows diffusion of *p*-xylene, *m*- or *o*-xylene formed in the crossings of the channel system cannot diffuse out of the crystals and become entrapped until they rearrange to the *p*-xylene that is the only one that can go out of the pores.

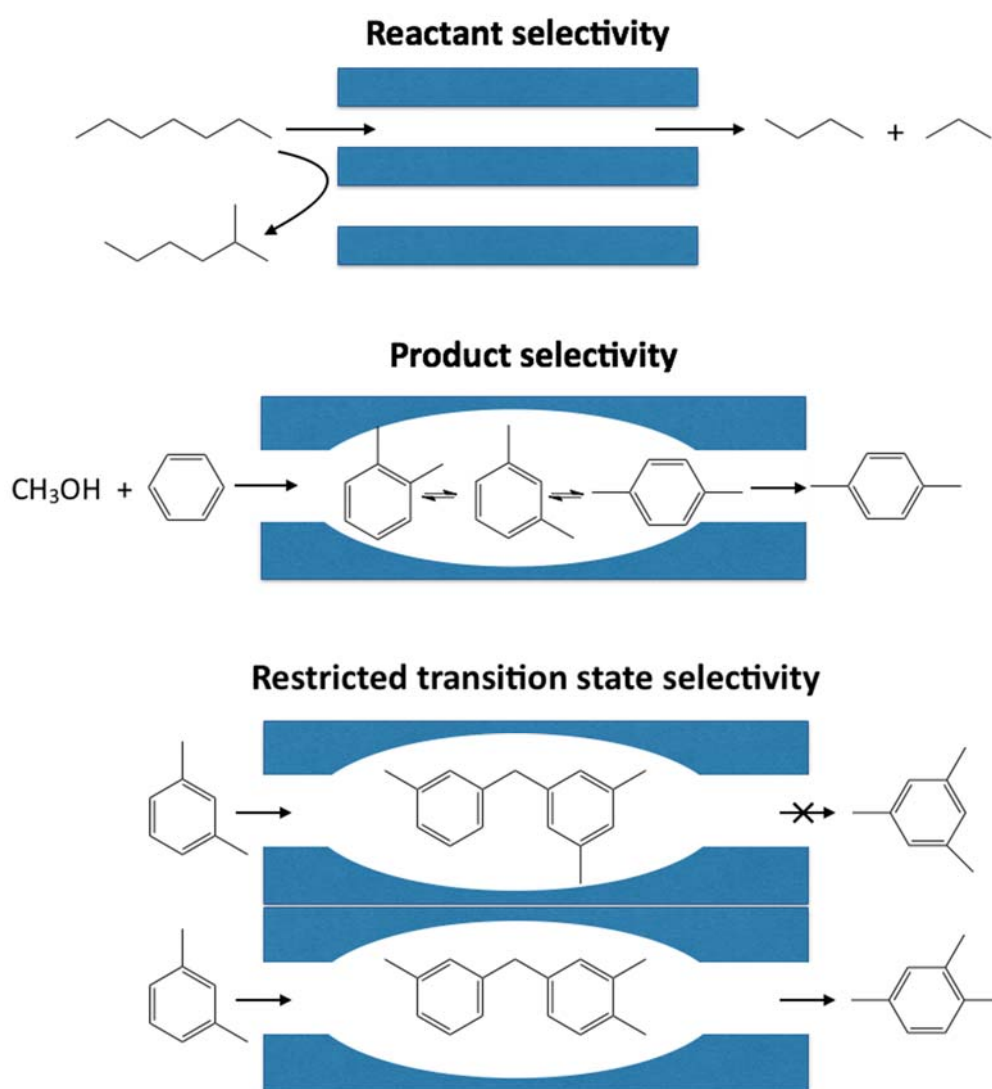


Figure 1.13 Schematic representation of shape-selectivity in the pores of zeolite molecular sieves. Reproduced by Roduner *et al.*¹⁰⁵

Table 1.2 One-step deoxygenation-isomerization of vegetable oils over bifunctional catalysts.

Entry/Refs.	Catalyst	Reactant	Reaction conditions	iso-/n-alkanes ratio	Max. iso-alkanes yield (%)	Cracking Selectivity (%)
1	1%Pd/SAPO-31	Sunflower oil	T = 310-360 °C	2~16	n.m. ^a	9.3~72.1
			P = 2 MPa WHSV = 0.9-1.6 h ⁻¹ H ₂ /oil ratio = 1000 (cm ³ /cm ³) T = 350-370 °C			
2	NiMoS/Al ₂ O ₃ /F	Sunflower oil	P = 2-4 MPa LHSV = 1 h ⁻¹	n.m.	38	n.m.
			H ₂ /oil ratio = 500 (cm ³ /cm ³)			
3	NiMoS/SiO ₂ NiMoS/ γ -Al ₂ O ₃ NiMoS/SiO ₂ -Al ₂ O ₃ NiMoS/HY NiMoS/HZSM-5	Jatropha oil	T = 350 °C	0.03 0.08 0.26 0.87 1.21	n.m.	0.8 2.5 9.8 48.9 77.8
			P = 4 MPa LHSV = 7.6 h ⁻¹			
			H ₂ /oil ratio = 800 (v/v)			
			T = 357 °C P = 4 MPa LHSV = 1 h ⁻¹			
4	1%Pt/SAPO-11	Soybean oil	H ₂ /oil ratio = 500-2000 (cm ³ /cm ³)	n.m.	42 ^b	28.6
			LHSV = 1 h ⁻¹			
5	7%Ni/SAPO-11	Palm oil	P = 2 MPa LHSV = 4 h ⁻¹	n.m.	64 ^b	27.7
			H ₂ /oil ratio = 1000 (cm ³ /cm ³) T = 340 °C			
6	1%Pt/SAPO-31	Sunflower oil	P = 2.5 MPa WHSV = 0.74 h ⁻¹	10	75	n.m.
			H ₂ /oil ratio = 2000 (cm ³ /cm ³)			

^a Not mentioned in the literature; ^b total isomerization yield (iso-C₅₋₁₈).

Table 1.2 lists the representative of recent literatures concerning the one-step reaction. The first report about this process used a 1% Pd/SAPO-31 catalyst (Table 1.2, entry 1).⁷⁰ Although a high *iso-/n*-alkanes ratio could be obtained at higher reaction temperatures and lower WHSV, cracking was also severe under the corresponding reaction conditions. The high cracking activity of the catalyst could be due to the unbalanced hydrogenation/acid function; if the acid function of support is much stronger than the hydrogenation function of metal, the carbenium intermediate would undergo cracking rather than skeleton isomerization. Additionally, deactivation was followed after several hours' reaction due to sintering of Pd particles. Recently, the same group used a series of 1% Pt/SAPO-31 catalysts prepared at different calcination temperatures for hydrotreating of sunflower oil (Table 1.2, entry 6). Due to the higher hydrogenation function of Pt, extremely high isomerization yield (> 70%) was obtained. In a long-term test (45 h on stream), high stability was achieved over the catalyst calcined at 450 °C.

The acidity of support plays a key role in isomerization as well as the one-step hydroconversion process. Liu *et al.* investigated NiMo sulfided catalysts supported on various supports.¹⁰⁶ The isomerization activity of these catalysts increased in the following order: SiO₂ > γ -Al₂O₃ > SiO₂-Al₂O₃ > HY > HZSM-5 (Table 1.2, entry 3). This result is consistent with the acidity of these supports that obtained by NH₃-TPD. The pour points of the liquid products over NiMoS/SiO₂-Al₂O₃, NiMoS/HY and NiMoS/HZSM-5 were lower than -15 °C, indicating good cold flow properties of these products. However, high cracking selectivity (48.9% and 77.8%) was found over NiMoS/HY and NiMoS/HZSM-5. In general, two factors have large influences on the pour point of final products; one is the isomer content and the other is the carbon number distribution of the liquid product. Although the hydrocarbon with less carbon numbers (*e.g.*, C₅-C₁₀) has lower pour point, these compounds do not cover the boiling range of diesel and have a lower cetane number. Therefore, isomers obtained from hydrotreating of vegetable oils with carbon numbers of 10-18, preferable 15-18, can be the appropriate component for diesel fuel.

Early studies used ZSM-5 as the support because of its high acid function.^{106, 107} However, the high cracking activity of these catalysts limits their use in the one-step process. Even a diluted ZSM-5/Al₂O₃ also showed high cracking activity.¹⁰⁸ Therefore, it is concluded that this kind of zeolite is not suitable for this process. Research interest was changed to zeolites with a one-dimension and ten-membered ring structure. SAPO-11 (-21 and -31) and ZSM-11 (-12 and -22) have this kind of pore structures. These materials were reported to have shape-selectivity in isomerization of *n*-alkenes.¹⁰⁹ Our research group investigated the effects of acidity and structure of the support on the catalytic performance in hydrotreating of methyl stearate.²⁷ NiMo/SAPO-11 and NiMo/AlSBA-15 (Si/Al = 10) have similar acidity; however, the NiMo/AlSBA-15 catalyst showed higher cracking activity, while NiMo/SAPO-11 was more selective to isomerization. Based on this result, it is suggested that the pore structure is another important parameter during isomerization of long chain molecules. As shown in **Figure 1.14**, the microspores structure of SAPO-11 gives a shape-selectivity that inhibits the multi-branched isomer formation inside its pores. In contrast, the SBA-15 with a mesoporous structure favors further isomerization of the mono-branched carbenium intermediate to produce a multi-branched intermediate. It is known that the multi-branched intermediate is more

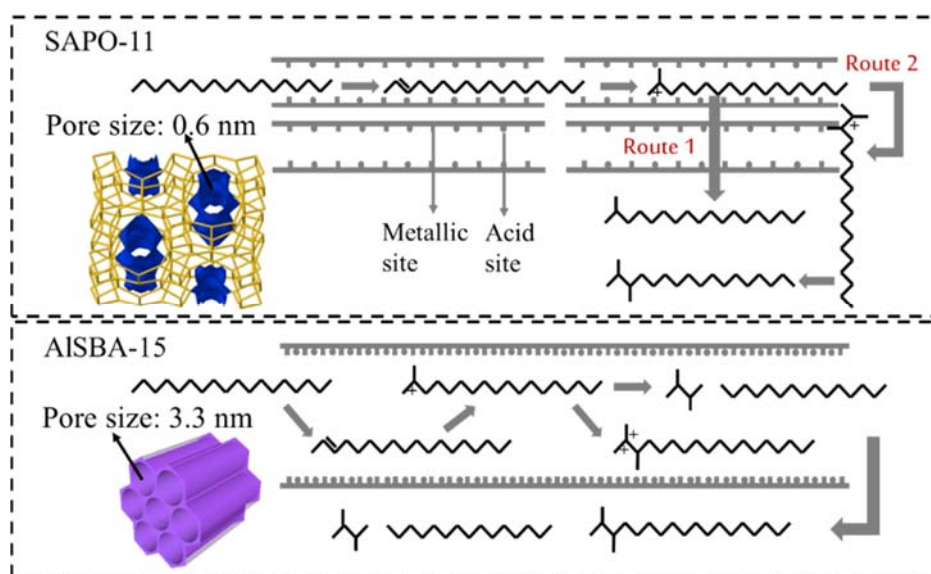


Figure 1.14 Isomerization mechanisms for long chain paraffin over NiMo/SAPO-11 and NiMo/AlSBA-15 catalysts.

active to be cracked into small alkanes rather than to be hydrogenated into alkanes. Consequently, SAPO-11 is more suitable for long-chain alkane isomerization than SBA-15.

Many studies used SAPO-11 as a support in hydrotreating of vegetable oils. Our group used Pt/SAPO-11 catalysts for hydrotreating of Jatropha oil. The effects of Si/Al ratio of SAPO-11 and Pt content were investigated. As increased the Si/Al ratio (from 0.05 to 0.4) or Pt loading (from 0.6 wt% to 3 wt%), the isomerization selectivity increased. Furthermore, the Pt content showed a larger influence. In addition, much higher isomerization selectivity was obtained in isomerization of deoxygenated hydrocarbons (*i.e.*, *n*-C₁₅₋₁₈ alkanes) compared to the one-step hydrotreating of Jatropha oil. Based on these results, it is suggested that Pt metal sites work as the active site for both deoxygenation and isomerization, and an insufficient noble metal content would cause a lower isomerization activity. Although an increase of the noble metal content could render the catalyst more active, the higher cost will prohibit the large-scale industrialization of this process.

Wang *et al.* used 1% Pt/SAPO-11 and 1% Pt/ZSM-22 for the hydrotreating of soybean oil (Table 1.2, entry 4). The SAPO-11 supported catalyst showed higher isomerization selectivity, while the ZSM-22 supported catalyst showed higher cracking selectivity. Although the high cracking activity for Pt/ZSM-22 can be due to its higher acidity, the insufficient hydrogenation function of 1 wt% Pt, which causes an unbalanced hydrogenation/acid function, should not be ignored. Nickel-based catalysts showed higher deoxygenation of TG-related compounds, and therefore used as the hydrogenation function for a Ni/SAPO-11 catalyst.⁸⁶ Although this catalyst showed high yield of total isomers (*i.e.*, *iso*-C₅₋₁₈ alkanes), high cracking selectivity was also obtained due to the high C-C bond cleavage ability of nickel particles.

1.6 Purpose of This Study

To obtain “ready-to-use” hydrocarbon biofuels from hydrotreating of vegetable oils, both complete deoxygenation and further isomerization of obtained *n*-alkanes are indispensable. Taking into consideration of the cost and efficiency of the process, combining deoxygenation and isomerization into a single step is highly desirable. While some interesting information has been forwarded from previous studies, several issues still remain in this very important research area.

Firstly, although many research groups put their interest on TMS, nickel and noble metal catalysts, these catalysts are still not fully appropriate for simultaneous deoxygenation-isomerization of TG-related compounds to produce “ready-to-use” fuels. Indeed, TMS catalysts are the only catalysts applied in industrial processes. However, the issue of the stability of the catalyst and the product contamination still remained, which would destroy the original purpose of producing green biofuels. In this sense, the development of a sulfur-free catalyst is environmentally favorable. While nickel catalysts have high deoxygenation activity and a good potential for the deoxygenation process, there are still many issues remain; for example, lower liquid yield due to the reaction proceeding *via* the DCO route and high hydrogen consumption due to further methanation of the generated CO. Additionally, most studies using these catalysts were conducted using batch type reactors, which would decrease the efficiency in industrial application.

Secondly, catalysts employed in simultaneous deoxygenation-isomerization reaction were simple combinations of a deoxygenation metal and an acid support. Although this kind of catalyst can be suitable for *n*-alkanes isomerization, they are not highly active in the simultaneous reaction due to the insufficient hydrogenation ability of the monometallic metal. In addition, water formation in the deoxygenation reaction would largely influence the stability of the metal phase and cause sintering during reaction. Recently, many studies suggested that the addition of a second metal to form a bimetallic phase could be an efficient method to improve the catalytic activity and stability of the monometallic catalyst. However, the application of

bimetallic metal catalysts in hydrotreating of TG-related compounds has been less extensively studied.

Thirdly, deep isomerization would lead to the formation of multi-branched alkanes (MuBI), which have good cold flow properties. However, this property should not be the only evaluation index for “ready-to-use” diesel fuel because the combustion performance is also important and cannot be ignored. Unfortunately, MuBI have much lower cetane numbers (<60) compared to mono-branched alkanes (MoBI) (>85). Therefore, how to make the isomerization stop in the stage of producing MoBI is another issue for this process.

Finally, although several studies have investigated hydrotreating of TG-related compounds, the role of active metal in deoxygenation and the reaction mechanism is still unclear. Understanding the fundamental chemistry in catalysis, *i.e.*, the surface reaction mechanism and structure-performance relationship, is of high value to help designing new catalysts for other highly integrated processes.

Consequently, the purpose of this study is to develop efficient bifunctional catalysts for the simultaneous deoxygenation-isomerization of fatty acid esters to produce “ready-to-use” fuels and elucidate the structure-performance relationship of the catalyst. In order to understand the fundamental chemistry in catalysis, model compounds that are structurally similar to the main component in vegetable oils were used in most cases of the study. Three catalytic concepts were applied in this study. First, metal oxides were added into a monometallic catalyst to enhance its HDO selectivity. In heterogeneous catalysis, adsorption of the substrate and subsequent activation are the key steps. In a monometallic catalyst, the metal site functions as both hydrogen activation and adsorption sites. Therefore, competing adsorption between the substrate and hydrogen would occur, which could reduce the hydrogenation efficiency (**Figure 1.15, left**). Some metal oxides showed Lewis acidity which can function as strong adsorption sites for carbonyl groups. Adding this kind of metal oxides into the monometallic catalyst, carbonyl groups of a substrate could be adsorbed on the metal oxides and hydrogen is dissociated on the other metal site (**Figure 1.15, right**). This synergetic effect between metal and metal oxides was

supported to substantially improve the hydrodeoxygenation rate. Second, zeolites with one-dimension and ten-membered ring structures were used in this study. In previous studies, one-dimension channel was proved to efficiently suppress the undesired cracking reaction. A pore mouth with ten-membered ring is on the same order of size as the alkane molecule. Therefore, this kind of zeolites have shape-selectivity to separate various isomers which have different molecular sizes (**Figure 1.16**). SAPO-11 and ZSM-22 zeolites were used in most of the cases of this study because multi-branched isomers, which have lower cetane numbers, could not be generated inside their pore channels. This behavior could be responsible for enhancing the formation of mono-branched isomers. Third, a core-shell structural zeolite was synthesized for improving the shape-selectivity. Although multi-branched isomers could not be generated inside the pore channel of SAPO-11 or ZSM-22, they could be formed by the external acid sites, which have no shape-selectivity. Therefore, silica with no acidity was coated onto the surface of the zeolite to passivate the external acid site and further inhibit the formation of multi-branched isomers.

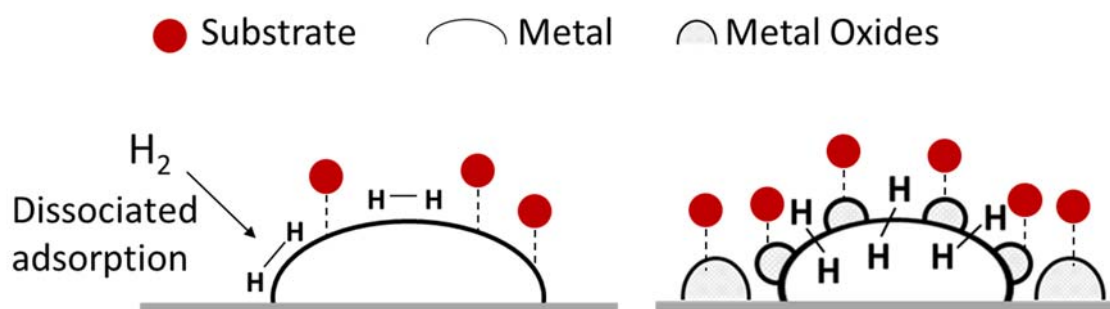


Figure 1.15 Surface reaction mechanism for hydrogenation of an oxygen-containing substrate.

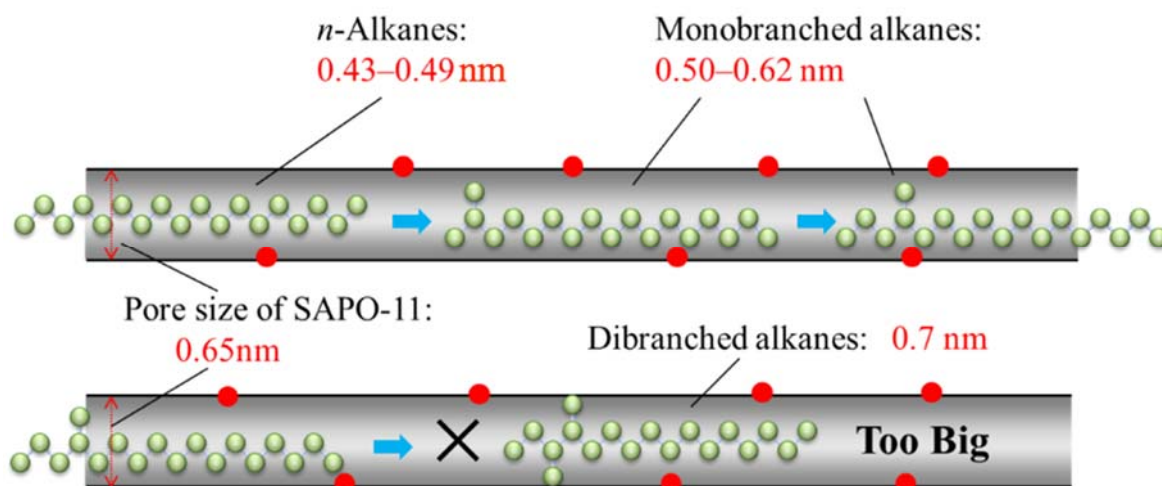


Figure 1.16 Reactant shape-selectivity for isomerization of octadecane over SAPO-11 zeolite.

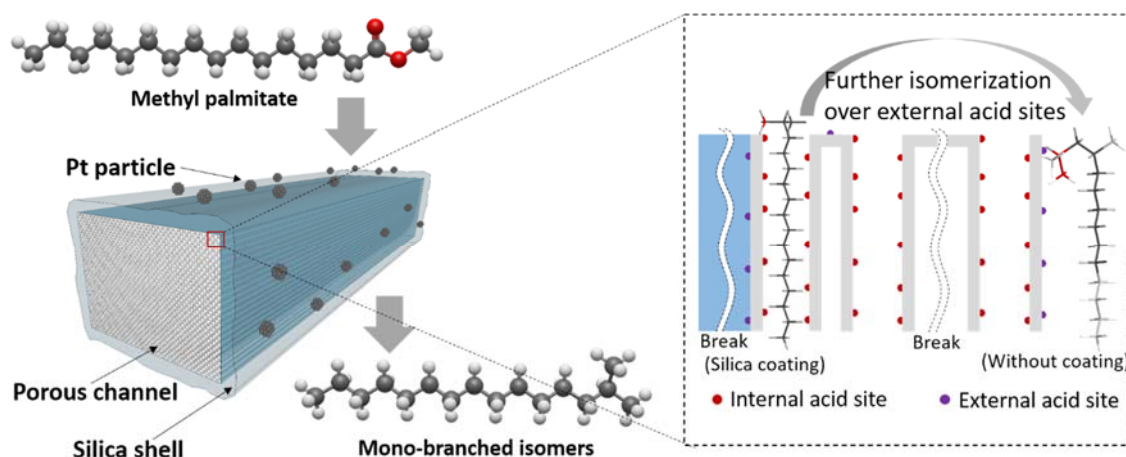


Figure 1.17 Deoxygenation of methyl palmitate and selective isomerization of *in situ* generated *n*-alkanes to produce mono-branched isomers over a bifunctional catalyst with silica-coated zeolite as the support.

A research flowchart in this thesis is presented in **Figure 1.16**. In brief, chapters 2 and 3 focused on the study of bimetallic metal species, *i.e.* reduced NiMo and PtSn; chapter 4 focus on the silica surface modification of a conventional zeolite – ZSM-22. Finally, new bifunctional catalysts based on the reduced NiMo and PtSn bimetallic metals and ZSM-22@SiO₂ were developed for the simultaneous deoxygenation-isomerization reaction. Details of the research work are introduced as follows.

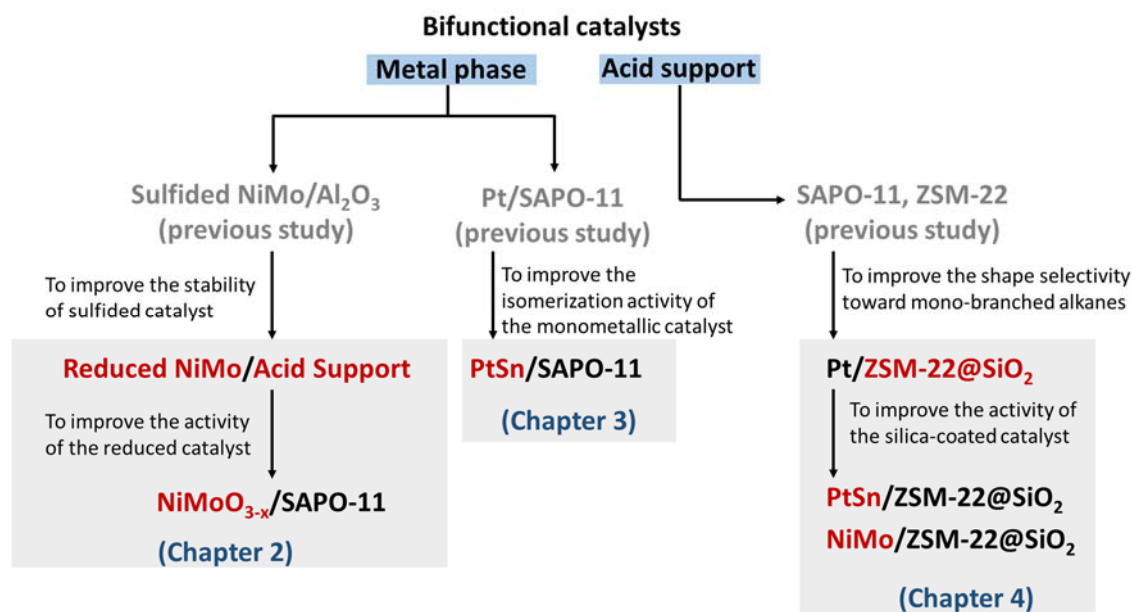


Figure 1.15 Research flowchart for used catalysts in this thesis.

In *Chapter 2*, hydrotreating of TG-related compounds was conducted over NiMo catalysts activated by hydrogen reduction in response to the low stability of sulfided catalysts. First, the feasibility of using a reduced commercial NiMo/Al₂O₃ catalyst was confirmed by comparing the catalytic activity and stability with the sulfided catalyst in hydrotreating of *Jatropha* oil. Then, various acid supports with different structures and acidities (SiO₂-Al₂O₃, SAPO-11 and ALSBA-15) were used for preparing NiMo catalysts, and the screening of these catalysts was conducted in hydrotreating of *Jatropha* oil. Subsequently, further investigation on reduction temperature was carried out using the hydrotreating reaction of methyl laurate as a model compound. Finally, many characterizations were performed to find out the structure-performance relationship and elucidation of the surface reaction mechanism of the reduced NiMo catalyst.

In *Chapter 3*, research interest was focused on improving the activity Pt/SAPO-11, which used in simultaneous deoxygenation-isomerization of vegetables in previous studies. Although the Pt/SAPO-11 catalyst with a high Pt content (1.5 wt%) showed high efficiency in the simultaneous reaction, high cost of the catalyst limited its application for industrialization. In this chapter, the promotion effect of second metal species, *i.e.*, Pd, Re, Cu and Sn, which exhibited activity in other hydrogenation

reactions combined with Pt, was applied for the simultaneous reaction of a model compound-methyl palmitate. Then, PtSn was selected for further investigation because of its high isomerization activity. The Pt catalyst was lowered to 0.3 wt%, and the atomic ratio of Sn/Pt was varied from 1 to 3 to elucidate the active phase in the PtSn catalyst and the promotion effect of Sn.

In *Chapter 4*, a core@shell structural zeolite was designed to improve the shape-selectivity of the support, which can reduce the MuBI formation. ZSM-22@SiO₂ was synthesized by using a facile crystal growth method. The core zeolite, ZSM-22, has a one-dimension channel structure and high isomerization selectivity similar to SAPO-11. In addition, the aluminosilicate composition of ZSM-22 makes it more appropriate for silica coating procedure than SAPO-11. The outer shell - silica is expected to cover the acid site on the external surface of the zeolite and promote the formation of mono-branched alkanes (MoBI), which have much higher cetane number than MuBI (>85 vs <60). A series of ZSM-22@SiO₂ zeolites with different amounts of shell silica were prepared to investigate the effect of the support acidity, including external and total acidity, on the catalytic performance of Pt catalysts (Pt loading = 0.6 wt%). Subsequently, two facile methods, changing Si/Al ratio of the core ZSM-22 zeolite and adding Sn as a promoter, were considered to improve the activity and isomerization selectivity of the silica-coated catalysts.

References

1. R. A. van Santen, Renewable Catalytic Technologies – a Perspective. In *Catalysis for Renewables*, Wiley-VCH Verlag GmbH & Co. KGaA: **2007**; pp 1-19.
2. I. Kubičková; D. Kubička, Utilization of Triglycerides and Related Feedstocks for Production of Clean Hydrocarbon Fuels and Petrochemicals: A Review, *Waste Biomass Valor.*, **2010**, *1* (3), 293-308.
3. R. W. Gosselink; S. A. Hollak; S. W. Chang; J. van Haveren; K. P. de Jong; J. H. Bitter; D. S. van Es, Reaction pathways for the deoxygenation of vegetable oils and related model compounds, *ChemSusChem*, **2013**, *6* (9), 1576-94.
4. S. Lestari ; P. Mäki-Arvela; J. Beltramini; G. Q. M. Lu; D. Y. Murzin, Transforming Triglycerides and Fatty Acids into Biofuels, *ChemSusChem*, **2009**, *2* (12), 1109-1119.
5. D. Kubička; L. Kaluža, Deoxygenation of vegetable oils over sulfided Ni, Mo and NiMo catalysts, *Appl. Catal., A*, **2010**, *372* (2), 199-208.
6. H. Zhang; H. Lin; W. Wang; Y. Zheng; P. Hu, Hydroprocessing of waste cooking oil over a dispersed nano catalyst: Kinetics study and temperature effect, *Appl. Catal., B*, **2014**, *150-151*, 238-248.
7. D. Kubička; P. Šimáček; N. Žilková, Transformation of Vegetable Oils into Hydrocarbons over Mesoporous-Alumina-Supported CoMo Catalysts, *Top. Catal.*, **2009**, *52* (1-2), 161-168.
8. S. Gong; A. Shinozaki; M. Shi; E. W. Qian, Hydrotreating of Jatropha Oil over Alumina Based Catalysts, *Energy Fuels*, **2012**, *26* (4), 2394-2399.
9. C. Lamy; C. Coutanceau; J.-M. Leger, The Direct Ethanol Fuel Cell: a Challenge to Convert Bioethanol Cleanly into Electric Energy. In *Catalysis for Sustainable Energy Production*, Wiley-VCH Verlag GmbH & Co. KGaA: 2009; pp 1-46.
10. M. Ruinat de Brimont; C. Dupont; A. Daudin; C. Geantet; P. Raybaud, Deoxygenation mechanisms on Ni-promoted MoS₂ bulk catalysts: A combined experimental and theoretical study, *J. Catal.*, **2012**, *286*, 153-164.
11. A. E. Nelson, Fundamentals of Industrial Catalytic Processes, 2nd Edition. C. H. Bartholomew and Robert J. Farrauto John Wiley and Sons, Hoboken, NJ, 966 pp., 2006, *The Canadian Journal of Chemical Engineering*, **2007**, *85* (1), 127-128.
12. D. L. Trimm, *Design of industrial catalysts / David L. Trimm*. Elsevier Scientific Pub. Co. ; distributors for the U.S. and Canada, Elsevier/North-Holland: Amsterdam ; New York : New York, **1980**.
13. T. Badstube; H. Papp; R. Dziembaj; P. Kustrowski, Screening of catalysts in the oxidative dehydrogenation of ethylbenzene with carbon dioxide, *Appl. Catal., A*, **2000**, *204* (1), 153-165.
14. C. Dupont; R. Lemeur; A. Daudin; P. Raybaud, Hydrodeoxygenation pathways catalyzed by MoS₂ and NiMoS active phases: A DFT study, *J. Catal.*, **2011**, *279* (2), 276-286.

15. E. Laurent; B. Delmon, Study of the hydrodeoxygenation of carbonyl, carboxylic and guaiacyl groups over sulfided CoMo/ γ -Al₂O₃ and NiMo/ γ -Al₂O₃ catalyst: II. Influence of water, ammonia and hydrogen sulfide, *Appl. Catal., A*, **1994**, *109* (1), 97-115.
16. O. İ. Şenol; T. R. Viljava; A. O. I. Krause, Effect of sulphiding agents on the hydrodeoxygenation of aliphatic esters on sulphided catalysts, *Appl. Catal., A*, **2007**, *326* (2), 236-244.
17. E.-M. Ryymin; M. L. Honkela; T.-R. Viljava; A. O. I. Krause, Insight to sulfur species in the hydrodeoxygenation of aliphatic esters over sulfided NiMo/ γ -Al₂O₃ catalyst, *Appl. Catal., A*, **2009**, *358* (1), 42-48.
18. D. Kubička; M. Bejblová; J. Vlk, Conversion of Vegetable Oils into Hydrocarbons over CoMo/MCM-41 Catalysts, *Top. Catal.*, **2010**, *53* (3-4), 168-178.
19. R. K. Sharma; M. Anand; B. S. Rana; R. Kumar; S. A. Farooqui; M. G. Sibi; A. K. Sinha, Jatropha-oil conversion to liquid hydrocarbon fuels using mesoporous titanosilicate supported sulfide catalysts, *Catal. Today*, **2012**, *198* (1), 314-320.
20. O. İ. Şenol; E. M. Ryymin; T. R. Viljava; A. O. I. Krause, Reactions of methyl heptanoate hydrodeoxygenation on sulphided catalysts, *J. Mol. Catal. A: Chem.*, **2007**, *268* (1-2), 1-8.
21. F. E. Massoth; P. Politzer; M. C. Concha; J. S. Murray; J. Jakowski; J. Simons, Catalytic Hydrodeoxygenation of Methyl-Substituted Phenols: Correlations of Kinetic Parameters with Molecular Properties, *J. Phys. Chem. B*, **2006**, *110* (29), 14283-14291.
22. Y. Romero; F. Richard; S. Brunet, Hydrodeoxygenation of 2-ethylphenol as a model compound of bio-crude over sulfided Mo-based catalysts: Promoting effect and reaction mechanism, *Appl. Catal., B*, **2010**, *98* (3-4), 213-223.
23. V. N. Bui; D. Laurenti; P. Afanasiev; C. Geantet, Hydrodeoxygenation of guaiacol with CoMo catalysts. Part I: Promoting effect of cobalt on HDO selectivity and activity, *Appl. Catal., B*, **2011**, *101* (3-4), 239-245.
24. E.-M. Ryymin; M. L. Honkela; T.-R. Viljava; A. O. I. Krause, Competitive reactions and mechanisms in the simultaneous HDO of phenol and methyl heptanoate over sulphided NiMo/ γ -Al₂O₃, *Appl. Catal., A*, **2010**, *389* (1-2), 114-121.
25. P. Šimáček; D. Kubička; G. Šebor; M. Pospíšil, Fuel properties of hydroprocessed rapeseed oil, *Fuel*, **2010**, *89* (3), 611-615.
26. H. Iki; Y. Iguchi, Development of Bio Hydro-fined Diesel (BHD) Technology: Hydrodeoxygenation of Palm Oil and Adaptability of BHD for Diesel Fuel, *J. Jpn. Pet. Inst.*, **2012**, *55* (6), 349-357.
27. E. W. Qian; N. Chen; S. Gong, Role of support in deoxygenation and isomerization of methyl stearate over nickel-molybdenum catalysts, *J. Mol. Catal. A*, **2014**, *387*, 76-85.
28. A. Guzman; J. E. Torres; L. P. Prada; M. L. Nuñez, Hydroprocessing of crude palm oil at pilot plant scale, *Catal. Today*, **2010**, *156* (1-2), 38-43.
29. E. Laurent; B. Delmon, Study of the hydrodeoxygenation of carbonyl, carboxylic and guaiacyl groups over sulfided CoMo/ γ -Al₂O₃ and NiMo/ γ -Al₂O₃ catalysts: I. Catalytic reaction schemes, *Appl. Catal., A*, **1994**, *109* (1), 77-96.

30. M. Philippe; F. Richard; D. Hudebine; S. Brunet, Transformation of dibenzothiophenes model molecules over CoMoP/Al₂O₃ catalyst in the presence of oxygenated compounds, *Appl. Catal., B*, **2013**, 132–133, 493-498.
31. S. Brillouet; E. Baltag; S. Brunet; F. Richard, Deoxygenation of decanoic acid and its main intermediates over unpromoted and promoted sulfided catalysts, *Appl. Catal., B*, **2014**, 148–149, 201-211.
32. D. Kubička; J. Horáček; M. Setnička; R. Bulánek; A. Zukal; I. Kubičková, Effect of support-active phase interactions on the catalyst activity and selectivity in deoxygenation of triglycerides, *Appl. Catal., B*, **2014**, 145, 101-107.
33. I. Borges Jr; A. M. Silva; A. P. Aguiar; L. E. P. Borges; J. C. A. Santos; M. H. C. Dias, Density functional theory molecular simulation of thiophene adsorption on MoS₂ including microwave effects, *J. Mol. Struct. THEOCHEM*, **2007**, 822 (1–3), 80-88.
34. J. Mijoin; V. Thévenin; N. Garcia Aguirre; H. Yuze; J. Wang; W. Z. Li; G. Pérot; J. L. Lemberon, Thio reduction of cyclopentanone and hydrodesulfurization of dibenzothiophene over sulfided nickel or cobalt-promoted molybdenum on alumina catalysts, *Appl. Catal., A*, **1999**, 180 (1–2), 95-104.
35. V. C. H. Kroll; H. M. Swaan; C. Mirodatos, Methane Reforming Reaction with Carbon Dioxide Over Ni/SiO₂ Catalyst: I. Deactivation Studies, *J. Catal.*, **1996**, 161 (1), 409-422.
36. H. Zhang; H. Lin; Y. Zheng, The role of cobalt and nickel in deoxygenation of vegetable oils, *Appl. Catal., B*, **2014**, 160–161, 415-422.
37. T. V. Choudhary; C. B. Phillips, Renewable fuels via catalytic hydrodeoxygenation, *Appl. Catal., A*, **2011**, 397 (1–2), 1-12.
38. M. Krár; S. Kovács; D. Kalló; J. Hancsók, Fuel purpose hydrotreating of sunflower oil on CoMo/Al₂O₃ catalyst, *Bioresour. Technol.*, **2010**, 101 (23), 9287-9293.
39. H. Wang; J. Male; Y. Wang, Recent Advances in Hydrotreating of Pyrolysis Bio-Oil and Its Oxygen-Containing Model Compounds, *ACS Catal.*, **2013**, 3 (5), 1047-1070.
40. E. Furimsky, Catalytic hydrodeoxygenation, *Appl. Catal., A*, **2000**, 199 (2), 147-190.
41. P. M. Mortensen; J. D. Grunwaldt; P. A. Jensen; K. G. Knudsen; A. D. Jensen, A review of catalytic upgrading of bio-oil to engine fuels, *Appl. Catal., A*, **2011**, 407 (1–2), 1-19.
42. D. Kubička; J. Horáček, Deactivation of HDS catalysts in deoxygenation of vegetable oils, *Appl. Catal., A*, **2011**, 394 (1-2), 9-17.
43. M. Badawi; J. F. Paul; S. Cristol; E. Payen; Y. Romero; F. Richard; S. Brunet; D. Lambert; X. Portier; A. Popov; E. Kondratieva; J. M. Goupil; J. El Fallah; J. P. Gilson; L. Mariey; A. Travert; F. Maugé, Effect of water on the stability of Mo and CoMo hydrodeoxygenation catalysts: A combined experimental and DFT study, *J. Catal.*, **2011**, 282 (1), 155-164.
44. M. Snåre; I. Kubičková; P. Mäki-Arvela; D. Chichova; K. Eränen; D. Y. Murzin, Catalytic deoxygenation of unsaturated renewable feedstocks for production of diesel fuel hydrocarbons, *Fuel*, **2008**, 87 (6), 933-945.
45. P. Mäki-Arvela; M. Snåre; K. Eränen; J. Myllyoja; D. Y. Murzin, Continuous decarboxylation of lauric acid over Pd/C catalyst, *Fuel*, **2008**, 87 (17–18), 3543-3549.

46. S. Lestari; I. Simakova; A. Tokarev; P. Mäki-Arvela; K. Eränen; D. Murzin, Synthesis of Biodiesel via Deoxygenation of Stearic Acid over Supported Pd/C Catalyst, *Catal. Lett.*, **2008**, *122* (3-4), 247-251.
47. M. Snåre; I. Kubičková; P. Mäki-Arvela; K. Eränen; J. Wärnä; D. Y. Murzin, Production of diesel fuel from renewable feeds: Kinetics of ethyl stearate decarboxylation, *Chem. Eng. J.*, **2007**, *134* (1-3), 29-34.
48. P. Mäki-Arvela; I. Kubickova; M. Snåre; K. Eränen; D. Y. Murzin, Catalytic Deoxygenation of Fatty Acids and Their Derivatives, *Energy Fuels*, **2007**, *21* (1), 30-41.
49. I. Kubičková; M. Snåre; K. Eränen; P. Mäki-Arvela; D. Y. Murzin, Hydrocarbons for diesel fuel via decarboxylation of vegetable oils, *Catal. Today*, **2005**, *106* (1-4), 197-200.
50. M. Snåre; I. Kubičková; P. Mäki-Arvela; K. Eränen; D. Y. Murzin, Heterogeneous Catalytic Deoxygenation of Stearic Acid for Production of Biodiesel, *Ind. Eng. Chem. Res.*, **2006**, *45* (16), 5708-5715.
51. J. A. Lopez-Ruiz; R. J. Davis, Decarbonylation of heptanoic acid over carbon-supported platinum nanoparticles, *Green Chemistry*, **2014**, *16* (2), 683-694.
52. M. Ahmadi; A. Nambo; J. B. Jasinski; P. Ratnasamy; M. A. Carreon, Decarboxylation of oleic acid over Pt catalysts supported on small-pore zeolites and hydrotalcite, *Catal. Sci. Technol.*, **2015**, *5* (1), 380-388.
53. Y. Wang; Z. Tao; B. Wu; J. Xu; C. Huo; K. Li; H. Chen; Y. Yang; Y. Li, Effect of metal precursors on the performance of Pt/ZSM-22 catalysts for n-hexadecane hydroisomerization, *J. Catal.*, **2015**, *322*, 1-13.
54. Y. Rezgui; M. Guemini, Effect of acidity and metal content on the activity and product selectivity for n-decane hydroisomerization and hydrocracking over nickel-tungsten supported on silica-alumina catalysts, *Appl. Catal., A*, **2005**, *282* (1-2), 45-53.
55. M. C. Román-Martínez; D. Cazorla-Amorós; A. Linares-Solano; C. S.-M. n. De Lecea; H. Yamashita; M. Anpo, Metal-support interaction in Pt/C catalysts. Influence of the support surface chemistry and the metal precursor, *Carbon*, **1995**, *33* (1), 3-13.
56. K. Kon; W. Onodera; S. Takakusagi; K.-i. Shimizu, Hydrodeoxygenation of fatty acids and triglycerides by Pt-loaded Nb₂O₅ catalysts, *Catal. Sci. Technol.*, **2014**, *4* (10), 3705-3712.
57. Y. Shao; Q. Xia; X. Liu; G. Lu; Y. Wang, Pd/Nb₂O₅/SiO₂ catalyst for the direct hydrodeoxygenation of biomass-related compounds to liquid alkanes under mild conditions, *ChemSusChem*, **2015**, *8* (10), 1761-7.
58. L. Zhou; A. Lawal, Hydrodeoxygenation of microalgae oil to green diesel over Pt, Rh and presulfided NiMo catalysts, *Catal. Sci. Technol.*, **2015**.
59. L. He; C. Wu; H. Cheng; Y. Yu; F. Zhao, Highly selective and efficient catalytic conversion of ethyl stearate into liquid hydrocarbons over a Ru/TiO₂ catalyst under mild conditions, *Catalysis Science & Technology*, **2012**, *2* (7), 1328.
60. A. Primo; P. Concepcion; A. Corma, Synergy between the metal nanoparticles and the support for the hydrogenation of functionalized carboxylic acids to diols on Ru/TiO₂, *Chem. Commun.*, **2011**, *47* (12), 3613-3615.
61. R. Liu; Y. Yu; K. Yoshida; G. Li; H. Jiang; M. Zhang; F. Zhao; S.-i. Fujita; M. Arai, Physically and chemically mixed TiO₂-supported Pd and Au catalysts: unexpected

- synergistic effects on selective hydrogenation of citral in supercritical CO₂, *J. Catal.*, **2010**, *269* (1), 191-200.
62. R. T. Yang; Y. Wang, Catalyzed Hydrogen Spillover for Hydrogen Storage, *J. Am. Chem. Soc.*, **2009**, *131* (12), 4224-4226.
63. K. Murata; Y. Liu; M. Inaba; I. Takahara, Production of Synthetic Diesel by Hydrotreatment of Jatropha Oils Using Pt–Re/H-ZSM-5 Catalyst, *Energy Fuels*, **2010**, *24* (4), 2404-2409.
64. D. A. Ruddy; J. A. Schaidle; J. R. Ferrell Iii; J. Wang; L. Moens; J. E. Hensley, Recent advances in heterogeneous catalysts for bio-oil upgrading via "ex situ catalytic fast pyrolysis": catalyst development through the study of model compounds, *Green Chem.*, **2014**, *16* (2), 454-490.
65. A. Boffa; C. Lin; A. T. Bell; G. A. Somorjai, Promotion of CO and CO₂ Hydrogenation over Rh by Metal Oxides: The Influence of Oxide Lewis Acidity and Reducibility, *J. Catal.*, **1994**, *149* (1), 149-158.
66. R. Pestman; R. M. Koster; J. A. Z. Pieterse; V. Ponec, Reactions of Carboxylic Acids on Oxides: 1. Selective Hydrogenation of Acetic Acid to Acetaldehyde, *J. Catal.*, **1997**, *168* (2), 255-264.
67. M. J. Mendes; O. A. A. Santos; E. Jordão; A. M. Silva, Hydrogenation of oleic acid over ruthenium catalysts, *Appl. Catal., A*, **2001**, *217* (1–2), 253-262.
68. C. H. Bartholomew, Mechanisms of catalyst deactivation, *Appl. Catal., A*, **2001**, *212* (1–2), 17-60.
69. A. Popov; E. Kondratieva; J. M. Goupil; L. Mariey; P. Bazin; J.-P. Gilson; A. Travert; F. Maugé, Bio-oils Hydrodeoxygenation: Adsorption of Phenolic Molecules on Oxidic Catalyst Supports, *J. Phys. Chem. C*, **2010**, *114* (37), 15661-15670.
70. O. V. Kikhtyanin; A. E. Rubanov; A. B. Ayupov; G. V. Echevsky, Hydroconversion of sunflower oil on Pd/SAPO-31 catalyst, *Fuel*, **2010**, *89* (10), 3085-3092.
71. G. Nagy; G. Pölczmán; D. Kalló; J. Hancsók, Investigation of hydrodearomatization of gas oils on noble metal/support catalysts, *Chemical Engineering Journal*, **2009**, *154* (1–3), 307-314.
72. V. A. Yakovlev; S. A. Khromova; O. V. Sherstyuk; V. O. Dundich; D. Y. Ermakov; V. M. Novopashina; M. Y. Lebedev; O. Bulavchenko; V. N. Parmon, Development of new catalytic systems for upgraded bio-fuels production from bio-crude-oil and biodiesel, *Catal. Today*, **2009**, *144* (3–4), 362-366.
73. B. Peng; Y. Yao; C. Zhao; J. A. Lercher, Towards Quantitative Conversion of Microalgae Oil to Diesel-Range Alkanes with Bifunctional Catalysts, *Angew. Chem. Int. Ed.*, **2012**, *51* (9), 2072-2075.
74. B. Peng; X. Yuan; C. Zhao; J. A. Lercher, Stabilizing Catalytic Pathways via Redundancy: Selective Reduction of Microalgae Oil to Alkanes, *J. Am. Chem. Soc.*, **2012**, *134* (22), 9400-9405.
75. H. Zuo; Q. Liu; T. Wang; L. Ma; Q. Zhang; Q. Zhang, Hydrodeoxygenation of Methyl Palmitate over Supported Ni Catalysts for Diesel-like Fuel Production, *Energy Fuels*, **2012**, *26* (6), 3747-3755.

76. W. Song; C. Zhao; J. A. Lercher, Importance of Size and Distribution of Ni Nanoparticles for the Hydrodeoxygenation of Microalgae Oil, *Chemistry – A European Journal*, **2013**, *19* (30), 9833-9842.
77. X.-f. Li; X.-g. Luo, Preparation of mesoporous activated carbon supported Ni catalyst for deoxygenation of stearic acid into hydrocarbons, *Environmental Progress & Sustainable Energy*, **2015**, *34* (2), 607-612.
78. R. G. Kukushkin; O. A. Bulavchenko; V. V. Kaichev; V. A. Yakovlev, Influence of Mo on catalytic activity of Ni-based catalysts in hydrodeoxygenation of esters, *Appl. Catal., B*, **2015**, *163*, 531-538.
79. C. Ochoa-Hernández; Y. Yang; P. Pizarro; V. A. de la Peña O'Shea; J. M. Coronado; D. P. Serrano, Hydrocarbons production through hydrotreating of methyl esters over Ni and Co supported on SBA-15 and Al-SBA-15, *Catal. Today*, **2013**, *210*, 81-88.
80. S. M. Schimming; O. D. LaMont; M. König; A. K. Rogers; A. D. D'Amico; M. M. Yung; C. Sievers, Hydrodeoxygenation of Guaiacol over Ceria–Zirconia Catalysts, *ChemSusChem*, **2015**, *8* (12), 2073-2083.
81. M. Shetty; K. Murugappan; T. Prasomsri; W. H. Green; Y. Román-Leshkov, Reactivity and stability investigation of supported molybdenum oxide catalysts for the hydrodeoxygenation (HDO) of m-cresol, *J. Catal.*, **2015**, *331*, 86-97.
82. K. Kandel; J. W. Anderegg; N. C. Nelson; U. Chaudhary; I. I. Slowing, Supported iron nanoparticles for the hydrodeoxygenation of microalgal oil to green diesel, *J. Catal.*, **2014**, *314*, 142-148.
83. A. Chen; Y. Zhou; N. Ta; Y. Li; W. Shen, Redox properties and catalytic performance of ceria-zirconia nanorods, *Catalysis Science & Technology*, **2015**, *5* (8), 4184-4192.
84. S. T. Gentry; S. F. Kendra; M. W. Bezpalko, Ostwald Ripening in Metallic Nanoparticles: Stochastic Kinetics, *The Journal of Physical Chemistry C*, **2011**, *115* (26), 12736-12741.
85. P. Dagtepe; V. Chikan, Quantized Ostwald Ripening of Colloidal Nanoparticles, *The Journal of Physical Chemistry C*, **2010**, *114* (39), 16263-16269.
86. Q. Liu; H. Zuo; T. Wang; L. Ma; Q. Zhang, One-step hydrodeoxygenation of palm oil to isomerized hydrocarbon fuels over Ni supported on nano-sized SAPO-11 catalysts, *Appl. Catal., A*, **2013**, *468*, 68-74.
87. B. Ma; C. Zhao, High-grade diesel production by hydrodeoxygenation of palm oil over a hierarchically structured Ni/HBEA catalyst, *Green Chem.*, **2015**, *17* (3), 1692-1701.
88. B. Ma; J. Hu; Y. Wang; C. Zhao, Ni nanoparticles encapsulated into mesoporous single-crystalline HBEA: application for drainage oil hydrodeoxygenation to diesel, *Green Chem.*, **2015**, *17* (9), 4610-4617.
89. G. W. Huber; P. O'Connor; A. Corma, Processing biomass in conventional oil refineries: Production of high quality diesel by hydrotreating vegetable oils in heavy vacuum oil mixtures, *Appl. Catal., A*, **2007**, *329*, 120-129.
90. J. G. Immer; M. J. Kelly; H. H. Lamb, Catalytic reaction pathways in liquid-phase deoxygenation of C18 free fatty acids, *Appl. Catal., A*, **2010**, *375* (1), 134-139.

91. B. Peng; C. Zhao; S. Kasakov; S. Foraita; J. A. Lercher, Manipulating catalytic pathways: deoxygenation of palmitic acid on multifunctional catalysts, *Chemistry*, **2013**, *19* (15), 4732-41.
92. P. Kumar; S. R. Yenumala; S. K. Maity; D. Shee, Kinetics of hydrodeoxygenation of stearic acid using supported nickel catalysts: Effects of supports, *Appl. Catal., A*, **2014**, *471*, 28-38.
93. S. Krompiec; J. Mrowiec-Białoń; K. Skutil; A. Dukowicz; L. Pająk; A. B. Jarzębski, Nickel–alumina composite aerogel catalysts with a high nickel load: a novel fast sol–gel synthesis procedure and screening of catalytic properties, *J. Non-Cryst. Solids*, **2003**, *315* (3), 297-303.
94. T. Yokoyama; T. Setoyama; N. Fujita; M. Nakajima; T. Maki; K. Fujii, Novel direct hydrogenation process of aromatic carboxylic acids to the corresponding aldehydes with zirconia catalyst, *Appl. Catal., A*, **1992**, *88* (2), 149-161.
95. R. Pestman; R. M. Koster; E. Boellaard; A. M. van der Kraan; V. Ponec, Identification of the Active Sites in the Selective Hydrogenation of Acetic Acid to Acetaldehyde on Iron Oxide Catalysts, *J. Catal.*, **1998**, *174* (2), 142-152.
96. T. Yokoyama; N. Yamagata, Hydrogenation of carboxylic acids to the corresponding aldehydes, *Appl. Catal., A*, **2001**, *221* (1–2), 227-239.
97. W. Song; C. Zhao; J. A. Lercher, Importance of size and distribution of Ni nanoparticles for the hydrodeoxygenation of microalgae oil, *Chemistry*, **2013**, *19* (30), 9833-42.
98. A. Srifa; N. Viriya-empikul; S. Assabumrungrat; K. Faungnawakij, Catalytic behaviors of Ni/ γ -Al₂O₃ and Co/ γ -Al₂O₃ during the hydrodeoxygenation of palm oil, *Catal. Sci. Technol.*, **2015**, *5* (7), 3693-3705.
99. J. Hancsók; T. Kasza; S. Kovács; P. Solymosi; A. Holló, Production of bioparaffins by the catalytic hydrogenation of natural triglycerides, *Journal of Cleaner Production*, **2012**, *34*, 76-81.
100. A. Corma, From Microporous to Mesoporous Molecular Sieve Materials and Their Use in Catalysis, *Chemical Reviews*, **1997**, *97* (6), 2373-2420.
101. A. Corma; V. Fornés; F. V. Melo; J. Herrero, Comparison of the information given by ammonia t.p.d. and pyridine adsorption—desorption on the acidity of dealuminated HY and LaHY zeolite cracking catalysts, *Zeolites*, **1987**, *7* (6), 559-563.
102. A. Corma; V. Fornes; M. T. Navarro; J. Perezpariente, Acidity and Stability of MCM-41 Crystalline Aluminosilicates, *J. Catal.*, **1994**, *148* (2), 569-574.
103. J. Huang; Y. Jiang; V. R. R. Marthala; A. Bressel; J. Frey; M. Hunger, Effect of pore size and acidity on the coke formation during ethylbenzene conversion on zeolite catalysts, *J. Catal.*, **2009**, *263* (2), 277-283.
104. J. M. NEWSAM, The Zeolite Cage Structure, *Science*, **1986**, *231* (4742), 1093-1099.
105. E. Roduner, Understanding catalysis, *Chem. Soc. Rev.*, **2014**, *43* (24), 8226-8239.
106. Y. Liu; R. Sotelo-Boyás; K. Murata; T. Minowa; K. Sakanishi, Hydrotreatment of Vegetable Oils to Produce Bio-Hydrogenated Diesel and Liquefied Petroleum Gas Fuel over Catalysts Containing Sulfided Ni–Mo and Solid Acids, *Energy Fuels*, **2011**, *25* (10), 4675-4685.

107. D. Verma; R. Kumar; B. S. Rana; A. K. Sinha, Aviation fuel production from lipids by a single-step route using hierarchical mesoporous zeolites, *Energy & Environmental Science*, **2011**, 4 (5), 1667.
108. S. Gong; A. Shinozaki; E. W. Qian, Role of Support in Hydrotreatment of Jatropha Oil over Sulfided NiMo Catalysts, *Ind. Eng. Chem. Res.*, **2012**, 51 (43), 13953-13960.
109. V. M. Akhmedov; S. H. Al-Khowaiter, Recent Advances and Future Aspects in the Selective Isomerization of High n-Alkanes, *Catal. Rev. Sci. Eng*, **2007**, 49 (1), 33-139.

Chapter 2

Simultaneous Hydrodeoxygenation-Isomerization of Jatropha Oil and Methyl Laurate over Reduced NiMo Catalysts

Abstract

To develop a sulfide-free catalyst for one-step deoxygenation and isomerization of triglyceride-related compounds to produce hydrocarbon fuels with good cold flow properties, NiMo (nickel and molybdenum) catalysts were prepared by using various acid supports, *i.e.*, SiO₂-Al₂O₃, SAPO-11 or AISBA-15, and activated by hydrogen reduction. Time-on-stream experiment (over 130 h) for hydrotreating of Jatropha oil showed that the NiMo catalyst reduced at 400 °C had extremely high stability. High deoxygenation degree could be obtained at a relatively high reaction temperature compared to the sulfided catalyst. Isomerization activity was largely affected by the acidity of the support. The SAPO-11 support had moderate acidity and exhibited the highest isomerization selectivity, on which the formation of branched alkanes with lower melting point could be enhanced. Further investigation on the reduction temperature of NiMo/SAPO-11 was performed using the hydrotreating of methyl laurate as a model compound. The reduction temperature had a significant influence on the percentage of different Mo species in the catalyst. Experimental results disclosed that Mo species with different valences possessed distinct catalytic functions. The hydrotreating reaction was also conducted over Ni/SAPO-11 and Mo/SAPO-11 to confirmed different active phases in the NiMo/SAPO-11 catalyst. Reaction results demonstrated a synergistic effect based on nickel metal and Mo⁴⁺ species.

2.1 Introduction

Vegetable oils contain a considerable amount of oxygenates such as triglycerides and free fatty acids. To convert these compounds into hydrocarbons that have identical properties to fossil-derived transportation fuels, complete removal of oxygen atoms by hydrotreating is required. The commercial hydrotreating catalyst is based on γ -Al₂O₃ supported molybdenum sulfides, which are promoted with lesser amounts of cobalt or nickel.^{1, 2} In order to maintain the sulfided active phase, an external sulfur source such as dimethyl disulfide should be co-fed with the feedstock.³ However, a large amount of sulfur species would remain in the final products, resulting in a contamination.^{3, 4} In fact, there is only a trace amount of sulfur (< 10 ppm) in vegetable oils, and therefore, clean energy can be easily obtained without the hydrodesulfurization process compared to the energy derived from petroleum. In this sense, there is an apparent need to develop a non-sulfide catalyst for hydrotreating of vegetable oils. Supported noble metal catalysts, *i.e.*, Pd/SAPO-31 or Pt/SAPO-11, were used as sulfide-free catalysts.^{5, 6} The acid support used in these catalysts is expected to improve isomerization selectivity, and endows the liquid product with good cold flow properties.⁷ However, rapid deactivation and high cost become obstacles to their industrial utilization. In an effort to establish a more environmentally friendly and economic process for upgrading vegetable oils, Lercher's group developed nickel-based catalysts.^{8, 9} Although these catalysts have obvious advantages compared to previous catalysts, extremely high decarboxylation/decarbonylation (DCO) selectivity (> 95 %) was observed, which would lower the yield of liquid products. Even worse, the *in situ* generated CO and CO₂ could be transformed to methane due to the high methanation activity of the nickel phase, which would substantially increase the hydrogen consumption.

In this chapter, a new catalytic system involving reduced nickel-molybdenum oxides (Ni-MoO_{3-x}) as the deoxygenation function and an acid support as the isomerization function was designed to achieve the one-step conversion of vegetable oils. First, the activity and stability of reduced NiMo/Al₂O₃ were investigated by a time-on-stream experiment for hydrotreating of Jatropha oil. Then, various acid

supports, *i.e.*, γ -Al₂O₃, SiO₂-Al₂O₃, SAPO-11 or AISBA-15, were used for preparing bifunctional catalysts, and the screening of these catalysts was conducted in hydrotreating of Jatropha oil. Subsequently, further investigation on the reduction temperature of NiMo/SAPO-11 was performed using hydrotreating of methyl laurate as a model compound. In addition, the catalyst was characterized using NO pulse chemisorption, transmission electron microscope (TEM), H₂ temperature-programmed reduction (H₂-TPR), NH₃ temperature-programmed desorption (NH₃-TPD) and X-ray photoelectron spectroscopy (XPS). Finally, the correlation between Mo species with different valences and the catalytic performance, *i.e.*, deoxygenation activity, reaction pathway and isomerization selectivity, was elucidated through combining the result of characterization and reaction.

2.2 Experimental Section

2.2.1 Catalyst Preparation

Al_2O_3 and $\text{SiO}_2\text{-Al}_2\text{O}_3$ (Si/Al = 0.12) were supplied by Nippon Ketjen. SAPO-11 (Si/Al = 0.1 mol/mol) was supplied by Nikki-Universal. Al-incorporated SBA-15 (Si/Al = 5 mol/mol) was synthesized according to an early report.¹⁰ NiMo catalysts were prepared by an incipient wetness impregnation method.¹¹ First, the Al_2O_3 , $\text{SiO}_2\text{-Al}_2\text{O}_3$, SAPO-11 and AlSBA-15 samples were grounded and sieved to yield 425-850 μm particles as supports. Subsequently, the support was impregnated with an aqueous solution of $(\text{NH}_4)_6\text{Mo}_7\text{O}_{24}\cdot 4\text{H}_2\text{O}$ (99.9%, Wako Pure Chem. Ltd.). After drying at 120 °C for 2 h and calcining at 500 °C for 5 h in air, the molybdenum catalyst was impregnated with an aqueous solution of $\text{Ni}(\text{NO}_3)_2\cdot 6\text{H}_2\text{O}$ (99.9%, Wako Pure Chem. Ltd.). After the impregnation, the precursor was dried at 120 °C for 2 h and calcined at 450 °C for 16 h. The loading amount of MoO_3 and NiO are 20 wt% and 3.5 wt%, respectively. Before using, the catalyst was activated by reduction with pure hydrogen (50 mL/min) at different temperatures (400–550 °C) for 3 h or by sulfidation with a mixture of 5 vol.% H_2S in H_2 (50 mL/min) at an increased temperature of 100 °C, 200 °C and 300 °C for 30 min and finally 400 °C for 3 h. The reduced catalyst is denoted as $x\text{R-M}$ and the sulfided catalyst is denoted as S-M , where x and M refer to reduction temperature and metal species, respectively. Monometallic Ni/SAPO-11 and Mo/SAPO-11 catalysts were prepared by the same procedure with the NiMo catalyst.

2.2.2 Catalyst Characterization

Textural properties of the support and catalyst were determined by nitrogen physisorption at -196 °C using a Belsorp-mini II automated sorption system. The specific surface area, average pore diameter and total pore volume were calculated using the Brunauer–Emmett–Teller method at a relative partial pressure of 0.05–0.3.¹² Prior to the measurement, the sample was degassed under vacuum ($p < 10^{-2}$ kPa) at 400 °C for 1 h.

H₂-TPR measurements were performed using a ChemBET Pulsar TPR/TPD instrument (Quantachrome Instruments). First, a measured amount of the calcined catalyst (100 mg) was loaded in a U shaped quartz tube, and the sample was pretreated in a highly pure He flow at 500 °C for 3 h to remove adsorbed impurities. Then, the sample was cooled to 30 °C under helium flow, followed by changing the gas to 5 vol.% H₂/Ar. H₂-TPR was performed by linearly increasing the temperature from 30 to 1000 °C at a heating rate of 5 °C/min. Water generated during the experiment was adsorbed by a column which was filled with soda lime. Hydrogen consumption was monitored using a thermal conductivity detector (TCD). A calibration curve for hydrogen was made for quantification. To obtain information regarding the reduction degree at different temperatures, the other H₂ reduction experiment was performed under a constant temperature (at a heating rate of 20 °C). The amount of hydrogen consumption was estimated by using a calibration curve.

The acidity of the catalyst was measured by NH₃-TPD using the same instrument as H₂-TPR. Typically, a 200 mg sample was pre-reduced *in situ* in a hydrogen flow (15 mL/min) for 3 h, followed by cooling to 30 °C in a helium flow. Ammonia adsorption was conducted for 40 min under a 15 mL/min 10 vol.% NH₃/He flow. Physically adsorbed ammonia was removed under helium flow at 100 °C for 2 h, and TPD was performed by linearly increasing the cell temperature from 100 °C to 800 °C at a heating rate of 10 °C/min under a 15 mL/min helium flow. The amount of desorbed ammonia was calculated by using a calibration curve.

XPS spectra were acquired using an ESCA-3200 (Shimadzu) spectrometer with monochromatic Mg K α radiation (240 W, 8 kV, $E = 1253.6$ eV). The spectrometer was interfaced to a SUN PC compatible for data collection. The CasaXPS software package (Casa Software Ltd., Teignmouth, UK) was used for subsequent data analysis. The binding energy (BE) value was referenced to adventitious carbon (C 1s at 284.6 eV). A Shirley-type background was subtracted for Mo 3d envelopes, and the linear-type background was subtracted for Ni 2p envelopes. The recorded spectra were fitted using Gaussian–Lorentzian curves. After reduction, the sample was prepared

in a dry box under an argon flow. A degassing pretreatment was carried out prior to analysis.

NO pulse chemisorption was performed using the same instrument as H₂-TPR. 400 mg catalyst was used for each experiment. After reduction, the sample was further heated to 550 °C under a helium flow to remove the adsorbed hydrogen. The NO pulse adsorption was performed at 40 °C. He was used as the carrier gas, and successive doses of 10% NO/He gas were subsequently introduced using a calibrated injection valve (25 μL NO pulse⁻¹).

TEM observations were performed on a JEOL 2100 microscope (JEOL, Japan), working at 200 kV. The sample power after reduction was deposited on a carbon coated Cu grid.

2.2.3 Activity Test

Hydrotreating of Jatropa oil was performed in a high-pressure fixed-bed continuous-flow stainless steel reactor with a diameter of 30 mm. Prior to the reaction, the catalyst was reduced at 400 °C under a H₂ flow for 3 h or sulfided at 100, 200, 300 °C for 30 min and finally 400 °C for 3 h using a 5 vol% H₂S/H₂ mixture gas. Jatropa oil was introduced into the reactor by a high-pressure liquid pump. The reaction was conducted at 375–425 °C, under 3 MPa, with a liquid hourly liquid hourly space velocity (LHSV) of 1 h⁻¹, and Gas/Oil ratio of 1000 (ml/ml).

Hydrotreating of methyl laurate (ML) was performed as a model reaction to evaluate deoxygenation and isomerization activity of the catalyst. The reaction was performed in another continuous-flow reactor (8 mm in diameter and 40 mm in length), which is operated in the down-flow mode. For each activity test, 1.5 g calcined catalyst was diluted with quartz and charged into the reactor. The catalyst was reduced under a 50 mL/min H₂ flow for 3 h. The reaction was conducted at various temperatures (275–375 °C), under 3 MPa of hydrogen pressure, with a weight hourly space velocity (WHSV) of 5 h⁻¹ and a H₂/feed ratio of 800 (ml/ml). The catalytic activity was measured after stabilization (from TOS = 5 h). No significant deactivation of the catalyst could be observed during the experiment.

After the reaction, liquid products were diluted with carbon tetrachloride and analyzed using a gas chromatograph (GC-2025, Shimadzu Corp.) equipped with a flame ionization detector (FID) and a DB-5HT column (Agilent, 30 m × 0.25 mm i.d., 0.25 μm). The product identification was performed using a gas chromatograph-mass spectrometer (GC-MS-QP5050A, Shimadzu Corp.) equipped with the same capillary column. Another gas chromatograph with a thermal conductivity detector (TCD) and a Unibeads C column (GL Sciences Inc., 3 m × 3 mm i.d.) was used to measure other gaseous products such as CO and CO₂.

The amount of products was quantified using GC standards. The conversion of the feedstock, deoxygenation degree and selectivity were calculated by the following equations.

$$\text{Conversion (\%)} = \left(1 - \frac{n_{\text{Feed}}}{n_{\text{Feed0}}}\right) \times 100$$

$$\text{HDO (\%)} = \left(1 - \frac{\sum_{\text{Product}}}{\sum_{\text{Feedstock}}}\right) \times 100$$

$$\text{Selectivity (\%)} = \frac{n_i \times a_i}{\sum n_i \times a_i} \times 100$$

where n_{Feed0} is the number of molecules of triglycerides or methyl laurate in the feedstock, n_{Feed} is the number of molecules of triglycerides or methyl laurate in the product, $\sum_{\text{Feedstock}}$ is the molar amount of total oxygen in the feedstock, \sum_{Product} is the molar amount of total oxygen in the products, n_i is the mole number of product i , and a_i is the carbon atom number of product i .

The turnover frequency was determined using the following equation.

$$\text{TOF} = -\frac{F/W}{M} \times \ln(1 - X)$$

where X is the conversion (%), F is the reactant molar flow (mol/s), W is the catalyst weight (g) and M is number of the active sites measured by NO pulse chemisorption.

2.3 Results and Discussion

2.3.1 Catalyst Characterization

The metal loading determined by XRF and textural properties derived from nitrogen adsorption-desorption isotherms are listed in **Table 2.1**. Metal loadings of the catalyst were similar to the target values, indicating that metals were successfully loaded on the support. After reduction, although there is a little increase in the BET surface area, no considerable change could be observed among the catalysts reduced at different temperatures.

Table 2.1 Chemical analysis and textural properties of various catalysts.

Catalyst	Chemical Composition		Textural properties		
	NiO (wt%)	MoO ₃ (wt%)	$S_{\text{BET}}^{\text{a}}$ (m ² /g)	$V_{\text{total}}^{\text{b}}$ (cm ³ /g)	$d_{\text{avg}}^{\text{c}}$ (nm)
NiMo/Al ₂ O ₃	3.3	19.3	219	0.62	11.2
NiMo/SiO ₂ -Al ₂ O ₃	3.4	18.6	215	0.69	12.8
NiMo/AlSBA-15	3.5	18.1	424	0.67	6.3
Ni/SAPO-11	3.5	-	126	0.22	7.0
Mo/SAPO-11	-	19.5	94	0.19	7.9
NiMo/SAPO-11	3.3	18.3	52	0.12	9.6
400R-NiMo	-	-	75	0.12	6.3
450R-NiMo	-	-	74	0.12	6.3
500R-NiMo	-	-	76	0.13	6.5
550R-NiMo	-	-	79	0.13	6.6

^a Specific surface area. ^b Total pore volume. ^c Average pore size.

H₂-TPR patterns for the Ni/SAPO-11, Mo/SAPO-11 and NiMo/SAPO-11 catalysts are compared in **Figure 2.1**. The reduction peaks appeared in two regions; one started at 400 °C and ended at 720 °C, and the other was observed at a higher temperature. For Ni/SAPO-11, the lower temperature reduction peak was due to the reduction of bulk nickel oxide species with less interaction with SAPO-11, and the higher one was attributed to the dispersed nickel. In addition, the reduction peak at temperatures higher than 900 °C may correspond to the reduction of nickel aluminate (NiAl₂O₄).¹³ For MoO₃/SAPO-11, the maximum hydrogen consumption was

observed at 652 °C, which was assigned to the reduction of Mo^{6+} in octahedral coordination to Mo^{5+} and Mo^{4+} . Another reduction peak at temperatures higher than 900 °C corresponded to the further reduction of Mo^{4+} , forming lower molybdenum oxidation state such as Mo^{2+} or zerovalent molybdenum species. For NiMo/SAPO-11, the TPR profile exhibited two reduction peaks in region I, *i.e.*, one at 612 °C and another shoulder peak at 551 °C. The latter peak was attributed to the reduction of MoO_3 , and the former peak was due to the reduction of nickel oxide and a portion of the molybdenum oxide. Interestingly, the reduction peak of NiMo/SAPO-11 in region I shifted to a lower temperature side compared to that of Mo/SAPO-11. This result can be explained by the hydrogen spillover from nickel to molybdenum, which promoted the reduction rate of molybdenum oxide.¹⁴

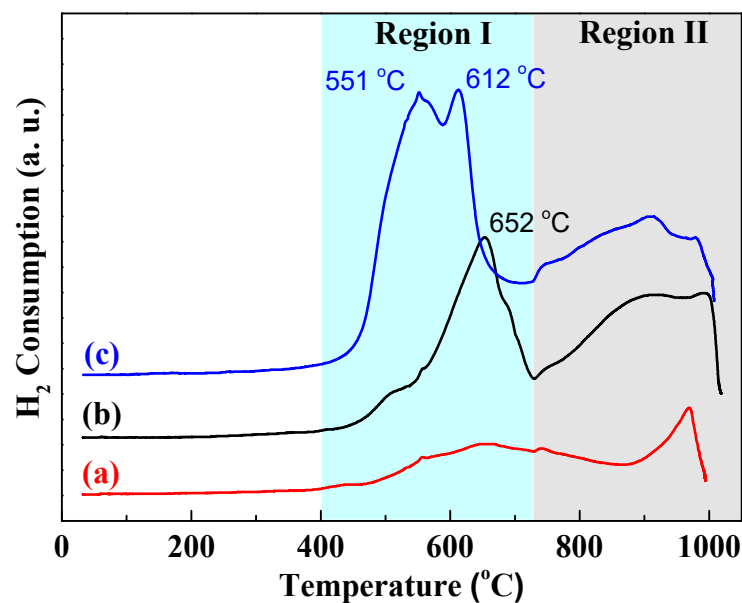


Figure 2.1 H_2 -TPR profiles of (a) Ni/SAPO-11, (b) Mo/SAPO-11 and (c) NiMo/SAPO-11.

Table 2.2 Hydrogen consumption during H₂-TPR.

Reduction temperature	H ₂ consumption (mmol/g)		
	NiMo/SAPO-11	Mo/SAPO-11	Ni/SAPO-11
Hydrogen consumption calculated from H ₂ -TPR.			
Region I	0.15	0.10	0.05
Region II	0.11	0.09	0.03
Region I + II	0.26	0.19	0.08
Hydrogen consumption estimated at different reduction temperatures.			
400 °C	0.05	0.02	0.01
450 °C	0.15	0.03	0.02
500 °C	0.17	0.06	0.03
550 °C	0.18	0.10	0.04
600 °C	0.18	0.10	0.04

The amount of hydrogen consumption are listed in **Table 2.2**. For region I, the aggregate hydrogen consumption of Ni/SAPO-11 and MoO₃/SAPO-11 was consistent with that of NiMo/SAPO-11, indicating that nearly all of the NiO species in NiMo/SAPO-11 were reduced to nickel metal in this region. For region II, the hydrogen consumption of Mo/SAPO-11 was similar to that of NiMo/SAPO-11, suggesting that the reduction degree was not improved by nickel addition.

To further investigate the reduction degree of the catalyst, hydrogen reduction profiles were recorded at a constant temperature (**Figure 2.2**). It should be noted that in every case the final temperature had been reached prior to the appearance of the hydrogen consumption peak due to the high heating rate (20 °C/min). The reduction degree derived from different temperatures is listed in **Table 2.2**. For NiMo/SAPO-11, a nearly threefold increase was observed when the reduction temperature increased from 400 to 450 °C. However, only a slight increase was observed above 450 °C. In contrast, the reduction degree of Ni/SAPO-11 and Mo/SAPO-11 exhibited tendency to continuous increase with an increasing reduction temperature.

The acidity of supports and catalysts determined by NH₃-TPD is showed in **Figure 2.3**. Al₂O₃ sample emerged three distinct NH₃ desorption peaks at around 230, 360 and 470 °C. Compared to Al₂O₃, SAPO-11 and SiO₂-Al₂O₃ showed only two distinct peak at around 260 and 350 °C. For AlSBA-15, the profile was broad and

showed the biggest area among the four supports. On an areal basis, the amount of total acid sites followed the order: AISBA-15 > SAPO-11 > SiO₂-Al₂O₃ > Al₂O₃.

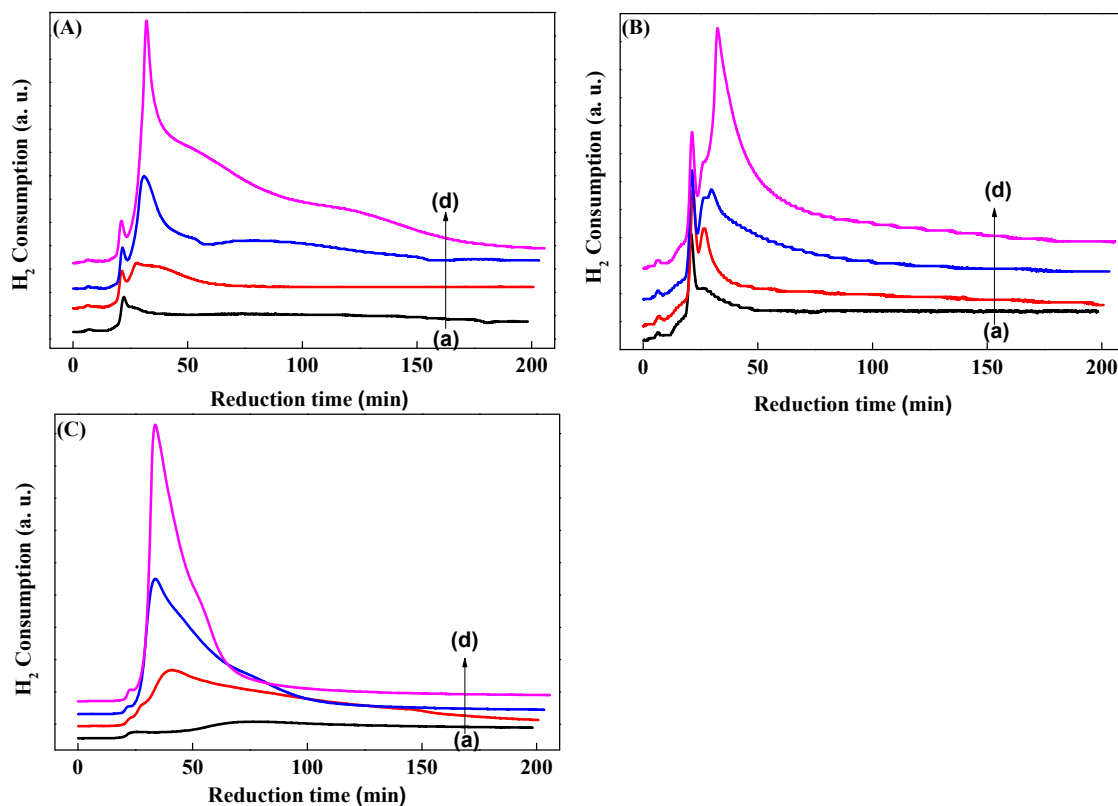


Figure 2.2. H₂ reduction profiles of (A) Mo/SAPO-11, (B) Ni/SAPO-11 and (C) NiMo/SAPO-11. The reduction temperature was constant at (a) 400 °C, (b) 450 °C and (c) 500 °C and (d) 550 °C.

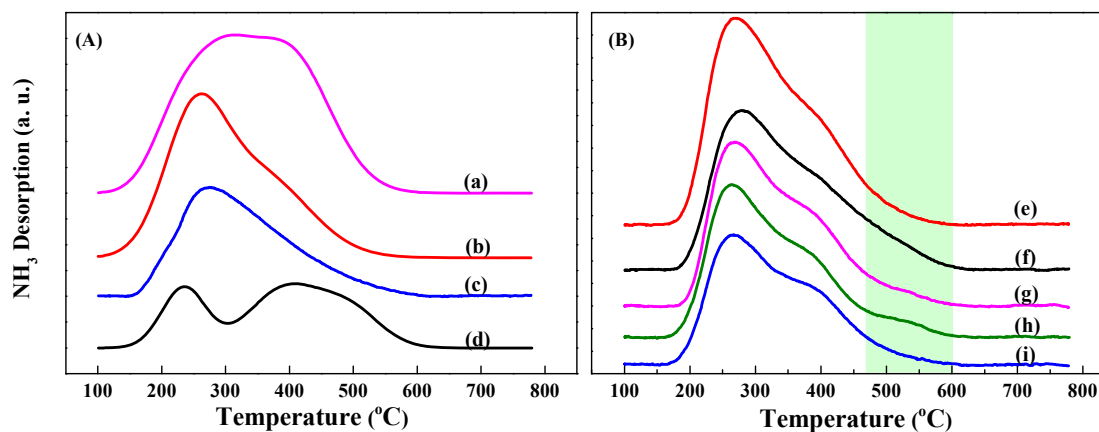


Figure 2.3 NH₃-TPD profiles of (A) supports and (B) catalysts: (a) AISBA-15, (b) SAPO-11, (c) SiO₂-Al₂O₃, (d) Al₂O₃, (e) oxidized NiMo/SAPO-11, (f) 400R-NiMo, (g) 450R-NiMo, (h) 500R-NiMo and (i) 550R-NiMo.

Table 2.3 Acidity of the support and catalysts determined by NH₃-TPD.

Sample	Weak		Medium		Strong		Total acidity (μmol/g)
	<i>T</i> /°C	Acidity (μmol/g)	<i>T</i> /°C	Acidity (μmol/g)	<i>T</i> /°C	Acidity (μmol/g)	
SAPO-11	265	160	370	269	-	-	426
Oxidized	266	207	361	324	-	-	531
400R-NiMo	261	123	322	151	416	194	468
450R-NiMo	262	144	341	194	436	101	440
500R-NiMo	258	148	345	204	472	47	399
550R-NiMo	262	121	361	232	-	-	353

For the reduced NiMo/SAPO-11 catalyst, all of the profiles exhibited two similar desorption peaks centered at approximately 260 °C and 350 °C, which respectively correspond to weak and medium acid sites primarily originate from SAPO-11. In addition, another peak emerged at ca. 550 °C was observed in the catalyst reduced at 400, 450 or 500 °C. However, this peak was not observed for the support, oxidized catalyst or catalyst reduced at 550 °C. This result indicates that new acid sites were generated after reduction at 400 – 500 °C. To compare the number of acid sites, the NH₃ desorption peak was divided into two or three regions, and the acidity of each individual region is listed in **Table 2.3**. The number of total acid sites substantially increased after impregnating the NiMo metals. However, it decreased gradually as the reduction temperature increased. The number of new acid sites observed at the desorption temperatures higher than 400 °C also decreased as the reduction temperature increased. Suarez and co-workers studied the acid properties of Mo/Al₂O₃ reduced to different extents by infrared spectroscopy of adsorbed pyridine.¹⁵ Two interesting conclusions provide evidence to explain the variation in our NH₃-TPD results. First, the IR spectroscopy showed the presence of Brønsted acid sites on the oxidized catalyst but not on the alumina. Second, the Brønsted acid sites increased at low extents of reduction and decreased to zero with further reduction. In contrast, the Lewis acidity passed through a maximum as a function of the reduction degree but was not eliminated with reduction. In this study, the increase in the number of acid sites after impregnation may be related to both of the Brønsted and Lewis acid sites that were generated by molybdenum oxide, and the decrease in

these sites was due to the gradual elimination of Brønsted acid sites. The new acid sites generated after reduction may correspond to hydroxide groups bond to Mo⁵⁺ species.

XPS study was conducted to determine the oxidation states of the metal after different reduction processes. **Figure 2.4** shows the Mo 3d curve-fitted spectra for the reduced NiMo/SAPO-11 catalysts. Three sets of Mo 3d doublets were observed: Mo⁶⁺, Mo⁵⁺ and Mo⁴⁺. Yamada studied the distribution of molybdenum oxidation states in reduced Mo/ γ -Al₂O₃ and found that Mo³⁺ was obtained after 500 °C reduction.¹⁶ However, other results indicate that no valence lower than +4 was obtained at the same reduction temperature.^{17, 18} Based on these results, the reduction degree of molybdenum is strongly dependent on the preparation method and acidity of the support. Therefore, the interaction between the metal and support would change the reduction difficulty. In this sense, Brønsted acid sites in SAPO-11 caused more difficulties for the reduction of supported molybdenum oxide. The binding energies (BE) and relative abundance of each Mo oxidation state are listed in **Table 2.4**. The BE value for the Mo⁶⁺ was obtained from the XPS spectra of oxide catalyst (Mo 3d_{5/2}, 232.9 eV; Mo 3d_{3/2}, 236.0 eV). A good agreement with the BE values is observed in other literatures.^{16, 17, 18, 19, 20} The XPS parameters for Mo⁵⁺ and Mo⁴⁺ were a result of the curve fitting procedure. For the 500R-NiMo and 550R-NiMo catalysts, the BE of Mo⁵⁺ and Mo⁴⁺ shifted to lower values compared to 400R-NiMo and 450R-NiMo, suggesting that a higher reduction degree was obtained and more coordinately unsaturated sites (CUS) were generated. The relative concentration of each Mo oxidation state was calculated by dividing the Mo 3d area for a given oxidation state by the total area of the Mo 3d envelope. The concentration of Mo⁵⁺ or Mo⁴⁺ species exhibited a significant change in the different catalysts. The percentage of Mo⁴⁺ exhibited a steady increase from 27.6% to 51.4% with increasing reduction temperature, whereas that of Mo⁵⁺ dropped from an initial high value of 43.5 % to 20.0 %. These result indicates that a higher temperature favors the formation of a lower valence of Mo⁴⁺ rather than Mo⁵⁺. Many studies investigated the reduction kinetics of supported MoO₃, and the results indicated that different valences of

molybdenum oxides showed quite different distributions in the initial state of reduction, but they could remain the same after a certain time period (approximately 3-5 h).^{21, 22} In this study, a sufficient time of 3 h was maintained for each reduction process. Therefore, the final oxidation state was reached in each case, and the reduction degree only depends on the reduction temperature. On the other hand, the Mo⁶⁺ showed a constant concentration in the different catalysts. These Mo⁶⁺ species strongly interacted with the support and required a higher energy for reduction.

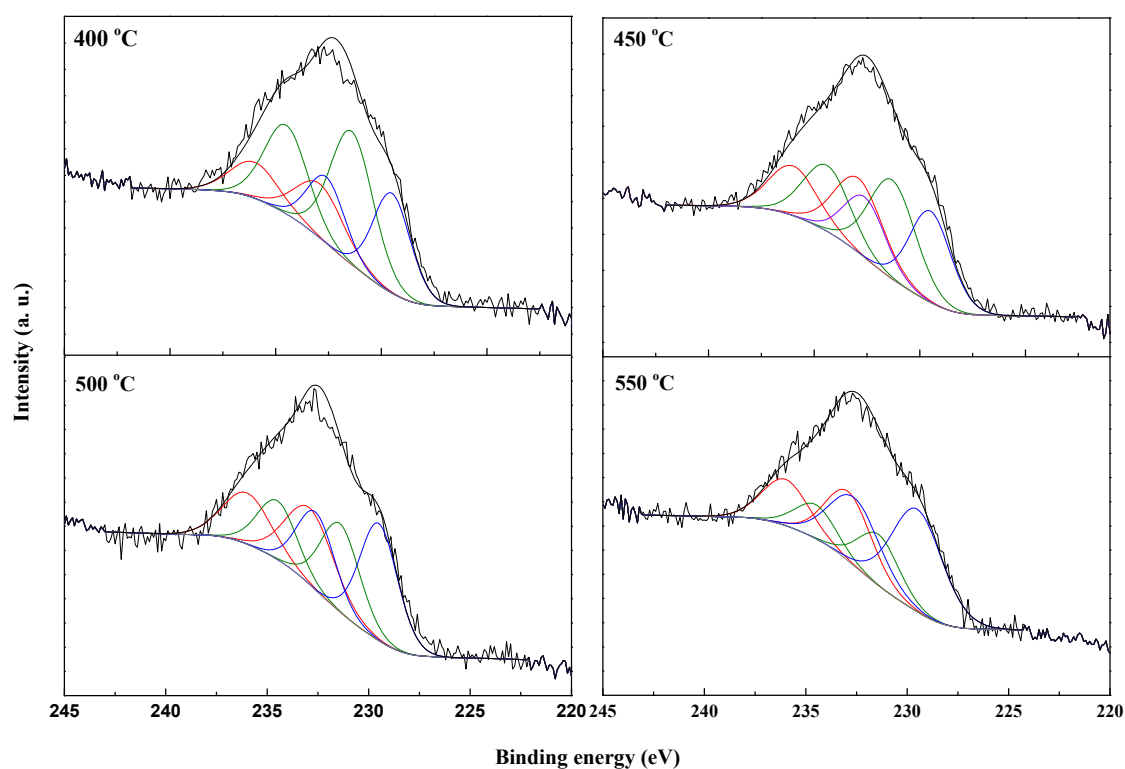


Figure 2.4 XPS spectra of the Mo 3d region for NiMo/SAPO-11 reduced at different temperatures.

Table 2.4 Binding energy and distribution of molybdenum species with different valences of the reduced catalysts.

Sample	Binding energy ^a (eV)			Concentration ^b (%)		
	Mo ⁶⁺	Mo ⁵⁺	Mo ⁴⁺	Mo ⁶⁺	Mo ⁵⁺	Mo ⁴⁺
400R-NiMo	232.9	231.4	229.5	28.9	43.5	27.6
450R-NiMo	232.9	231.3	229.5	28.1	34.4	37.5
500R-NiMo	232.9	231.1	229.1	28.6	30.1	41.3
550R-NiMo	232.9	231.1	229.1	28.6	20.0	51.4

^a The value of binding energy referred to Mo 3d_{5/2}. The difference between the binding energy value of 3d_{5/2} and 3d_{3/2} was kept constant (3.1 eV) for all oxidation states.^b Concentration of different valences of molybdenum species was obtained from the areal percentage.

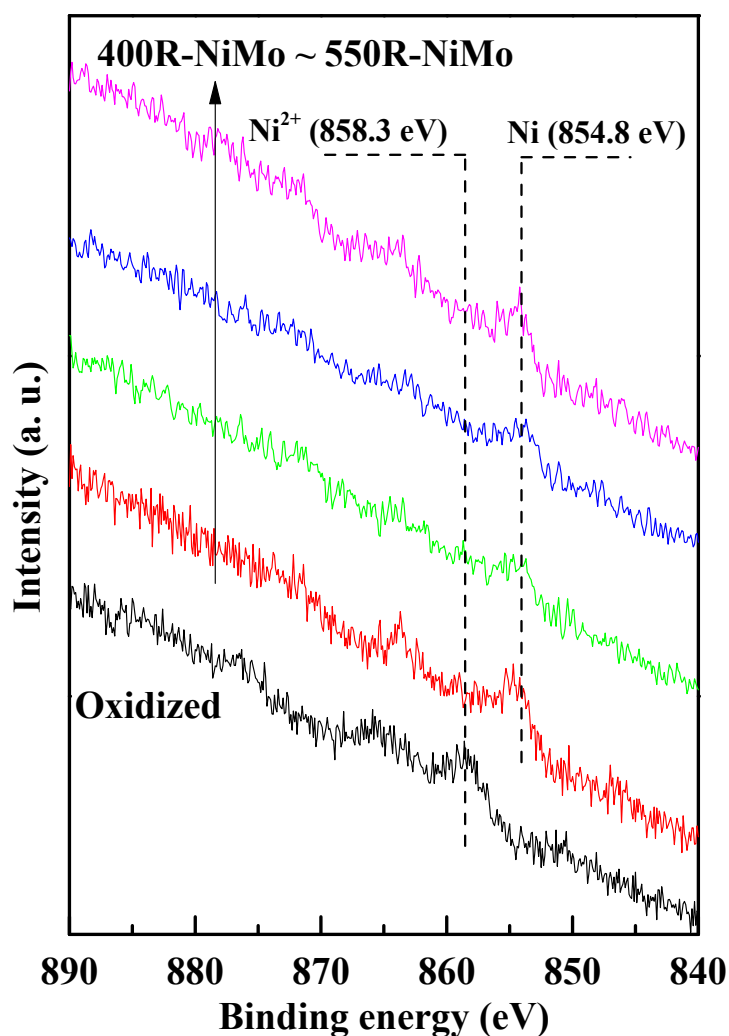


Figure 2.5 Ni 2p envelopes for the oxidized and reduced NiMo/SAPO-11 catalysts.

The XPS spectra for Ni 2p are shown in **Figure 2.5**. For oxidized NiMo/SAPO-11, the peak at 858.3 eV was due to NiO. After reduction, the value of the binding energy shifted to lower side (854.8 eV), and only zerovalent nickel was observed in each case, indicating that the nickel oxide on the surface of NiMo/SAPO-11 was completely reduced even when the temperature was relatively low (400 °C), which correlates well with the H₂-TPR results.

TEM images of the reduced NiMo/SAPO-11 catalysts are displayed in **Figure 2.6**. The average size of 400R-NiMo was approximately 9 nm. The increase in the reduction temperature only resulted in a slight migration of the metal particles, and the average particle size of the 550R-NiMo was estimated to be approximately 10 nm. Based on these results, it can be concluded that the reduction temperature cannot significantly influence the particle size of metal.

NO is frequently used for quantifying the active site in hydrotreating catalysts. It is widely accepted that NO was adsorbed on the anion vacancy as dinitrosyl species.^{23, 24, 25, 26} The NO uptake for the reduced catalysts is listed in **Table 2.7**. The adsorption amount of NO for the reduced NiMo/SAPO-11 catalyst gradually increased with increasing reduction temperature. Based on the TEM result, the average particle size for these catalysts was similar, indicating that the metal dispersion cannot be changed considerably by the reduction at different temperatures. Therefore, the reason for the variation in NO adsorption amount may be the increase in the CUS sites. In addition, the monometallic Mo/SAPO-11 catalyst possessed lower NO adsorption capacity, while the Ni/SAPO-11 catalyst exhibited much higher NO adsorption amount than the other catalysts.

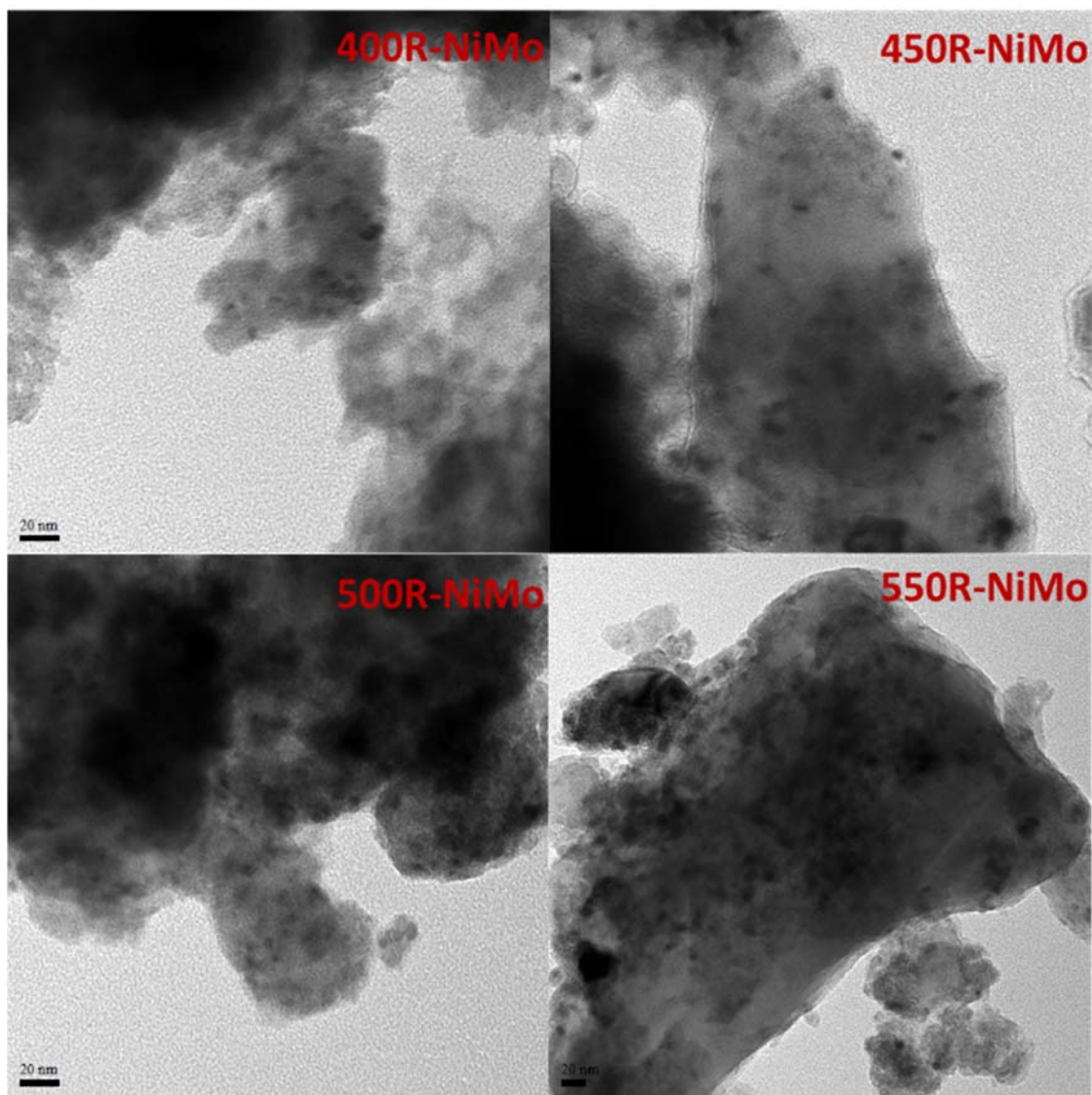


Figure 2.6 TEM images of the NiMo/SAPO-11 catalyst reduced at different temperatures.

2.3.2 Hydrotreating of Jatropha Oil over Reduced NiMo Catalysts

The stability of reduced NiMo catalyst was evaluated by a long-term reaction. Sulfided hydrotreating catalysts had low stability due to gradual sulfur leaching during the reaction. A recent study showed that a sulfided catalyst started deactivation at the time on stream of 120 h, and a partial transformation of the metal phase from sulfides to oxides was considered as the main reason.² To evaluate the stability of the reduced NiMo catalyst, a long-term experiment of hydrotreating of Jatropha oil was conducted over NiMo/Al₂O₃. The conversion of Jatropha oil and the selectivity of C₅-

C₁₈ hydrocarbons and C₁₈₊ fraction were shown in **Figure 2.7**. During the reaction, the conversion of 100 % kept constant, and the selectivity exhibited no considerable change as well.

For a sulfided catalyst, the metal sulfide phase could be partially reduced by hydrogen and formed a vacancy. The heteroatom in a substrate would adsorb on the vacancy and be activated by dissociated hydrogen. In the case of deoxygenation, the vacancy would be filled with oxygen atoms. It is well known that the sulfide molybdenum has a hexagonal crystal structure, which would make the recovery of the oxidized vacancy by hydrogen reduction become difficult. For a reduced catalyst, the reduction of oxidized metal phases could be much easier due to its distinct crystal structure. In addition, the hydrotreating reaction over the reduced catalyst was conducted at 375 °C, which is much higher than that for the sulfided catalyst (300 °C), because under this temperature deoxygenation could not efficiently occur. Another reason for the high stability of the reduced catalysts would be the reaction conduction, which would be more favorable to reduce the oxidized vacancy.

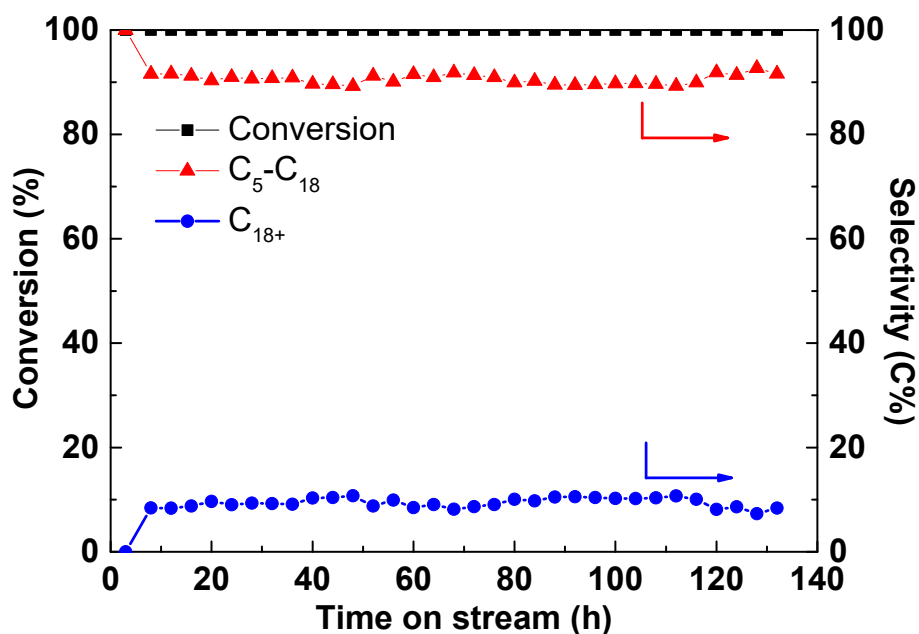


Figure 2.7 Conversion of Jatropa oil and selectivity of different fractions as a function of time on stream over reduced NiMo/Al₂O₃ catalyst. Reaction conditions: $T = 375$ °C, $P = 3$ MPa, $LHSV = 1$ h⁻¹ and $H_2/oil = 1000$.

The conversion of triglyceride, product yield and selectivity in hydrotreating of Jatropha oil are summarized in **Table 2.5**. For all studied catalysts, the conversion of Jatropha oil reached 98.2-100%, indicating that the reduced NiMo catalyst also has high deoxygenation activity. The liquid product is limpid and slightly green after hydrotreating at the reaction temperature higher than 375 °C. However, little yellow liquid with relatively higher viscosity was observed at a lower reaction temperature such as 350 °C, indicating that some oxygenates or unreacted triglycerides remained. In contrast, the liquid product obtained from hydrotreating over the sulfided NiMo catalyst looks clear even at 300 °C. These results suggest that the reduced catalyst showed lower deoxygenation activity than the sulfided catalyst at a lower reaction temperature. On the other hand, high yield (78.1–83.8 wt%) of liquid hydrocarbon products was achieved for all catalysts. The yield of liquid hydrocarbon products decreased in the following order: NiMo/Al₂O₃ > NiMo/SiO₂-Al₂O₃ > NiMo/SAPO-11 > NiMo/Al-SBA-15. This could be due to the fact that the use of a catalyst with higher acidity would increase the cracking selectivity, and therefore, a larger amount of C₁₋₄ and C₅₋₁₀ products were generated, thereby reducing the C₁₁₋₁₈ selectivity.

Table 2.5 Hydrotreating of Jatropha oil over various catalysts.

Catalyst	A	B	C	D	E
Conversion	100	100	98.2	100	100
Yields based on feedstock, mass %					
Liquid	83.8	82.1	81.2	78.1	83.7
Gas					
C ₁₋₄	6.5	8.1	9.4	11.7	4.3
CO	0.3	0.1	-	-	0.2
CO ₂	0.5	0.5	0.9	0.7	1.1
Water	9.1	8.3	7.0	6.6	8.8
Selectivity of liquid hydrocarbon fraction, C%					
C ₅₋₁₀	6.1	15.7	25.1	37.3	6.6
C ₁₁₋₁₈	85.7	74.6	58.1	59.6	85.0
C ₁₈₊	8.3	9.7	16.9	3.2	8.4
<i>iso-/n</i> -alkanes	0.1	0.9	3.3	4.2	0.1
C ₁₅₊₁₇ /C ₁₆₊₁₈	0.3	0.8	1.0	1.0	0.8

A. NiMo/Al₂O₃, B. NiMo/SiO₂-Al₂O₃, C. NiMo/SAPO-11, D. NiMo/AlSBA-15, E. sulfided NiMo/Al₂O₃. Reaction conditions: $T = 375$ °C, $P = 3$ MPa, $LHSV = 1$ h⁻¹, H₂/Oil = 1000 (ml/ml).

Figure 2.8 shows the change of *iso*-C₁₅₋₁₈ selectivity over three reduced catalysts as a function of reaction temperature. The selectivity decreased in the order of NiMo/SAPO-11 > NiMo/AlSBA-15 and NiMo/SiO₂-Al₂O₃. This result is consistent with the acidity of the support (**Figure 2.3**). NiMo/SAPO-11 and NiMo/Al-SBA-15 showed much higher isomerization activity than NiMo/SiO₂-Al₂O₃ due to their higher Brønsted acidity, which has been considered to be the active site in alkane isomerization.²⁷ Although NiMo/AlSBA-15 had much higher acidity than NiMo/SAPO-11, the isomerization activity was lower. It is well known that in alkane isomerization, the metallic and acid function should be well balanced.²⁸ If the acid function is stronger than the metallic function, the intermediate carbenium ion, which generated from dehydrogenation of normal alkane, would undergo cracking through β -scission and transfer into lighter hydrocarbons (C₁-C₁₅) rather than undergo isomerization. Based on the above result and discussion, SAPO-11 can be considered as the best support among the studied supports.

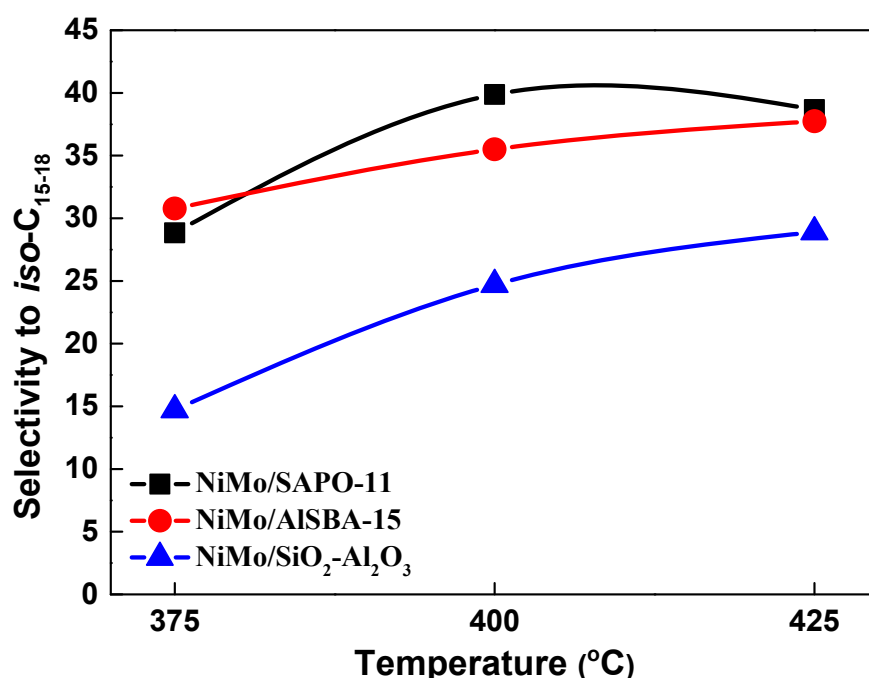


Figure 2.8 Selectivity of *iso*-C₁₅₋₁₈ over various catalysts. Reaction conditions: $T = 375$ °C, $P = 3$ MPa, $LHSV = 1$ h⁻¹ and $H_2/oil = 1000$.

2.3.3 Effect of Reduction Temperature on NiMo/SAPO-11 in Hydrotreating of Methyl Laurate

In last section, the possibility of using a reduced NiMo catalyst for hydrotreating of a vegetable oil was demonstrated. Higher isomerization activity and better stability of reduced catalysts were observed compared to the sulfided catalyst. However, the reduced catalyst showed much lower deoxygenation activity at lower reaction temperatures. In general, sulfidation is preferred at a lower temperature, while reduction is preferred at higher temperature. Therefore, the lower deoxygenation activity of the reduced catalyst could be due to the insufficient reduction, which would result in the decrease of active sites. In this section, the focus is switched to the effect of reduction temperature on the catalyst performance. The NiMo/SAPO-11 catalyst showed the highest isomerization activity and relatively lower cracking activity in hydrotreating of Jatropha oil. Therefore, SAPO-11 is considered as a suitable acid support for the simultaneous deoxygenation-isomerization reaction.

Methyl laurate, which is structurally similar to the triglyceride in vegetable oils, was used as a model compound to test the catalyst performance. A typical chromatogram of the liquid products (diluted with carbon tetrachloride) displaying peaks of solvent, unreacted reactant and products of HDO of ML is shown in **Figure 2.9**. The HDO of ML resulted in the formation of two types of liquid products, *i.e.*, oxygenates and hydrocarbons. The main hydrocarbons were dodecane and undecane. In addition, hydrocarbons with a carbon number less than 10 were observed at a higher temperature (375 °C), and are considered to be the cracking products. Some oxygenates, *i.e.*, dodecanol, dodecanal, laurate acid and lauryl laurate, were observed as intermediate products at low temperatures, and these compounds were further transformed into hydrocarbons with the increasing reaction temperature. Moreover, a small amount of methanol was also detected, and the amount of methanol decreased as the reaction temperature increased. In each case, water formation was observed in addition to the other liquid organic products. These results were consistent with other literatures that used triglyceride, fatty acid or fatty acid methyl ester as the feedstock.^{8, 29, 30, 31} CH₄ and CO were observed as the main gaseous products. In addition, a small

amount of CO₂ was observed at the reaction temperature higher than 325 °C. Interestingly, a small amount of dimethyl ether was detected and the amount was decreased as the temperature increased, indicating that dimethyl ether was formed by the reaction of the intermolecular dehydration of two methanol molecules, which was favored at lower temperatures.

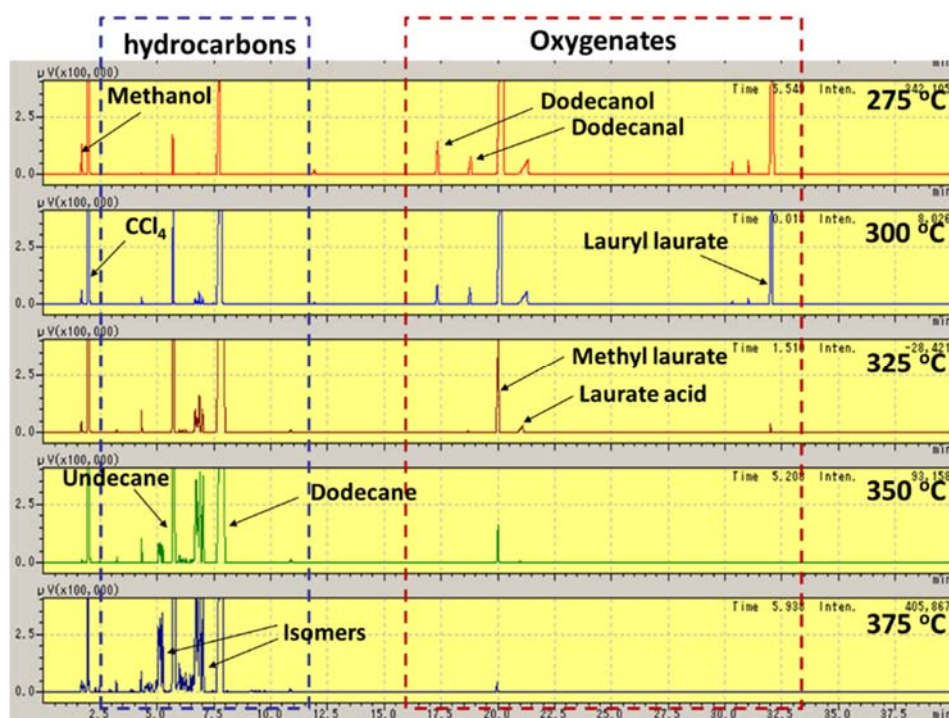
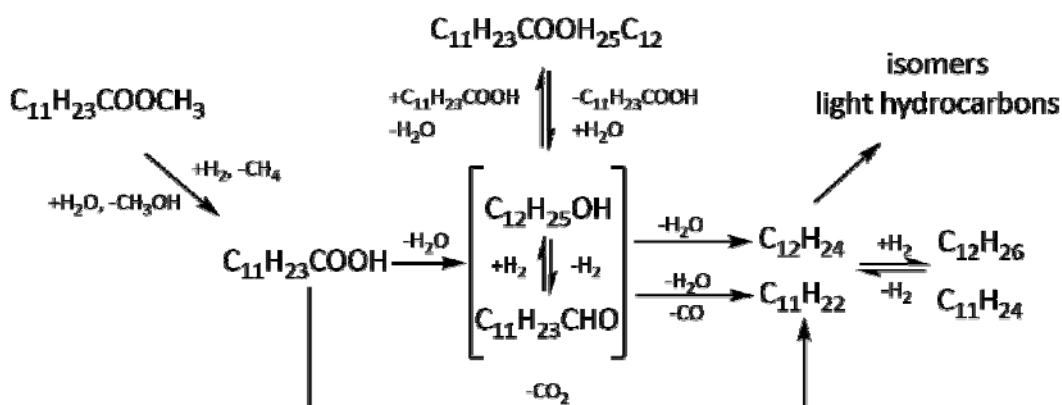


Figure 2.9 Typical chromatogram of liquid products from hydrotreating of methyl laurate over 550R-NiMo. Reaction conditions: WHSV = 5 h⁻¹, P = 3 MPa and H₂/Feed = 800 (ml/ml).

The hydrotreating of ML is a complex process involving several reactions, *i.e.*, hydrogenation/hydrolysis of ester, deoxygenation of intermediate oxygenates and isomerization/cracking/hydrogenation of the resulting hydrocarbons. Possible reaction network is presented in **Scheme 2.1**. First, methyl laurate is transformed into laurate acid *via* hydrogenation or hydrolysis, yielding methane or methanol, respectively. Secondly, the deoxygenation of laurate acid proceeds *via* two pathways: hydrodeoxygenation (HDO), which results in the formation of hydrocarbons with the same carbon number as the fatty acid (C₁₂ hydrocarbons), and hydrodecarbonylation/

decarboxylation (DCO), which results in hydrocarbons with one carbon atom less than the fatty acid (C_{11} hydrocarbons). There is a large amount of lauryl laurate was formed at lower reaction temperatures. The formation of lauryl laurate can be due to the esterification of laurate acid and dodecanol. Due to the easy transformation between dodecanol and dodecanal as well as esterification, laurate acid, dodecanol and dodecanal were considered to be the key intermediates in the deoxygenation step. Finally, the deoxygenated hydrocarbons, *i.e.*, dodecene and undecene, were further transformed into isomers and light hydrocarbons (C_5 - C_{11}) *via* isomerization and cracking, or hydrogenated to saturated alkanes.



Scheme 2.1 Possible reaction network for hydrotreating of methyl laurate.

Hydrotreating of ML over the NiMo/SAPO-11 catalyst reduced at different temperatures were conducted under the following reaction conditions: $T = 275$ – 375 °C, $WHSV = 5$ h^{-1} , $P = 3$ MPa, and $H_2/Feed = 800$ ml/ml to investigate the effects of reduction temperature. **Figure 2.10** shows the effect of the reduction temperature on the catalyst activity. The catalyst reduced at 400 °C exhibited the lowest activity, and the ML conversion over this catalyst was much lower than that over the sulfided catalyst (**Table 2.6**) at reaction temperatures of 275 – 350 °C. When the reduction temperature increased to 450 °C, the activity increased dramatically and was higher than that of the sulfided one. However, above 450 °C, only a slight increase in the conversion was observed. In addition, the conversion was close to 100% at a higher reaction temperature (375 °C).

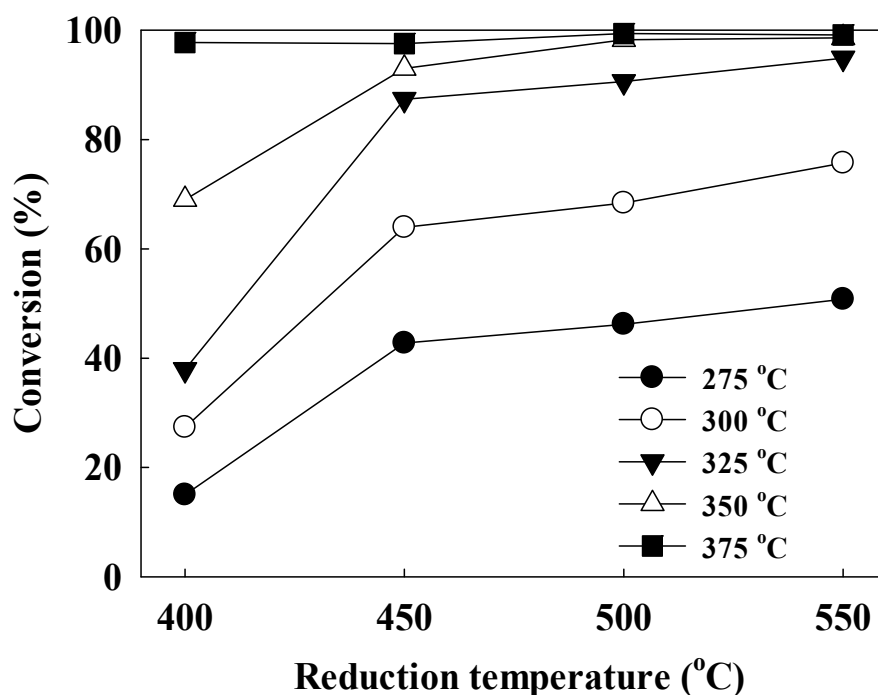


Figure 2.10 Effect of reduction temperature on the conversion of methyl laurate over NiMo/SAPO-11 catalyst reduced at different temperatures.

Table 2.6 Hydrotreating of methyl laurate over S-NiMo.

	Reaction temperature (°C)				
	275	300	325	350	375
Conversion (%)	32.3	55.2	82.7	99.8	100
Selectivity to various products (C %)					
CO/CO ₂	0.5	1.4	4.7	6.4	7.8
CH ₄	1.7	2.8	5.2	7.5	7.7
C ₂₋₁₀	0.4	0.5	0.7	2.6	8.7
Methanol/ Dimethyl ether	0.9	0.4	0.1	0.0	0.0
iso-C ₁₁	0.0	0.3	1.9	2.5	3.3
C ₁₁₌	3.3	7.6	15.3	0.0	0.0
n-C ₁₁	9.3	22.6	24.1	43.4	41.2
iso-C ₁₂	0.1	0.6	2.4	12.9	13.9
C ₁₂₌	2.1	5.0	10.1	0.0	0.0
n-C ₁₂	5.0	14.7	19.0	22.0	14.9
C ₁₂₊	1.9	3.3	1.8	2.7	2.5
dodecanol/ dodecanal	6.4	2.1	0.9	0.0	0.0
Laurate acid	27.4	17.6	10.8	0.0	0.0
Lauryl laurate	41.0	21.2	3.0	0.0	0.0

Reaction conditions: $P = 3$ MPa, $WHSV = 5$ h⁻¹, $H_2/Oil = 800$ (ml/ml).

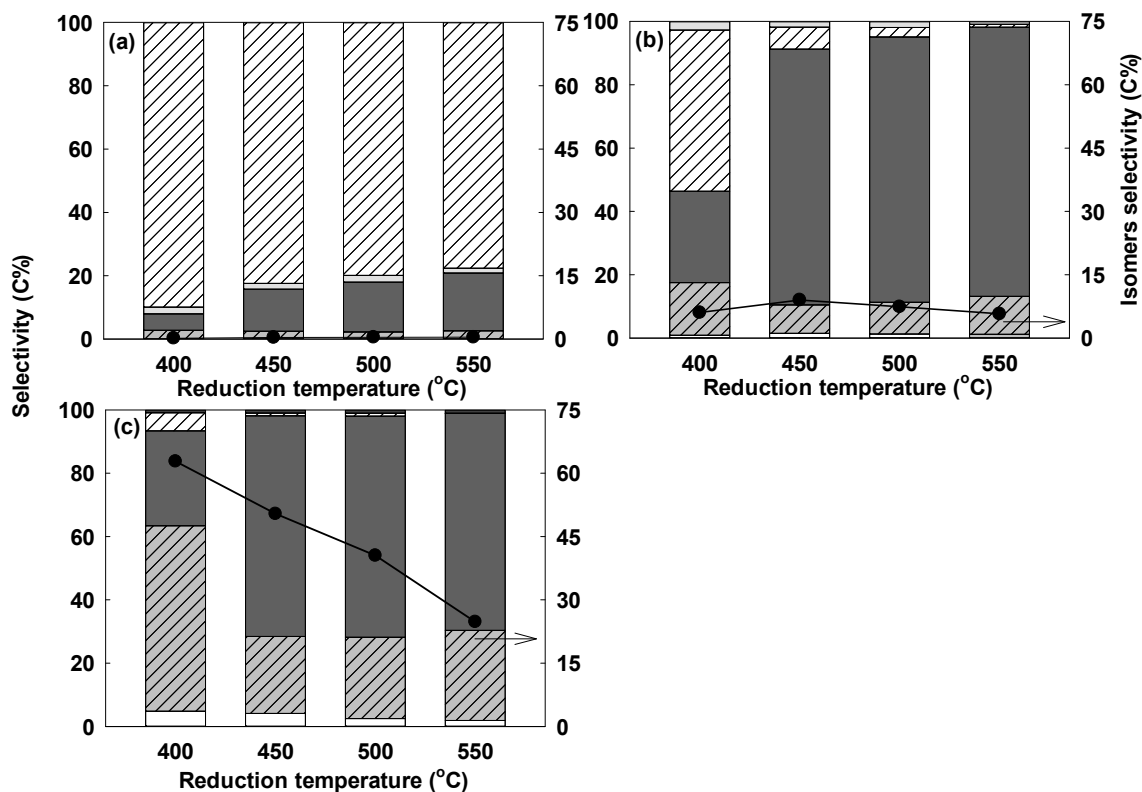


Figure 2.11 Effect of reduction temperature on the liquid product distribution (□ C₅₋₁₀ hydrocarbons, ▨ C₁₁ hydrocarbons, ■ C₁₂ hydrocarbons, ▩ Oxygenates, ■ C₁₂₊) and isomers selectivity at (a) 275 °C, (b) 325 °C and (c) 375 °C. The black circle represents the isomer selectivity and can be read on the right axis. Reaction conditions: $WHSV = 5 \text{ h}^{-1}$, $P = 3 \text{ MPa}$ and $\text{H}_2/\text{oil} = 800 \text{ (ml/ml)}$.

In **Figure 2.11**, the liquid product distribution and isomerization selectivity over reduced catalysts are compared. At a lower reaction temperature (275 °C), the main products over the four catalysts were oxygenates, especially lauryl laurate. Other oxygenates such as dodecanol, dodecanal and laurate acid were observed in trace amounts. At 325 °C, C₁₁ and C₁₂ hydrocarbons were observed as the main products over the catalyst reduced at higher temperatures (450-550 °C). However, oxygenates were also observed in large quantities over the catalysts reduced at 400 °C. This result is consistent with the ML conversion, in which catalyst reduced at 400 °C showed the lowest activity. At a higher reaction temperature (375 °C), oxygenates were barely observed in each case. For the C₁₁ and C₁₂ hydrocarbons, the formation of C₁₁ was favored at a higher reaction temperature. On the other hand, the isomers selectivity (*iso*-C₁₁ and *iso*-C₁₂) increased with increasing reaction temperature. Interestingly,

the isomers selectivity remained constant among the different catalysts at a reaction temperature of 325 °C, but this selectivity was altered at 375 °C. It is noted that in the HDO of ML, deoxygenation and isomerization were consecutive reactions because no isomerized oxygenates were observed in the products. Therefore, the deoxygenation degree has a large influence on the isomerization, that is, the deoxygenation is a prerequisite for subsequent isomerization. In this sense, the isomerization selectivity at 275 °C and 325 °C was influenced by the deoxygenation. The formation of the C₅-C₁₀ hydrocarbons as well as the gaseous cracking products (C₂-C₄, not shown) was lower than 5% in every case even though the reaction temperature increased to 375 °C.

To investigate the effect of the reduction temperature on the isomerization selectivity, the ratio of isomerized to normal paraffins is shown in **Figure 2.12**. The isomerization selectivity increased with increasing reaction temperature, but it decreased with increasing reduction temperature. At lower reaction temperatures, *i.e.*, 275 and 300 °C, only trace amounts of the isomers (< 2%) were generated, resulting in a ratio close to zero. When the reaction temperature was higher than 325 °C, 400R-NiMo exhibited a much higher activity for isomerization than that of other catalysts. These results are consistent with the acidity of the catalyst (**Figure 2.3** and **Table 2.3**). In isomerization, the skeleton isomerization and cracking are competitive reactions, and the ratio of them is strongly dependent on the acidity of support. SAPO-11 with moderate acidity was suitable as a support for long chain paraffin isomerization. In addition, the addition of another small amount of strong acid sites can promote the isomerization as well. Therefore, the new acid sites generated after reduction contribute to isomerization, and the decrease in these sites can inhibit the isomerization activity of the catalyst.

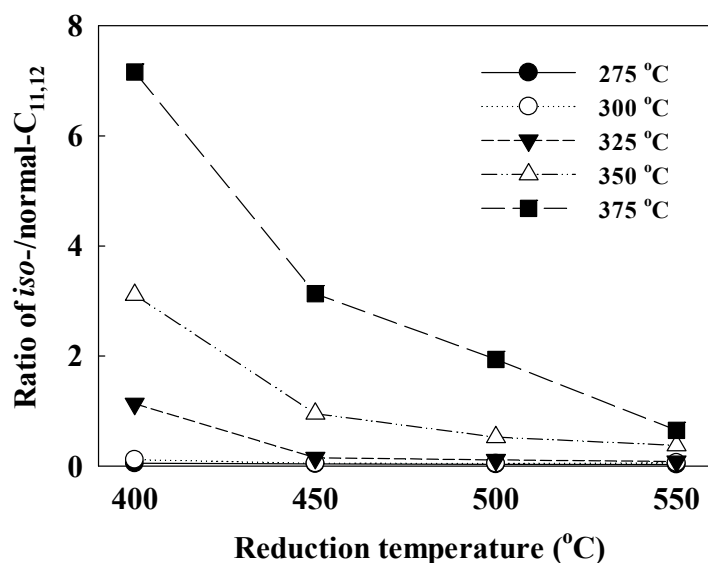


Figure 2.12 Effect of reduction temperature on the isomerization activity of reduced NiMo/SAPO-11 catalysts.

The change in the C_{11}/C_{12} ratio that illustrate the deoxygenation pathways (HDO or DCO) are presented in **Figure 2.13**. For the different reduction temperatures, the ratio decreased in the following order: 400R-NiMo \gg 450R-NiMo $>$ 500R-NiMo $>$ 550R-NiMo. For 500R-Ni and 400R-NiMo, the high C_{11}/C_{12} ratio suggests that DCO is the main pathway, and the oxygen atoms are nearly all removed in the form of CO or CO_2 . However, HDO was favorable over the catalyst reduced at a higher temperature (450-550 °C), with the formation of H_2O . On the other hand, the ratio over catalysts with different active metals decreased in the order of 500R-Ni $>$ 500R-NiMo $>$ 500R-Mo. For 550R-Mo, in particular, C_{11} hydrocarbons were not detected below a reaction temperature of 350 °C, indicating that this catalyst has a high HDO selectivity. Furthermore, the ratio increased with increasing reaction temperature, indicating that an elevated reaction temperature favors the DCO reaction. For 500R-Ni the ratio increased after the first decrease with the increasing reaction temperature. In fact, an extremely high DCO/HDO ratio (DCO selectivity $>$ 90%) was obtained over catalysts with nickel supported on typical metal oxides, *e.g.*, ZrO_2 , Al_2O_3 , SiO_2 or CeO_2 .⁸ However, HDO can be promoted by supported zeolite (H β , HZSM-5) catalysts and strong acidity. The reason for this result is not clear, but appears to be

due to the presence of acid sites in the zeolite, on which the C=O bond can be adsorbed, and thus inhibit decarbonylation. Therefore, the low acid strength in SAPO-11 does not provide sufficient energy for C=O bond adsorption.

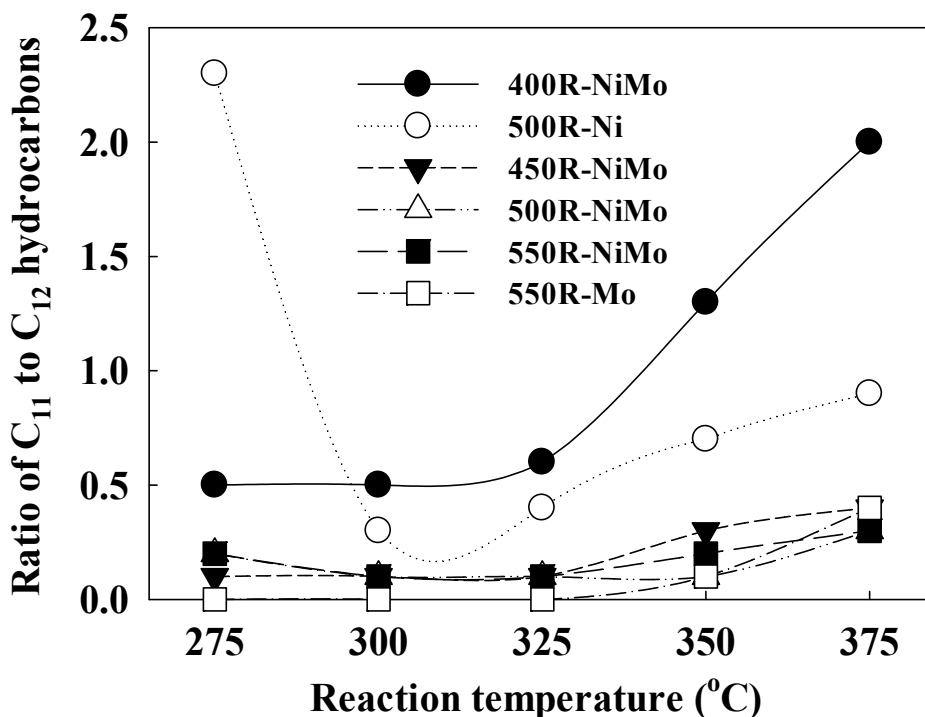


Figure 2.13 Evolutions in the ratio of C₁₁ to C₁₂ hydrocarbons as a function of reaction temperature.

2.3.4 Catalyst Structure-Performance Relationship

Based on the XPS and H₂-TPR analyses, nickel oxides were completely reduced to nickel metal in the NiMo/SAPO-11 catalyst under the studied reduction temperature (400-550 °C). In contrast, only a portion of the nickel oxide in the Ni/SAPO-11 catalyst was reduced. For Ni/SAPO-11, the difficulty in reduction may be attributed to the high dispersion of the nickel species caused by the strong interaction between nickel and the surface -OH groups of SAPO-11. For NiMo/SAPO-11, two possible effects may lead to a lower dispersion of nickel species. (i) A large amount of MoO₃ loading (20 wt%) caused the subsequent loading of nickel being on the top of MoO₃. Therefore, the interaction between nickel and MoO₃ was

much lower than that of SAPO-11, and caused nickel oxide to be more easily reduced; (ii) After MoO₃ loading, the surface area of SAPO-11 was dramatically reduced (from 167 to 94 m²/g). Therefore, the remaining surface area of SAPO-11 for nickel loading was much lower than that in pure SAPO-11. This would cause an agglomeration of nickel particles. The agglomerated nickel species are more easily reduced than the highly dispersed ones.

In sulfided molybdenum-based catalysts, the coordinatively unsaturated site located at the edges of molybdenum crystals, which exhibit Lewis acidity and can adsorb atoms with unpaired electrons, is considered to be the active site. Nickel or cobalt just play a promoter role and does not have high activity in these catalysts. However, the active site changes in the NiMo catalyst after a reduction pretreatment. It has been reported that nickel is an active metal for deoxygenation.^{8, 13, 32} In this study, 500R-Ni exhibited much higher activity than 550R-Mo. Therefore, in contrast to the sulfided NiMo catalyst, in which NiMoS is the active site, the metallic nickel is considered to be more active than the partially reduced molybdenum species in the reduced NiMo/SAPO-11 catalyst.

The oxidation state of molybdenum substantially changes in NiMo/SAPO-11 catalysts reduced at different temperatures. A lower reduction temperature, *i.e.*, 400 °C, favored the formation of Mo⁵⁺ species. When the reduction temperature increased, Mo⁵⁺ was continuously transformed to Mo⁴⁺. Massoth proposed a mechanism using two Mo⁶⁺ species to explain the reduction process.³³ After forming Mo⁵⁺, dehydroxylation leads to reduction of two isolated Mo⁵⁺ to an intermediate Mo⁵⁺ pair. Interestingly, further hydrogenation of this Mo⁵⁺ pair can lead to a Mo⁶⁺ and Mo⁴⁺ species, and a site containing a vacancy is generated. These results can help explain why the amount of Mo⁶⁺ did not change much with increasing reduction temperature.

Figure 2.14 displays the relationships between the concentration of Mo⁵⁺ and isomerization selectivity (375 °C) as well as the amount of acid sites. Both parameters shown on the Y axis varies linearly with the Mo⁵⁺ species. In general, isomerization occurs over bifunctional catalysts containing a metallic function for hydrogenation/dehydrogenation and an acid function for skeletal isomerization.

NiMo catalysts with different reduction degree have different amount of Mo^{5+} species. The Mo^{5+} species, which possess $-\text{OH}$ groups, exhibit Brønsted acidity and catalyze the isomerization reaction. Similarly, the Mo^{5+} species are active in other acid-catalyzed reactions such as metathesis and ethylene polymerization.^{17, 21, 34, 35}

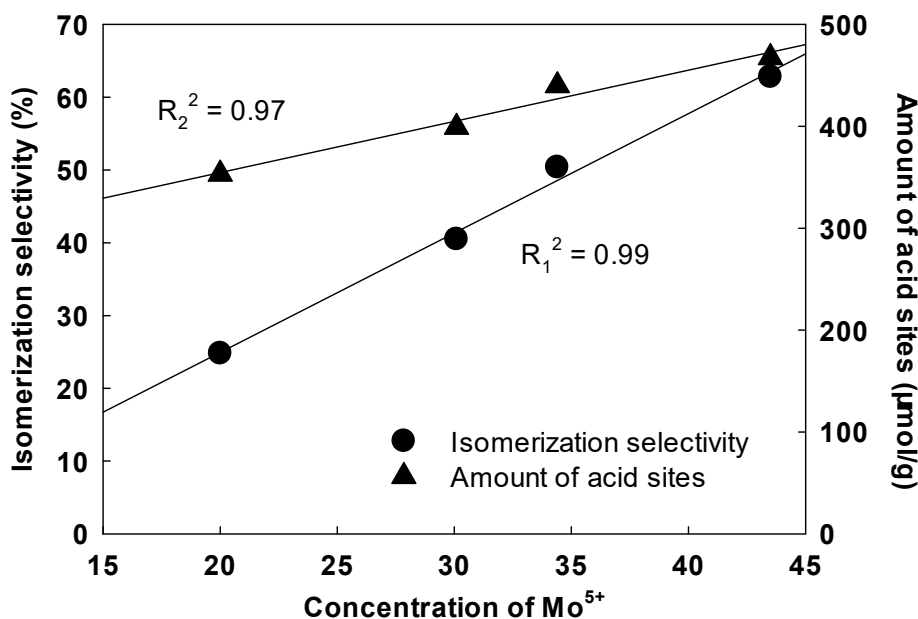


Figure 2.14 Correlation between Mo^{5+} species and isomerization selectivity as well as the amount of acid sites.

The main intermediate oxygenate, lauryl laurate, can only be generated by the esterification of laurate acid and dodecanol. Therefore, laurate acid is considered to be the key intermediate compound in ML deoxygenation. Laurate acid is used as the initial reactant for explaining the surface reaction mechanism. The result of the activity test indicates that C–C bond cleavage, which results in DCO, was the primarily deoxygenation pathway over 400R-NiMo, 500R-Ni and S-NiMo catalysts, whereas C=O bond hydrogenation, which leads to HDO, is promoted by 500R-Mo and 450(500/550)R-NiMo catalysts. The C=O hydrogenation and decarbonylation

are competitive reactions, which are severely affected by the nature of the catalyst surface. Deoxygenation mechanisms over reduced Ni/SAPO-11, Mo/SAPO-11 and NiMo/SAPO-11 (referring to the catalyst that reduced at a temperature higher than 450 °C) are presented in **Schemes 2.2-2.4**.

Table 2.7 Transformation of methyl laurate over various catalysts at 275 and 300 °C.

	500R-Ni		550R-Mo		400R-NiMo		450R-NiMo		500R-NiMo		550R-NiMo	
	275 ^f	300 ^f	275 ^f	300 ^f	275 ^f	300 ^f	275 ^f	300 ^f	275 ^f	300 ^f	275 ^f	300 ^f
Conv. ^a (%)	19.2	74.1	30.8	49.5	15.0	27.3	46.8	69.9	46.2	68.4	50.78	75.72
NO ad. ^b ($\mu\text{mol/g}$)	462		197		171		225		230		275	
TOF ^c ($10^{-3}/\text{g}$)	0.64	4.06	2.59	4.81	1.32	2.59	3.89	7.42	3.74	6.96	3.58	7.15
DCO ^d (mol %)	19.9	24.1	0.5	0.9	3.0	5.6	2.4	4.7	2.3	5.0	2.6	6.4
HDO ^d (mol %)	6.4	68.1	17.6	41.3	5.1	10.4	13.1	36.2	13.6	44.0	18.1	65.1
DCO /HDO ^e	3.11	0.35	0.03	0.02	0.59	0.54	0.18	0.13	0.17	0.11	0.14	0.10

^a Conversion of methyl laurate.

^b NO adsorption was measured by NO pulse chemisorption at 40 °C.

^c Turnover frequency, defined as reacted methyl laurate molecules per active site per second.

^d DCO and HDO represented the selectivity to C₁₁ and C₁₂ hydrocarbons, respectively.

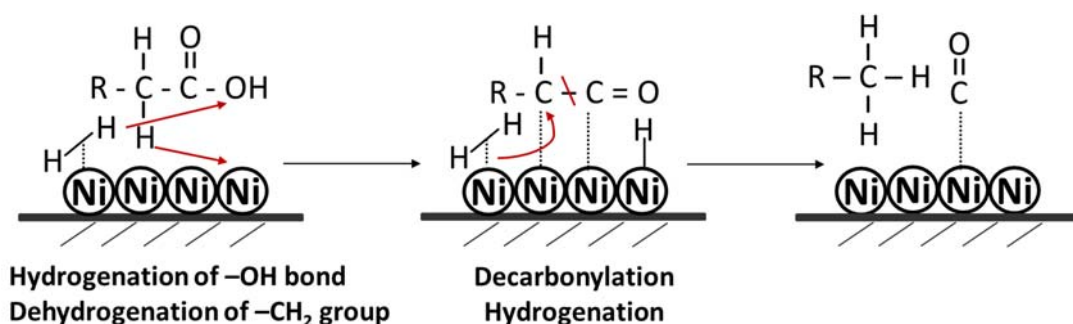
^e Molar ratio between DCO and HDO.

^f Reaction temperature (°C).

Reaction conditions: $WHSV = 5 \text{ h}^{-1}$, $P = 3 \text{ MPa}$, $H_2/\text{reactant} = 800$.

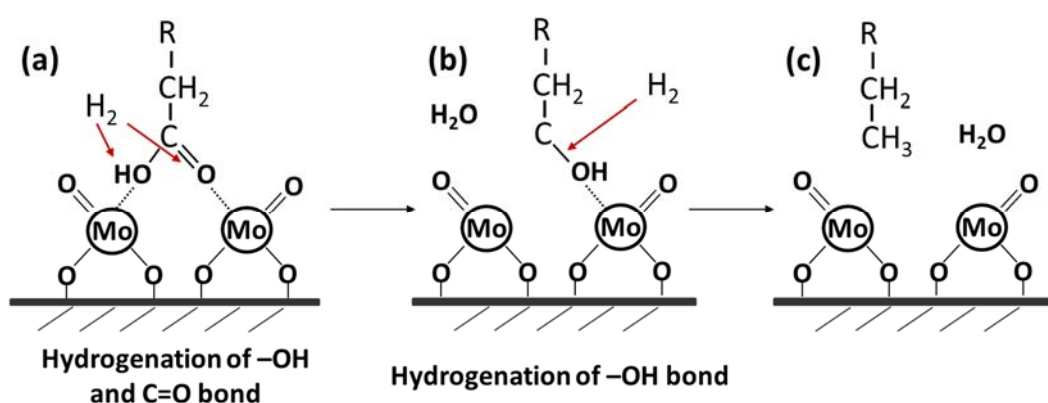
For Ni/SAPO-11, the decarbonylation is favorable on bare nickel sites (**Scheme 2.2**). (a) First, hydrogen is dissociated, yielding two hydrogen atoms adsorbed on the nickel surface. Hydrogenation results in the transformation of a carboxylic acid to an aldehyde. (b) Meanwhile, one hydrogen atom is dehydrogenated from the carboxylic acid to the surface of the nickel, forming an adsorbed C–C bond on two adjacent nickel atoms. (c) Subsequently, the cleavage of the C–C bond occurs, and a hydrocarbon with one carbon number less than the carboxylic acid is generated. In this study, although higher DCO selectivity was observed over the 500R-Ni catalyst,

the ratio of C_{11} to C_{12} was less than 1, indicating that more C_{12} hydrocarbons were generated compared to C_{11} . As mentioned above, the nickel supported on metal oxides, such as Al_2O_3 , can achieve an extremely high DCO selectivity. Indeed, the adsorption of the C–C bond requires adjacent nickel atoms, and this kind of nickel site is not abundant on the surface of the Ni/SAPO-11 catalyst due to the high dispersion. Another reason for the lower ratio over Ni/SAPO-11 is that SAPO-11 contains a large amount of phosphorus, and the Ni_2P species can lead to the adsorption being replaced by other forms.^{36, 37}



Scheme 2.2 Surface reaction model of C–C bond cleavage for the decarbonylation of lauric acid over the 500R-Ni catalyst.

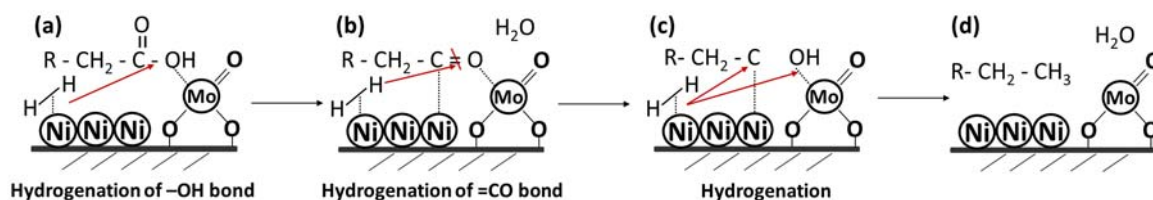
For Mo/SAPO-11, the main deoxygenation pathway is hydrodeoxygenation (**Scheme 2.3**). (a) The reduction of MoO_3 can generate MoO_2 , which has an oxygen vacancy. The $-C=O$ and $-OH$ bonds can be adsorbed on two adjacent Mo^{4+} species. (b) Hydrogenation of these bonds breaks the $-OH$ bond, resulting in the formation of the adsorbed alcohol. (c) C_{12} hydrocarbons are generated by subsequently hydrogenating the $-OH$ bond. The extremely high selectivity toward C_{12} hydrocarbons (C_{11}/C_{12} was close to zero) at a lower reaction temperature (< 350 °C) suggests that the deoxygenation can only occur in this way. On the other hand, the deoxygenation activity of 550R-Mo was much lower than the NiMo/SAPO-11 catalyst reduced at 450-550 °C (Table 5). Because the dissociated hydrogen is more difficult to generate on the molybdenum oxides than on the metal nickel.



Scheme 2.3 Surface reaction model of C=O hydrogenation for the hydrodeoxygenation of lauric acid over the 550R-Mo catalyst.

For NiMo/SAPO-11, hydrodeoxygenation is the main deoxygenation pathway, and deoxygenation activity is promoted by nickel compared to $\text{MoO}_3/\text{SAPO-11}$. The ratio of C_{11} to C_{12} was similar over 450(500/550)R-NiMo, while 400R-NiMo showed higher decarbonylation selectivity than other three reduced NiMo/SAPO-11 catalysts. This result indicates that the deoxygenation mechanism is different for 400R-NiMo and 450(500/550)R-NiMo. In 400R-NiMo, the amount of Mo^{4+} (27.6%) was low, and thus the number of adsorption sites for the C=O group was in low supply, which results in little hydrodeoxygenation over this catalyst. Therefore, metal nickel catalyzed decarbonylation became the dominant pathway. In contrast, the NiMo/SAPO-11 catalyst reduced above 450 °C exhibited a similarly high $\text{C}_{11}/\text{C}_{12}$ ratio compared to the reduced $\text{MoO}_3/\text{SAPO-11}$, indicating that the deoxygenation mechanism was similar over these catalysts (**Scheme 2.4**). (a) First, the -OH group of the carboxylic acid is hydrogenated on the Ni or Mo^{4+} sites, resulting in the formation of an intermediate aldehyde. (b) Then the C=O bond in the aldehyde is adsorbed on Mo^{4+} . The partially reduced molybdenum species, i.e., Mo^{4+} , can be considered as Lewis acid site, and thus the carbonyl group can be easily adsorbed on an electron acceptor rather than on the nickel site. (c) Hydrogenation of the C=O bond by the dissociated hydrogen generated from the adjacent nickel sites occurs, resulting in the formation of C_{12} hydrocarbons and adsorbed -OH group on Mo^{4+} . (d) Finally, hydrogenation of the adsorbed -OH groups can transform the molybdenum species

into the initial form. In short, the co-presence of metallic Ni species and partially reduced MoO₂ may be responsible for the high HDO selectivity and deoxygenation activity.



Scheme 2.4 Surface reaction model of C=O hydrogenation for the hydrodeoxygenation of lauric acid over the 450(500/550)R-NiMo catalyst.

2.4 Conclusions

High stability of a traditional NiMo/Al₂O₃ catalyst was achieved by changing the activation method from sulfidation to hydrogen reduction. The reduced catalyst showed similar activity to the sulfided catalyst in hydrotreating of Jatropha oil at a relatively high reaction temperature (375 °C). Reduced NiMo bimetal was loaded onto acid supports, *i.e.*, SiO₂-Al₂O₃, SAPO-11, and Al-SBA-15, to prepare bifunctional catalysts. These catalysts were highly active in isomerization due to their Brønsted acidity. NiMo/SAPO-11 gave the highest isomerization but relatively lower cracking selectivity, and therefore, it was considered to be a suitable bifunctional catalyst for simultaneous deoxygenation-isomerization. Further investigation of the effect of the reduction temperature on NiMo/SAPO-11 was conducted in hydrotreating of a model compound – methyl laurate. At all reduction temperatures (400–550 °C), nickel oxides were completely reduced to nickel metal, whereas the molybdenum oxides were reduced to lower valent molybdenum species (Mo⁴⁺ and Mo⁵⁺). Elevated reduction temperature decreased the concentration of Mo⁵⁺ species as well as the catalyst acidity, resulting in lower isomerization activity. In contrast, deoxygenation activity increased with increasing reduction temperature due to the increased concentration of Mo⁴⁺ species, which are considered to be adsorption sites for oxygen in the substrate. For the reaction pathway, Ni/SAPO-11 and NiMo/SAPO-11 reduced at 400 °C favored decarbonylation due to the strong C-C bond cleavage capacity of the nickel phase, whereas hydrodeoxygenation, *i.e.*, C=O bond hydrogenation, was favored over Mo/SAPO-11 and NiMo/SAPO-11 reduced at higher temperatures (> 450 °C). These behaviors could be related to a synergistic effect between Ni metal and Mo⁴⁺ species. Therefore, it is important to control the concentration of different valences of molybdenum species. In this study, NiMo/SAPO-11 reduced at 450 °C possessed a good balance between its deoxygenation activity and isomerization selectivity.

References

1. G. W. Huber; P. O'Connor; A. Corma, Processing biomass in conventional oil refineries: Production of high quality diesel by hydrotreating vegetable oils in heavy vacuum oil mixtures, *Appl. Catal., A*, **2007**, *329*, 120-129.
2. S. Gong; A. Shinozaki; M. Shi; E. W. Qian, Hydrotreating of Jatropha Oil over Alumina Based Catalysts, *Energy Fuels*, **2012**, *26* (4), 2394-2399.
3. D. Kubička; J. Horáček, Deactivation of HDS catalysts in deoxygenation of vegetable oils, *Appl. Catal., A*, **2011**, *394* (1-2), 9-17.
4. T. R. Viljava; E. R. M. Saari; A. O. I. Krause, Simultaneous hydrodesulfurization and hydrodeoxygenation: interactions between mercapto and methoxy groups present in the same or in separate molecules, *Appl. Catal., A*, **2001**, *209* (1-2), 33-43.
5. O. V. Kikhtyanin; A. E. Rubanov; A. B. Ayupov; G. V. Echevsky, Hydroconversion of sunflower oil on Pd/SAPO-31 catalyst, *Fuel*, **2010**, *89* (10), 3085-3092.
6. N. Chen; S. Gong; H. Shirai; T. Watanabe; E. W. Qian, Effects of Si/Al ratio and Pt loading on Pt/SAPO-11 catalysts in hydroconversion of Jatropha oil, *Appl. Catal., A*, **2013**, *466*, 105-115.
7. C. Wang; L. Liu, Mechanism of Imidazole-Promoted Ligation of Peptide Phenyl Esters, *Chin. J. Chem.*, **2012**, *30* (9), 1974-1979.
8. B. Peng; X. Yuan; C. Zhao; J. A. Lercher, Stabilizing Catalytic Pathways via Redundancy: Selective Reduction of Microalgae Oil to Alkanes, *J. Am. Chem. Soc.*, **2012**, *134* (22), 9400-9405.
9. B. Peng; Y. Yao; C. Zhao; J. A. Lercher, Towards Quantitative Conversion of Microalgae Oil to Diesel-Range Alkanes with Bifunctional Catalysts, *Angew. Chem. Int. Ed.*, **2012**, *51* (9), 2072-2075.
10. E. W. Qian; N. Chen; S. Gong, Role of support in deoxygenation and isomerization of methyl stearate over nickel-molybdenum catalysts, *J. Mol. Catal. A*, **2014**, *387*, 76-85.
11. T. Kabe; W. Qian; Y. Hirai; L. Li; A. Ishihara, Hydrodesulfurization and Hydrogenation Reactions on Noble Metal Catalysts: I. Elucidation of the Behavior of Sulfur on Alumina-Supported Platinum and Palladium Using the ³⁵S Radioisotope Tracer Method, *J. Catal.*, **2000**, *190* (1), 191-198.
12. S. Brunauer; P. H. Emmett; E. Teller, Adsorption of Gases in Multimolecular Layers, *J. Am. Chem. Soc.*, **1938**, *60* (2), 309-319.
13. P. Kumar; S. R. Yenumala; S. K. Maity; D. Shee, Kinetics of hydrodeoxygenation of stearic acid using supported nickel catalysts: Effects of supports, *Appl. Catal., A*, **2014**, *471*, 28-38.
14. H. Sakagami; T. Ohno; H. Itoh; Z. Li; N. Takahashi; T. Matsuda, Physical and catalytic properties of Pt/MoO₃ reduced at different H₂ flow rates, *Appl. Catal., A*, **2014**, *470*, 8-14.
15. W. Suarez; J. A. Dumesic; C. G. Hill Jr, Acidic properties of molybdena-alumina for different extents of reduction: Infrared and gravimetric studies of adsorbed pyridine, *J. Catal.*, **1985**, *94* (2), 408-421.

16. M. Yamada; J. Yasumaru; M. Houalla; D. M. Hercules, Distribution of molybdenum oxidation states in reduced molybdenum/alumina catalysts: correlation with benzene hydrogenation activity, *J. Phys. Chem.*, **1991**, *95* (18), 7037-7042.
17. I. Oliveros; M. J. Pérez Zurita; C. Scott; M. R. Goldwasser; J. Goldwasser; S. Rondón; M. Houalla; D. M. Hercules, The Isomerization of Cyclopropane over Reduced Molybdena–Alumina Catalysts, *J. Catal.*, **1997**, *171* (2), 485-489.
18. F. Barath; M. Turki; V. Keller; G. Maire, Catalytic Activity of Reduced MoO₃/α-Al₂O₃ for Hexanes Reforming: I. Preparation, Characterization, and X-Ray Photoelectron Spectroscopy Studies, *J. Catal.*, **1999**, *185* (1), 1-11.
19. Y. Holl; R. Touroude; G. Maire; A. Muller; P. A. Engelhard; J. Grosmanin, Skeletal isomerization of hydrocarbons on molybdenum catalysts: I. X-ray photoelectron spectroscopy study of alumina-supported catalysts, *J. Catal.*, **1987**, *104* (1), 202-210.
20. W. Grünert; A. Y. Stakheev; W. Mörke; R. Feldhaus; K. Anders; E. S. Shpiro; K. M. Minachev, Reduction and metathesis activity of MoO₃/Al₂O₃ catalysts: I. An XPS investigation of MoO₃/Al₂O₃ catalysts, *J. Catal.*, **1992**, *135* (1), 269-286.
21. V. Keller; F. Barath; G. Maire, Catalytic Activity of Reduced MoO₃/α-Al₂O₃ for Hexanes Reforming: II. Catalytic Activity and Mechanistic Approach Using ¹³C Tracer Studies and Probe Molecules, *J. Catal.*, **2000**, *189* (2), 269-280.
22. F. E. Massoth, Characterization of Molybdena Catalysts. In *Advances in Catalysis*, D.D. Eley, H. P.; Paul, B. W., Eds. Academic Press: 1979; Vol. Volume 27, pp 265-310.
23. L. Portela; P. Grange; B. Delmon, The Adsorption of Nitric Oxide on Supported Co-Mo Hydrodesulfurization Catalysts: A Review, *Catalysis Reviews*, **1995**, *37* (4), 699-731.
24. X. Wang; U. S. Ozkan, Correlation of NO and CO₂ adsorption sites with aldehyde hydrogenation performance of sulfided NiMo/Al₂O₃ catalysts, *J. Catal.*, **2004**, *227* (2), 492-501.
25. A. Y. Bunch; X. Wang; U. S. Ozkan, Adsorption characteristics of reduced Mo and Ni–Mo catalysts in the hydrodeoxygenation of benzofuran, *Appl. Catal., A*, **2008**, *346* (1–2), 96-103.
26. M. Mihaylov; K. Hadjiivanov, FTIR Study of CO and NO Adsorption and Coadsorption on Ni-ZSM-5 and Ni/SiO₂, *Langmuir*, **2002**, *18* (11), 4376-4383.
27. H. Deldari, Suitable catalysts for hydroisomerization of long-chain normal paraffins, *Appl. Catal., A*, **2005**, *293*, 1-10.
28. S. Gong; N. Chen; S. Nakayama; E. W. Qian, Isomerization of *n*-alkanes derived from jatropha oil over bifunctional catalysts, *J. Mol. Catal. A*, **2013**, *370*, 14-21.
29. L. Boda; G. Onyestyák; H. Solt; F. Lónyi; J. Valyon; A. Thernesz, Catalytic hydroconversion of tricapylin and caprylic acid as model reaction for biofuel production from triglycerides, *Appl. Catal., A*, **2010**, *374* (1–2), 158-169.
30. O. İ. Şenol; E. M. Ryymin; T. R. Viljava; A. O. I. Krause, Reactions of methyl heptanoate hydrodeoxygenation on sulphided catalysts, *J. Mol. Catal. A: Chem.*, **2007**, *268* (1–2), 1-8.
31. B. Donnis; R. Egeberg; P. Blom; K. Knudsen, Hydroprocessing of Bio-Oils and Oxygenates to Hydrocarbons. Understanding the Reaction Routes, *Top Catal*, **2009**, *52* (3), 229-240.

32. B. Peng; C. Zhao; S. Kasakov; S. Foraita; J. A. Lercher, Manipulating Catalytic Pathways: Deoxygenation of Palmitic Acid on Multifunctional Catalysts, *Chem. Eur. J.*, **2013**, *19* (15), 4732-4741.
33. F. E. Massoth, Studies of molybdena-alumina catalysts: II. Kinetics and stoichiometry of reduction, *J. Catal.*, **1973**, *30* (2), 204-217.
34. J. Engelhardt; J. Goldwasser; W. K. Hall, The isomerization and metathesis of n-butenes: III. Reduced molybdena-alumina catalyst, *J. Catal.*, **1982**, *76* (1), 48-60.
35. D. Zhang; X. Li; S. Liu; X. Zhu; F. Chen; L. Xu, Investigations into the C4 olefin metathesis over Mo/Al₂O₃: Effects of support nature and pretreatment conditions on the product distribution, *Appl. Catal., A*, **2014**, *472*, 92-100.
36. H. Song; J. Wang; Z. Wang; H. Song; F. Li; Z. Jin, Effect of titanium content on dibenzothiophene HDS performance over Ni₂P/Ti-MCM-41 catalyst, *J. Catal.*, **2014**, *311*, 257-265.
37. J.-S. Moon; E.-G. Kim; Y.-K. Lee, Active sites of Ni₂P/SiO₂ catalyst for hydrodeoxygenation of guaiacol: A joint XAFS and DFT study, *J. Catal.*, **2014**, *311*, 144-152.

Chapter 3

Enhanced Activity of PtSn/SAPO-11 for Simultaneous Hydrodeoxygenation-Isomerization of Methyl Palmitate

Abstract

PtX (X = Pd, Re, Cu or Sn) bimetallic catalysts supported on SAPO-11, *i.e.*, PtX/SAPO-11 (Pt = 0.6 wt%, Pt/X = 1:1), were prepared using a co-impregnation method for simultaneous deoxygenation-isomerization of TG-related compounds. The PtSn catalyst showed the highest activity in hydrotreating of methyl stearate. The Pt loading was reduced to 0.3 wt% for further investigation of the effect of Sn/Pt atomic ratio (changed from 1 to 3). All PtSn catalysts exhibited high isomerization activity and hydrodeoxygenation (HDO) selectivity, and were superior to the monometallic Pt/SAPO-11 catalyst. In addition, The PtSn/SAPO-11 catalyst was more efficient for C=O bond hydrogenation, affording higher selectivity to C₁₆ hydrocarbons. Experimental results disclosed that the Sn species with different valence possessed distinct catalytic functions. Both Sn oxides and alloyed Sn species could catalyzed the reaction. The highest performance in the simultaneous deoxygenation-isomerization of methyl palmitate was observed over the catalyst with a Sn/Pt ratio of 2; for this catalyst, the isomerization yield obtained at 375 °C was 4 times higher than the monometallic Pt catalyst. Characterization results indicate that a portion of Sn interacted with Pt, forming Pt-Sn alloys; other Sn species were formed in the form of tin oxides, likely SnO_{2-x} (0 < x < 2), and were mainly present on the periphery of Pt nanoparticles. The SnO_{2-x} species is crucial to improve the hydrodeoxygenation (HDO) pathway; however, excessive addition of tin would block Pt and PtSn active sites, resulting in a decrease in the catalytic activity. The presence of Pt-Sn alloys is the most remarkable reason for its high isomerization activity.

3.1 Introduction

Due to limited fossil fuels and environmental issues, the development of new transformation processes for converting biomass into fuels or value added chemicals has become a real necessity.¹ Vegetable oils, which can be converted into transportation fuels or value added chemicals *via* a hydrotreating process, are considered as a potential substitute.² Total deoxygenation of the vegetable oil can yield long-chain *n*-alkanes (C₁₁₋₂₂) with boiling points in the range of diesel or jet fuels.³ In order to improve the cold flow property of deoxygenated hydrocarbons, a subsequent isomerization process is usually conducted for converting *n*-alkanes into *iso*-alkanes.⁴

The deoxygenation of vegetable oils and related compounds has been widely studied and performed efficiently using the conventional hydrotreating catalyst such as sulfided Ni(/Co)Mo/Al₂O₃.^{5, 6, 7, 8} It is necessary to add a sulfur-containing compound into the feedstock in order to maintain the active phases on the sulfided catalyst. However, this would cause a contamination of the final product.^{9, 10} Supported Ni, Pt and Pd catalysts also exhibit high deoxygenation activity. Lercher's group reported a new route for converting microalgae oils into alkanes using ZrO₂- or Hbeta zeolite-supported Ni catalysts.^{11, 12, 13} Although these Ni-based catalysts have obvious advantages compared to the sulfided catalyst, sintering would occur easily in the pre-reduction stage and also during the reaction. In addition, Ni-catalyzed deoxygenation favored the decarbonylation pathway, resulting in C-C bond cleavage, and thus the liquid yield would be reduced. The addition of reducible metal oxides into the nickel catalyst has been reported to be efficient for promoting the hydrodeoxygenation pathway.¹⁴ On the other hand, Shimizu *et al.* demonstrated a synergistic effect between Pt and Nb₂O₅ that substantially promoted both the deoxygenation rate and the hydrodeoxygenation selectivity.¹⁵

Isomerization is a side reaction in hydrotreating of vegetable oils. The isomerization of a *n*-alkane can be promoted by using an acidic support such as amorphous SiO₂-Al₂O₃, zeolite and aluminum doped mesoporous silica.¹⁶ Recently, converting vegetable oils into *iso*-alkanes through a single process, *i.e.*, combining

deoxygenation and isomerization, was reported by using metal-zeolite catalysts. Kikhtyanin *et al.* reported the first one-step process for the hydroconversion of sunflower oil over a Pd/SAPO-31 catalyst; however, the catalyst was rapidly deactivated.¹⁷ Zhang *et al.* designed a bifunctional catalyst with 7 wt% Ni as the metal site and a modified SAPO-11 zeolite as the acid site, achieving a high total isomerization yield (*i.e.*, isomerized C₅₋₁₈ hydrocarbons) of approximately 65% ($T = 280\text{ }^{\circ}\text{C}$, $P = 4\text{ MPa}$, $LHSV = 2\text{ h}^{-1}$); however, the formation of C₄₋₁₅ hydrocarbons would reduce the burning quality of fuel oil.¹⁸ Tian *et al.* investigated the effect of acid or alkali treatment on SAPO-11 and ZSM-22 in soybean oil hydrotreatment. A 1 wt% Pt/SAPO-11 catalyst showed high isomerization activity, yielding approximately 63% *iso*-C₁₅₋₁₈ hydrocarbons ($T = 357\text{ }^{\circ}\text{C}$, $P = 4\text{ MPa}$, $LHSV = 1\text{ h}^{-1}$).¹⁹ On the other hand, we studied the effects of Pt amount and the Si/Al ratio of SAPO-11 on the hydroconversion of Jatropha oil. The isomerization activity was substantially dependent on the Pt amount rather than the acidity of the support.²⁰ Moreover, the isomerization rate of deoxygenated products that obtained from hydrotreated Jatropha oil (*i.e.*, normal C₁₅₋₁₈ paraffins) was much higher than that of the natural Jatropha oil under the same reaction conditions.²¹ Consequently, the metal site works as the active site for both deoxygenation and isomerization, and the insufficient noble metal content would cause a lower isomerization activity in the tandem hydrodeoxygenation-isomerization of vegetable oils. Although an increase of the noble metal content could render the catalyst more active, the higher cost will prohibit the large-scale industrialization of this process. For these reasons, it is of great importance to improve the metal function *via* increasing its efficiency.

Bimetallic catalysts have attracted immense interest in heterogeneous catalysis. Synergistic effects between the two metals provide unique properties that are different from their monometallic counterparts, resulting in improved activity, selectivity and/or stability.²² Murata designed a Pt-Re bimetallic catalyst for the vegetable oil hydrotreatment.^{23, 24} Substantially higher activity was observed from a 1 wt% Pt–20 wt% Re/HZSM-5 catalyst compared to the monometallic Pt catalyst. PtSn catalysts were reported to be active for the formation of olefins in the hydrogen-

free deoxygenation of ester and fatty acid.^{25, 26} However, the influence of Sn on the Pt particles was not clear. On the other hand, alloying platinum with tin has attracted much attention in the isomerization or dehydrogenation of paraffins. However, detailed investigations of the Sn added Pt catalyst for the deoxygenation of vegetable oils have not been performed.

In this chapter, bimetallic Pt-based catalysts were designed for simultaneous deoxygenation-isomerization. First, Pd, Re, Cu or Sn was added into a monometallic Pt/SAPO-11 catalyst (Pt = 0.6 wt%) to enhance its performance. The PtSn/SAPO-11 catalyst, which showed the highest activity in hydrotreating of methyl stearate, was then selected for further investigation. PtSn catalysts with a lower Pt loading of 0.3 wt% and various Sn/Pt ratios (1 – 3) were prepared for hydrotreating of methyl palmitate. Finally, characterizations, *e.g.*, High-resolution transmission electron microscopy (HRTEM), X-ray Photoelectron Spectroscopy (XPS) and Fourier transform infrared spectroscopy (FT-IR) studies of adsorbed CO or pyridine, were performed to elucidate the active phase in PtSn/SAPO-11 and the structure-performance relationship. In addition, *in situ* FT-IR study – adsorption of propionic acid and propionaldehyde were performed to understand the surface reaction mechanism.

3.2 Experimental Section

3.2.1 Catalyst Preparation

PtX/SAPO-11 (X = Pd, Re, Cu or Sn) bimetallic catalysts were prepared by a co-impregnation method. Prior to impregnation, SAPO-11 pellets (Nikki-Universal, Japan; Si/Al = 0.1 mol/mol) were ground and sieved to yield 425-850 μm particles. Then, an aqueous solution of $\text{H}_2\text{PtCl}_6 \cdot 6\text{H}_2\text{O}$ (Sigma-Aldrich, 98.5%) and the other metal precursor was prepared and added into a calculated amount of SAPO-11 particles. PdCl_2 (Sigma-Aldrich, 99%), NH_4ReO_4 (Sigma-Aldrich, 99%), $\text{Cu}(\text{NO}_3)_2$ (Sigma-Aldrich, 99%) and SnCl_2 (Sigma-Aldrich, 98%) were used as metal precursors for PtPd, PtRe, PtCu and PtSn, respectively. In the case of PtPd catalyst, a trace amount of HCl was added to the solution to dissolve the metal precursor. These catalysts were calcined in air at 450 $^\circ\text{C}$ for 10 h after drying at 120 $^\circ\text{C}$ for 4 h. The loading amount of Pt was 0.6 wt% and the X/Pt atomic ratio was 1. PtSn catalysts with various Sn/Pt atomic ratios were prepared by the similar method. The Pt loading was lowered to 0.3 wt% and the Sn/Pt atomic ratio was varied in the range of Sn/Pt = 1-3 (atomic ratio). For comparison, monometallic Pt/SAPO-11 was also prepared. Monometallic Pt/SAPO-11 and bifunctional PtX/SAPO-11 catalysts are denoted PtX $_x$, respectively, where x refers to the atomic ratio of X to Pt.

3.2.2 Catalyst Characterization

Surface area and pore volume of calcined catalysts were measured by the nitrogen physisorption at -196 $^\circ\text{C}$ using a Belsorp-mini II automated sorption system. Brunauer–Emmett–Teller and t -plot methods were used to determine the specific surface area and the pore volume, respectively. Prior to each measurement, the sample was degassed under vacuum ($p < 10^{-2}$ kPa) at 350 $^\circ\text{C}$ for 2 h.

To determine the amount of active sites on the catalyst, pulse CO chemisorption was performed on a ChemBET Pulsar TPR/TPD instrument (Quantachrome Instruments). Prior to adsorption, a measured amount of the calcined catalyst (400 mg) was reduced *in situ* under H_2 flow at 400 $^\circ\text{C}$ for 3 h, and then pretreated in a

highly pure helium flow at the same temperature for 2 h to remove the adsorbed hydrogen, followed by cooling to 40 °C. After the baseline being stable, successive doses of 10 % CO/He gas were introduced by a calibrated injection valve (100 μ L CO pulse⁻¹).

The FT-IR spectra of CO adsorption were recorded on an IRPrestige-21 instrument (Shimadzu), by adding 64 scans for the sample at a resolution of 4 cm⁻¹. The catalyst powder was pressed into a self-supporting wafer (10 mg/cm⁻², diameter = 10 mm), which was inserted into a measurement cell with CaF₂ windows. The cell was purged by H₂ flow (30 mL/min) at room temperature for 0.5 h, followed by raising the cell temperature to 400 °C at a rate of 20 °C/min. After a 3 h reduction, the sample was degassed under evacuation (pressure < 10⁻⁵ Torr) at the same temperature for 2 h. Subsequently, the cell was cooled to 40 °C with He, and an IR spectrum was collected as a background spectrum. CO adsorption (50 Torr) was performed at 40 °C for 0.5 h, followed by evacuation at the same temperature for 20 min to remove gaseous and weakly adsorbed CO species. Another IR spectrum were then obtained in the absorbance mode and are shown after subtraction of the background spectrum to make the adsorbate peaks more clear. Pyridine adsorption was performed under the procedure similar to CO adsorption. For pyridine adsorption, a calculated amount of pyridine (4 Torr) was introduced to the cell by a vacuum pump and the adsorption was conducted for 30 min at 100 °C. Prior to recording IR spectra, the sample was degassed at each temperature for 20 min. FT-IR spectra of adsorbed propionic acid and propionaldehyde were obtained by using the same instrument as used for other IR measurements. After reduced *in situ* at 400 °C, the sample was cooled to 50 °C in an H₂ flow, and the background spectrum was recorded under evacuation. Subsequently, propionic acid (~10 Torr) or propionaldehyde (~100 Torr) was injected into the sample cell, and the adsorption was conducted for 30 min. Then, weakly adsorbed molecules were removed by evacuation. IR spectra were recorded at 50 °C, 100 °C, 200 °C and 300 °C.

The amount of acid sites was measured by NH₃-TPD using the same instrument as CO adsorption. Typically, a 200 mg sample was reduced by a pure H₂ gas (15

cm³/min) at 400 °C for 3 h, followed by cooling to 30 °C in a He flow. The ammonia adsorption was conducted for 40 min under a 15 cm³ min⁻¹ 10 vol.% NH₃/He flow. The physically adsorbed ammonia was removed under helium flow at 100 °C for 2 h, and the TPD was measured by linearly increasing the cell temperature from 100 to 800 °C at a heating rate of 10 °C/min. Similarly, the amount of desorbed ammonia was monitored using a thermal conductivity detector (TCD) and quantified by pulse calibration.

XPS spectra were acquired using an ESCA-3200 (Shimadzu) spectrometer with monochromatic Mg K α radiation (240 W, 8 kV, $E = 1253.6$ eV). The binding energy (BE) value was referenced to the adventitious carbon (C 1s at 284.6 eV). The sample was prepared in a dry box under argon flow. A degassing pretreatment was performed prior to analysis.

HRTEM and HAADF-STEM measurements were performed on a JEM-2200FS (JEOL) electron microscope operating at 200 kV. The sample powder was pretreated *ex situ* in H₂ flow at 400 °C for 3 h, and deposited on copper grids without carbon film coating.

3.2.3 Activity Test

Hydrotreating of model compounds, *i.e.*, methyl stearate and methyl palmitate, was performed in a stainless steel fixed-bed continuous-flow reactor (i.d. 8 mm, length 40 mm) operated in the down-flow mode. The calcined catalyst (1.5g) was diluted with quartz and charged into the isothermal region of the reactor. Prior to each test, the catalyst was reduced at 400 °C under a 100 mL/min H₂ flow for 3 h at atmospheric pressure. After reduction, methyl palmitate was continuously pumped into the reactor. Because the melting point of the reactant was higher than room temperature, the piping and pump were heated using ribbon heaters. The reaction was conducted under 3 MPa hydrogen pressure, with a weight hourly space velocity (WHSV) of 5 h⁻¹, a H₂/Feedstock ratio of 800 (ml/ml) and at a temperature range of 300–375 °C. The catalytic activity was measured after 4 h stabilization. After the reaction at 375 °C, the temperature was returned to 300 °C, and the catalytic test was

repeated to confirm the deactivation. There was no considerable change in the catalyst activity, thus the deactivation of the catalyst can be ignored.

After the reaction, liquid products were diluted with carbon tetrachloride, and analyzed with a gas chromatograph (GC-2025, Shimadzu) equipped with a flame ionization detector (FID) and a DB-5HT column (Agilent, 30 m × 0.25 mm i.d., 0.25 μm). Product identification was performed on a gas chromatograph-mass spectrometer (GC-MS-QP5050A, Shimadzu) equipped with the same capillary column. Other gas chromatographs 1) with a thermal conductivity detector (TCD) and a Unibeads C column (GL Sciences, 3 m × 3 mm i.d.) and 2) with a FID and a DB-1 column (Agilent, 60 m × 0.25 mm i.d., 0.25 μm) were used to analyze the gaseous product.

The amount of the product was quantified using GC standards. The conversion was defined as the moles of the reactant converted to other products (intermediate oxygenates and hydrocarbons) and the selectivity was based on a carbon percentage. The conversion and selectivity were calculated using the following equations:

Conversion (%) = (the number of molecules of the converted reactant) / (the number of molecules of the starting reactant) × 100.

Selectivity (%) = (carbon atoms in product *i*) / (carbon atoms in the product) × 100.

3.3 Results and Discussion

3.3.1 Screening of PtX/SAPO-11 Catalysts for Hydrotreating of Methyl Stearate

The catalytic performance of bifunctional PtX/SAPO-11 catalysts was evaluated by hydrotreating of a model compound – methyl stearate (MS). MS conversion, the selectivity of isomerization and cracking were presented in **Figure 3.1**. It is obvious that the PtSn catalysts showed extremely high activity and isomerization selectivity compared to other catalysts. Apart from the PtSn catalyst, other bimetallic catalysts gave lower MS conversions than the monometallic Pt catalyst. In addition, the PtPd catalyst showed higher isomerization activity than the Pt catalyst. For cracking, there was no considerable difference between Pt, PtRe, PtPd and PtCu. In contrast, PtSn showed higher cracking activity than other catalysts. This might be related to its higher deoxygenation activity, on which the formation of hydrocarbons was enhanced.

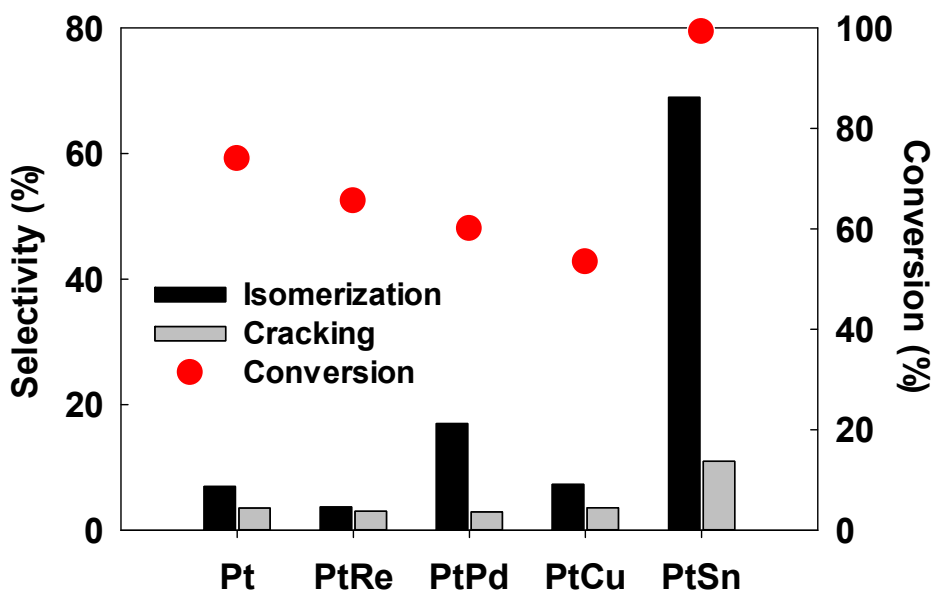


Figure 3.1 Catalytic performance of various bimetallic PtX/SAPO-11 catalysts in hydrotreating of methyl stearate. Reaction conditions: $T = 350\text{ }^{\circ}\text{C}$, $P = 3\text{ MPa}$, $\text{WHSV} = 5\text{ h}^{-1}$ and $\text{H}_2/\text{reactant} = 800\text{ (ml/ml)}$.

3.3.2 Effect of Sn/Pt Ratio on the Activity of PtSn/SAPO-11

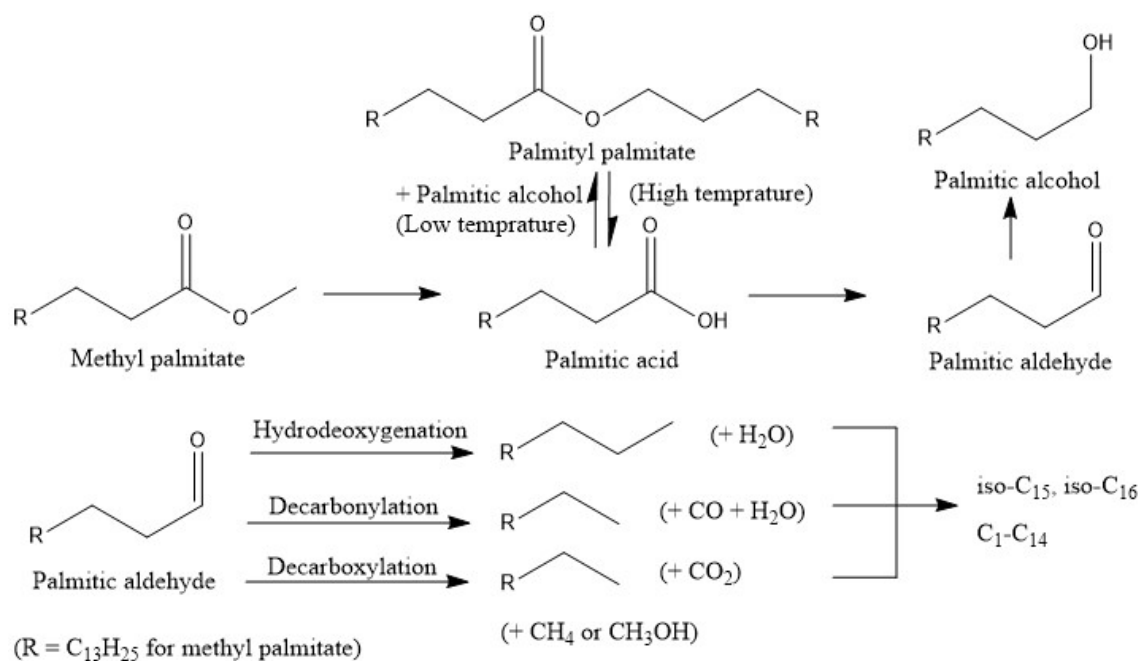
The PtSn/SAPO-11 catalyst was chosen for further investigation to understand the promotion effect of tin. To lower the cost, Pt loading amount was reduced to 0.3 wt%. Hydrotreating of another model compound – methyl palmitate (MP) was conducted over PtSn catalysts with various Sn/Pt atomic ratios. **Table 3.1** lists the hydrogenation products generated at 300 °C and 375 °C. It is obvious that oxygenates, *e.g.*, palmitic acid and palmityl palmitate, are the primary liquid products at a lower reaction temperature. The formation of hydrocarbon products increased with increasing reaction temperature. CO, CO₂ and CH₄ were generated as gaseous products. It is worth noting that water formation can be observed in every case, although it was not shown in the table.

Possible reaction pathways for MP hydrogenation are proposed based on these products. As shown in **Scheme 3.1**, MP hydrogenation was a complex reaction that involved several elementary reactions. MP hydrogenation generates palmitic acid as a key intermediate oxygenate. The palmitic acid is then transformed to aldehyde by hydrogenation of the –OH group. Subsequently, deoxygenation of the palmitic aldehyde occurs *via* two competitive reaction pathways: hydrogenation of a C=O group in the aldehyde (HDO) to yield a C₁₆ hydrocarbon *versus* hydrogenolysis of a C–C bond adjacent to the C=O group (DCO) to yield a C₁₅ hydrocarbon. Furthermore, these deoxygenated products would undergo isomerization and cracking, yielding isomerized C_{15,16} hydrocarbons and C₁₋₁₄ hydrocarbons, respectively. In addition, a large amount of palmityl palmitate was observed at a lower reaction temperature, indicating that the esterification of palmitic acid and hexadecanol occurred rapidly. Generally, the esterification of a fatty acid and an alcohol is an acid-catalyzed reaction. In this study, Lewis acid sites on the SAPO-11 zeolite can promote this reaction. The formation of the ester decreased with increasing reaction temperature due to the fact that higher reaction temperatures give rise to enhancing the reverse reaction (from the ester to acid and alcohol).

Table 3.1. Methyl palmitate hydrogenation over the Pt and PtSn catalysts.

	Pt		PtSn1		PtSn1.5		PtSn2		PtSn2.5		PtSn3	
	300 °C	375 °C	300 °C	375 °C	300 °C	375 °C	300 °C	375 °C	300 °C	375 °C	300 °C	375 °C
Conversion (%)	24.2	81.3	22.9	72.7	26.9	76.7	39.5	86.6	21.4	43.2	18.5	42.9
Isomer yield (wt%)	0.1	12.1	0.5	31.4	1.8	38.8	1.6	50.0	0.6	13.7	0.2	7.4
Selectivity to various products. (C%)												
CO	3.0	14.1	0.0	5.1	0.0	1.9	0.0	1.0	0.0	0.9	0.0	0.5
CO ₂	-	0.4	-	0.4	-	0.4	-	0.4	-	0.0	-	-
CH ₄	0.8	1.3	1.5	2.1	0.7	1.8	0.4	1.2	0.4	1.8	0.4	0.8
CH ₃ OH	1.1	4.3	1.2	4.1	1.5	3.9	2.1	3.1	1.2	2.5	0.9	3.0
C ₂ -C ₁₄	1.6	6.6	1.6	13.9	2.9	3.7	2.0	5.6	1.4	3.1	1.6	2.8
i-C _{15,16}	0.3	14.8	2.0	43.2	6.6	50.6	4.1	57.8	2.9	31.8	0.8	17.3
n-C _{15,16}	37.8	50.4	8.2	16.1	4.5	12.9	10.9	21.3	2.9	13.7	5.6	39.7
C ₁₆₊	1.2	1.5	2.3	2.9	2.6	2.9	2.3	2.6	3.4	3.2	3.6	3.9
Hexadecanol/ hexadecanal	6.2	1.7	12.1	4.0	7.0	6.1	5.5	3.2	7.7	7.6	6.6	4.1
Palmitic acid	27.7	4.8	22.5	7.8	20.6	15.4	13.4	3.6	26.0	32.6	17.0	16.7
Palmityl palmitate	20.2	0.0	48.6	0.4	53.6	0.4	59.4	0.2	54.1	2.8	63.6	11.4

Reaction conditions: $P = 3$ MPa, $WHSV = 5$ h⁻¹, $H_2/Feedstock = 800$ (v/v).



Scheme 3.1 Possible pathways for the hydrotreating of methyl palmitate. Compounds in brackets refer to by-products.

As shown in **Table 3.1**, tin addition leads to some variations in the hydrogenation property of Pt/SAPO-11. **Figure 3.2** shows the evolution of MP conversion as a function of Sn/Pt ratio at different reaction temperatures. The Pt catalyst gave a higher MP conversion than the PtSn catalyst except PtSn2. For PtSn catalysts, the conversion increased gradually with an increasing Sn/Pt ratio until the ratio reached 2; after that, it dropped rapidly. On the other hand, the isomerization activity of Pt/SAPO-11 was significantly improved by the tin addition. The PtSn2 catalyst exhibited the highest isomerization activity, on which the total isomer yield was approximately 4 times higher than the Pt catalyst at 375 °C. Pt/SAPO-11 catalyst with a 0.6 wt% Pt loading was also tested, and the isomer yield of PtSn2 (50.0%) was even two times higher than that of the 0.6 wt% Pt/SAPO-11 (21.4%). These results indicate that the isomerization activity of a Pt catalyst can be substantially improved by tin modification.

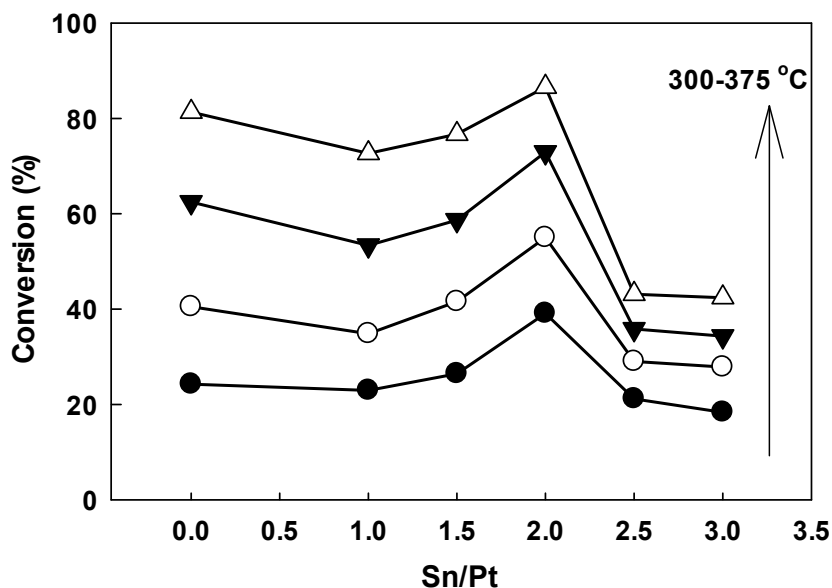


Figure 3.2 Conversion of methyl palmitate over the Pt and PtSn catalysts. Legend: (●) 300 °C, (○) 325 °C, (▼) 350 °C, (△) 375 °C. Reaction conditions: $T = 300 - 375$ °C, $P = 3$ MPa, $WHSV = 5$ h⁻¹ and $H_2/\text{reactant} = 800$ (ml/ml).

HDO and DCO are competing reactions during the deoxygenation of MP. The dominant reaction pathway can be illustrated by the comparison of the formation of C₁₅ and C₁₆ hydrocarbons (**Figure 3.3**). For the Pt catalyst, the main deoxygenated products were C₁₅ hydrocarbons, indicating that DCO was the main reaction pathway. In contrast, the main deoxygenated products over the PtSn catalysts were C₁₆ hydrocarbons, indicating that HDO became dominant. These results suggest that the reaction mechanism is different for the Pt and PtSn catalysts, and the DCO reaction can be inhibited by the tin addition. For the PtSn1 catalyst, however, the DCO route became dominant when the reaction temperature was raised to 350 °C. It should be noted that DCO is more thermodynamically advantageous than HDO at a high temperature, and the increase of the reaction temperature can also increase the DCO/HDO ratio. Therefore, the change in the reaction pathway from HDO to DCO over PtSn1 at a higher reaction temperature is attributed to the insufficient amount of tin. DCO involves a cleavage of the C-C bond that adjacent to the carbonyl group (C=O), producing a hydrocarbon with one carbon number less than the corresponding fatty acid. It is noted that liquid yield will be reduced by 5–6% if the reaction proceeds via the DCO pathway.²⁷ In this sense, the Sn/Pt ratio should be higher than 1.5 for inhibiting the undesired DCO reaction.

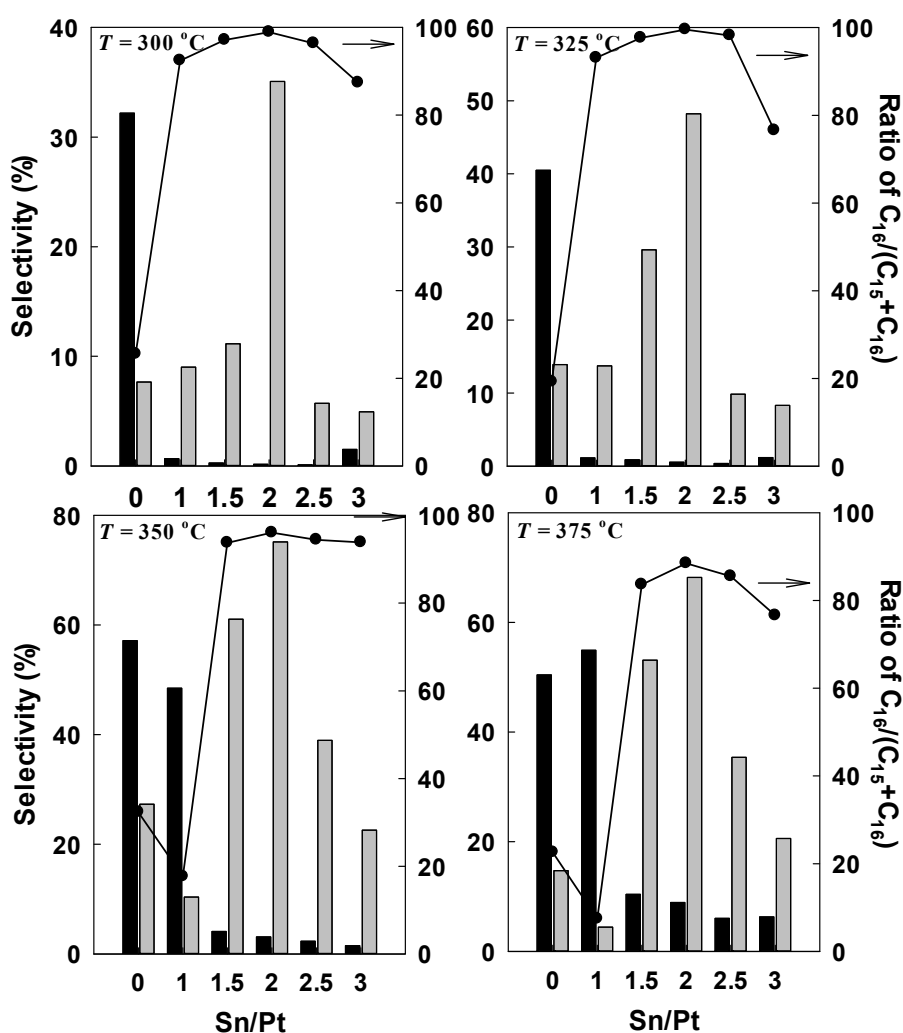


Figure 3.3 Effect of the Sn/Pt ratio on the formation of (■) C₁₅ and (▒) C₁₆ hydrocarbons at different reaction temperatures. Reaction conditions: $P = 3$ MPa, $WHSV = 5 \text{ h}^{-1}$ and $H_2/\text{reactant} = 800$ (ml/ml).

3.3.3 Catalyst Characterization

Multiple characterizations were employed to investigate the variations of the Pt/SAPO-11 catalyst after tin modification. The nitrogen physisorption measurement, as shown in **Table 3.2**, showed that the specific surface area and the pore volume of the catalysts were reduced after metal loading. This could be due to the blocking or filling of SAPO-11 micropores when the metal species were introduced. The amounts of platinum and tin were roughly identical to the calculated values.

Table 3.2 Physical and chemical characteristics of the Pt and PtSn catalysts.

Sample	Pt ^a (wt%)	Sn ^a (wt%)	$S_{\text{BET}}^{\text{b}}$ ($\text{m}^2 \cdot \text{g}^{-1}$)	V_{p}^{c} ($\text{cm}^3 \cdot \text{g}^{-1}$)	CO uptake ^d ($\mu\text{mol} \cdot \text{g}^{-1}$)	Pt particle size (nm) ^e
SAPO-11	-	-	175	0.25	-	-
Pt	0.33	-	113	0.22	6.48	8.0
PtSn1	0.26	0.18	99	0.21	2.69	5.4
PtSn1.5	0.32	0.29	86	0.15	2.11	-
PtSn2	0.34	0.37	76	0.16	1.62	4.4
PtSn2.5	0.29	0.49	74	0.12	0.93	-
PtSn3	0.31	0.58	68	0.11	0.52	4.1

^a Chemical composition determined by XRF.

^b Specific surface area calculated by the BET method.

^c Pore volume calculated by the *t*-plot method.

^d Amount of adsorbed CO measured by pulse chemisorption at 40 °C.

^e Determined by HAADF-STEM.

The adsorption of carbon monoxide followed by infrared spectroscopy has often been used to qualitatively evaluate the electronic properties of supported metal particles. Differences in the electronic state of the metal, *e.g.*, the electron transfer from one metal to the other metal in an alloy phase, can be reflected in the variation of the vibrational characteristics of the metal-CO bond.²⁸ **Figure 3.4** shows the FT-IR spectra of CO adsorbed at 40 °C on the Pt/SAPO-11 and PtSn/SAPO-11 catalysts after *in situ* reduction in H₂ at 400 °C. All of the studied samples showed the IR band in the range of 2050-2080 cm⁻¹. The bands in this range are attributed to linearly adsorbed CO and are assigned to CO interacting with a less dense close-packed arrangement of Pt atoms.²⁹ Compared to the Pt catalyst, the band in PtSn1.5 and PtSn 2 catalysts shifted by approximately 10 cm⁻¹ to a lower wavenumber. This phenomenon can be associated with the electronic effect of the Pt-Sn interaction, indicating that a certain amount of Pt-Sn alloys was generated in these two catalysts.³⁰ In addition, pulse CO chemisorption was used to measure the exposed Pt atoms. As shown in **Table 3.2**, the amount of adsorbed CO decreased significantly with increasing tin loading. This result indicates that the amount of exposed Pt atoms is reduced by surface coverage of tin.

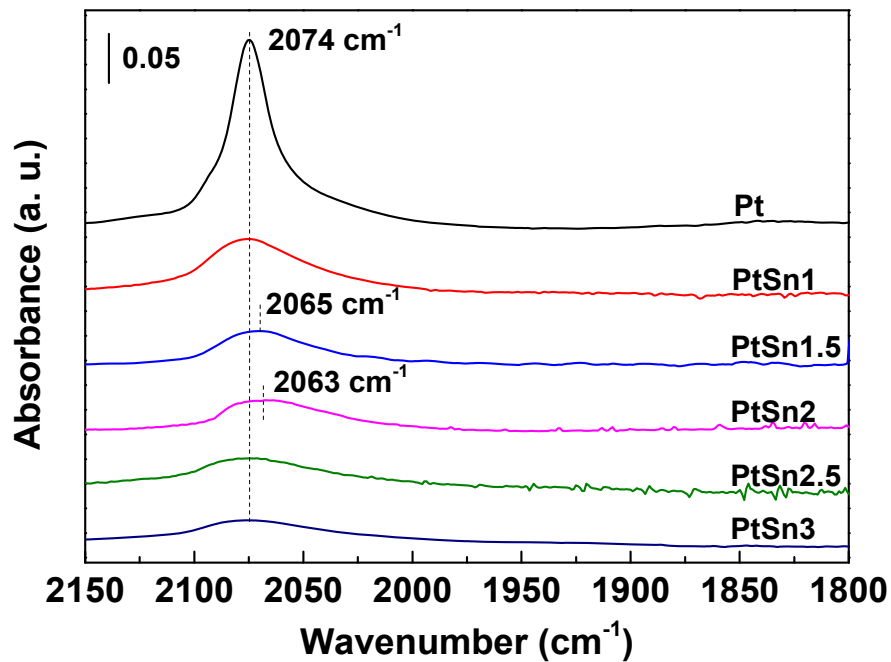


Figure 3.4 FT-IR spectrum of CO adsorption at 40 °C on the Pt/SAPO-11 and PtSn/SAPO-11 catalysts.

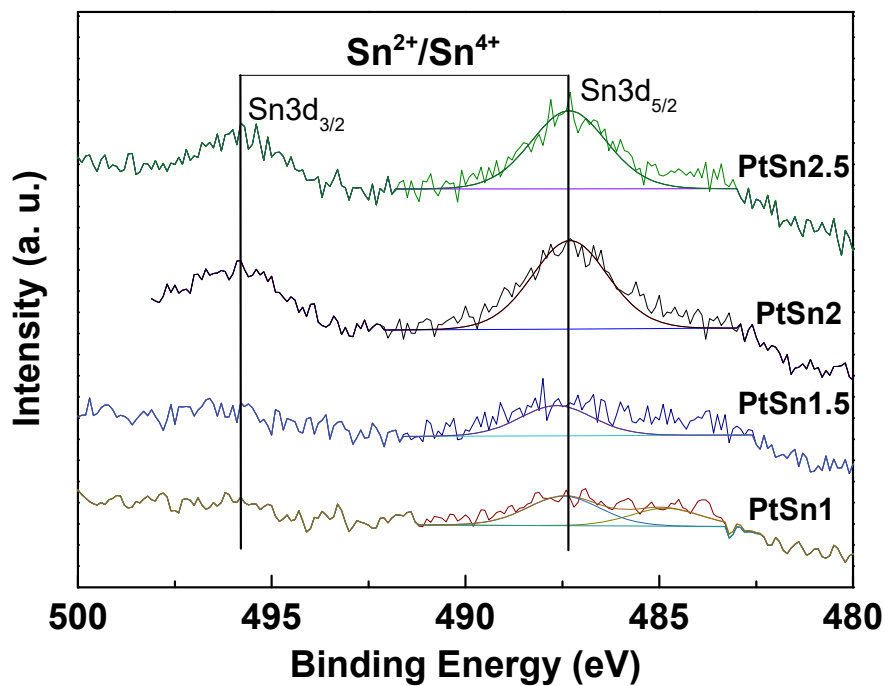


Figure 3.5 XPS results of Sn 3d spectra for the reduced PtSn/SAPO-11 catalysts.

XPS provides information about the chemical state of surface atoms. Although the Pt-Sn system has been widely studied, the tin valence in a PtSn catalyst has been disputed, because several factors, such as the acidity of a support, the preparation method or even the amount of platinum loading, could influence the valence of tin. **Figure 3.5** shows the Sn 3d region of the XPS spectrum for PtSn catalysts. For all PtSn catalysts, only one pair of peaks located at 487.1 eV (Sn 3d_{5/2}) and 495.5 eV (Sn 3d_{3/2}) is detected. These peaks are assigned to the oxidized Sn species.

NH₃-TPD was used to compare the acidity of the Pt and PtSn catalysts. As shown in **Figure 3.6**, different catalysts displayed similar distributions of acid sites, *i.e.*, weak acid sites centered at around 265 °C, and medium and strong acid sites located at approximately 390 °C. According to the NH₃ desorption profile for SAPO-11, these two peaks primarily are originated from the SAPO-11 support, indicating that the introduction of metal species cannot significantly affect the distribution of the acid site. In addition, the number of the acid site is calculated by a calibration curve, and the result is listed in **Table 3.3**. As the tin loading increased, the total acidity exhibited a slightly increasing tendency.

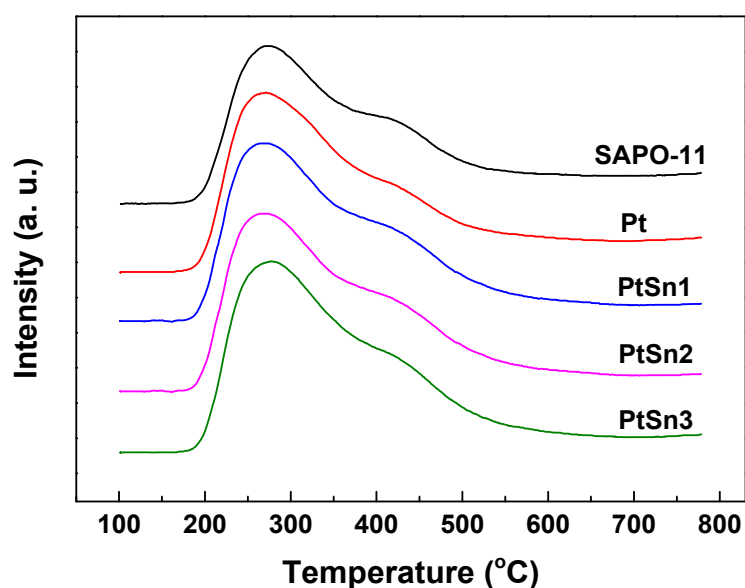


Figure 3.6 NH₃-TPD profiles of the support and reduced catalysts.

Table 3.3 Acidity of the support and reduced catalysts.

Sample	Ratio of Lewis to Brønsted acid sites			Total acidity ^b ($\mu\text{mol NH}_3/\text{g}$)
	150 °C ^a	250 °C ^a	350 °C ^a	
SAPO-11	2.7	0.8	0.6	496
Pt	2.6	0.8	0.6	603
PtSn1	12.0	0.7	0.4	632
PtSn2	16.9	0.6	0.3	661
PtSn3	79.8	0.8	0.5	692

^a Evacuation temperature in the pyridine adsorption experiment.

^b Total amount of acid sites determined by NH_3 -TPD.

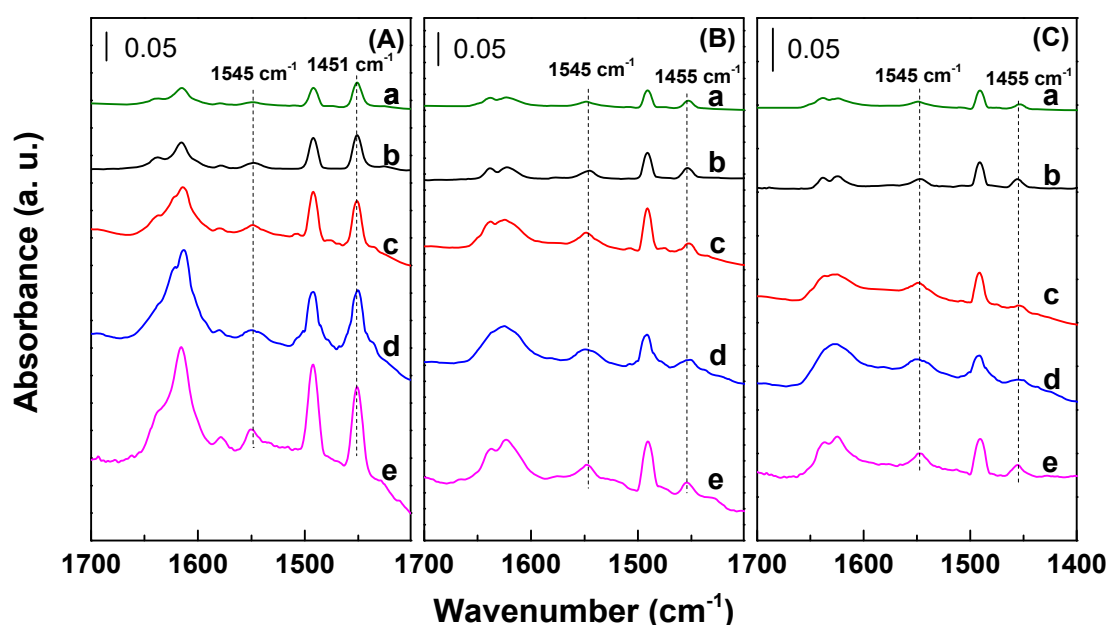


Figure 3.7 FT-IR spectra of pyridine adsorption on the (a) SAPO-11 (b) Pt, (c) PtSn1, (d) PtSn2 and (e) PtSn3 catalysts after evacuation at (A)150 °C, (B) 250 °C and (C) 350 °C.

To identify the type of acidity, FT-IR investigations were conducted using pyridine as a base probe molecule. The pyridine-FTIR spectra for SAPO-11, Pt and PtSn catalysts are shown in **Figure 3.7**, and the concentration ratio of Lewis to Brønsted acid sites (L/B) at different evacuation temperatures are listed in **Table 3.3**. As evidenced by the IR band due to coordinated pyridine at 1455 cm^{-1} and ionized pyridine at 1545 cm^{-1} , the SAPO-11 support and the studied catalysts possessed both Lewis and Brønsted acidity.³¹ The introduction of Pt onto SAPO-11 did not change

the L/B ratio. In contrast, the concentration of weak Lewis acid sites (*i.e.*, after evacuation at 150 °C) as well as the L/B ratio significantly increased after tin addition. Many studies have found that the reducible metal oxides, *e.g.*, Fe₂O₃, ReO₂, MoO₃ and SnO₂, can be easily reduced to their lower valences, but it is difficult to reduce these metal oxides to metal.^{32, 33, 34, 35, 36} In this study, the PtSn catalysts were prereduced at a high temperature (*i.e.*, 400 °C); thus, a portion of the SnO₂ can be transformed into partially reduced SnO_{2-x} species. These ionic Sn species (Sn^{δ+}) can exhibit Lewis acidity. On the other hand, there was no considerable change in the L/B ratio for the sample evacuated at higher temperatures (*i.e.*, 250 °C and 350 °C), indicating that the new Lewis acid sites exhibited weak acidity. In conclusion, acid sites on these PtSn/SAPO-11 catalysts consist of two parts; one is from the SAPO-11 support and exhibits both Lewis and Brønsted acidity, and the other is from the partially reduced SnO_{2-x} species and exhibits weak Lewis acidity.

TEM studies of the Pt, PtSn1, PtSn2 and PtSn3 catalysts were performed to investigate the effect of Sn addition on the Pt particle size and potential formation of Pt-Sn alloys. **Figure 3.8** shows the HAADF-STEM images and the statistic distributions of the Pt particle size. The PtSn catalysts exhibited smaller particle sizes (4.09–5.39 nm) compared to the Pt catalyst (7.95 nm). This result indicates that higher Pt dispersion can be obtained by Sn addition. Additionally, the average Pt particle size also decreased with increasing tin loading. These results can be explained by the "ensemble size effect", that is, Pt particles are isolated into smaller ensembles by Sn dilution.³⁷

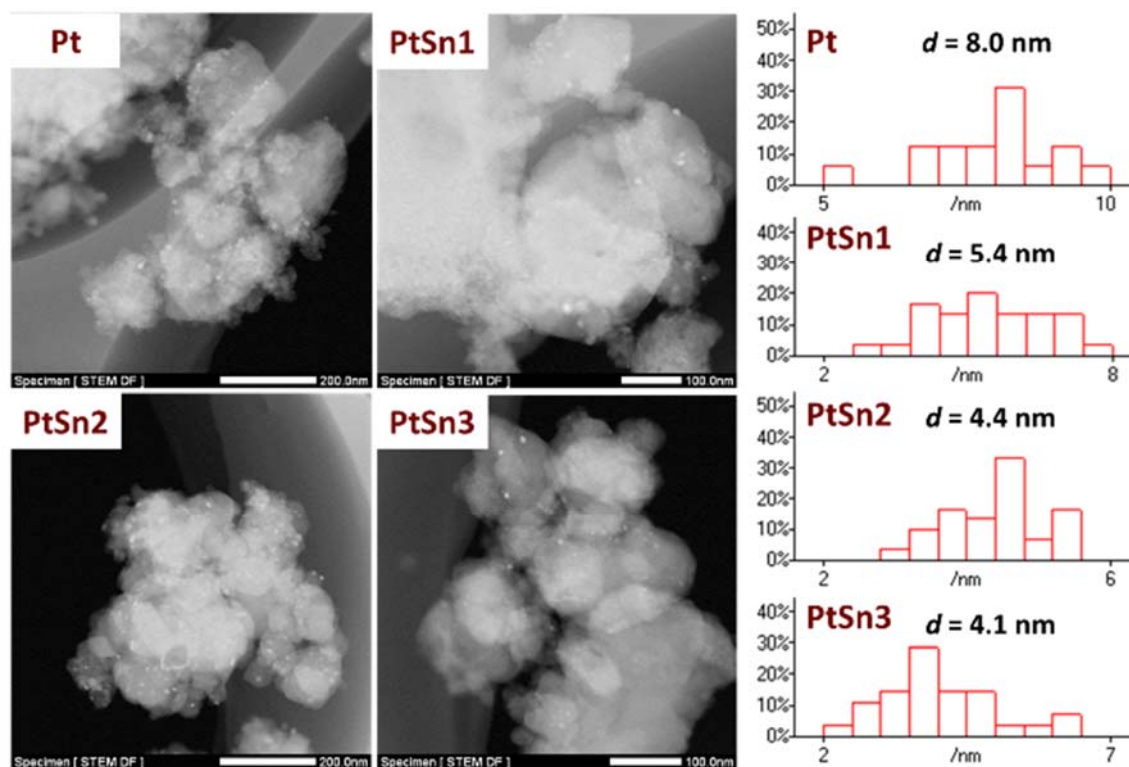


Figure 3.8 HAADF-STEM images and particle size distribution of the Pt and PtSn catalysts.

High-resolution TEM was further used to verify the formation of Pt-Sn alloy. **Figure 3.9** shows the HRTEM image with the digital diffraction patterns (DDPs) corresponding to the nanoparticles in these samples. In the Pt catalyst, the calculated lattice distance from the DDPs is 2.27 Å, which matches well with the expected d-spacing of the Pt(111) plane.³⁸ In contrast, for the PtSn1, PtSn2 and PtSn3 catalysts, the DDPs of the particles showed some larger lattice spacings that could not be assigned to any orientation of the metallic Pt, but could be indexed to orientations of Pt-Sn alloy phases.^{39, 40, 41, 42} These results provide evidence indicating the formation of Pt-Sn alloys in the PtSn catalyst. For the PtSn3 catalyst, however, only some Sn surface-enriched PtSn particles such as the particle whose lattice distance was 3.13 Å, and a SnO₂(110) surface ($d = 3.37$ Å) were observed.^{43, 44}

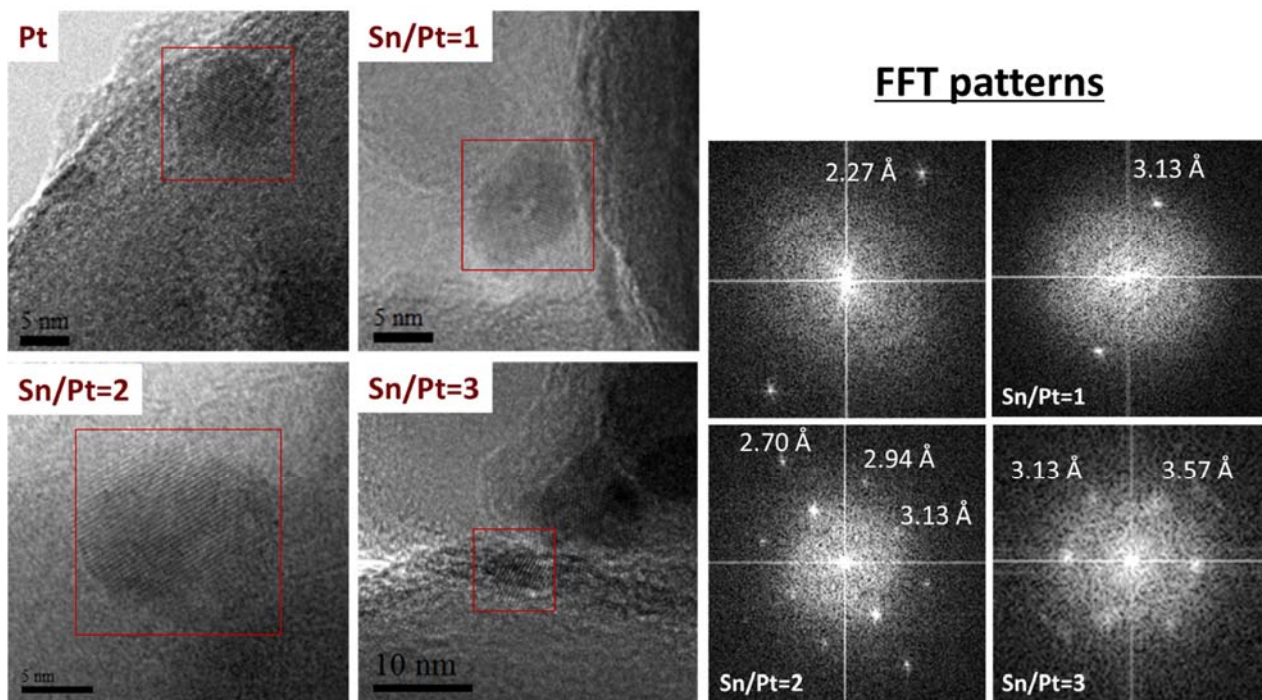


Figure 3.9 HRTEM images recorded on Pt and PtSn catalysts, together with their digital diffraction patterns.

In order to obtain information about adsorbed species on Pt and PtSn catalysts, FT-IR spectra of propionic acid adsorption was conducted for Pt/SiO₂ and PtSn₂/SiO₂ catalysts (**Figure 3.10**). It is noted that the reactant can be also adsorbed on the support, especially on an acid support. Therefore, a relatively inert support (*i.e.*, SiO₂) was used for inhibiting the support effect. Major features in the IR spectra for the two catalysts were similar. The spectra showed negative peaks at around 3750 cm⁻¹, which are attributed to Si–OH groups. They appeared negative because the hydroxyl groups are consumed by interaction with the propionic acid. Both spectra showed three bands at 2990–2890 cm⁻¹. These bands can be attributed to the stretching frequencies of the aliphatic C–H bonds in CH₃, CH₂ and CH groups. The intensity of the band that centered at 1749 cm⁻¹, which can be attributed to molecular propionic acid adsorbing on the support, are very strong and dominant even at a high temperature. The band appeared at the range of 1470–1360 cm⁻¹, which can be attributed to symmetric $\nu_s(\text{COO})$ and anti-symmetric $\nu_a(\text{COO})$, also showed strong intensity at a lower temperature for both catalysts. This feature is due to propionate species adsorbing on

the active metal surface, indicating that initial adsorption modes for Pt and PtSn₂ catalysts are similar. As the temperature increased, some bands appeared below 1400 cm⁻¹. These bands are due to C–H bending and scissoring in some reaction intermediates.

The main differences between the spectra for Pt and PtSn catalysts are considered to be the band at 2038 cm⁻¹, which is attributed to the linear adsorbed CO on the metal surface, and the band at ~1663 cm⁻¹, which can be attributed to the C=O stretching of propanoyl species. The band of CO only appeared in the spectra of Pt catalyst, indicating that the decarbonylation reaction occurred on the Pt catalyst. This behavior is consistent with the result of catalytic test. In addition, the formation of propanoyl species, especially in the spectrum that was recorded after 15 min reaction, give strong evidence that the aldehyde intermediate can be adsorbed on the PtSn catalyst through bonding with its C=O bond. In contrast, there was no peak corresponding to the propanoyl species in the spectrum of the Pt catalyst.

To further investigate the adsorption behavior over Pt and PtSn catalysts, an intermediate compound – propionaldehyde was used for the adsorption experiment. FT-IR spectra for Pt/SiO₂ and PtSn/SiO₂ after propionaldehyde adsorption were displayed in **Figure 3.11**. Similar to the adsorption of propionic acid, the stretching vibration band of CO at 2053 cm⁻¹ was obvious in the spectra of Pt/SiO₂, while the C=O stretching of propanoyl species at 1467 cm⁻¹ could be only observed in the spectra of PtSn/SiO₂. In addition, the intensity of bands at 2851-2981 cm⁻¹, which are attributed to the stretching frequencies of aliphatic C–H bonds, was much stronger in the spectra of Pt/SiO₂ than in those of the PtSn/SiO₂. Evidently, propionaldehyde adsorbed on the Pt catalyst through its C-C bond, whereas the bonding of C=O group of propionaldehyde on other surface species was the main adsorption mode for the PtSn catalyst.

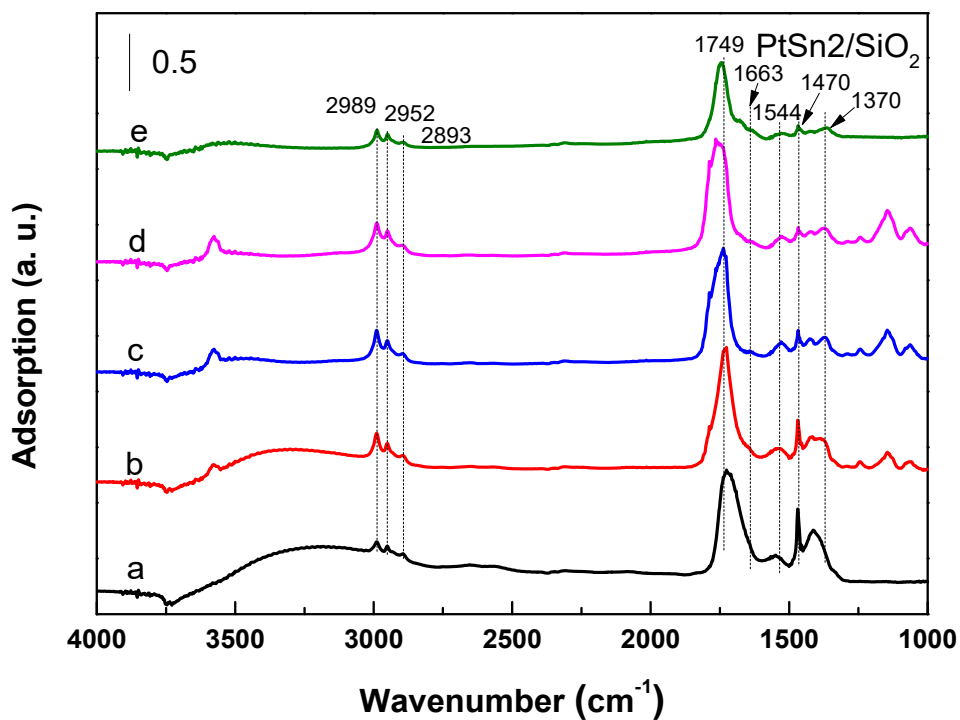
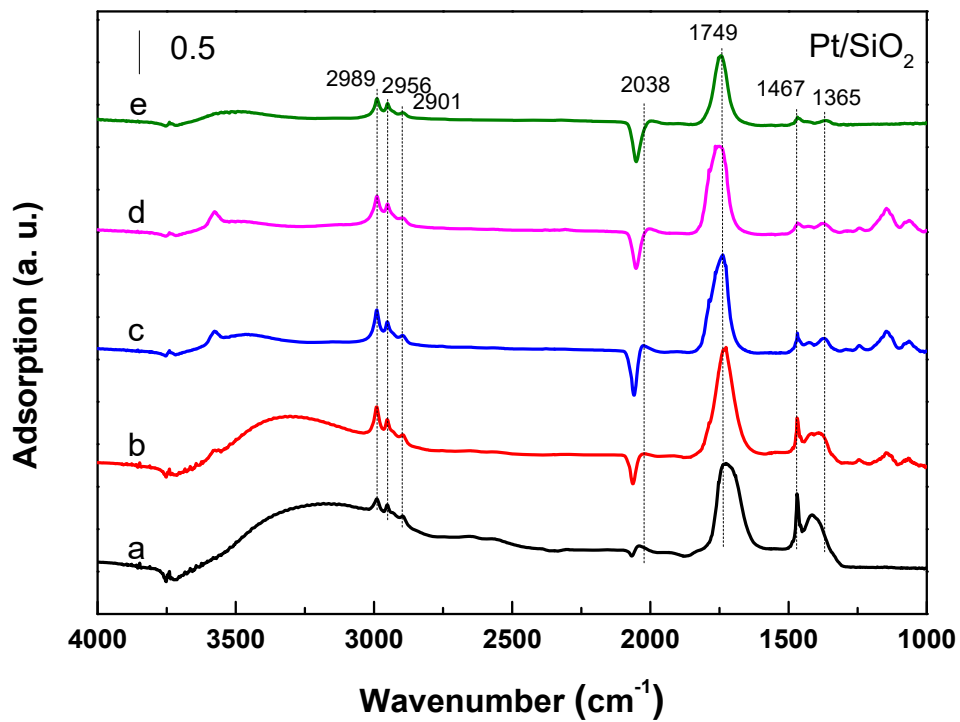


Figure 3.10 FT-IR spectra of propionic acid adsorption on Pt/SiO₂ and PtSn₂/SiO₂ catalysts. IR spectra were recorded after evacuating at (a) 50 °C, (b) 100 °C, (c) 200 °C, (d) 300 °C, and (e) after waiting for 15 min at 300 °C followed by evacuation.

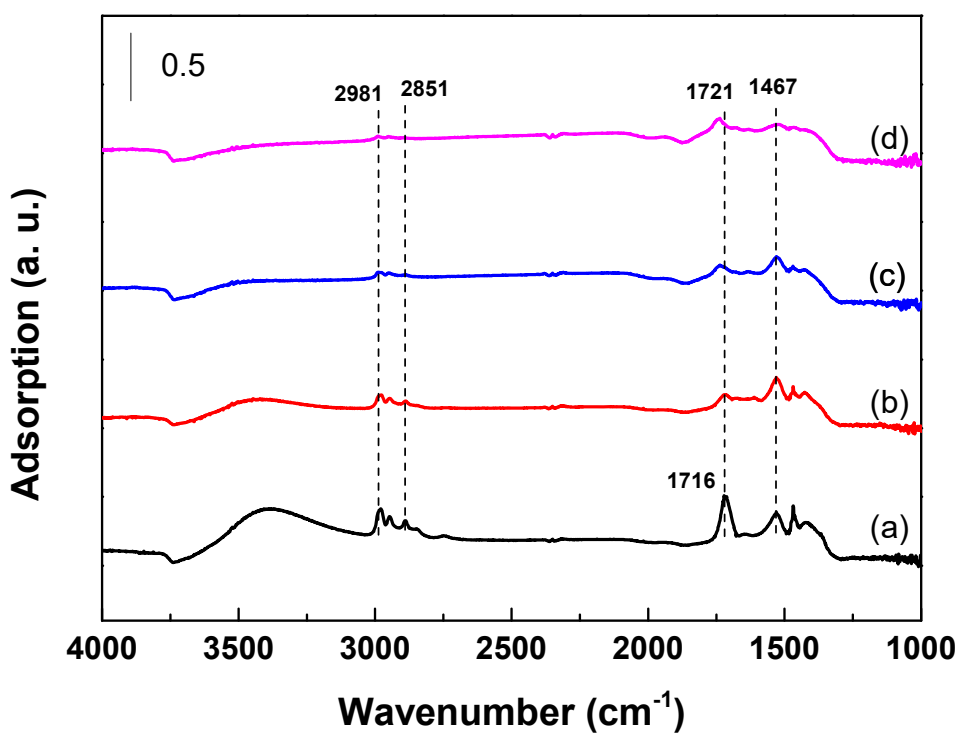
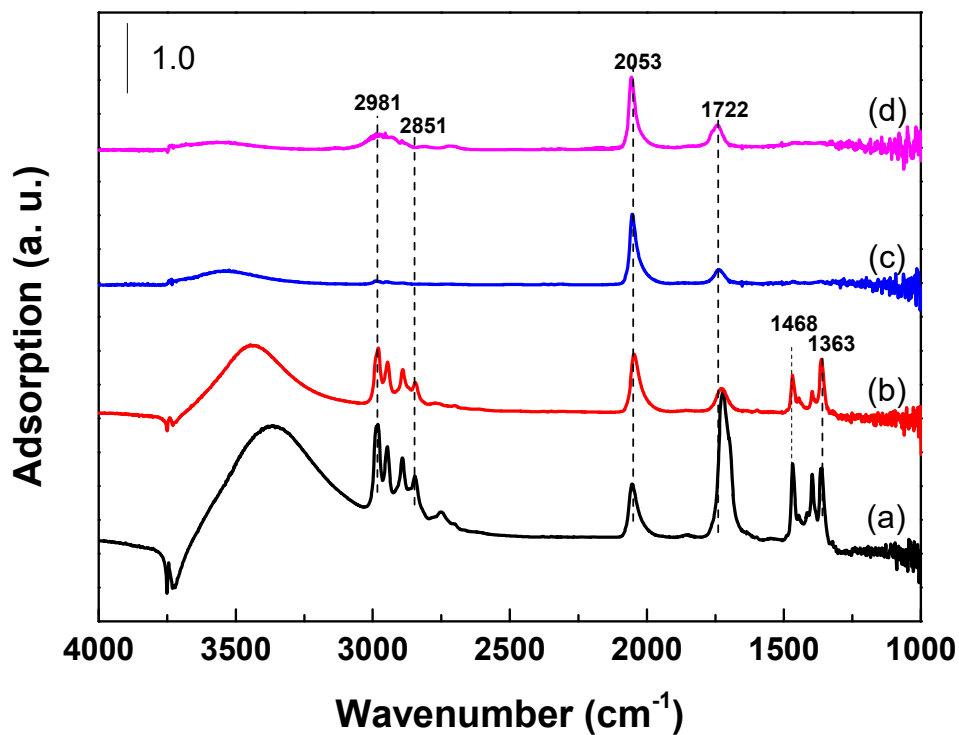
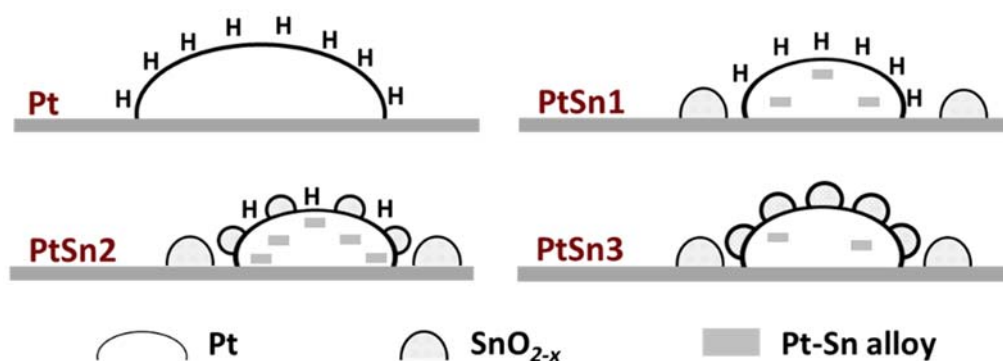


Figure 3.11 FT-IR spectra of propionaldehyde adsorption on Pt/SiO₂ and PtSn₂/SiO₂ catalysts. IR spectra were recorded after evacuating at (a) 50 °C, (b) 100 °C, (c) 200 °C and (d) 300 °C.

3.3.4 Catalyst Structure-Performance Relationship

According to the characterization results of pyridine-FTIR and XPS, it is obvious that Lewis acidity increased after tin addition due to the presence of partially reduced tin oxides. In addition, Pt-Sn alloy phase was found in some of the PtSn catalysts from the HRTEM observation. Based on the results of characterization and catalytic test, we proposed a representation of the catalyst structure as shown in **Scheme 3.2**. (i) Before tin addition, the Pt particle is larger, but the dissociated hydrogen is abundant on its surface. (ii) When the tin content is low (*i.e.*, Sn/Pt = 1), Pt particles are more highly dispersed on the support. Most of the Sn on the support is in an oxidation state, while a small amount of Sn is alloyed with Pt. Note that it is difficult to dissociate hydrogen by the Sn species. Therefore, the amount of the dissociated hydrogen decreases with increasing amount of added Sn. (iii) The structure of PtSn₂ catalyst is similar to PtSn₁. As tin content increases, the number of mixed species (*i.e.*, SnO_x-Pt) increase. Additionally, PtSn alloys also form on the surface of Pt particles. Therefore, the number of the adsorption site for oxygenates would largely increase, whereas the amount of dissociated hydrogen would reduce due to the partial coverage of the Pt surface. (iv) After increasing the relative Sn amount to Sn/Pt = 3, there would be a rather complete covering of the Pt particles by tin oxides. Additionally, the amount of Pt-Sn alloy also decreases.



Scheme 3.2 Proposed structure of the Pt and PtSn catalysts.

Table 3.4 Kinetic parameters for hydrotreating of methyl palmitate.

Catalyst	Deoxygenation		TOF _{C=O}		TOF _{C-C}	
	rate ($\mu\text{mol g}_{\text{cat}}^{-1} \text{s}^{-1}$) ^a		(10 s ⁻¹) ^b		(10 s ⁻¹) ^c	
	300 °C	375 °C	300 °C	375 °C	300 °C	375 °C
Pt	1.78	10.80	0.15	1.05	0.64	4.89
PtSn1	0.50	9.83	0.40	0.78	0.03	10.80
PtSn1.5	0.70	10.52	0.72	11.92	0.02	2.79
PtSn2	1.24	13.57	1.91	32.21	0.02	2.56
PtSn2.5	0.28	4.96	1.67	33.15	0.02	2.52
PtSn3	0.27	4.74	0.90	32.95	0.27	1.77

^a Defined as formation rate of the hydrocarbon products. ^{b, c} Calculated with (rate constant of C₁₆ or C₁₅ formation)/(CO adsorption), in which the rate constant is pseudo-first-order). Reaction conditions: $P = 3 \text{ MPa}$, $\text{WHSV} = 5 \text{ h}^{-1}$ and $\text{H}_2/\text{Oil} = 800 \text{ (ml/ml)}$.

The PtSn catalysts gave lower MP conversion than the Pt catalyst except PtSn2 (**Table 3.1**). MP can be transformed into palmitic acid *via* hydrogenolysis and hydrolysis. The Pt catalyst showed the highest CO adsorption capacity (**Table 3.2**). The higher MP conversion on the Pt catalyst could be due to the larger amount of dissociated hydrogen existed on the Pt surface. This behavior accelerates the hydrogenolysis reaction. However, tin addition would reduce the dissociated hydrogen, and thus suppress the hydrolysis reaction. On the other hand, the incorporation of tin enhances the total acidity of the catalyst, as observed from the NH₃-TPD result. In addition, L/B ratio increased with increasing tin loading due to the generation of partially reduced tin oxides, as shown in the FTIR spectra of pyridine. Based on these results, it could be concluded that the number of Lewis acid site increased after tin addition. This fact causes a promotion of the hydrolysis reaction. Although this reaction cannot occur at the entrance of reactor, it can occur after the water formation. Consequently, the addition of tin can enhance the hydrogenolysis reaction and suppress the hydrolysis reaction. The PtSn2 catalyst had the best balance of the hydrogenolysis and hydrolysis, and thus exhibited the highest activity.

Table 3.4 lists the deoxygenation activity, including the total deoxygenation rate, and turnover frequency of C=O bond hydrogenation (TOF_{C=O}) as well as C-C bond hydrogenolysis (TOF_{C=C}) over the Pt, PtSn1, PtSn2 and PtSn3 catalysts. TOF_{C=O} was

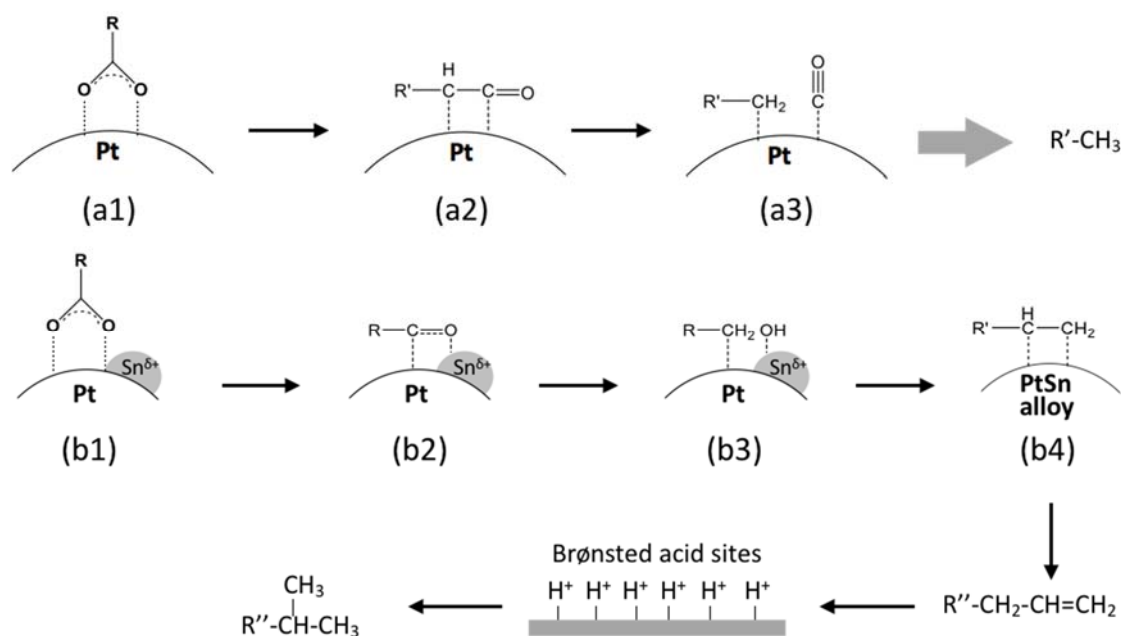
substantially larger than $\text{TOF}_{\text{C-C}}$ for most PtSn catalysts, whereas $\text{TOF}_{\text{C-C}}$ of the Pt catalyst showed a larger value than its $\text{TOF}_{\text{C=O}}$. This result indicates that the C=O bond hydrogenation prevails over the PtSn catalyst, while the C-C bond cleavage is favored over the Pt catalyst. Based on the above results and discussion, we proposed a surface reaction model to explain the deoxygenation of a reaction intermediate, *i.e.*, fatty acid, over Pt and PtSn catalysts (**Scheme 3.3**).

FT-IR of propionic acid adsorption showed that a fatty acid could be adsorbed on the Pt surface through its two oxygen atoms in a chelating bidentate mode (a1). Almost no CO_2 was found in the gaseous product, indicating that decarboxylation reaction is hard to occur. Then hydrogenolysis of one of the oxygen atom in the carboxyl species proceeded to generate an aldehyde. Strong adsorption of the C-C bond on a Pt(111) surface has been reported.^{45, 46} DFT calculations showed that fatty acids, esters or unsaturated aldehydes can be stably adsorbed on Pt(111) by their C-C bonds. Additionally, decarbonylation of aldehydes or alcohols was reported to proceed by the formation of an acetyl intermediate on the metal surface.^{47, 48, 49} In this sense, it is possible that the generated aldehyde was first desorbed from the Pt surface, followed by adsorbing through the C-C bond that adjacent to the carbonyl group (a2). Finally, hydrogenolysis of the C-C bond occurred to generate CO and the hydrocarbon with one carbon number less than the fatty acid (a3).

For the PtSn catalyst, fatty acids are first bound on the Pt surface, similar to the Pt catalyst, in a chelating bidentate mode (b1). The second step could be also the hydrogenolysis of the adsorbed species, giving aldehyde intermediate. Different to the Pt catalyst, the partially reduced tin oxides, which showed Lewis acidity, tend to adsorb the O atom in the carbonyl group as a $[-\text{C}=\text{O}\cdots\text{Sn}^{\delta+}]$ complex because the oxygen is nucleophilic in this bond (b2). A nearby Pt particle provides the dissociated hydrogen, and activates the C=O group to generate a C_{16} alcohol. Finally, the C_{16} alcohol undergoes dehydration to generate a C_{16} hydrocarbon. The remaining -OH group over SnO_{2-x} species is hydrogenated by H_2 to give H_2O . This synergistic effect, involving a hydrogenation metal (*e.g.*, Ni, Pt and Ru) combining with partially reduced metal oxides (*e.g.*, MoO_x , FeO_x , SnO_x and NbO_x) has been recently

demonstrated for the selective hydrogenation of fatty acids, organic acids and unsaturated aldehydes.^{32, 50, 51, 52} On the other hand, there is an exception to the PtSn1 catalyst, on which $\text{TOF}_{\text{C=O}}$ was much lower than $\text{TOF}_{\text{C-C}}$ at a higher reaction temperature (*i.e.*, 375 °C). As mentioned above, this behavior can be attributed to the insufficient amount of tin. The $\text{TOF}_{\text{C-C}}$ of PtSn1 (10.80) is higher than that of Pt (4.89) at 375 °C. The particle size of the PtSn1 catalyst (4.4 nm) is much smaller than that of the Pt catalyst (8.0 nm). Therefore, the higher $\text{TOF}_{\text{C-C}}$ of the PtSn1 catalyst could be due to its higher Pt dispersion.

Theoretical calculations demonstrated that an alloy can change the adsorption energy and adsorption geometry.⁵³ Additionally, several studies showed that the decarbonylation can be suppressed by using an alloy, *e.g.*, PtFe, PdZn or PdIr, which contains a Group 10 metal and a more oxophilic metal.^{32, 54, 55} In this study, Pt-Sn alloys were detected by HRTEM and CO-FTIR characterizations. Therefore, the higher HDO selectivity over PtSn catalysts can be also attributed to the presence of Pt-Sn alloy. Unfortunately, it is difficult to distinguish which effect, the $\text{Sn}^{\delta+}$ or Pt-Sn alloys, would better facilitate the HDO pathway.



Scheme 3.3 Surface reaction model for palmitic acid hydrogenation over the Pt and PtSn catalysts.

On the other hand, the total deoxygenation rate obtained at 300 °C decreased in the order of Pt ($1.78 \mu\text{mol s}^{-1}$) > PtSn2 ($1.24 \mu\text{mol s}^{-1}$) > PtSn1 ($0.50 \mu\text{mol s}^{-1}$) > PtSn3 ($0.27 \mu\text{mol s}^{-1}$). At a higher reaction temperature (375 °C), however, the deoxygenation rate of PtSn2 ($13.6 \mu\text{mol s}^{-1}$) became higher than Pt ($10.8 \mu\text{mol s}^{-1}$). In addition, PtSn1 ($9.8 \mu\text{mol s}^{-1}$) also showed a similar rate to Pt. These results indicate that the activation energy is lowered by tin addition.

Alkane isomerization has been realized by bifunctional catalysis, in which the metal functions as a dehydrogenation–hydrogenation site and the acid support functions as a protonation provider. In addition, the balance of metal function and acid function is also important. An exorbitant ratio of acid/metal function would result in undesired cracking, which occurs simultaneously and competitively with skeleton isomerization. We chose SAPO-11 as the acid function because it has a moderate acidity that favors skeleton isomerization rather than cracking. In the PtSn/SAPO-11 catalyst, Brønsted acid sites on SAPO-11 support can act as the protonation provider, while the Pt-Sn alloy undertakes the dehydrogenation and hydrogenation.

Deoxygenation and isomerization are sequential reactions in MP hydrogenation.¹⁰ Therefore, isomerization selectivity is strongly dependent on deoxygenation activity. Thus, we compared the isomerization activity by using the percentage of isomers in total hydrocarbon products in order to inhibit the influence of the deoxygenation. **Figure 3.12** presents the percentages of normal alkanes (*n*-C_{15,16}) and isomers (*iso*-C_{15,16}) in total hydrocarbon products. PtSn1, PtSn1.5 and PtSn2 exhibited higher isomer percentages than the Pt catalyst. In contrast, PtSn catalysts with higher Sn/Pt ratios, *i.e.*, PtSn2.5 and PtSn3, showed lower activity.

Generally, isomerization can be promoted by increasing the Brønsted acidity. However, the number of Brønsted acid sites in the PtSn catalyst did not increase after tin addition, as can be observed from the pyridine and NH₃ adsorption. Therefore, there should be other reasons for the higher activity of PtSn catalyst. A large number of PtSn alloys can be found in PtSn1 and PtSn2, as characterized by HRTEM. In contrast, only some Sn surface-enriched PtSn particles or SnO₂ surface were observed

in the PtSn3 catalyst. Therefore, it can be reasonably inferred that the Pt-Sn alloy participates the isomerization reaction. In previous studies, the Pt-Sn alloy is known to be one of the most efficient materials for the alkane dehydrogenation.^{56, 57} The high isomerization activity and excellent cracking suppression capacity are likely due to so-called geometric and electronic factors.^{58, 59, 60} In addition, the PtSn catalyst was reported to be more active to produce olefins in the deoxygenation of ester and fatty acid in the absence of hydrogen.^{25, 26} It is known that olefin is more reactive than *n*-alkane in isomerization. As shown in **Scheme 3.3**, the Pt-Sn alloy can improve the isomerization activity by increasing the formation of unsaturated bonds.

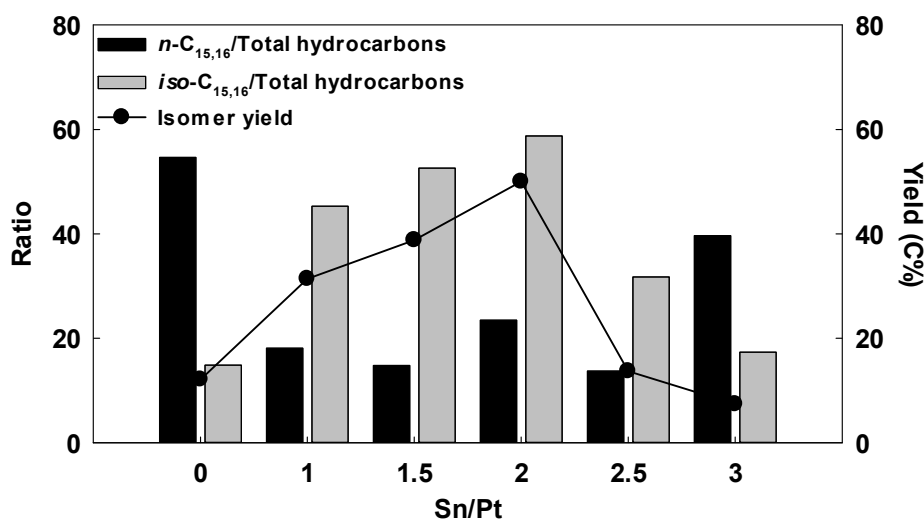


Figure 3.12 Effect of the Sn addition on the isomerization activity of the catalysts. Reaction conditions: $T = 375$ °C, $P = 3$ MPa and $H_2/\text{reactant} = 800$ (ml/ml).

3.4 Conclusions

Bifunctional Pt-based catalysts with SAPO-11 as the support were designed to catalyze the simultaneous deoxygenation-isomerization of TG-related compounds. Among various bimetallic PtX (X = Pd, Re, Cu and Sn) catalysts, the PtSn catalyst showed the highest activity in hydrotreating of methyl stearate. Further investigation of the PtSn catalyst was conducted by changing the Sn/Pt atomic ratio in hydrotreating of methyl palmitate. PtSn/SAPO-11 showed higher isomerization activity and HDO selectivity than the monometallic Pt/SAPO-11 catalyst. Characterization results disclosed that different Sn species, *i.e.*, PtSn alloys and partially reduced tin oxides – SnO_{2-x}, were formed in PtSn catalysts, and it is important to control tin surface density to obtain a well-balanced Pt-SnO_{2-x} function and Pt-Sn alloys. The number of Lewis acid sites increased after tin addition, which could be originated from partially reduced SnO_{2-x} species. These Lewis acid sites could change the adsorption mode and enhance the HDO selectivity. The Sn/Pt ratio should be higher than 1 to give sufficient Lewis acid sites. However, excessive tin addition would block Pt and PtSn phases, leading to a decrease in the deoxygenation activity. Based on the results of *in situ* FT-IR study of the adsorption of propionic acid and propionaldehyde, surface reaction mechanisms for Pt and PtSn catalysts were proposed. Pt-Sn alloys are present in the PtSn1, PtSn1.5 and PtSn2 catalysts, while only some Sn surface-enriched PtSn particles and SnO₂ were observed in the PtSn2.5 and PtSn3 catalysts. The higher isomerization activity of PtSn1, PtSn1.5 and PtSn2 is related to the presence of Pt-Sn alloys, which could enhance the formation of unsaturated hydrocarbons and improve further isomerization.

References

1. M. Besson; P. Gallezot; C. Pinel, Conversion of Biomass into Chemicals over Metal Catalysts, *Chem. Rev.*, **2014**, *114* (3), 1827-1870.
2. M. J. Climent; A. Corma; S. Iborra, Conversion of biomass platform molecules into fuel additives and liquid hydrocarbon fuels, *Green Chem.*, **2014**, *16* (2), 516.
3. I. Kubičková; D. Kubička, Utilization of Triglycerides and Related Feedstocks for Production of Clean Hydrocarbon Fuels and Petrochemicals: A Review, *Waste Biomass Valor.*, **2010**, *1* (3), 293-308.
4. V. M. Akhmedov; S. H. Al - Khowaiter, Recent Advances and Future Aspects in the Selective Isomerization of High n - Alkanes, *Catal. Rev. Sci. Eng.*, **2007**, *49* (1), 33-139.
5. D. Kubička; L. Kaluža, Deoxygenation of vegetable oils over sulfided Ni, Mo and NiMo catalysts, *Appl. Catal., A*, **2010**, *372* (2), 199-208.
6. D. Kubička; P. Šimáček; N. Žilková, Transformation of Vegetable Oils into Hydrocarbons over Mesoporous-Alumina-Supported CoMo Catalysts, *Top. Catal.*, **2008**, *52* (1-2), 161-168.
7. S. Gong; A. Shinozaki; M. Shi; E. W. Qian, Hydrotreating of Jatropha Oil over Alumina Based Catalysts, *Energy Fuels*, **2012**, *26* (4), 2394-2399.
8. S. Gong; A. Shinozaki; E. W. Qian, Role of Support in Hydrotreatment of Jatropha Oil over Sulfided NiMo Catalysts, *Ind. Eng. Chem. Res.*, **2012**, *51* (43), 13953-13960.
9. D. Kubička; J. Horáček, Deactivation of HDS catalysts in deoxygenation of vegetable oils, *Appl. Catal., A*, **2011**, *394* (1-2), 9-17.
10. E. W. Qian; N. Chen; S. Gong, Role of support in deoxygenation and isomerization of methyl stearate over nickel–molybdenum catalysts, *J. Mol. Catal. A*, **2014**, *387*, 76-85.
11. B. Peng; X. Yuan; C. Zhao; J. A. Lercher, Stabilizing Catalytic Pathways via Redundancy: Selective Reduction of Microalgae Oil to Alkanes, *J. Am. Chem. Soc.*, **2012**, *134* (22), 9400-9405.
12. W. Song; C. Zhao; J. A. Lercher, Importance of size and distribution of Ni nanoparticles for the hydrodeoxygenation of microalgae oil, *Chemistry*, **2013**, *19* (30), 9833-42.
13. B. Peng; Y. Yao; C. Zhao; J. A. Lercher, Towards quantitative conversion of microalgae oil to diesel-range alkanes with bifunctional catalysts, *Angew. Chem. Int. Ed. Engl.*, **2012**, *51* (9), 2072-5.
14. N. Chen; S. Gong; E. W. Qian, Effect of reduction temperature of NiMoO_{3-x}/SAPO-11 on its catalytic activity in hydrodeoxygenation of methyl laurate, *Appl. Catal., B*, **2015**, *174-175*, 253-263.
15. K. Kon; W. Onodera; S. Takakusagi; K.-i. Shimizu, Hydrodeoxygenation of fatty acids and triglycerides by Pt-loaded Nb₂O₅ catalysts, *Catal. Sci. Technol.*, **2014**, *4* (10), 3705-3712.
16. H. Deldari, Suitable catalysts for hydroisomerization of long-chain normal paraffins, *Appl. Catal., A*, **2005**, *293*, 1-10.

17. O. V. Kikhtyanin; A. E. Rubanov; A. B. Ayupov; G. V. Echevsky, Hydroconversion of sunflower oil on Pd/SAPO-31 catalyst, *Fuel*, **2010**, *89* (10), 3085-3092.
18. Q. Liu; H. Zuo; T. Wang; L. Ma; Q. Zhang, One-step hydrodeoxygenation of palm oil to isomerized hydrocarbon fuels over Ni supported on nano-sized SAPO-11 catalysts, *Appl. Catal., A*, **2013**, *468*, 68-74.
19. C. Wang; Z. Tian; L. Wang; R. Xu; Q. Liu; W. Qu; H. Ma; B. Wang, One-step hydrotreatment of vegetable oil to produce high quality diesel-range alkanes, *ChemSusChem*, **2012**, *5* (10), 1974-83.
20. N. Chen; S. Gong; H. Shirai; T. Watanabe; E. W. Qian, Effects of Si/Al ratio and Pt loading on Pt/SAPO-11 catalysts in hydroconversion of Jatropha oil, *Appl. Catal., A*, **2013**, *466*, 105-115.
21. S. Gong; N. Chen; S. Nakayama; E. W. Qian, Isomerization of n-alkanes derived from jatropha oil over bifunctional catalysts, *J. Mol. Catal. A*, **2013**, *370*, 14-21.
22. M. Sankar; N. Dimitratos; P. J. Miedziak; P. P. Wells; C. J. Kiely; G. J. Hutchings, Designing bimetallic catalysts for a green and sustainable future, *Chem. Soc. Rev.*, **2012**, *41* (24), 8099-8139.
23. K. Murata; Y. Liu; M. Inaba; I. Takahara, Production of Synthetic Diesel by Hydrotreatment of Jatropha Oils Using Pt–Re/H-ZSM-5 Catalyst, *Energy Fuels*, **2010**, *24* (4), 2404-2409.
24. K. Murata; Y. Liu; M. M. Watanabe; M. Inaba; I. Takahara, Hydrocracking of Algae Oil into Aviation Fuel-Range Hydrocarbons Using a Pt–Re Catalyst, *Energy Fuels*, **2014**, *28* (11), 6999-7006.
25. M. Chiappero; P. T. M. Do; S. Crossley; L. L. Lobban; D. E. Resasco, Direct conversion of triglycerides to olefins and paraffins over noble metal supported catalysts, *Fuel*, **2011**, *90* (3), 1155-1165.
26. T. M. Yeh; R. L. Hockstad; S. Linic; P. E. Savage, Hydrothermal decarboxylation of unsaturated fatty acids over PtSn_x/C catalysts, *Fuel*, **2015**, *156*, 219-224.
27. D. Kubička; J. Horáček; M. Setnička; R. Bulánek; A. Zukal; I. Kubičková, Effect of support-active phase interactions on the catalyst activity and selectivity in deoxygenation of triglycerides, *Appl. Catal., B*, **2014**, *145*, 101-107.
28. G. S. Lane; J. T. Miller; F. S. Modica; M. K. Barr, Infrared Spectroscopy of Adsorbed Carbon Monoxide on Platinum/Nonacidic Zeolite Catalysts, *J. Catal.*, **1993**, *141* (2), 465-477.
29. P. Concepcion; Y. Perez; J. C. Hernandez-Garrido; M. Fajardo; J. J. Calvino; A. Corma, The promotional effect of Sn-beta zeolites on platinum for the selective hydrogenation of α,β -unsaturated aldehydes-unsaturated aldehydes, *Phys. Chem. Chem. Phys.*, **2013**, *15* (29), 12048-12055.
30. J. Ruiz-Martínez; A. Sepúlveda-Escribano; J. A. Anderson; F. Rodríguez-Reinoso, Influence of the preparation method on the catalytic behaviour of PtSn/TiO₂ catalysts, *Catal. Today*, **2007**, *123* (1–4), 235-244.
31. T. Barzetti; E. Selli; D. Moscotti; L. Forni, Pyridine and ammonia as probes for FTIR analysis of solid acid catalysts, *J. Chem. Soc., Faraday Trans.*, **1996**, *92* (8), 1401-1407.

32. J. P. Stassi; P. D. Zgolicz; S. R. de Miguel; O. A. Scelza, Formation of different promoted metallic phases in PtFe and PtSn catalysts supported on carbonaceous materials used for selective hydrogenation, *J. Catal.*, **2013**, *306* (0), 11-29.
33. K. Balakrishnan; J. Schwank, A chemisorption and XPS study of bimetallic Pt-Sn/Al₂O₃ catalysts, *J. Catal.*, **1991**, *127* (1), 287-306.
34. T. Ekou; A. Vicente; G. Lafaye; C. Especel; P. Marecot, Bimetallic Rh-Ge and Pt-Ge catalysts supported on TiO₂ for citral hydrogenation: II. Catalytic properties, *Appl. Catal., A*, **2006**, *314* (1), 73-80.
35. M. Yamada; J. Yasumaru; M. Houalla; D. M. Hercules, Distribution of molybdenum oxidation states in reduced molybdenum/alumina catalysts: correlation with benzene hydrogenation activity, *J. Phys. Chem.*, **1991**, *95* (18), 7037-7042.
36. L. Zhang; A. M. Karim; M. H. Engelhard; Z. Wei; D. L. King; Y. Wang, Correlation of Pt-Re surface properties with reaction pathways for the aqueous-phase reforming of glycerol, *J. Catal.*, **2012**, *287* (0), 37-43.
37. V. Ponec; W. M. H. Sachtler, The reactions between cyclopentane and deuterium on nickel and nickel-copper alloys, *J. Catal.*, **1972**, *24* (2), 250-261.
38. Y. Wang; Z. Tao; B. Wu; J. Xu; C. Huo; K. Li; H. Chen; Y. Yang; Y. Li, Effect of metal precursors on the performance of Pt/ZSM-22 catalysts for n-hexadecane hydroisomerization, *J. Catal.*, **2015**, *322*, 1-13.
39. P. Durussel; R. Massara; P. Feschotte, Le système binaire Pt-Sn, *J. Alloys Compd.*, **1994**, *215* (1-2), 175-179.
40. H. Zhu; D. H. Anjum; Q. Wang; E. Abou-Hamad; L. Emsley; H. Dong; P. Laveille; L. Li; A. K. Samal; J.-M. Basset, Sn surface-enriched Pt-Sn bimetallic nanoparticles as a selective and stable catalyst for propane dehydrogenation, *J. Catal.*, **2014**, *320*, 52-62.
41. V. Galvita; G. Siddiqi; P. Sun; A. T. Bell, Ethane dehydrogenation on Pt/Mg(Al)O and PtSn/Mg(Al)O catalysts, *J. Catal.*, **2010**, *271* (2), 209-219.
42. Z.-Z. Jiang; Z.-B. Wang; Y.-Y. Chu; D.-M. Gu; G.-P. Yin, Ultrahigh stable carbon riveted Pt/TiO₂-C catalyst prepared by in situ carbonized glucose for proton exchange membrane fuel cell, *Energy Environ. Sci.*, **2011**, *4* (3), 728-735.
43. J. Shi; M. Zhang; W. Du; W. Ning; Z. Hou, SnO₂-isolated Pt₃Sn alloy on reduced graphene oxides: an efficient catalyst for selective hydrogenation of C=O in unsaturated aldehydes, *Catal. Sci. Technol.*, **2015**.
44. H. Zhu; D. H. Anjum; Q. Wang; E. Abou-Hamad; L. Emsley; H. Dong; P. Laveille; L. Li; A. K. Samal; J.-M. Basset, Sn surface-enriched Pt-Sn bimetallic nanoparticles as a selective and stable catalyst for propane dehydrogenation, *J. Catal.*, **2014**, *320* (0), 52-62.
45. M. Saliccioli; S. M. Edie; D. G. Vlachos, Adsorption of Acid, Ester, and Ether Functional Groups on Pt: Fast Prediction of Thermochemical Properties of Adsorbed Oxygenates via DFT-Based Group Additivity Methods, *J. Phys. Chem. C*, **2012**, *116* (2), 1873-1886.
46. F. Delbecq; P. Sautet, Influence of Sn additives on the selectivity of hydrogenation of α - β -unsaturated aldehydes with Pt catalysts: a density functional study of molecular adsorption, *J. Catal.*, **2003**, *220* (1), 115-126.

47. M. Mavrikakis; M. A. Barteau, Oxygenate reaction pathways on transition metal surfaces, *J. Mol. Catal. A: Chem.*, **1998**, *131* (1–3), 135-147.
48. J. L. Davis; M. A. Barteau, Polymerization and decarbonylation reactions of aldehydes on the Pd(111) surface, *J. Am. Chem. Soc.*, **1989**, *111* (5), 1782-1792.
49. R. Shekhar; M. A. Barteau; R. V. Plank; J. M. Vohs, Adsorption and Reaction of Aldehydes on Pd Surfaces, *J. Phys. Chem. B*, **1997**, *101* (40), 7939-7951.
50. K. Kon; W. Onodera; S. Takakusagi; K.-i. Shimizu, Hydrodeoxygenation of fatty acids and triglycerides by Pt-loaded Nb₂O₅ catalysts, *Catal. Sci. Technol.*, **2014**, *4* (10), 3705-3712.
51. K.-i. Shimizu; S. Kanno; K. Kon, Hydrogenation of levulinic acid to γ -valerolactone by Ni and MoO_x co-loaded carbon catalysts, *Green Chem.*, **2014**, *16* (8), 3899.
52. L. Chen; Y. Zhu; H. Zheng; C. Zhang; Y. Li, Aqueous-phase hydrodeoxygenation of propanoic acid over the Ru/ZrO₂ and Ru–Mo/ZrO₂ catalysts, *Appl. Catal., A*, **2012**, *411–412* (0), 95-104.
53. D. Tas; R. F. Parton; K. Vercruyse; P. A. Jacobs, Regio selectivity in the hydrogenation of geraniol over platinum containing zeolites. In *Stud. Surf. Sci. Catal.*, Hakze Chon, S.-K. I.; Young Sun, U., Eds. Elsevier: **1997**; Vol. Volume 105, pp 1261-1268.
54. T. H. Parsell; B. C. Owen; I. Klein; T. M. Jarrell; C. L. Marcum; L. J. Hauptert; L. M. Amundson; H. I. Kenttamaa; F. Ribeiro; J. T. Miller; M. M. Abu-Omar, Cleavage and hydrodeoxygenation (HDO) of C-O bonds relevant to lignin conversion using Pd/Zn synergistic catalysis, *Chemical Science*, **2013**, *4* (2), 806-813.
55. Y. Nakagawa; K. Takada; M. Tamura; K. Tomishige, Total Hydrogenation of Furfural and 5-Hydroxymethylfurfural over Supported Pd–Ir Alloy Catalyst, *ACS Catal.*, **2014**, *4* (8), 2718-2726.
56. L. Bednarova; C. E. Lyman; E. Rytter; A. Holmen, Effect of Support on the Size and Composition of Highly Dispersed Pt–Sn Particles, *J. Catal.*, **2002**, *211* (2), 335-346.
57. L. Nykänen; K. Honkala, Density Functional Theory Study on Propane and Propene Adsorption on Pt(111) and PtSn Alloy Surfaces, *J. Phys. Chem. C*, **2011**, *115* (19), 9578-9586.
58. M.-L. Yang; Y.-A. Zhu; X.-G. Zhou; Z.-J. Sui; D. Chen, First-Principles Calculations of Propane Dehydrogenation over PtSn Catalysts, *ACS Catal.*, **2012**, *2* (6), 1247-1258.
59. R. D. Cortright; J. A. Dumesic, Microcalorimetric, Spectroscopic, and Kinetic Studies of Silica Supported Pt and Pt/Sn Catalysts for Isobutane Dehydrogenation, *J. Catal.*, **1994**, *148* (2), 771-778.
60. R. Burch; L. C. Garla, Platinum-tin reforming catalysts: II. Activity and selectivity in hydrocarbon reactions, *J. Catal.*, **1981**, *71* (2), 360-372.

Chapter 4

Selective Formation of Mono-Branched Isomers in Hydrotreating of Methyl Palmitate Using Bifunctional Catalysts Supported on Core-shell Structural Zeolite

Abstract

To obtain high quality diesel fuels with high combustion properties from hydrotreating of vegetable oils, inhibiting the formation of multi-branched isomers (MuBI) is highly desirable. In this chapter, a core@shell structural ZSM-22@SiO₂ zeolite was designed to passivate the external acid site and promote the formation of mono-branched isomers (MoBI), which have much higher cetane number than MuBI (>85 vs <60). A series of ZSM-22@SiO₂ zeolites with different amounts of shell silica were synthesized through a facile crystal growth method. The external acid site could be covered by using the proposed method. The synthesized zeolites were used as the support for bifunctional Pt catalysts in hydrodeoxygenation of a model compound – methyl palmitate. The MoBI percentage in total isomers reached to 95% at 300 °C in the case of Pt/Z-120@20Si, Pt/Z-120@50Si and Pt/Z-120@100Si, which showed superior performance than the uncoated catalyst (71%). However, deoxygenation activity and isomerization selectivity decreased with increasing amount of shell silica. Fourier transform infrared spectroscopy of CO adsorption (CO-FTIR) combining with transmission electron microscope (TEM) demonstrated that Pt particles favored the formation of Pt(100) rather than Pt(111) in silica-coated catalysts, which could be the most likely reason for the decrease of the deoxygenation activity. Catalytic performance could be enhanced by reducing the SiO₂/Al₂O₃ ratio of core ZSM-22 or by using PtSn as the active metal site. A novel catalyst, PtSn/Z-60@20Si (Pt = 0.3 wt%, Sn/Pt = 2, SiO₂/Al₂O₃ = 60, silica coating amount = 20%), gave an *iso*-C_{15,16} yield of 53% with MoBI percentage of 83% under the condition of T = 350 °C and WHSV = 5 h⁻¹.

4.1 Introduction

Due to environmental concerns and petroleum exhaustion, refinement of renewable bioresources has become a promising way to produce transportation fuels.¹ Triglycerides have been considered as an important renewable feedstock for the production of middle-distillate fuels because of the suitable carbon numbers in their fatty acid side chains (*i.e.*, C₁₆ and C₁₈ fatty acids).^{2, 3, 4} Hydrodeoxygenation is an efficient approach for upgrading triglycerides into transportation fuels, which can remove oxygen-containing functional groups and produce green hydrocarbons identical to diesel fuel. Supported metal catalysts such as NiMoS/Al₂O₃,^{5, 6} Pt/C,⁷ Pd/Nb₂O₅/SiO₂⁸ and Ni/ZrO₂⁹ possess high deoxygenation activity. However, these catalysts are inclined to produce normal alkanes (*n*-alkanes), which have melting points higher than 20 °C, leading to poor cold-flow properties that limit their use for the so-called “ready-to-use” fuels.

Hydroisomerization of *n*-alkanes into isomerized alkanes (*iso*-alkanes) is an efficient approach to reduce the melting point and improve their cold flow properties.^{10, 11} A two-steps hydrotreating process, *i.e.*, deoxygenation of triglycerides and isomerization of the obtained *n*-alkanes being conducted separately, has been commercialized by Neste Oil. Several studies used acid supports, *e.g.*, complex metal oxides,^{12, 13} zeolites,^{14, 15} and Al doped mesoporous materials,^{16, 17} to improve the isomerization activity of a catalyst. Taking into account of the cost and process efficiency, however, combining deoxygenation and isomerization into single-step is highly desirable. Recently, many studies focused on simultaneous deoxygenation-isomerization of triglycerides or related model compounds by using a metal-acid bifunctional catalyst. Pt, Pd or Ni was used as a metal site while the zeolite such as SAPO-11 or ZSM-22 was used as an acid site. Although supported Ni catalysts showed higher activity in deoxygenation, severe cracking was found over Ni-based catalysts.^{18, 19} In contrast, Pt/zeolite catalysts exhibited higher potential in the simultaneous reaction. Conversion of vegetable oils into *iso*-alkanes was reported with the yield of 60–80% by using Pt/SAPO-11, Pt/SAPO-31 or Pt/ZSM-22.^{20, 21, 22, 23}

Apart from cold flow properties, combustion property is another important factor for transportation fuels. Branched alkanes can be divided into two categories, *i.e.*, mono-branched isomers (MoBI) and multi-branched isomers (MuBI). Although MuBI have relatively lower melting points, their exceptionally low cetane number would reduce the ignition quality of fuels.²⁴ It has been reported that a zeolite with 1-dimensional 10-membered ring channels, *e.g.*, ZSM-22 (TON)²⁵ and SAPO-11 (AEL)²⁶ can achieve high selectivity to MoBI due to their shape-selectivity.²⁷ Nevertheless, MuBI can be also generated by acid sites on the external surface of the zeolite. In addition, the formation rate of MuBI usually increases with increasing reaction temperature.^{28, 29} Unfortunately, simultaneous deoxygenation-isomerization of vegetable oils need to be conducted at higher temperature (300-375 °C) compared to isomerization of *n*-alkanes (200-260 °C). As a result, the formation of MuBI would become much higher even though those zeolites (*i.e.*, SAPO-11 and ZSM-22) were used as supports. Therefore, it is of importance to design a new catalyst to passivate the external acid site, and thus inhibiting the formation of MuBI.

Composite materials with a core@shell structure have recently attracted extensive research attention in many areas, especially catalysis.³⁰ Passivating the external acid site by coating an inactive shell is an attractive and efficient approach to enhance the shape-selectivity of a zeolite. MFI-type zeolite has been widely used in the catalysis of disproportionation of toluene and methylation of toluene with methanol to yield *para*-xylene. The silica coating of the parent zeolite can substantially improve the shape-selectivity of zeolite, resulting in a high *para*-xylene selectivity.^{31, 32} On the other hand, Okamoto synthesized a TON-type zeolite with core@shell structure using fluoride ion as a mineralizing agent, and used the material for tetradecane isomerization.³³ Cracking reaction could be substantially inhibited and the isomerization selectivity increased by approximately 20%.

In this chapter, a bifunctional catalyst composed of Pt nanoparticles supported on a silica-coated TON-type zeolite, *i.e.*, Pt/ZSM-22@SiO₂, was designed for the simultaneous deoxygenation-isomerization of methyl palmitate. First, a series of ZSM-22@SiO₂ zeolites with different amounts of shell silica were synthesized and used as

supports for Pt catalysts in hydrotreating of methyl palmitate. The effect of acidity, including total acidity and external acidity, on deoxygenation activity of the catalyst was discussed. Then, two methods, *i.e.*, changing Si/Al ratio of the core ZSM-22 and adding Sn as a promoter, were applied to improve the activity and isomerization selectivity of the silica-coated catalyst.

4.2 Experimental Section

4.2.1 Materials

All chemicals were obtained from commercial suppliers and used as received: Ludox® HS-40 colloidal silica (Sigma-Aldrich, containing 40% silica), $\text{Al}_2(\text{SO}_4)_3 \cdot 18\text{H}_2\text{O}$ (Wako Pure Chemical Industries, 51.0-57.5% $\text{Al}_2(\text{SO}_4)_3$ basis), 1,6-diaminohexane (Tokyo Chemical Industry Co., $\geq 99.0\%$ GC assay), ethanol (Wako Pure Chemical Industries, $\geq 99.5\%$), KOH (Wako Pure Chemical Industries, $\geq 85\%$), HNO_3 (Wako Pure Chemical Industries, 60~61%), NH_4NO_3 (Wako Pure Chemical Industries, $\geq 98.0\%$), $\text{H}_2\text{PtCl}_6 \cdot 6\text{H}_2\text{O}$ (Sigma-Aldrich, $\geq 98.5\%$) and methyl palmitate (Sigma-Aldrich, $\geq 97\%$ GC assay). Distilled water was used in all cases.

4.2.2 Synthesis of ZSM-22 and ZSM-22@SiO₂

ZSM-22 zeolite was synthesized by a hydrothermal method.²⁹ A typical synthesis procedure is described as follows: KOH and $\text{Al}_2(\text{SO}_4)_3 \cdot 18\text{H}_2\text{O}$ were dissolved in water and stirred to generate a clear solution. Afterward, 1,6-diaminohexane (DAH) and colloidal silica were added. The solution was stirred for 1 h at room temperature, followed by heating in an autoclave at 150 °C for 60 h with stirring at 500 rpm. The precursor suspension had a mole composition of Si : Al : K₂O : DAH : H₂O = 60 : 1 : 17.5 : 35 : 8360. The as-synthesized KZSM-22 was washed and filtered before being dried at 120 °C for 6 h and calcined at 550 °C for 12 h in air.

The KZSM-22 was converted into NH₄-form by ion exchange using a 0.5 M NH_4NO_3 aqueous solution (50 ml solution per gram zeolite). The reflux procedure was conducted at 70 °C for 3 h, which was repeated for 3 times in order to achieve a high exchange degree. Afterward, the sample was filtered, dried and converted into H-form by calcining at 450 °C for 10 h in air.

Silica coating for ZSM-22 was performed by crystal overgrowth to obtain a core-shell structure.³⁴ In a typical synthesis, water, colloidal silica, ethanol and 1,6-diaminohexane were mixed and stirred for 1 h at room temperature. Afterward, the H-

form ZSM-22 sample was added into the precursor suspension and stirred for another 1 h. The resulting mixture had a mole composition of Si (shell) : Si' (core) : Ethanol : DAH : H₂O = 1 : x : 4 : 0.3 : 70 ($x = 1, 2, 5$ and 10). In all cases, a small amount of nitric acid was added to keep the synthesis solution in a close-to-neutral state. The mixture was heated in an autoclave at 150 °C for 60 h with stirring at 500 rpm. Afterward, solid products were recovered by filtration, washed with water, dried at 120 °C for 6 h and calcined at 550 °C for 12 h in air. The obtained sample was denoted as Z- y @ z Si, where y and z refer to the bulk SiO₂/Al₂O₃ ratio and the percentage of shell silica.

4.2.3 Catalyst Preparation

Platinum catalysts were prepared by an incipient wetness impregnation method. The synthesized zeolite sample was compressed into solid disks under a pressure of 60 MPa, which were subsequently grounded into 425-850 μ m particles. An aqueous solution of H₂PtCl₆·6H₂O was prepared was added into the particle. The loading amount of Pt of 0.6 wt%. After the impregnation, the catalyst was dried at 120 °C for 2 h and calcined at 450 °C for 10 h. The method of preparing NiMo and PtSn catalysts were similar to previous chapters.

4.2.4 Catalyst Characterization

Nitrogen physisorption was performed at -196 °C with an automated gas sorption system – Belsorp-mini II. Prior to measurement, the sample was degassed under vacuum at 350 °C for 2 h. Micropore surface area, pore volume, pore diameter and external surface area were determined by the t -plot method.

X-ray powder diffraction (XRD) patterns were measured on an X-ray diffractometer (RAD-IIC; Rigaku Corp.) with Cu-K α radiation (40 kV and 30 mA). Diffraction data were collected by a continuous scan mode at a scanning speed of 1° (2 theta) min⁻¹.

SEM images were recorded on a JSM-6500 (JEOL) microscope operated at an accelerating voltage of 13 kV. The sample was dispersed in ethanol, followed by depositing the suspension solution on the sample holder. EDS analysis was performed on a TM3000 (Hitachi) microscope equipped with a Quantax70 (Bruker nano GmbH) detector. The sample was fixed to the sample holder with conductive adhesive carbon tape.

Transmission Electron Microscope (TEM) images were recorded on a JEM-2200FS (JEOL) transmission microscope operated at 200 kV. The sample powders were pre-reduced *ex situ* in H₂ flow at 400 °C for 3 h, and deposited on a copper grid. Statistical analysis of particle size was performed by measuring approximately 150 particles per sample.

Temperature programmed desorption of ammonia (NH₃-TPD) measurement was performed on a ChemBET Pulsar TPR/TPD instrument (Quantachrome Instruments).²⁰ The sample was purged by heating to 550 °C with He for 2 h, followed by cooling to 50 °C. Afterward, NH₃ was introduced, and the adsorption experiment was performed for 40 min. Physically adsorbed NH₃ was removed by flushing with He at 100 °C for 2 h. The TPD measurement was performed by linearly increasing the cell temperature from 100 to 800 °C at a heating rate of 10 °C min⁻¹ under a 15 mL min⁻¹ He flow. The amount of desorbed ammonia was monitored using a thermal conductivity detector (TCD) and quantified by pulse calibration.

Fourier transform infrared spectroscopy (FT-IR) of pyridine adsorption were recorded on an IRPrestige-21 instrument (Shimadzu) by adding 64 scans for the sample at a resolution of 4 cm⁻¹.³⁵ The sample powders were pressed into self-supporting wafers ($d = 10$ mm). Before adsorption, the sample was degassed under evacuation (pressure < 10⁻⁵ Torr) at 500 °C for 3 h. The pyridine adsorption was carried out under 4 Torr pyridine pressure for 30 min at 100 °C. Prior to recording the IR spectra, the sample was evacuated at 150 °C for 20 min. The procedure for 2,6-lutidine adsorption was similar to the pyridine adsorption.

The FT-IR study of CO adsorption was performed on the same instrument with the pyridine adsorption. The sample was purged with H₂ flow (30 mL/min) for 0.5 h,

followed by raising the cell temperature to 400 °C and kept for 3 h. After reduction, the sample was degassed under evacuation at the same temperature for 1 h. The CO adsorption (50 Torr) was performed at 25 °C for 0.5 h, followed by evacuation at the same temperature for 20 min.

4.2.5 Activity Test

Hydrotreating of methyl palmitate (MP) was performed in a stainless steel fixed-bed continuous-flow reactor (i.d. 8 mm, length 40 mm) operated in the down-flow mode.³⁶ In a typical experiment, the catalyst diluted with quartz was charged into the reactor and prerduced *in situ* with a flow of pure H₂ (100 cm³/min) at 400 °C for 3 h. The reaction was conducted under 3 MPa hydrogen pressure, with a weight hourly space velocity (WHSV) of 5–40 h⁻¹, a H₂/Feedstock ratio of 800 (ml/ml), and at a temperature range of 300–360 °C. The effect of external mass transfer resistance in the catalyst bed was negligible under the given condition because a further increase of the space velocity had no impact on the reaction rate. After achieving a steady state (TOS = 5 h), the liquid product was analyzed by a gas chromatograph (GC-2025, Shimadzu) equipped with a flame ionization detector (FID) and a DB-5HT capillary column (Agilent Technology, 30 m × 0.25 mm). The product identification was performed using a gas chromatograph equipped with a mass spectrometer (GCMS-QP5050A, Shimadzu) and the same DB-5HT capillary column. The gaseous product was analyzed by another two gas chromatographs (TCD and FID).

Internal standard (*i.e.*, decane) was used for quantification. Conversion and selectivity were determined by equations (1) and (2).

$$\text{Conversion (\%)} = \frac{\sum m_i}{(\sum m_i + m_r)} \times 100 \quad (1)$$

$$\text{Selectivity (\%)} = \frac{m_i}{\sum m_i} \times 100 \quad (2)$$

where m_i is the molar percentage of the product i , m_r is the molar percentage of the reactant.

Reaction rate constant was calculated assuming a first-order reaction with plug-flow reactor model. Pseudo-first order rate constant, called k (h^{-1}), was calculated using the following equation (3).

$$k = F / W \times \ln [100 / (100 - X)] \quad (3)$$

where X is the molar percentage of deoxygenated products (mol%), F is the molar flow of products (mol h^{-1}) and W is the weight of catalyst (g).

4.3 Results and Discussion

4.3.1 Characterization of ZSM-22 and ZSM-22@SiO₂

Figure 4.1 shows XRD patterns of ZSM-22 and ZSM-22@SiO₂ with different amounts of shell silica. All the samples presented diffraction peaks at $2\theta = 8.1, 10.1, 12.8, 16.5, 19.4, 20.3, 20.4, 24.1, 24.2, 25.7, 35.6, 36.9$ and 38.0° , attributed to the typical ZSM-22 phase with TON structure. These diffraction peaks exhibit high intensity and low background, indicating that the silica coating process could not destroy the crystal structure of the zeolite and no considerable amorphous phase was generated after silica coating. Compared to the parent ZSM-22, *i.e.*, Z-120@0Si, the intensity of the diffraction peak at $2\theta = 8.1^\circ$, which is attributed to (100) plane of the zeolite structure, had a slightly increase for Z-120@20Si, Z-120@50Si and Z-120@100Si. This result indicates that the shell silica is not amorphous and has the same TON-type crystal.

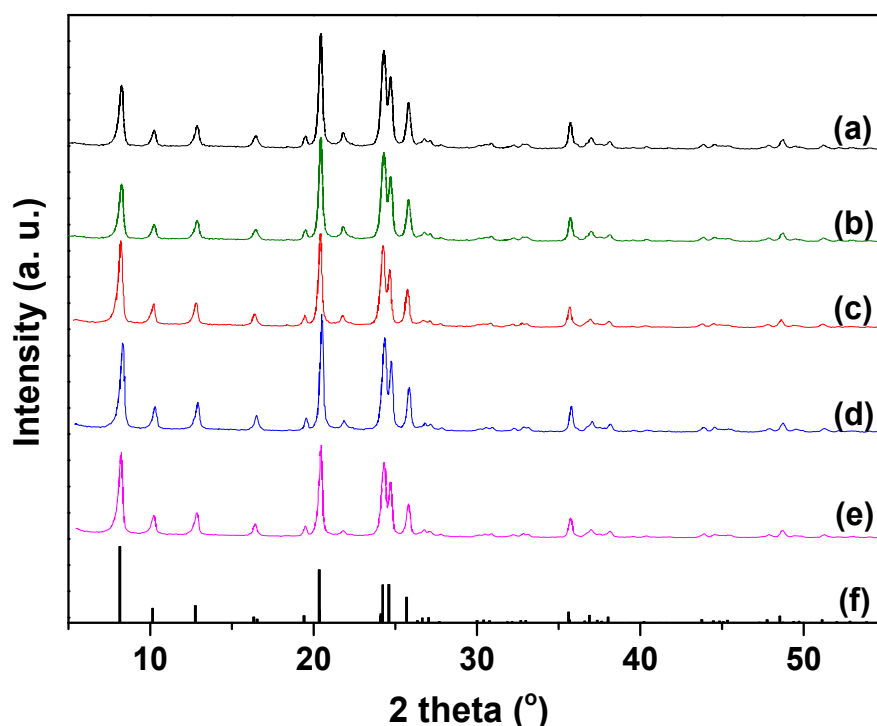


Figure 4.1 XRD patterns of ZSM-22 and ZSM-22@SiO₂ samples: (a) Z-120@0Si, (b) Z-120@10Si, (c) Z-120@20Si, (d) Z-120@50Si, (e) Z-120@100Si and (f) typical TON-type zeolite.

Nitrogen adsorption-desorption isotherms are shown in **Figure 4.2**. All the samples displayed steep uptakes in a low-pressure region ($p/p_0 < 0.1$), indicating a microporous structure of the material. The parent ZSM-22 showed a larger nitrogen adsorption in a high-pressure region, *i.e.*, $p/p_0 > 0.9$, which can be attributed to the macropore adsorption. This behavior could be due to some holes generated by the aggregation of primary particles, but these holes could be eliminated by redispersion of crystals during the silica coating process. Textural parameters derived from the nitrogen physisorption are listed in **Table 4.1**. The micropore surface area and pore volume gradually decreased with increasing amount of shell silica. The external surface area also had a slight decrease after silica coating due to some coverage of the crystal surface. In contrast, the micropore diameter had no considerable change and maintained at 0.57 nm.

Bulk $\text{SiO}_2/\text{Al}_2\text{O}_3$ ratio of synthesized zeolites were determined by EDS analysis. Modified samples showed lower experimental values than their target values, indicating that a portion of colloidal silica in the synthesis solution was not coated on the parent zeolite.

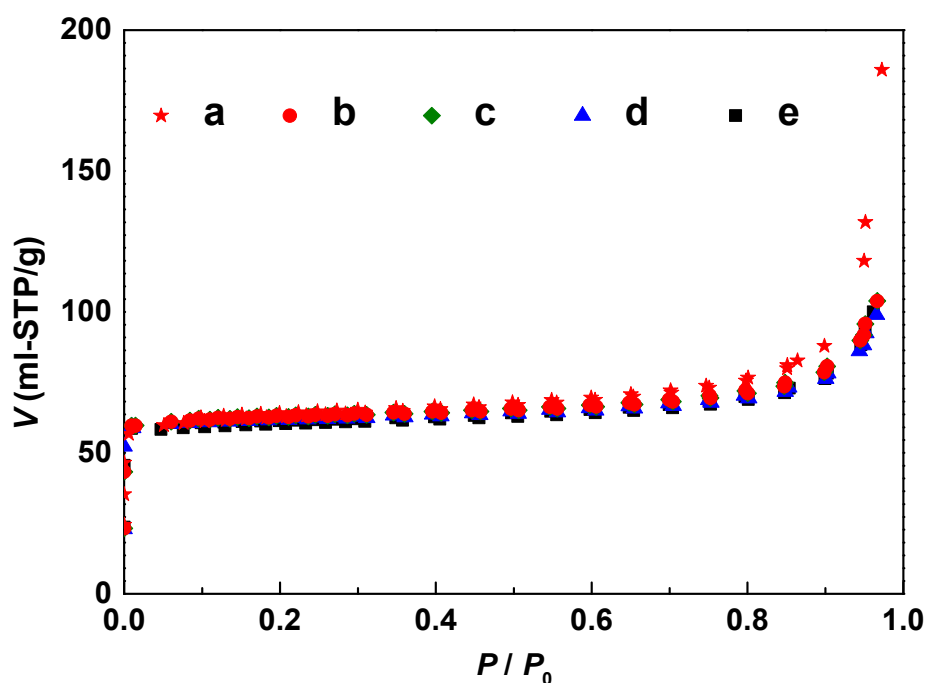


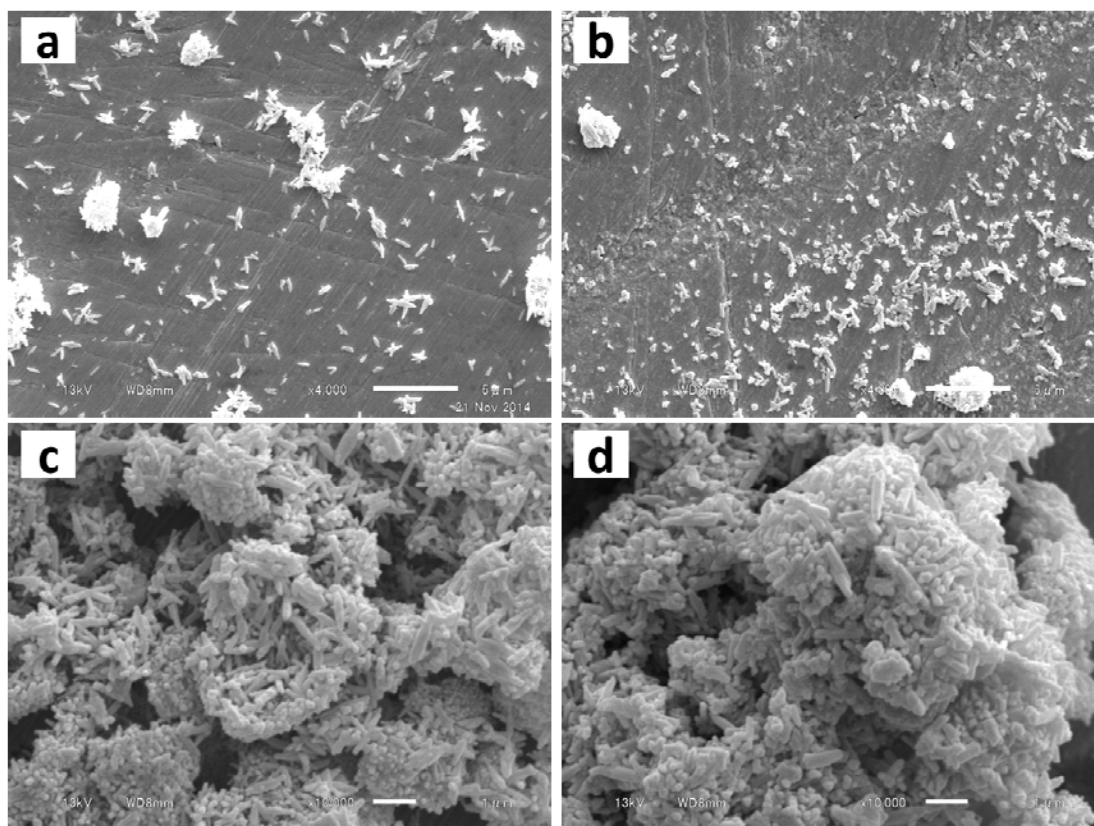
Figure 4.2 N_2 adsorption-desorption isotherms of ZSM-22 and ZSM-22@ SiO_2 samples: (a) Z-120@0Si, (b) Z-120@10Si, (c) Z-120@20Si, (d) Z-120@50Si and (e) Z-120@100Si.

Table 4.1 The physicochemical properties of ZSM-22 and ZSM-22@SiO₂ samples.

Sample	$S_{\text{micro}}^{\text{a}}$ (m ² /g)	$V_{\text{micro}}^{\text{b}}$ (cm ³ /g)	d_{p}^{c} (nm)	$S_{\text{ext}}^{\text{d}}$ (m ² /g)	Si/Al ^e	
					Experimental value	Target value
Z-120@0Si	326	0.089	0.57	36	113	120
Z-120@10Si	324	0.087	0.57	35	124	132
Z-120@20Si	315	0.085	0.57	26	135	144
Z-120@50Si	313	0.083	0.57	26	163	180
Z-120@100Si	312	0.082	0.57	26	183	240

^{a, b, c, d} Micropore surface areas, micropore volumes, micropore diameters, external surface areas calculated by the *t*-plot method. ^e Bulk SiO₂/Al₂O₃ ratio measured by EDS.

SEM images of Z-120@0Si and Z-120@100Si are shown in **Figure 4.3**. Both of the two samples presented typical agglomerate of needle-shaped ZSM-22 crystals. The average crystal size of the parent ZSM-22 was approximately $0.87 \times 0.23 \mu\text{m}$. After silica coating, there was a slight but not obvious increase in the crystal size; the average width of the crystal increased to $0.29 \mu\text{m}$. Therefore, a thin sheet-like silica grew on the surface of the parent zeolite.

**Figure 4.3** SEM images of (a, c) Z-120@0Si and (b, d) Z-120@100Si at low- and high-magnification.

X-ray emission mappings of Al K_{α} and Si K_{α} for Z-120@100Si are shown in **Figure 4.4**. It is obvious that the Si mapped crystal was wider than the Al mapped one. This result is consistent with that obtained from XRD, which revealed that the shell silica was coated on the (100) plane of the parent zeolite.

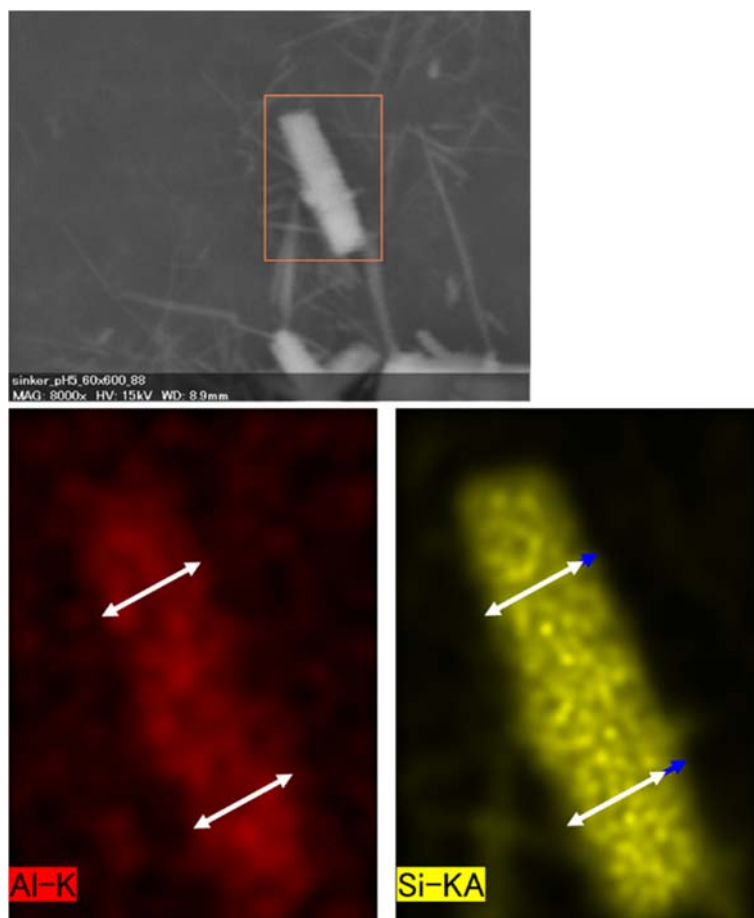


Figure 4.4 Elemental mappings (Al and Si) of the Z-120@100Si sample.

FT-IR spectroscopy for the catalyst after chemisorption of an alkaline molecule has been widely used in determining the acidity of a porous material. Choosing an alkaline molecule that has a larger molecule size than the pore mouth of the zeolite can expediently determine the external acid site. The kinetic diameter of 2,6-lutidine is 0.67 nm,³⁷ while the pore mouth of ZSM-22 is 0.57 nm. Therefore, 2,6-lutidine could be used to probe the external acidity of ZSM-22. FT-IR spectra of 2,6-lutidine adsorption are shown in **Figure 4.5**. Bands at 1630-1650 cm⁻¹ are attributed to the adsorption of 2,6-lutidine on external Brønsted acid sites.³⁸ Compared to the parent ZSM-22, silica coated samples displayed much lower intensity of those bands; especially for Z-120@100Si, which has almost no external acid site. This result is in good agreement with the element mapping, providing evidence that silica was successfully coated onto the surface of the parent zeolite and covered the external acid site. Although the adsorption of 2,6-lutidine for the sample have the same amount of coated silica but lower SiO₂/Al₂O₃ ratios, Z-90@20Si and Z-60@20Si, was slightly larger than Z-120@20Si, their external acid sites were much less than the parent zeolite (Z-120@0Si).

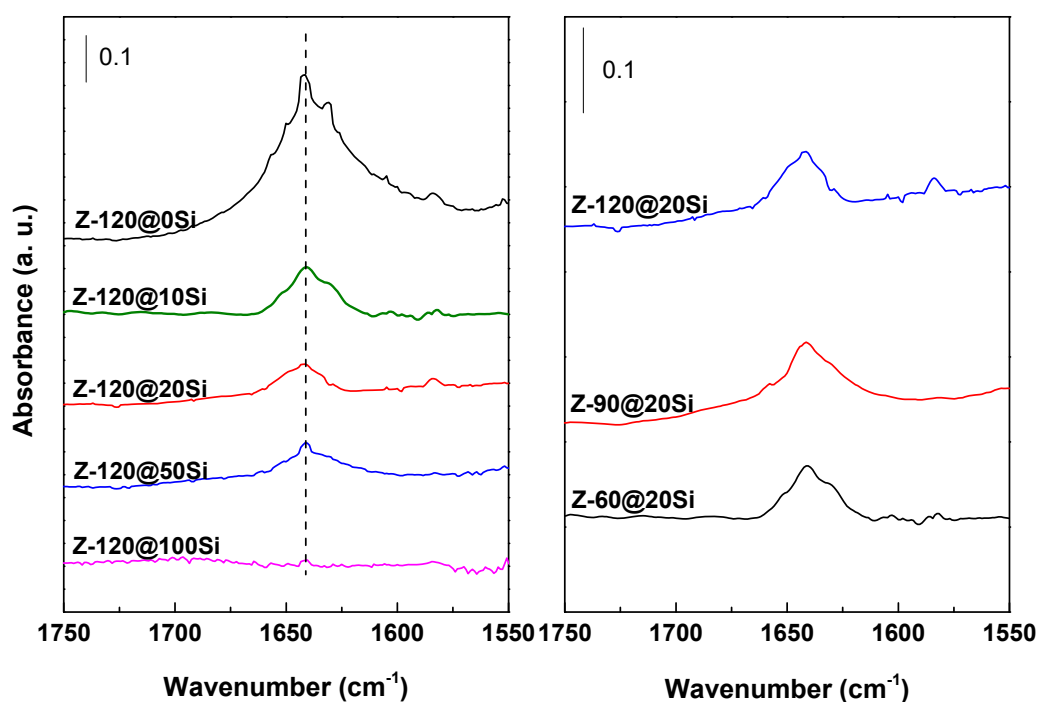


Figure 4.5 FT-IR spectra of 2,6-lutidine adsorption on various samples.

NH₃-TPD was performed to determine the amount of acid sites on the samples. From TPD profiles (**Figure 4.6**), it can be found that all the samples showed two desorption peaks; one was at around 300 °C and the other was at around 550–600 °C, corresponding to medium and strong acid sites, respectively. The center and intensity of the desorption peaks are different from each other. The amount of acid sites calculated by the calibration curve is listed in **Table 4.2**. As the amount of shell silica increased, the amount of acid sites decreased, and the center also shifted to lower temperatures. The amount of medium acid sites decreased from 327 to 139 μmol/g for Z-120@0Si and Z-120@100Si, respectively, whereas that of strong acid sites decreased from 231 to 20 μmol/g. The decrease of strong acid sites (91%) is larger than that of medium acid sites (57%). However, it is hard to believe that there are so many external acid sites that were passivated by silica coating. This significant reduction in the number of acid sites might be related to two reasons: one is that a portion of acid sites inside the pore of the zeolite are covered by silica as well; the other is that silica was deposited on the edge of pore mouth and narrowed the pore mouth. Noted that the silica source used in this study contains amorphous silica of nominal 12 nm particle size. Therefore, silica cannot enter into ZSM-22 channels during the synthesis process because the pore mouth was much smaller (0.57 nm). Consequently, the decrease in the acidity could be due to the silica deposition on the pore mouth. The N₂ physisorption result showed that the pore diameter had no change after silica coating. The contradiction between NH₃ and N₂ adsorption could be due to their different molecular diameters. N₂ can enter into the pore channel even if the pore mouth was partially blocked by silica deposition; in contrast, NH₃ has a larger molecular size and it cannot enter into those pores which was partially blocked by silica deposition. On the other hand, as the SiO₂/Al₂O₃ ratio decreased from 120 to 60, the amount of total acid sites increased from 446 to 724 μmol/g. In addition, there was no distinct difference in center of strong acid sites among the three catalysts that have different SiO₂/Al₂O₃ ratio, but new acid sites could be observed at around 200-250 °C for Z-90@20Si and Z-60@20Si.

FT-IR study for synthesized samples after pyridine adsorption was performed to determine the type of the acid site. Although the kinetic diameter of pyridine (5.9 Å) is a little larger than the pore mouth of ZSM-22 (5.7 Å), literatures suggested that the fluctuation in the pore mouth

due to thermal vibrations or flexibility of the lattice can make the pore size change by $\sim 0.5 \text{ \AA}$.³⁹ In this sense, pyridine molecules can enter into the pore channels of ZSM-22. As shown in **Figure 4.7**, a sharp strong feature is present at 1545 cm^{-1} , while almost no peak is present at approximately 1450 cm^{-1} , indicating that the predominant type of the acid sites in the sample exhibits only Brønsted acidity.

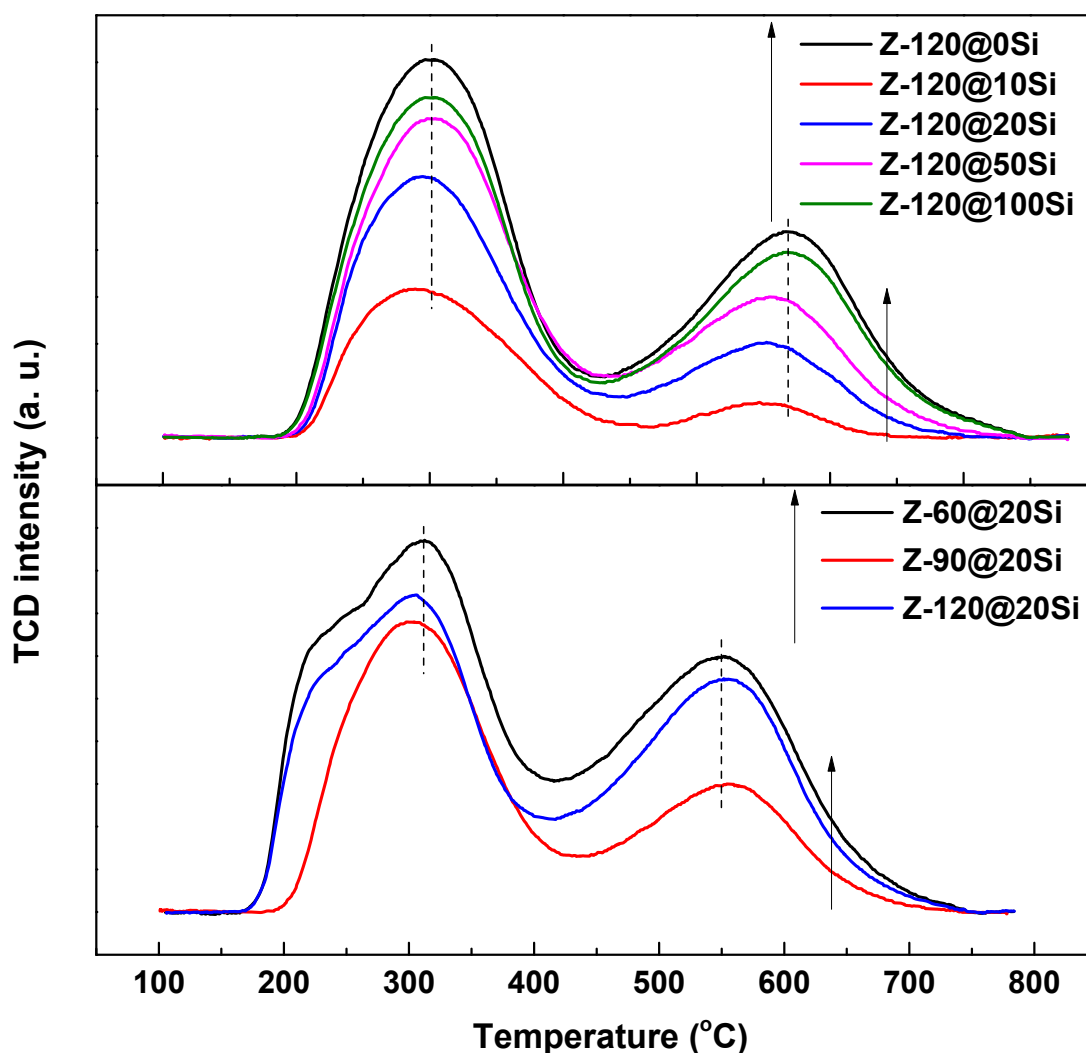


Figure 4.6 NH_3 -TPD profiles of various samples.

Table 4.2 Acidic properties of ZSM-22 samples determined by NH₃-TPD.

Sample	Amount of Acid sites ($\mu\text{mol NH}_3/\text{g}$)			Ratio	
	Medium acid sites ($< 400\text{ }^\circ\text{C}$)	Strong acid sites ($> 400\text{ }^\circ\text{C}$)	Total	Medium/ Strong ^a	Surface/ Total ^b
Z-120@0Si	327 (304 °C)	231 (570 °C)	558	1.42	0.24
Z-120@10Si	299 (304 °C)	211 (570 °C)	510	1.42	0.15
Z-120@20Si	264 (301 °C)	182 (556 °C)	446	1.45	0.06
Z-120@50Si	244 (295 °C)	96 (552 °C)	340	2.54	0.03
Z-120@100Si	139 (286 °C)	20 (546 °C)	159	6.95	0.00
Z-90@20Si	404 (314 °C)	251 (556 °C)	446	1.61	0.05
Z-60@20Si	412 (319 °C)	312 (556 °C)	724	1.32	0.09

^a The ratio of medium to strong acid sites calculated by NH₃-TPD.

^b The ratio of surface to total acid sites calculated by pyridine and 2,6-lutidine adsorption.

The temperatures in the brackets are the centers of the desorption peaks.

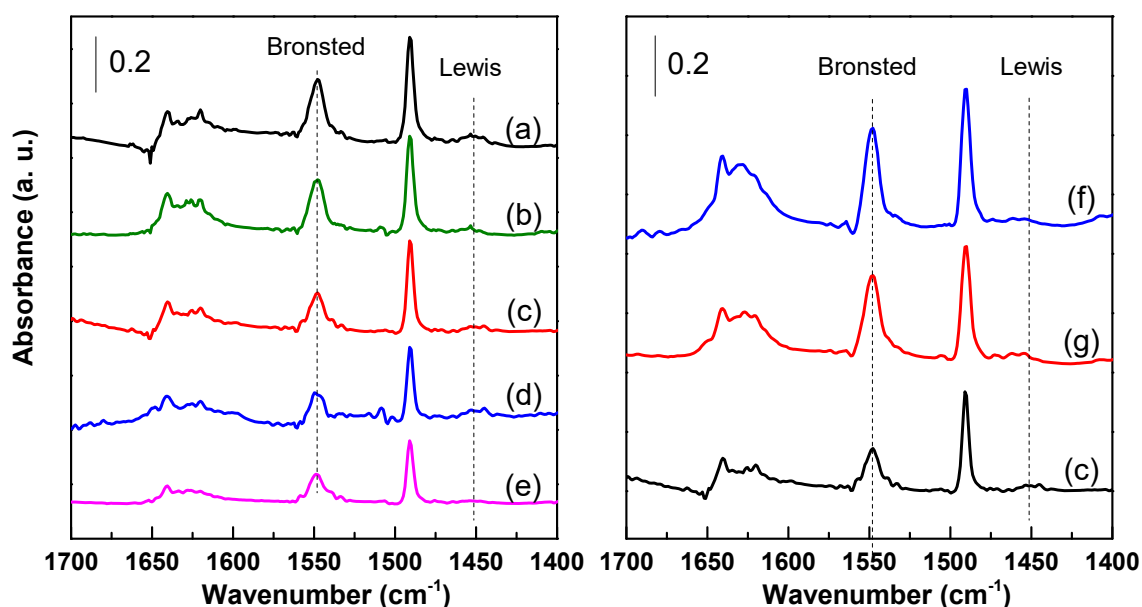
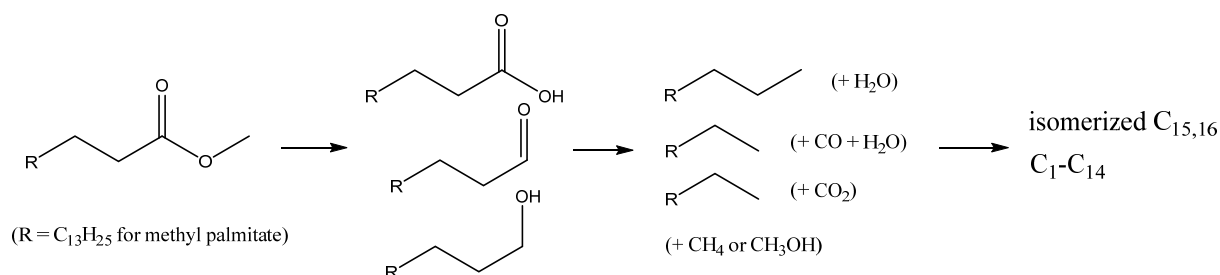


Figure 4.7 FT-IR spectra of pyridine adsorption after evacuation at 150 °C. (a). Z-120@0Si, (b) Z-120@10Si, (c) Z-120@20Si, (d) Z-120@50Si, (e) Z-120@100Si, (f) Z-60@20Si and (g) Z-90@20Si.

4.3.2 Effect of Silica Coating Amount and SiO₂/Al₂O₃ Ratio on the Catalytic Performance

The synthesized samples were loaded with 0.6 wt% platinum as a deoxygenation function, and the performance of prepared catalysts were evaluated by hydrotreating of MP. Hydrotreating of MP is a complex reaction that includes many elementary reactions. Fatty acid methyl ester was first transformed to some oxygenate intermediates, *e.g.*, fatty acid, fatty aldehyde or fatty alcohol. These intermediates were then deoxygenated to linear alkanes. Finally, linear alkanes were further isomerized to branched alkanes (Scheme 4.1).



Scheme 4.1 Possible reaction pathways of hydrodeoxygenation of methyl palmitate.

Table 4.3 Catalytic activity and product selectivity in hydrotreating of methyl palmitate.

Catalyst	Conversion (%)	Selectivity (C%)						MoBI ^b (%)
		CO	CH ₄	C ₂₋₁₄	<i>n</i> -C _{15,16}	<i>iso</i> -C _{15,16}	Oxygenates ^a	
Pt/ZSM-22	20.2	0.8	0.9	2.7	18.2	8.2	69.3	71.1
Pt/Z@10Si	18.2	0.9	0.9	2.2	16.6	7.1	72.3	85.2
Pt/Z@20Si	16.9	1.1	0.7	3.0	15.9	5.9	73.3	95.1
Pt/Z@50Si	14.2	0.9	0.9	2.6	14.8	5.5	75.4	99.5
Pt/Z@100Si	10.1	1.0	1.0	3.0	13.3	3.0	78.6	94.7

^a Oxygenates: hexadecanoic acid, 1-hexadecanol and 1-hexadecanal; percentage of MoBI in total isomers. Reaction conditions: T = 300 °C, WHSV = 10 h⁻¹, P_{H₂} = 3 MPa, H₂/reactant = 800 (ml/ml).

Table 4.3 lists MP conversion, product selectivity and MoBI percentage over the catalysts with different amounts of shell silica. Noted that a relatively higher weight hourly space velocity (WHSV) was used for the catalytic test in order to maintain the reaction at kinetic control. The MP conversion and isomerization selectivity decreased with increasing amount of shell silica. Combining with the result of NH₃-TPD, it could be reasonably inferred that a catalyst with more acid sites possess higher deoxygenation and isomerization activity. According to the isomerization mechanism on a bifunctional catalyst, the Brønsted acid site on the support plays a key role in the methyl group migration and cracking of carbenium ion.¹¹ Therefore, the decrease in the Brønsted acid site can result in the decreased isomerization and cracking selectivity. As the amount of shell silica changed from 0 to 20%, the MoBI percentage increased substantially with increasing shell silica amount until it reached to 20%. The Pt/Z-120@20Si, Pt/Z-120@50Si and Pt/Z-120@100Si gave high MoBI percentage of approximated 95%, indicating that the silica-coated catalysts showed higher shape-selectivity, and isomerization of MoBI into MuBI over the external acid site can be successfully inhibited through silica coating.

Figure 4.8 presents the effect of reaction temperature on the catalytic performance of Pt catalysts in hydrotreating of MP. MP conversion, isomerization and cracking selectivity increased with increasing reaction temperature. At the highest reaction temperature, *i.e.*, 360 °C, the cracking selectivity was lowered by silica coating; it largely decreased with increasing amount of shell silica. On the other hand, MoBI percentage showed a decreased tendency; for the Pt/ZSM-22@SiO₂ catalyst with silica coating amount higher than 20%, the MoBI percentage dropped from 95% to approximately 75%. These results indicate that the MoBI formation would be reduced with the improved isomerization selectivity. Hydrotreating of MP was also conducted under different space velocities to investigate the behavior of MoBI formation. As shown in **Table 4.4**, MoBI percentages were constant at around 75%, which was not sensitive to either MP conversion or isomerization selectivity. This result indicates that the MoBI formation could not be dependent on the isomerization degree, and its

decrease in the case of raising the reaction temperature was not due to the increased isomerization selectivity.

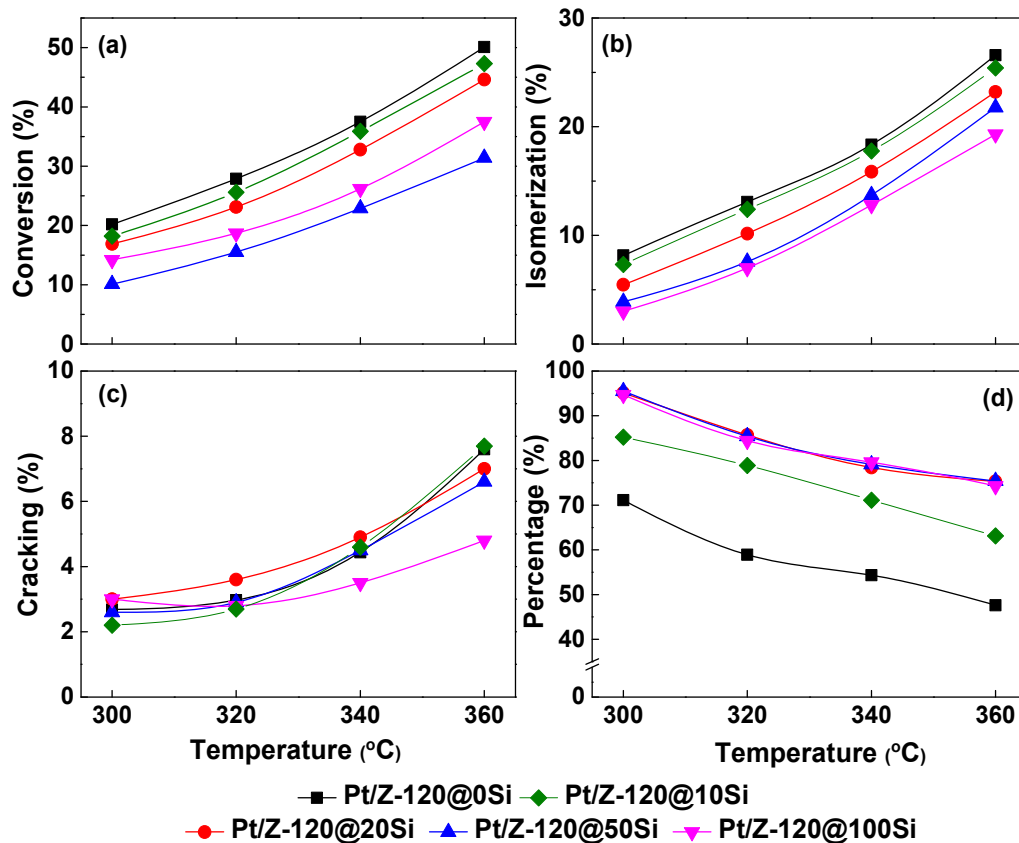


Figure 4.8 Effect of reaction temperature on the catalytic performance. (a) MP conversion; (b) isomerization selectivity; (c) cracking selectivity; (d) MoBI percentage in total isomers. Reaction conditions: $T = 300 - 360$ °C, $P = 3$ MPa, $WHSV = 10$ h⁻¹ and $H_2/\text{reactant} = 800$ (ml/ml).

Table 4.4 Hydrotreating of methyl palmitate over Pt/Z@20Si at different WHSVs.

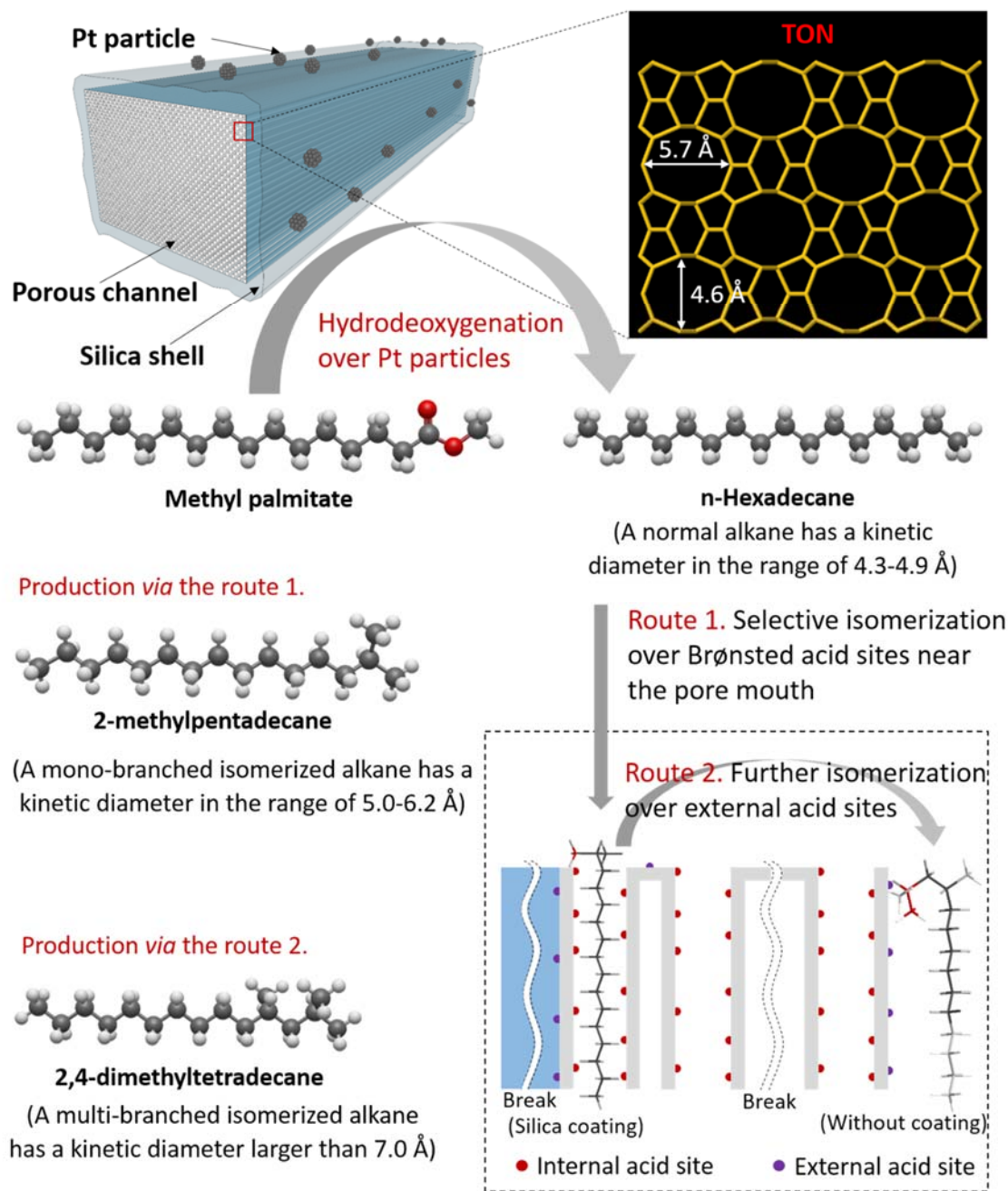
WHSV (h ⁻¹)	Conversion (%)	Selectivity (%)						MoBI (%)
		CO	CH ₄	C ₂₋₁₄	<i>n</i> -C _{15,16}	<i>iso</i> -C _{15,16}	Oxygenates	
5	93.1	5.9	2.4	7.5	18.6	30.9	34.7	74.9
10	44.6	3.6	1.3	5.3	16.5	21.2	52.1	75.3
20	27.6	2.5	0.6	5.1	11.6	19.2	61	76.3
30	21.0	1.8	0.6	4.6	10.3	17.3	65.4	74.1
40	16.9	1.6	0.5	4.4	9.5	16.9	67.1	76.8

Reaction conditions: $T = 360$ °C, $P_{H_2} = 3$ MPa and $H_2/\text{reactant} = 800$ (ml/ml).

Martens systematically studied the isomerization of long-chain *n*-alkanes on Pt/HZSM-22 catalyst and proposed “pore mouth” and “key-lock” mechanisms for explaining the isomerization behavior over the ZSM-22 zeolite.^{25, 40} The pore mouth of ZSM-22 zeolite is 0.55×0.45 nm, and the kinetic diameters of normal, mono-branched and multi-branched alkanes are approximately 0.43–0.49, 0.50–0.62 and 0.7 nm, respectively.⁴¹ The diameter of MoBI is similar to the pore mouth of ZSM-22, and therefore, the MoBI is somewhat difficult to be formed inside the channel of the ZSM-22 zeolite. In the “pore mouth” theory, acid sites on the pore mouth favor the formation of MoBI. In contrast, two ends of hydrocarbon chain penetrate each into different pore mouths, designated as the “key lock” type, favors more central branching of the chain and causes the MuBI formation. On the other hand, Corma investigated the isomerization behaviors of *n*-alkanes over Theta-1 (TON-type) zeolite, which has an identical channel structure to ZSM-22, and demonstrated that the an important part of MoBI should occur deep inside the pore channels, while MuBI are mainly formed at the external surface by further isomerization of MoBI.⁴² Consequently, it can be concluded that the MuBI formation is available under two pathways: carrying out on the acid sites that located on two pore mouths of ZSM-22 or on the external acid sites (**Scheme 4.2**).

In this study, the external acid site could be eliminated by silica coating. Therefore, it can be reasonably inferred that the portion of MuBI formed on the external acid site can be inhibited. However, other MuBI generated *via* a “key-lock” mode cannot be completely suppressed by silica coating. This portion of MuBI formation would increase along with the reaction temperature, which probably due to the intense thermal motion of molecule under a high temperature.

It was observed that silica coating could be an efficient approach for improving the MoBI formation, but it also reduced the catalytic activity due to the decrease in acid sites. Although higher isomerization selectivity can be achieved at a higher reaction temperature, the increased temperature would also reduce the MoBI formation. Herein, two methods were considered to increase the isomerization activity of the catalyst; one was realized by changing the Si/Al ratio of core ZSM-22 to improve its acidity and the other was realized by using a more active metal phase for the bifunctional catalyst.



Scheme 4.2 Deoxygenation of methyl palmitate and further isomerization of the deoxygenated n-alkane into mono-branched *iso*-alkane over Pt/ZSM-22@SiO₂. Hexadecane and the corresponding isomers are selected as examples. Kinetic diameters of these compounds are obtained from Ref.¹⁰

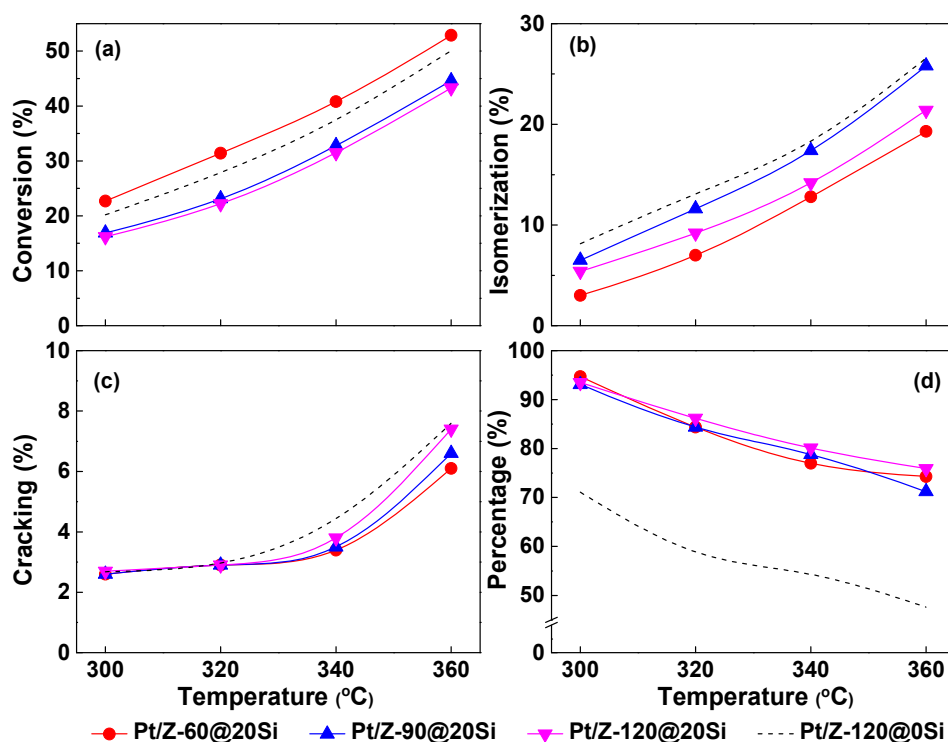


Figure 4.9 Effect of SiO₂/Al₂O₃ ratio on the catalytic performance. (a) MP conversion; (b) isomerization selectivity; (c) cracking selectivity; (d) MoBI percentage in total isomers. Reaction conditions: $T = 300 - 360$ °C, $P = 3$ MPa, $WHSV = 10$ h⁻¹ and $H_2/\text{reactant} = 800$ (ml/ml).

The catalytic performance of Pt/Z-60@20Si and Pt/Z-90@20Si are showed in **Figure 4.9**. The MP conversion and isomerization selectivity were markedly improved by reducing the SiO₂/Al₂O₃ ratio. Pt/Z-60@20Si exhibited the highest isomerization activity, which was close to the uncoated Pt/Z-120@0Si catalyst. For the cracking selectivity, there was no considerable difference among the four catalysts at 300 and 320 °C. In contrast, cracking selectivity was higher over the Pt/Z-60@20Si catalyst than over another two silica-coated catalysts at higher temperatures (*i.e.*, 340 and 360 °C). On the other hand, the MoBI percentages over the three silica-coated catalysts were similar to each other, superior to the uncoated catalyst, indicating that the decrease in SiO₂/Al₂O₃ ratio increases the internal acid site, but it can barely affect the external acid site.

4.3.3 Enhanced Activity of Silica-Coated Catalysts by Using Bimetals

The promotion effect of Sn on a Pt/SAPO-11 catalyst was demonstrated in *Chapter 3*. It is obvious that the presence of PtSn alloys can substantially improve isomerization selectivity. Thus, PtSn bimetal was applied as the active site for the silica coated zeolite in order to further improve the activity of the catalyst. Herein, PtSn/Z-60@20Si (Pt = 0.3 wt%, Sn/Pt = 2:1) was prepared and used for the hydrodeoxygenation of MP (**Table 4.5**). The PtSn catalysts gave a similar MP conversion with the Pt catalyst. However, the Pt loading in PtSn catalyst is only half of that in the Pt catalyst. In addition, the yield of total isomers over the PtSn catalyst was almost twofold higher than the Pt catalyst. Furthermore, the deoxygenation reaction over PtSn catalyst proceeds *via* the hydrodeoxygenation (HDO) route and gives higher C16 selectivity, while that over the Pt catalyst proceeds *via* the decarbonylation (DCO) route and gives higher C15 selectivity. These results are consistent with those in *Chapter 3*, in which the PtSn/SAPO-11 catalyst exhibited higher HDO and isomerization selectivity superior to the Pt/SAPO-11 catalyst, indicating that the promotion effect of Sn is not dependent on the support and it could be applied widely in other Pt catalysts. For MoBI percentage, there is no considerable difference between the Pt and PtSn catalysts. Based on the above results, it can be concluded that the catalytic activity of the silica-coated catalysts could be dramatically improved by using PtSn as its active site.

On the other hand, higher activity of NiMo bimetal has also been demonstrated in *Chapter 2*. The NiMo/SAPO-11 catalyst reduced at 450 °C had the best balance between activity and isomerization selectivity. Thus, the NiMo/Z-60@20Si was prepared and reduced at 450 °C prior to applying for the hydrodeoxygenation of methyl palmitate (**Table 4.5**). Although the MP conversion of the NiMo catalyst was slightly lower than that of the Pt catalyst, the yield of total isomers and the C16 percentage were similar to those of the Pt catalyst. However, for the MoBI percentage, the NiMo catalyst showed a much lower value than the Pt catalyst. As discussed in *Chapter 2*, the Mo⁵⁺ species show Brønsted acidity, and the metal particle size of the catalyst indicates that the NiMo particles are loaded on the external surface of the zeolite. In this sense, the Mo⁵⁺ species

would work as an isomerization active site and catalyzed the further isomerization of MoBI into undesired MuBI.

Table 4.5 Catalytic performance of catalysts with different active metals in hydrodeoxygenation of methyl palmitate.

	Pt/Z-60@20Si		PtSn/Z-60@20Si		NiMo/Z-60@20Si	
	325 °C	350 °C	325 °C	350 °C	325 °C	350 °C
Conversion (%)	77.7	98.1	76.5	99.1	76.3	93.0
Carbon distribution of liquid products (C%).						
C ₁₋₁₄	8.3	11.6	5.1	7.3	4.4	8.3
C ₁₅	15.2	38.2	1.5	2.3	4.6	5.9
C ₁₆	45.3	46.6	58.3	87.7	56.9	71.9
C ₁₆₊	0.7	1.6	1.3	2.0	1.8	3.2
Methyl palmitate	22.3	1.9	23.5	0	23.7	7.0
Palmitic acid	8.2	0.1	10.3	0.7	8.6	3.7
Other parameters.						
C ₁₆ /Total hydrocarbons	0.65	0.48	0.88	0.88	0.84	0.81
Yield of isomers (%)	14.7	25.0	28.3	53.0	8.6	32.3
MoBI/Total isomers	0.90	0.85	0.90	0.83	0.73	0.68

Reaction conditions: WHSV = 5 h⁻¹, P_{H₂} = 3 MPa, H₂/MP = 800 (ml/ml).

4.3.4 Structure-Performance Relationship

Generally, metal species in a catalyst are considered to be the hydrogenation active site in a hydrodeoxygenation reaction. We also used Z-60@20Si, which has the most highest acidity in the synthesized samples, for hydrodeoxygenation of MP, but only 3% conversion was obtained ($T = 360\text{ }^{\circ}\text{C}$, $\text{WHSV} = 10\text{ h}^{-1}$). This result suggested that the support was almost not active without cooperation from metal species. From experimental results, however, it is obvious that catalysts with different acidity showed distinct performance. Kinetic analysis was conducted to understand the catalytic behavior of the deoxygenation reaction. A pseudo-first-order model for MP deoxygenation was represented by Equation (3). Arrhenius plots for deoxygenation rate constants obtained from different reaction temperatures are shown in **Figure 4.10**, and the apparent activation energies (E_a) and pre-exponential factors (A) calculated from linear fitting of the Arrhenius plots are listed in **Table 4.6**. The E_a increased gradually with increasing amount of shell silica. Pt/Z-120@0Si (71 kJ/mol), Pt/Z-120@10Si (72 kJ/mol) and Pt/Z-120@20Si (75 kJ/mol) had similar E_a to each other, whereas Pt/Z@50Si (71 kJ/mol) and Pt/Z@100Si (94 kJ/mol) had much higher E_a . Especially the catalyst with the highest amount of shell silica, a 24 kJ mol^{-1} difference from the uncoated catalyst was observed. On the other hand, lower E_a were obtained from catalysts with lower $\text{SiO}_2/\text{Al}_2\text{O}_3$ ratios, *i.e.*, Pt/Z-90@20Si (69 kJ/mol) and Pt/Z-60@20Si (65 kJ/mol), respectively. It could be assumed that the support would have a impact on the structure of supported metal particles and thus influence the catalytic activity. The catalysts were characterized by CO-FTIR and TEM to get further information.

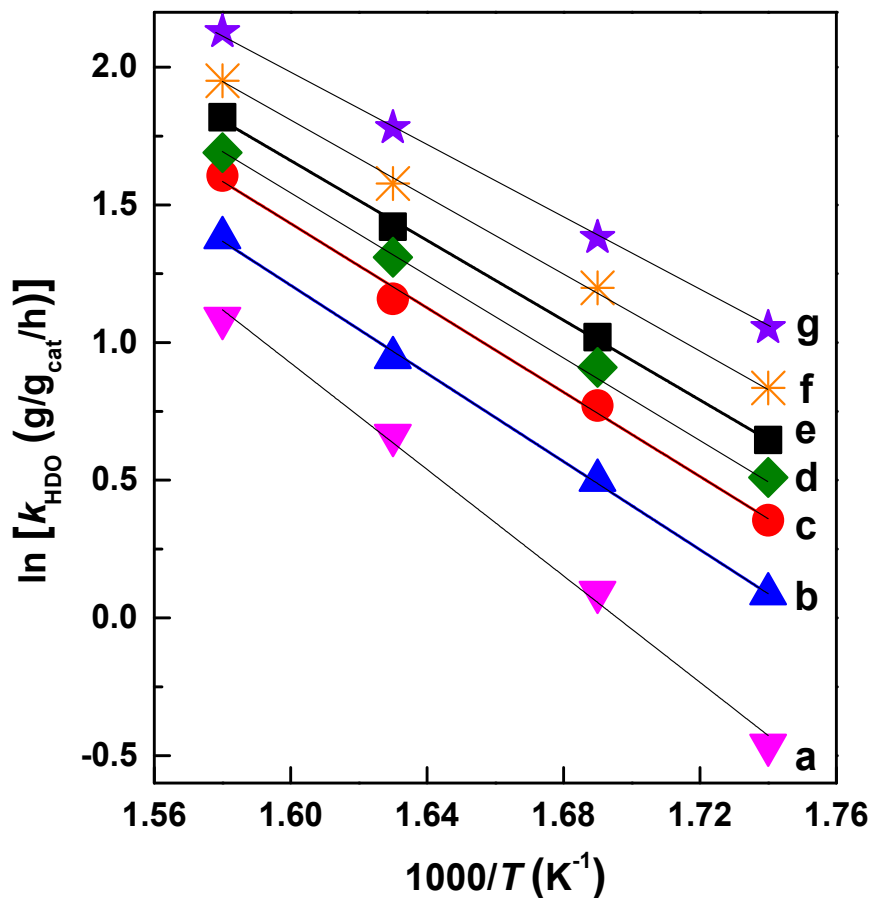


Figure 4.10 Arrhenius plot of deoxygenation rate constants (k_{HDO}) for (a) Pt/Z-120@100Si, (b) Pt/Z-120@50Si, (c) Pt/Z-120@20Si, (d) Pt/Z-120@10Si, (e) Pt/Z-120@0Si, (f) Pt/Z-90@20Si and (g) Pt/Z-60@20Si.

Table 4.6 Fitting parameters in the Arrhenius plot of the deoxygenation reaction of methyl palmitate over various Pt catalysts.

Catalyst	E_a^a (kJ·mol ⁻¹)	$\ln A^b$ (mol·h ⁻¹ ·g ⁻¹)	R^{2c}
Pt/Z-60@20Si	65	12.1	0.99
Pt/Z-90@20Si	69	12.7	0.99
Pt/Z-120@0Si	71	13.0	0.99
Pt/Z-120@10Si	72	13.1	0.99
Pt/Z-120@20Si	75	13.4	0.99
Pt/Z-120@50Si	80	13.7	0.99
Pt/Z-120@100Si	94	16.1	0.99

^a Activation energy. ^b Pre-exponential factor. ^c Relative error.

Carbon monoxide is a particularly useful probe molecule for determining the nature of active sites because the C-O stretching frequency is quite sensitive to the electronic properties of the bonding site.⁴³ FT-IR spectroscopy after CO adsorption was performed for Pt catalysts (**Figure 4.11**). FT-IR study for Pt catalysts after CO adsorption was performed (**Fig. 7**). IR spectra for the coated and uncoated catalysts displayed distinct features on the C-O stretching mode. For Pt/Z-120@0Si, there are two vibration bands observed in the studied wavenumber range; a stronger band located at around 2087 cm⁻¹ and a weaker band located at around 1858 cm⁻¹. Pt/Z-120@10Si displayed a similar IR spectrum with Pt/Z-120@0Si, yet the vibration band at the lower wavenumber site in Pt/Z-120@10Si shifted to 1886 cm⁻¹. In contrast, three vibration bands, *i.e.*, 2087, 2015 and 1886 cm⁻¹, were observed in the IR spectra of catalysts coated more silica. On the other hand, Pt/Z-90@20Si and Pt/Z-60@20Si showed similar spectra with Pt/Z-120@0Si, in which the band at 2082 cm⁻¹ was dominant. Compared with Pt/Z-120@0Si, however, this band shifted slightly to a lower wavenumber. This might be due to the strong interaction between the Pt particle and the support.

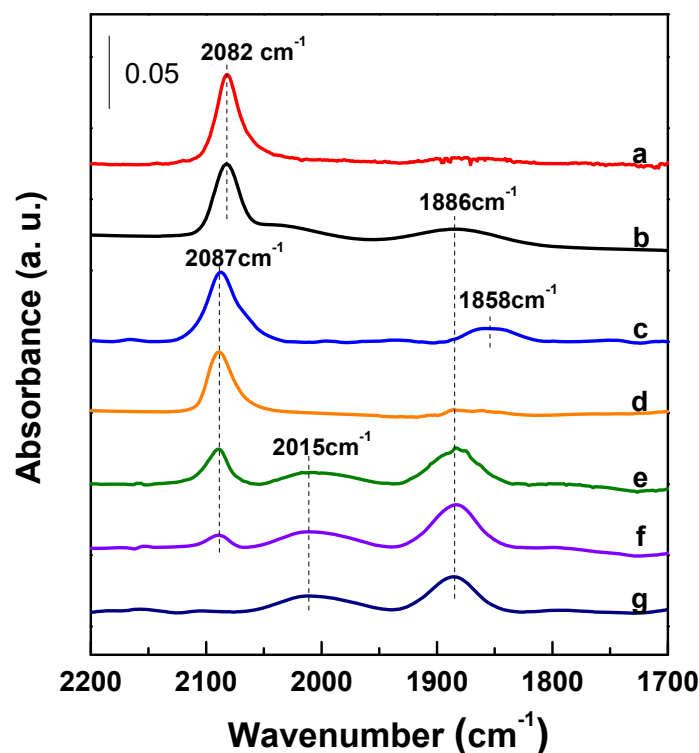
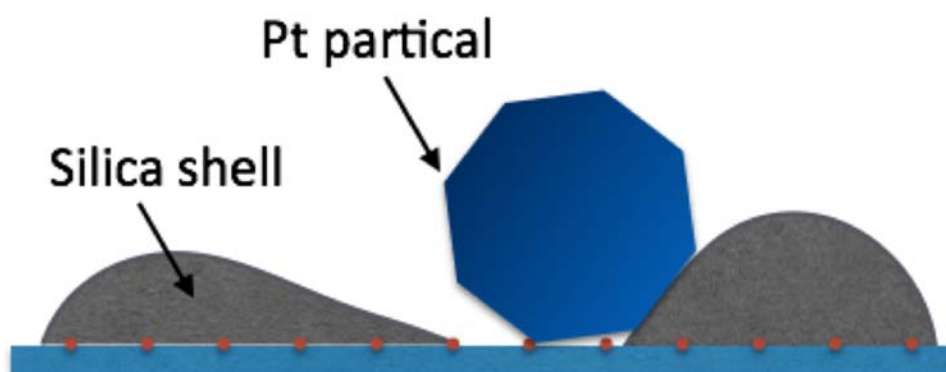


Figure 4.11 FT-IR spectra of CO adsorbed on (a) Pt/Z-60@20Si, (b) Pt/Z-90@20Si, (c) Pt/Z-120@0Si, (d) Pt/Z-120@10Si, (e) Pt/Z-120@20Si, (f) Pt/Z-120@50Si and (g) Pt/Z-120@100Si at 25 °C.

Vibration bands at 2087, 1886 and 1858 cm^{-1} can be associated with CO adsorption on Pt. Indeed, the band at $\sim 2087 \text{ cm}^{-1}$ is well known to correspond to the linear adsorption form, in which the carbon monoxide is bonded on atop sites of low Miller index terraces, most likely on Pt(111) planes.^{44, 45} The intensity of this band decreased with increasing amount of coated silica, and the band completely disappeared in Pt/Z-120@100Si. Bands at 1886 and 1858 cm^{-1} are assigned to the CO adsorption on bridges or other high-coordination sites.⁴⁶ Different to Pt/Z-120@0Si and Pt/Z-120@10Si, the main features of Pt/Z-120@20Si, Pt/Z-120@50Si and Pt/Z-120@100Si were identified as the bridge CO adsorption band at 1886 cm^{-1} .

A broader and weaker vibration band at around 2015 cm^{-1} can be assigned to the bridge adsorption form. This bond is likely to be due to CO adsorbed on interfacial Pt-SiO₂ sites, *i.e.*, on both a Pt atom and an adjacent Si atom. Although silica is successfully coated on the external surface of ZSM-22 zeolite, it is speculated that the coated silica is difficult to be uniformly laying on the surface. Thus, it seems plausible that the existence of Pt surface sites at the interface between the support and the Pt particles (close contact between silica and platinum as shown in **Scheme 4.3**) are accessible to CO. A similar particle-support interface effect on the CO adsorption can be seen in other literatures.⁴⁷



Scheme 4.3 Proposed platinum-silica interface.

Based on these results, it can be suggested that the silica coating influenced not only the amount but also the nature of the Pt active sites. In general, the CO adsorbed on the Pt catalyst displays a strong vibration band in the range of 2000–2100 cm^{-1} , yet seldom show a weak vibration band in the range of 1800–2000 cm^{-1} because the bridge mode adsorption on the Pt atom was too weak that the adsorbed CO can be easily desorbed by the evacuation. In this study, the significant change in the adsorption form is likely to be due to the different crystal structures of the Pt particle. On the other hand, Pt/Z-90@20Si and Pt/Z-60@20Si showed similar spectra with Pt/Z-120@0Si, in which the band at 2082 cm^{-1} was dominant. Compared with Pt/Z-120@0Si, however, this band shifted slightly to a lower wavenumber. This might be due to the strong interaction between the Pt particle and the support.

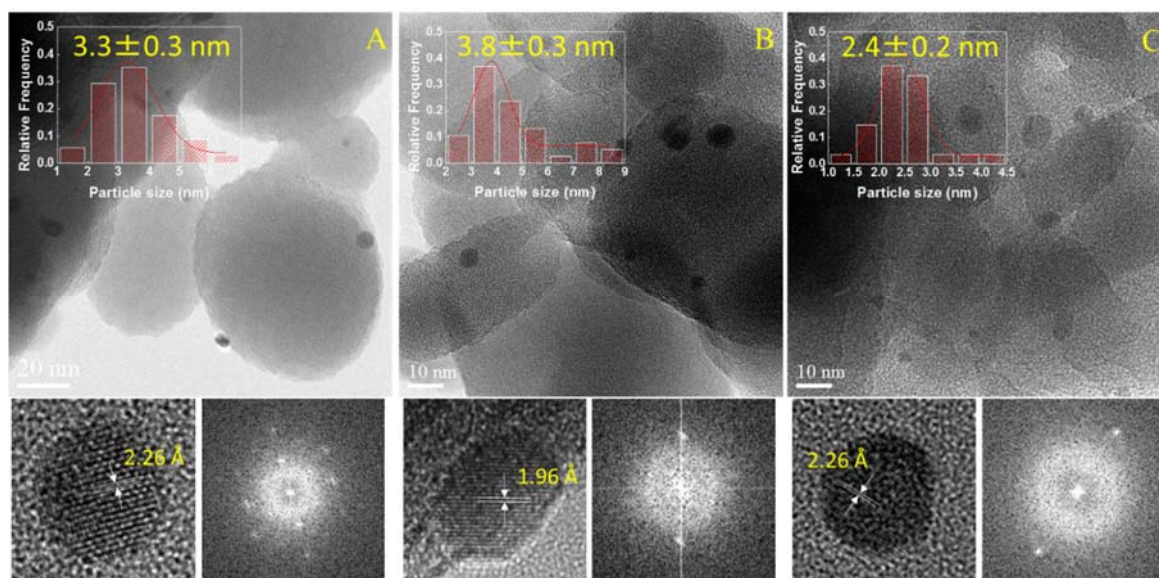


Figure 4.12 HRTEM images, FFT patterns and particle size distributions of the (A) Pt/Z-120@0Si, (B) Pt/Z-120@100Si and (C) Pt/Z-60@20Si catalysts.

Typical HRTEM images, fast Fourier transform (FFT) patterns and particle size distributions are displayed in **Figure 4.12**. Pt/Z-120@0Si, Pt/Z-120@100Si and Pt/Z-60@20Si were chosen as representations. The average particle sizes of these three catalysts decrease in the sequence Pt/Z-60@20Si < Pt/Z-120@0Si < Pt/Z-120@100Si. Moreover, there was no obvious distinction in the average particle size between Pt/Z-120@0Si (c.a. 3.3 nm) and Pt/Z-120@100Si (c.a. 3.8 nm); in contrast, the average

particle size of Pt/Z-120@0Si (c.a. 3.3 nm) and Pt/Z-60@20Si (c.a. 2.4 nm) are quite different. Although HRTEM observation was not conducted for other catalysts, it could be reasonably inferred that the trend of the average particle sizes would monotonically increase with increasing amount of coated silica, but decrease with decreasing SiO₂/Al₂O₃ ratio.

More information about the structure of Pt particles on different catalysts, correlated with the effect of the electronic state characterized by CO-FTIR, can be obtained from the FFT pattern. FFT patterns obtained from lattice fringes of particles reveal different spots at 2.26 Å for Pt/Z-120@0Si and at 1.96 Å for another two catalysts. According to other literatures, the value 2.26 Å corresponds to the Pt(111) crystallographic plane, while the value 1.96 Å is attributed to the Pt(100) crystallographic plane.¹⁵ This result implies that the acidity of the support would influence not only the dispersion but also the crystal orientation of Pt particles. In Pt/Z-120@0Si and those catalysts with smaller amount of shell silica, *i.e.*, Pt/Z-120@10Si, Pt/Z-90@20Si and Pt/Z-60@20Si, the most exposed Pt crystal facet might be Pt(111). In contrast, catalysts with larger amount of shell silica, *i.e.*, Pt/Z-120@50Si and Pt/Z-120@100Si, and with lower acidity, *i.e.*, Pt/Z-120@20Si, predominantly exhibited crystal facet exposure to Pt(100). TEM observation suggested that the modification of the support would mainly influence the crystal structure of the Pt catalyst, whereas changing the SiO₂/Al₂O₃ ratio would predominately improve the Pt dispersion.

Generally, a change in activation energy is due to the formation of new bonds between the substrate and the catalyst. Characterization results suggested that the Pt particles which predominantly exposed Pt(111) facet favor of exhibiting CO vibration bands at 2015 cm⁻¹, while the Pt particles which exposed Pt(100) facet prefer to displaying bands at 1886 cm⁻¹. In addition, the number of Pt(111) particles decreased with increasing amount of shell silica, while the number of Pt(100) particles increased. Combining with the result of activity test, it could be concluded that the Pt(111) facet is more active in the deoxygenation of MP. Consequently, the variation in the activation energy among catalysts with the same SiO₂/Al₂O₃ ratio but different amounts of coated silica are linked to different crystal structures of the Pt particles.

On the other hand, comparing the activation energy of catalysts with different $\text{SiO}_2/\text{Al}_2\text{O}_3$ ratios but the same amount of coated silica, it is obvious that the activation energy also decreased with increasing acidity of supports by lowering the $\text{SiO}_2/\text{Al}_2\text{O}_3$ ratio. From previous literatures, the deoxygenation of esters or fatty acids is not a structure sensitive reaction, suggesting that the dispersion of the Pt particles can barely change the activation energy. Therefore, $-\text{OH}$ groups on the support are likely to be a catalytically active site or adsorption sites in deoxygenation reaction. A relationship between catalytic activity and acidity of the catalyst was reported.⁴⁸ The catalytic activity of Ni/HZSM-5 or Ni/Hbeta with different $\text{SiO}_2/\text{Al}_2\text{O}_3$ ratios was investigated in deoxygenation of stearic acid, and the acid function of zeolite was likely to catalyze the dehydration of alcohol intermediates, thereby accelerating the deoxygenation reaction rate. In this study, the abundance of $-\text{OH}$ groups on Pt/Z-60@20Si is the most likely factor to lower the activation energy.

4.4 Conclusions

ZSM-22@SiO₂ with a core-shell structure was designed to passivate the external acid site and enhance the shape-selectivity of the zeolite. A series of samples with different amounts of shell silica were synthesized. There was no considerable change in the pore structure and crystallinity of ZSM-22 after silica coating. The (100) plane of TON structure grew slightly, indicating of the coating on the surface of the zeolite. The number of total and external acid sites decreased with increasing amount of shell silica. In the case of Z-120@100Si, the external acid site was completely covered.

The synthesized samples were used as the support to prepare Pt bifunctional catalysts. In hydrodeoxygenation of methyl palmitate, silica coating led to an enhanced formation of MoBI. As the amount of shell silica increased from 0 to 20%, the MoBI percentage in total isomers increased from 71% to 95% at 300 °C. However, further increase in the amount of shell silica could not change the MoBI percentage. Deoxygenation and isomerization activity decreased after silica coating. Characterization results implied that the exposed facet of Pt particles switched from (111) to (100), which was the most likely reason for the decrease in deoxygenation activity. Isomerization activity was also reduced due to the decrease in the acidity of support, on which the acid site was covered by silica. In consideration of the balance between MoBI percentage and catalytic activity, 20% shell amount could be the best choice in this study. Catalytic activity of the Pt/ZSM-22@SiO₂ catalyst could be improved by two methods; one is lowering the SiO₂/Al₂O₃ ratio of core ZSM-22 to increase its acidity, and the other is using PtSn as the active phase to raise the isomerization rate. A novel catalyst, PtSn/Z-60@20Si, exhibited high efficiency in tandem deoxygenation-isomerization of methyl palmitate, which gave an *iso*-C_{15,16} yield of 53% and MoBI percentage of 83% (T = 350 °C and WHSV = 5 h⁻¹). This study offered a promising prospect for producing “ready-to-use” transportation fuels with a lower melting point and a higher cetane number.

References

1. T. J. Benson; P. R. Daggolu; R. A. Hernandez; S. Liu; M. G. White, Chapter Three - Catalytic Deoxygenation Chemistry: Upgrading of Liquids Derived from Biomass Processing. In *Advances in Catalysis*, Bruce, C. G.; Friederike, C. J., Eds. Academic Press: 2013; Vol. Volume 56, pp 187-353.
2. C. Zhao; T. Bruck; J. A. Lercher, Catalytic deoxygenation of microalgae oil to green hydrocarbons, *Green Chem.*, **2013**, *15* (7), 1720-1739.
3. I. Kubičková; D. Kubička, Utilization of Triglycerides and Related Feedstocks for Production of Clean Hydrocarbon Fuels and Petrochemicals: A Review, *Waste Biomass Valor.*, **2010**, *1* (3), 293-308.
4. R. W. Gosselink; S. A. Hollak; S. W. Chang; J. van Haveren; K. P. de Jong; J. H. Bitter; D. S. van Es, Reaction pathways for the deoxygenation of vegetable oils and related model compounds, *ChemSusChem*, **2013**, *6* (9), 1576-94.
5. D. Kubička; L. Kaluža, Deoxygenation of vegetable oils over sulfided Ni, Mo and NiMo catalysts, *Appl. Catal., A*, **2010**, *372* (2), 199-208.
6. S. Gong; A. Shinozaki; M. Shi; E. W. Qian, Hydrotreating of Jatropha Oil over Alumina Based Catalysts, *Energy Fuels*, **2012**, *26* (4), 2394-2399.
7. J. A. Lopez-Ruiz; R. J. Davis, Decarbonylation of heptanoic acid over carbon-supported platinum nanoparticles, *Green Chem.*, **2014**, *16* (2), 683-694.
8. Y. Shao; Q. Xia; X. Liu; G. Lu; Y. Wang, Pd/Nb₂O₅/SiO₂ Catalyst for the Direct Hydrodeoxygenation of Biomass-Related Compounds to Liquid Alkanes under Mild Conditions, *ChemSusChem*, **2015**, *8* (10), 1761-7.
9. B. Peng; X. Yuan; C. Zhao; J. A. Lercher, Stabilizing catalytic pathways via redundancy: selective reduction of microalgae oil to alkanes, *J. Am. Chem. Soc.*, **2012**, *134* (22), 9400-5.
10. V. M. Akhmedov; S. H. Al-Khowaiter, Recent Advances and Future Aspects in the Selective Isomerization of High *n*-Alkanes, *Catal. Rev. Sci. Eng.*, **2007**, *49* (1), 33-139.
11. H. Deldari, Suitable catalysts for hydroisomerization of long-chain normal paraffins, *Appl. Catal., A*, **2005**, *293*, 1-10.
12. A. Corma; A. Martinez; S. Pergher; S. Peratello; C. Perego; G. Bellusi, Hydrocracking-hydroisomerization of *n*-decane on amorphous silica-alumina with uniform pore diameter, *Appl. Catal., A*, **1997**, *152* (1), 107-125.
13. S. Triwahyono; A. A. Jalil; N. N. Ruslan; H. D. Setiabudi; N. H. N. Kamarudin, C₅-C₇ linear alkane hydroisomerization over MoO₃-ZrO₂ and Pt/MoO₃-ZrO₂ catalysts, *J. Catal.*, **2013**, *303*, 50-59.
14. D. Hasha; L. Sierra de Saldarriaga; C. Saldarriaga; P. E. Hathaway; D. F. Cox; M. E. Davis, Studies of silicoaluminophosphates with the sodalite structure, *J. Am. Chem. Soc.*, **1988**, *110* (7), 2127-2135.
15. Y. Wang; Z. Tao; B. Wu; J. Xu; C. Huo; K. Li; H. Chen; Y. Yang; Y. Li, Effect of metal precursors on the performance of Pt/ZSM-22 catalysts for *n*-hexadecane hydroisomerization, *J. Catal.*, **2015**, *322*, 1-13.

16. S. Lin; H. Ning; S. Wan-Fu; L. Wei-Min; X. Qun-Ji, Preparation of Pd/Al-MCM-41 Catalyst and Its Hydroisomerization Properties for long chain alkane compounds. In *Stud. Surf. Sci. Catal.*, Sayari, A.; Jaroniec, M., Eds. Elsevier: **2002**; Vol. Volume 141, pp 517-524.
17. S. Gong; N. Chen; S. Nakayama; E. W. Qian, Isomerization of *n*-alkanes derived from jatropha oil over bifunctional catalysts, *J. Mol. Catal. A*, **2013**, *370*, 14-21.
18. Q. Liu; H. Zuo; T. Wang; L. Ma; Q. Zhang, One-step hydrodeoxygenation of palm oil to isomerized hydrocarbon fuels over Ni supported on nano-sized SAPO-11 catalysts, *Appl. Catal., A*, **2013**, *468*, 68-74.
19. H. Zuo; Q. Liu; T. Wang; L. Ma; Q. Zhang; Q. Zhang, Hydrodeoxygenation of Methyl Palmitate over Supported Ni Catalysts for Diesel-like Fuel Production, *Energy Fuels*, **2012**, *26* (6), 3747-3755.
20. N. Chen; S. Gong; H. Shirai; T. Watanabe; E. W. Qian, Effects of Si/Al ratio and Pt loading on Pt/SAPO-11 catalysts in hydroconversion of Jatropha oil, *Appl. Catal., A*, **2013**, *466*, 105-115.
21. M. Ahmadi; E. E. Macias; J. B. Jasinski; P. Ratnasamy; M. A. Carreon, Decarboxylation and further transformation of oleic acid over bifunctional, Pt/SAPO-11 catalyst and Pt/chloride Al₂O₃ catalysts, *J. Mol. Catal. A*, **2014**, *386*, 14-19.
22. M. Y. Smirnova; O. V. Kikhtyanin; M. Y. Smirnov; A. V. Kalinkin; A. I. Titkov; A. B. Ayupov; D. Y. Ermakov, Effect of calcination temperature on the properties of Pt/SAPO-31 catalyst in one-stage transformation of sunflower oil to green diesel, *Appl. Catal., A*, **2015**, *505*, 524-531.
23. C. Wang; Z. Tian; L. Wang; R. Xu; Q. Liu; W. Qu; H. Ma; B. Wang, One-Step Hydrotreatment of Vegetable Oil to Produce High Quality Diesel-Range Alkanes, *ChemSusChem*, **2012**, *5* (10), 1974-1983.
24. J. Hancsók; T. Kasza; S. Kovács; P. Solymosi; A. Holló, Production of bioparaffins by the catalytic hydrogenation of natural triglycerides, *Journal of Cleaner Production*, **2012**, *34*, 76-81.
25. M. C. Claude; J. A. Martens, Monomethyl-Branching of Long *n*-Alkanes in the Range from Decane to Tetracosane on Pt/H-ZSM-22 Bifunctional Catalyst, *J. Catal.*, **2000**, *190* (1), 39-48.
26. P. Mériaudeau; V. A. Tuan; V. T. Nghiem; S. Y. Lai; L. N. Hung; C. Naccache, SAPO-11, SAPO-31, and SAPO-41 Molecular Sieves: Synthesis, Characterization, and Catalytic Properties in *n*-Octane Hydroisomerization, *J. Catal.*, **1997**, *169* (1), 55-66.
27. S. M. Csicsery, Shape-selective catalysis in zeolites, *Zeolites*, **1984**, *4* (3), 202-213.
28. J. A. Martens; W. Souverijns; W. Verrelst; R. Parton; G. F. Froment; P. A. Jacobs, Selective Isomerization of Hydrocarbon Chains on External Surfaces of Zeolite Crystals, *Angewandte Chemie International Edition in English*, **1995**, *34* (22), 2528-2530.
29. I. R. Choudhury; K. Hayasaka; J. W. Thybaut; C. S. Laxmi Narasimhan; J. F. Denayer; J. A. Martens; G. B. Marin, Pt/H-ZSM-22 hydroisomerization catalysts optimization guided by Single-Event MicroKinetic modeling, *J. Catal.*, **2012**, *290*, 165-176.
30. H. Wang; L. Chen; Y. Feng; H. Chen, Exploiting Core–Shell Synergy for Nanosynthesis and Mechanistic Investigation, *Acc. Chem. Res.*, **2013**, *46* (7), 1636-1646.

31. M. Miyamoto; T. Kamei; N. Nishiyama; Y. Egashira; K. Ueyama, Single Crystals of ZSM-5/Silicalite Composites, *Adv. Mater.*, **2005**, *17* (16), 1985-1988.
32. D. Van Vu; M. Miyamoto; N. Nishiyama; Y. Egashira; K. Ueyama, Selective formation of para-xylene over H-ZSM-5 coated with polycrystalline silicalite crystals, *J. Catal.*, **2006**, *243* (2), 389-394.
33. M. Okamoto; L. Huang; M. Yamano; S. Sawayama; Y. Nishimura, Skeletal isomerization of tetradecane catalyzed by TON-type zeolites with a fragmented core-shell structure, *Appl. Catal., A*, **2013**, *455*, 122-128.
34. Y. Bouzizi; L. Rouleau; V. P. Valtchev, Factors Controlling the Formation of Core-Shell Zeolite-Zeolite Composites, *Chem. Mater.*, **2006**, *18* (20), 4959-4966.
35. E. W. Qian; N. Chen; S. Gong, Role of support in deoxygenation and isomerization of methyl stearate over nickel-molybdenum catalysts, *J. Mol. Catal. A*, **2014**, *387*, 76-85.
36. N. Chen; S. Gong; E. W. Qian, Effect of reduction temperature of NiMoO_{3-x}/SAPO-11 on its catalytic activity in hydrodeoxygenation of methyl laurate, *Appl. Catal., B*, **2015**, *174-175*, 253-263.
37. F. Thibault-Starzyk; I. Stan; S. Abelló; A. Bonilla; K. Thomas; C. Fernandez; J.-P. Gilson; J. Pérez-Ramírez, Quantification of enhanced acid site accessibility in hierarchical zeolites – The accessibility index, *J. Catal.*, **2009**, *264* (1), 11-14.
38. C. Morterra; G. Cerrato; G. Meligrana, Revisiting the Use of 2,6-Dimethylpyridine Adsorption as a Probe for the Acidic Properties of Metal Oxides, *Langmuir*, **2001**, *17* (22), 7053-7060.
39. G. Sastre; M. L. Cano; A. Corma; H. García; S. Nicolopoulos; J. M. González-Calbet; M. Vallet-Regí, On the Incorporation of Buckminsterfullerene C60 in the Supercages of Zeolite Y, *The Journal of Physical Chemistry B*, **1997**, *101* (49), 10184-10190.
40. M. C. Claude; G. Vanbutsele; J. A. Martens, Dimethyl Branching of Long n-Alkanes in the Range from Decane to Tetracosane on Pt/H-ZSM-22 Bifunctional Catalyst, *J. Catal.*, **2001**, *203* (1), 213-231.
41. G. C. Bond; R. Yahya, Studies on ruthenium catalysts: Part 1. Reactions of cyclopropane and of ethane with hydrogen on ruthenium/titania catalysts; reaction mechanisms, *J. Mol. Catal.*, **1991**, *68* (2), 243-254.
42. G. Sastre; A. Chica; A. Corma, On the Mechanism of Alkane Isomerisation (Isodewaxing) with Unidirectional 10-Member Ring Zeolites. A Molecular Dynamics and Catalytic Study, *J. Catal.*, **2000**, *195* (2), 227-236.
43. F. Zaera, New advances in the use of infrared absorption spectroscopy for the characterization of heterogeneous catalytic reactions, *Chem. Soc. Rev.*, **2014**, *43* (22), 7624-63.
44. G. S. Lane; J. T. Miller; F. S. Modica; M. K. Barr, Infrared Spectroscopy of Adsorbed Carbon Monoxide on Platinum/Nonacidic Zeolite Catalysts, *J. Catal.*, **1993**, *141* (2), 465-477.
45. P. Hollins, The influence of surface defects on the infrared spectra of adsorbed species, *Surf. Sci. Rep.*, **1992**, *16* (2), 51-94.
46. P. Bazin; O. Saur; J. C. Lavalley; M. Daturi; G. Blanchard, FT-IR study of CO adsorption on Pt/CeO₂: characterisation and structural rearrangement of small Pt particles, *Phys. Chem. Chem. Phys.*, **2005**, *7* (1), 187-194.

47. S. K. Cheah; V. P. Bernardet; A. A. Franco; O. Lemaire; P. Gelin, Study of CO and Hydrogen Interactions on Carbon-Supported Pt Nanoparticles by Quadrupole Mass Spectrometry and Operando Diffuse Reflectance FTIR Spectroscopy, *J. Phys. Chem. C*, **2013**, *117* (44), 22756-22767.
48. B. Peng; Y. Yao; C. Zhao; J. A. Lercher, Towards quantitative conversion of microalgae oil to diesel-range alkanes with bifunctional catalysts, *Angew. Chem. Int. Ed. Engl.*, **2012**, *51* (9), 2072-5.

Chapter 5

General Conclusions

In this study, metal-acid bifunctional catalysts were designed for simultaneous deoxygenation-isomerization of fatty acid esters to produce high quality hydrocarbon fuels with good cold flow and combustion properties. Hydrodeoxygenation rate, isomerization selectivity and the formation of mono-branched alkanes in the simultaneous reaction were improved. In addition, three new catalysis functions were elucidated from experimental results: 1) A synergistic effect involving a hydrogenation metal (Ni or Pt) as the hydrogen dissociated site and partially reduced metal oxides (MoO_x and SnO_x) as the adsorption site for oxygen-containing intermediates was proposed. This synergistic effect contributes to the adsorption and activation of the C=O bond in a fatty acid ester, and therefore suppresses the undesired decarbonylation reaction and promotes the hydrodeoxygenation rate; 2) the presence of Mo^{5+} species or Pt-Sn alloys enhanced the isomerization activity of catalyst. The -OH group in Mo^{5+} species exhibits Brønsted acidity and promotes the skeleton isomerization step in isomerization reaction. Pt-Sn alloys shows higher dehydrogenation activity than Pt and promotes the dehydrogenation step in isomerization reaction; 3) a core@shell structural ZSM-22@ SiO_2 zeolite with enhanced shape-selectivity was synthesized. The silica shell can cover external acid sites and prevent the further isomerization of a mono-branched isomer into a multi-branched isomer. Details are described as follows.

In *Chapter two*, one-step hydroconversion of Jatropha oil into green hydrocarbon fuels was achieved by using a reduced NiMo catalyst. The reduced NiMo catalyst showed high deoxygenation activity in hydrotreating of Jatropha oil at a relatively high temperature (375 °C). Compared to a commercial catalyst – NiMo/ Al_2O_3 , those catalysts with an acid function, *i.e.*, NiMo/ SiO_2 - Al_2O_3 , NiMo/SAPO-11 and NiMo/Al-SBA-15, were highly active in isomerization due to the Brønsted acidity of their supports. NiMo/SAPO-11 showed the highest isomerization activity and relatively lower cracking activity in hydrotreating of Jatropha oil. Therefore, SAPO-11 was considered as a suitable acid support for the simultaneous deoxygenation-isomerization reaction.

Subsequently, the effect of the reduction temperature on the structure and performance of NiMo/SAPO-11 was investigated. The percentage of different valent molybdenum species was strongly dependent on the reduction temperature. As the reduction temperature increased, the percentage of Mo⁵⁺ species decreased, while that of Mo⁴⁺ species increased. Based on the activity test of hydrogenation methyl laurate, it could be concluded that Mo⁵⁺ species are the active site of isomerization, whereas Mo⁴⁺ species act as the adsorption site and combine with nearby nickel particles to provide a synergistic effect for enhancing the hydrodeoxygenation rate.

In *Chapter three*, bifunctional PtSn/SAPO-11 catalyst was designed to enhance the activity of monometallic Pt catalyst. The tin addition substantially changed the performance of the catalyst. The PtSn catalyst favored hydrogenation of carbonyl group and was more efficient to produce isomerized alkanes. After tin addition, the number of Lewis acid sites increased, which could be originated from partial reduced SnO_{2-x} species. These Lewis acid sites can change the adsorption mode and improve the hydrodeoxygenation rate. As the tin addition increased, excessive surface coverage would block the activation of hydrogen on platinum particles, resulting in a decrease in the hydrodeoxygenation activity. Pt-Sn alloys are present in the PtSn1, PtSn1.5 and PtSn2 catalysts, while only some Sn surface-enriched PtSn particles and SnO₂ were observed in the PtSn2.5 and PtSn3 catalysts. The higher isomerization activity of PtSn1, PtSn1.5 and PtSn2 is attributed to an increased formation of unsaturated hydrocarbons by Pt-Sn alloys. It could be concluded that it is important to control the surface concentration of the second metal to obtain highly balanced functions.

In *Chapter four*, ZSM-22@SiO₂ zeolite with a core-shell structure was synthesized by a crystal overgrowth method to passivate acid sites on the external surface and enhance the shape-selectivity of the zeolite. ZSM-22@SiO₂ supports with different amounts of shell silica and SiO₂/Al₂O₃ ratios were used to prepared platinum catalysts. In hydrotreating of methyl palmitate, the amount of silica coating has a large influence on the catalytic performance. Deoxygenation and isomerization activities decreased with increasing amount of coated silica. Characterization results imply that the structure of platinum particles was changed, and the exposed facet varied from (111) to (100),

which most likely cause the decrease in deoxygenation activity. For isomerization, the decrease in the acidity of the support can be considered as the most important factor. On the other hand, the percentage of MoBI significantly increased with increasing amount of the coated silica to 20% (ratio of the amount of the coated silica to the total silica in the support); however, excessive silica coating could not further improve the formation of MoBI. A “pore mouth and key lock” model for alkane isomerization is used to interpret the isomerization behavior. Normal alkanes diffuse into the pore channel and isomerized to MoBI on acid sites near the pore mouth *via* the “pore mouth” model (major adsorption type); a less amount of MuBI can be formed by penetrating the two ends of a normal alkane into different pore mouths, which could not be suppressed by the silica coating approach. The activity and selectivity can be improved by using a support with higher acidity by lowering the SiO₂/Al₂O₃ ratio or by using the designed bimetallic PtSn as the metal function.

In summary, the designed bifunctional catalysts, *i.e.*, NiMo/SAPO-11 and PtSn/SAPO-11, exhibited high activity in hydrotreating of fatty acid esters to produce hydrocarbon fuels that possess high cold flow properties. ZSM-22@SiO₂ was designed as a novel zeolite for the substitution of SAPO-11 to achieve higher shape-selectivity and enhance the formation of mono-branched *iso*-alkanes, which have higher cetane numbers and greater combustion properties. By combining PtSn and ZSM-22@SiO₂ as metal and acid functions, respectively, a highly active bifunctional catalyst was developed for hydrotreating of triglyceride-related compounds. These findings should not only break a new path to produce high quality green transportation fuels, but also enhance our understanding of the structure-performance relationship in catalysis, which give us ideas to design catalysts for new processes.

List of Publications

- [1] Ning Chen, Shaofeng Gong and Eika W. Qian, Single-step hydroconversion of Jatropha Oil to high quality fuel oil over reduced nickel-molybdenum catalysts, *Journal of the Japan Petroleum Institute*, **2013**, 56, 249–252. (Chapter 2)
- [2] Ning Chen, Shaofeng Gong and Eika W. Qian, Effect of reduction temperature of NiMoO_{3-x}/SAPO-11 on its catalytic activity in hydrodeoxygenation of methyl laurate, *Applied Catalysis B: Environmental*, **2015**, 174, 253–263. (Chapter 2)
- [3] Ning Chen, Yuxiong Ren and Eika W. Qian, Elucidation of the active phase in PtSn/SAPO-11 for hydrodeoxygenation of methyl palmitate, *Journal of Catalysis*, **2016**, 334, 79–88. (Chapter 3)
- [4] Ning Chen, Yuxiong Ren and Eika W. Qian, Improved shape-selectivity of TON zeolite in Pt-based catalysts for simultaneous deoxygenation-isomerization of methyl palmitate, to be submitted. (Chapter 4)

List of Related Publications

- [1] Ning Chen, Shaofeng Gong, Hisakazu Shirai, Toshitaka Watanabe, Eika W. Qian, Effects of Si/Al ratio and Pt loading on Pt/SAPO-11 catalysts in hydroconversion of Jatropha oil, *Applied Catalysis A: General*, **2013**, 466, 105–115.
- [2] Shaofeng Gong, Ning Chen, Shinji Nakayama and Eika W. Qian, Isomerization of *n*-alkanes derived from Jatropha oil over bifunctional catalysts, *Journal of Molecular Catalysis A: Chemical*, **2013**, 370, 14–21.
- [3] Eika W. Qian, Ning Chen and Shaofeng Gong, Role of support in deoxygenation and isomerization of methyl stearate over nickel–molybdenum catalysts, *Journal of Molecular Catalysis A: Chemical*, **2014**, 387, 76–85.
- [4] Development of catalysts for upgrading of Jatropha oil, *Akita Convention of the Japan Petroleum Institute (the 42th Petroleum-Petrochemical Symposium of JPI)*, 11–12 October, **2012** (oral presentation).
- [5] Hydroconversion of Jatropha oil over Nickel-Molybdenum catalysts, *Kitakyushu Convention of Japan Petroleum Institute (the 43th Petroleum-Petrochemical Symp. of JPI)*, 14–15 November, **2013** (oral presentation).
- [6] Hydrodeoxygenation and Isomerization on Reduced NiMo Catalysts, *Seventh Tokyo Conference on Advanced Catalytic Science and Technology (TOCAT7)*, 1–6 June, **2014** (poster presentation).
- [7] Hydrodeoxygenation of methyl laurate over reduced NiMo/SAPO-11 catalyst, *114th Shokubai Toronkai of Catalysis Society of Japan*, 25–27, September, **2014** (oral presentation).
- [8] Effect of Sn addition on Pt/SAPO-11 catalyst in hydrogenation of methyl palmitate, *64th R&D Symposium of Japan Petroleum Institute*, 27 May, **2015** (oral presentation).
- [9] Effect of surface modification of zeolite in the hydrodeoxygenation of methyl palmitate, *Nagoya Convention of the Japan Petroleum Institute (the 45th Petroleum-Petrochemical Symposium of JPI)*, 5–6 November, **2015** (oral presentation).

Acknowledgements

The study presented in this doctoral dissertation is the summary of the author's work performed between 2013 and 2016 at the Department of Bio-Applications and Systems Engineering, Graduate School of Bio-Applications and Systems Engineering, Tokyo University of Agriculture and Technology. The financial support from the government of Japan is gratefully acknowledged.

The author wishes to express his sincerest gratitude to Professor Eika W. Qian, the author's supervisor, for providing a chance to study at this department, further for his invaluable suggestions and discussions. The author also wishes to express his gratitude to Associate Professors Nobuyuki Akai and Susumu Inasawa, and Professors Hidehiro Kamiya and Yoich Tominaga, for their precious suggestions.

The author would like to thank Dr. Shaofeng Gong and Dr. Takashi Toyoda, who has taught the author how to do research and guided the author into the field of catalysis. The author is also grateful to Mr. Yuxiong Ren and Mr. Toshitaka Watanabe, as well as other coauthors present in the publications for their valuable collaboration to this study. The author is indebted to all the members of the research group of Professor Eika W. Qian.

Finally, the author would like to give his greatest thanks to his parents, aunt-Fumiyo Tominaga and uncle-Yuqing Weng for their love and continuous encouragement throughout the present study. The author also grateful his fiancée-Xiangru Tang for her love and patience throughout the study.

February 2016

Ning Chen